SOILS and ROCKS

An International Journal of Geotechnical and Geoenvironmental Engineering

Soils and Rocks publishes papers in English in the broad fields of Geotechnical Engineering, Engineering Geology, and Geoenvironmental Engineering. The Journal is published quarterly in March, June, September and December. The first issue was released in 1978, under the name *Solos e Rochas*, being originally published by the Graduate School of Engineering of the Federal University of Rio de Janeiro. In 1980, the Brazilian Association for Soil Mechanics and Geotechnical Engineering took over the editorial and publishing responsibilities of *Solos e Rochas*, increasing its reach. In 2007, the journal was renamed Soils and Rocks and acquired the status of an international journal, being published jointly by the Brazilian Association for Soil Mechanics and Geotechnical Engineering, by the Portuguese Geotechnical Society, and until 2010 by the Brazilian Association for Engineering Geology and the Environment.

Soils and Rocks

1978,	1 (1, 2)
1979,	1 (3), 2 (1,2)
1980-1983,	3-6 (1, 2, 3)
1984,	7 (single number)
1985-1987,	8-10 (1, 2, 3)
1988-1990,	11-13 (single number)
1991-1992,	14-15 (1, 2)
1993,	16 (1, 2, 3, 4)
1994-2010,	17-33 (1, 2, 3)
2011,	34 (1, 2, 3, 4)
2012-2019,	35-42 (1, 2, 3)
2020,	43 (1, 2, 3, 4)
2021,	44 (1, 2, 3, 4)

ISSN 1980-9743
ISSN-e 2675-5475 CDU 624.131.1

Soils and Rocks
An International Journal of Geotechnical and Geoenvironmental Engineering
ISSN 1980-9743 ISSN-e 2675-5475

Publication of
ABMS - Brazilian Association for Soil Mechanics and Geotechnical Engineering
SPG - Portuguese Geotechnical Society
Volume 44, N. 4, October-December 2021

Table of Contents

LECTURE

Soils and Rocks
An International Journal of Geotechnical and Geoenvironmental Engineering
www.soilsandrocks.com
ISSN 1980-9743
ISSN-e 2675-5475

Large scaled field tests on soft Bangkok clay

Arumugam S. Balasubramaniam[1#]

Lecture

Keywords
Bangkok soft clay
Ground improvement schemes
Large scaled field tests
Asian Institute of Technology
Norwegian Geotechnical Institute

Abstract

In this lecture the interpretations of fully instrumented tests embankments and their role in the development of appropriate ground improvement techniques for highways, motorways and airfields on soft clay deposits is illustrated through well documented case studies in Bangkok, Thailand and Muar Flat Site in Kuala Lumpur. For the Bangkok Plain and with sand backfills the performance of embankments with different schemes of vertical drains was evaluated over a period of 25 years. Aspects such as recharging effects due to the drains, inadequate measures in maintaining vacuum during vacuum applications and possible hydraulic connections with large diameter drains are discussed. For the Muar test embankments, the role of fill strength in residual soil embankment and the field deformation analysis in separating consolidation settlement from immediate settlement and creep settlements is presented. Novel interpretations of settlement from pore pressure dissipations, secondary settlement from field measurements and decay of lateral deformation rate with time were also made.

1. Introduction

In the evaluation of geotechnical parameters, traditionally laboratory tests are performed. However, when the quality of undisturbed samples as taken from boreholes or block samples is in doubt, in-situ tests are performed. These in-situ tests can be on small scale such as vane tests, cone penetration tests, pressuremeter tests and dilatometers tests. Large scale field tests are also carried out in parallel and these tests are fully instrumented. Over the last 32 years the senior author has been involved in the interpretation of the test data on several embankments in Thailand, Malaysia and in Southeast Queensland. This paper touch upon some of the lessons learnt from these studies and how they have improved our understanding on soft clay behaviour and ground improvement schemes as studied with test embankment. Major emphasis will be on the cases in Thailand and Muar site Malaysia and these experiences will be presented in chronological order and not country wise. The concept of large scale field test arise from the need that our single element laboratory scale tests are not adequate to cover all the features that we encounter in sedimentary soils with varying layer thickness and soil properties; also the small scale field tests can at time mislead the large scale behaviour covering a much larger loaded area. Thus the concept of building test embankments began.

Typical soil profile in the Bangkok Plain is shown in Figure 1. Eide (1977) reported the results of a test section on the Bangkok-Siracha Highway as measured in 1966. The ground condition along the route was considered to be very soft. Sand drains of 0.2 m diameters were installed by the displacement method. They were placed in triangular pattern at 2 m spacing. Sand drains increased the rate of settlement but not to a sufficient degree. The most negative aspect quoted by Eide (1977) was that, even though the sand drains accelerated the consolidation in the first 18 months, yet even at the end of this period the rate of settlement was still as much as 0.03 m per month, which was considered to be high. Possibly due to the low factor of safety, a substantial part of the total settlement was due to continuous undrained creep without volumetric strain, when the stress states are close to failure. Further, Cox (1968), in his research report at AIT, concluded that the design and construction of road embankments over the soft deltaic clays in South East Asia is a very complex engineering problem. This is because the pore pressure response and settlement characteristics correspond to lightly over-consolidated states rather than normally consolidated states.

#Corresponding author. E-mail address: a.bala@griffith.edu.au
[1]Griffith University, Griffith School of Engineering, Gold Coast, Queensland, Australia.

Submitted on March 23, 2021; Final Acceptance on June 04, 2021; Discussion open until Invited Lecture. No discussions.
https://doi.org/10.28927/SR.2021.069921

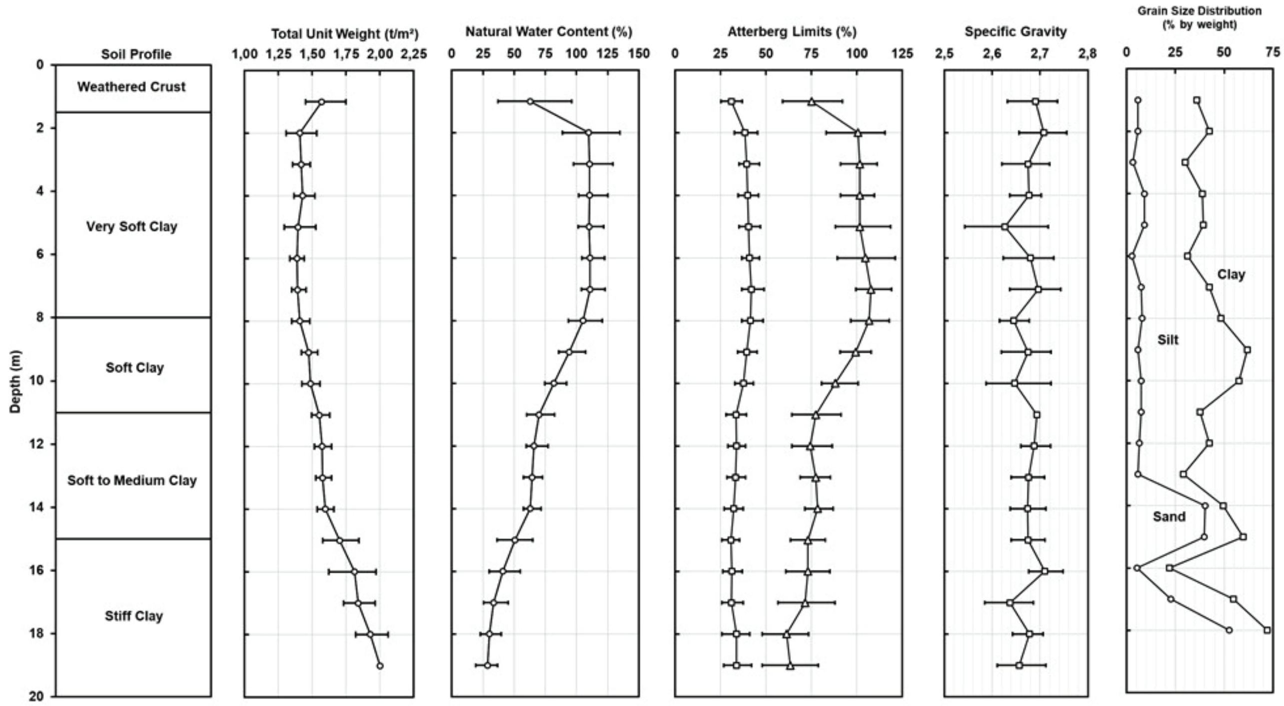

Figure 1. Typical soil profile in the Bangkok plain.

Dr. Za Chieh Moh and his colleagues were the pioneers in the study of test embankment at the Second International Airport site in Bangkok as early as 1970. Full scale test embankments were built at Nong Ngo Hao by Moh et al. (1973) to study the in-situ behaviour. Embankment I was built rapidly to failure. The failure height was only 3.4 m. Embankment II was in two sections - one was with height varying from 0.5 m to 2.9 m and the other had the 2.9 m constant height. These embankments were studied thoroughly for their behaviour by several masters and also Doctoral student at AIT.

The next major study was associated with the Royal Thai Navy Dockyard in Pomprachul, Thailand and work began on this scheme in 1975. The test site is situated at the mouth of the Chao Phraya River in Samut Prakarn province, approximately 20 km south of the Bangkok city. The embankment, which was built in two stages, was 90 m long, 33 m wide, 2.35 m high and consisted of three sections, namely a section with no drains, a section with 2.5 m spacing, and a section with drains of 1.5 m spacing (as shown in Figure 2a and Figure 2b). The soil profile is in Figure 2c. The sand drains consisted of small diameter (0.05 m) sand wicks and were installed to a depth of 17 m by the displacement method. These sand wicks were constructed at the site by pouring sand inside a permeable membrane. First a closed end steel casing 75 mm internal diameter was driven into the ground and the sand wick was lowered into the casing and the casing was subsequently withdrawn. A total of 166 piezometers were installed below the test fill area and outside of it. Surface and subsurface settlement points were installed to monitor the settlement along the centre line and the edges of the test embankment. Three hydrostatic profile gauges were installed, that is, one along each central cross-section of a test section. Also, eleven magnetic movement plates were used to monitor lateral displacements along the gauge. Three inclinometer casings were installed along the centre line of each test section.

At the airport site in Nong Ngu Hao, the most extensive sand drain studies on test embankments were performed in 1983 (see Moh et al., 1987) as part of the ground improvement scheme for the runway pavement and other sections of the taxiways and landside roads. Sand drains of minimum diameter 0.26 m were installed to a depth of 14.5 m by water jetting. The test program included three test areas, one with surcharge fill, and one with vacuum loading and a third with ground water lowering. Test Section 1 was 40 m × 40 m in plan and sand drains were installed at 2 m spacing in triangular pattern. The vacuum load was not successful as several leakages developed and finally the section was covered with plastic shield. Test Section 3 was similar to the Test Section 1 except that the spacing of the drain was increased to 2.4 m. Due to similar problem as in Section 1; the loading was not successful. The test Section 2 was slightly larger than test Section 1 and pre-loading of 60 kN/m^2 was applied in three stages. While difficulties were encountered in maintaining the vacuum load as well as

(a)

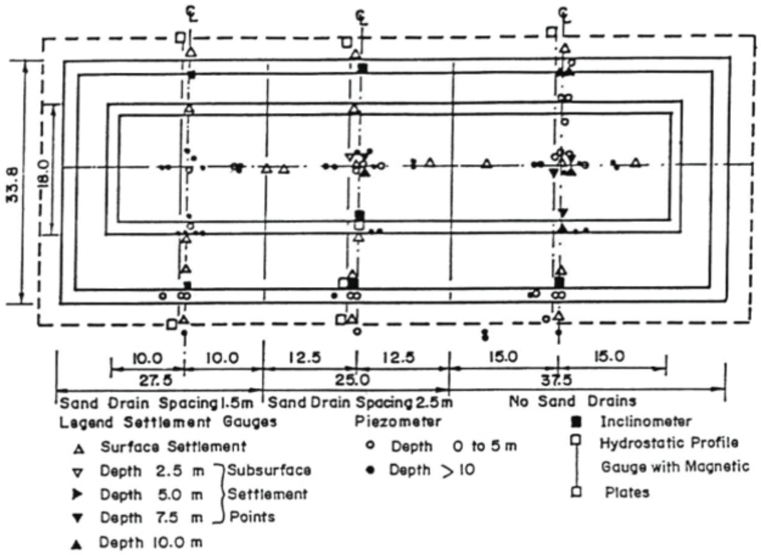

(b)

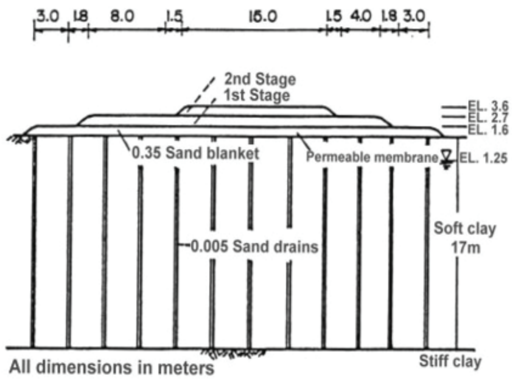

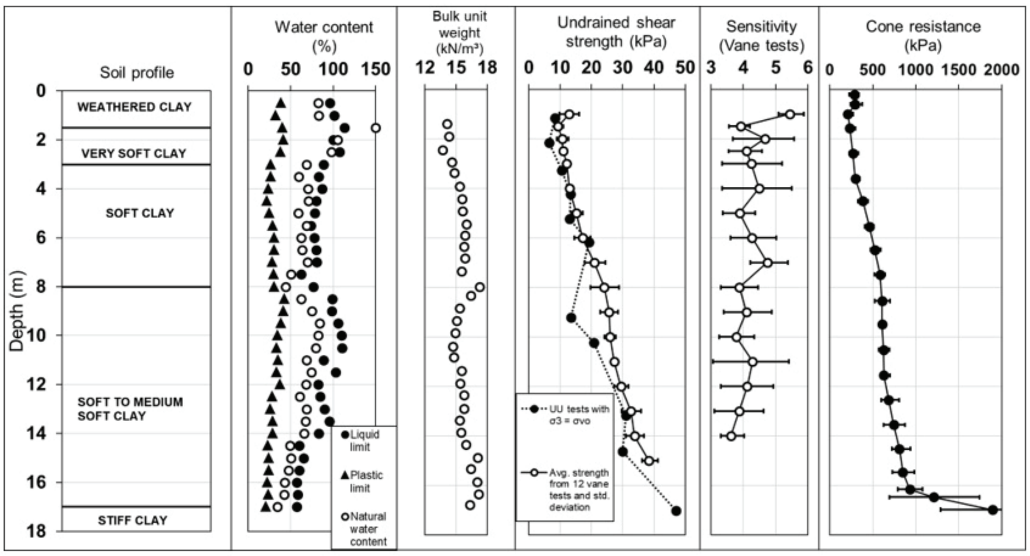

Figure 2. (a) plan of test embankment at RTN Dockyard site; (b) elevation of test embankment at RTN Dockyard site; (c) general properties of Pom Prachul Clay at RTN Dockyard site.

the ground water lowering, the embankment surcharge was found to be a reliable technique when compared to vacuum loading in accelerating the consolidation with sand drains.

A significant extent of the North-South Expressway from Bukit Kayu Hitam at the Malaysian-Thai border to Johor Baru at the southern most location passes through soft clay deposits. Fourteen soil improvement schemes were designed and constructed at Muar flat sites. These embankments were instrumented to measure the vertical settlements, lateral movements and pore pressures. Table 1 gives brief details of these embankments and also they are also shown in Figure 3. Several of these embankments were studied by the first author and his colleagues at AIT with a number of Masters Students as their thesis research. In particular the embankment built with residual soil and used as the embankment in a prediction symposium and the work of Balachandran (1990), Ratnayake (1991), Loganathan (1992) and Sivaneswaran (1993) in particular will be referenced. The work of Balachandran (1990) extends the prediction made by the first author on the embankment built to failure. Ratnayake (1991) analysed the embankment with vertical drains. Loganathan (1992) used the field deformation analysis to separate the immediate settlement from the consolidation settlement during the loading stage and to separate the consolidation settlement and the creep settlement during the performance stage. This technique was different from the Asaoka technique (Asaoka, 1978) used to estimate the consolidation settlement especially under one dimensional consolidation. When high embankments were built creep is a major factor and this makes it difficult to estimate the so-called residual settlements during the maintenance period in most road works and other projects. The work of Sivaneswaran illustrates the powerful tool of normalised settlement and normalized lateral deformation in studying the ground response under different schemes of ground improvement.

Table 1. Muar flats ground improvement schemes.

Scheme	Ground Improvement	Height
3/2, 6/6	Control	3 m, 6 m
3/1, 6/1	Electro Chemical Injection	3 m, 6 m
3/3	Sand Sandwick Method	3 m
3/4, 6/8	Preloading, Geogrid & Prefabricated Vertical Drain	3 m, 6 m
6/2	Well Point Preloading	6 m
6/3	Electro Osmosis	6 m
6/4	Prestressed Spun Piles	6 m
6/5	Sand Compaction Piles	6 m
6/7	Vacuum Preloading & Prefabricated Vertical drain	6 m
6/9	Preloading & Vertical Drain	6 m

The above experiences and the lessons learnt led to a rather cautious approach, on the final studies carried out (for a two year period from 1994 to 1995) for the construction of the runway and other structures at the Second Bangkok International Airport (SBIA) site. In this study, the use of pre-fabricated vertical drains (PVD) and surcharge was concluded as the most suitable ground improvement technique.

1.1 Vertical drain studies in Bangkok Siracha Highway (1967)

The potential use of surcharge and vertical drains as a ground improvement technique was explored as early as 1966 (see Eide (1977)) for its application in bridge approaches.

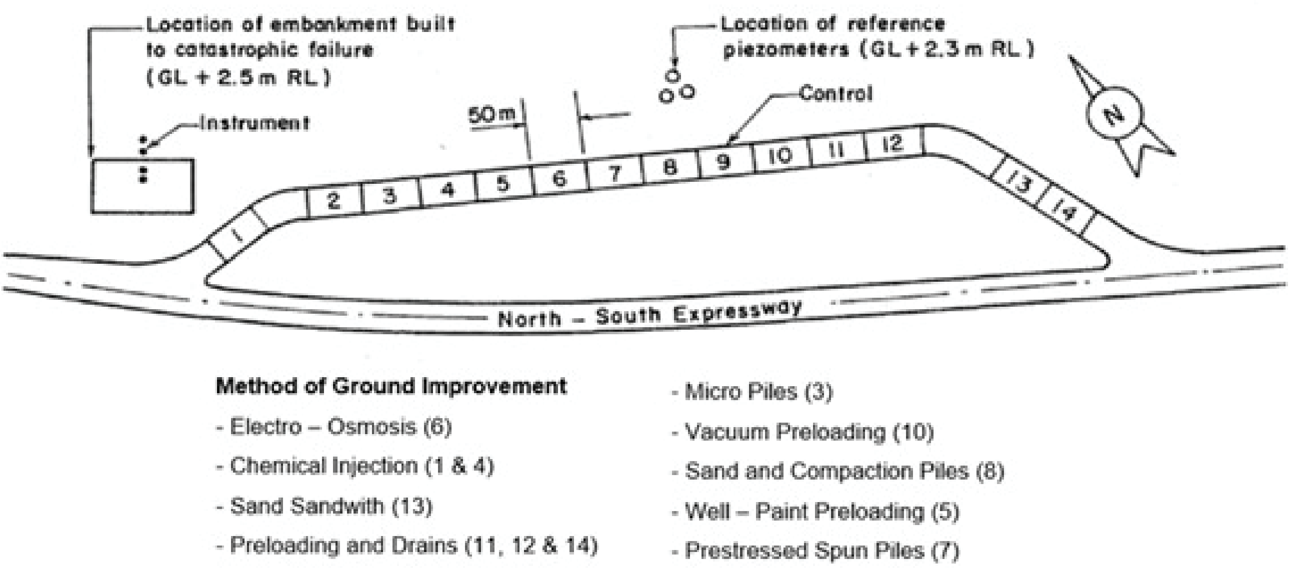

Figure 3. Locations of embankments.

A test section on the Bangkok-Siracha Highway was built and tested with 0.20 m diameter sand drains and the depth of sand drains varied in steps from 4 to 13 m. During construction, failure of the soft clay occurred in five locations and the 2.2 m high embankment was furnished with 8 m wide berms to assure stability. From the observed settlement of the test embankment, Eide (1977) concluded that the drained embankment section settled most to start with, but after one year the rate of settlement was almost the same, approximately 0.0025 m per month on both the drained and undrained sections. The practical conclusion reached by Eide (1977), was that this type of drain and spacing would not serve the purpose in bridge approaches. However, Eide (1977) agreed that the results obtained might have been affected by other factors such as slip failures, the remoulding effect from the installation of drains, the low permeability and greater secondary consolidation settlement of the soft clay.

1.2 Vertical drains study at the Dockyard site

A second attempt was made with vertical drains in 1975 to 1977, with the construction of a dockyard for the Royal Thai Navy, and a test embankment was built (see Figure 2a and Figure 2b) in order to evaluate the performance and suitability of sand drains (sand wick type of drains) as a mean to accelerate the consolidation of the soft clay. Without an understanding of the recharge effect due to the sand wicks on the piezometric drawdown, doubts were cast on the pore pressure measurements as revealed below the natural terrain in which the sand wick was installed and this led to the installation of additional piezometers and finally there were a total of 166 piezometers monitoring the pore pressures below the clay surface. It was found that, the installation of the sand wicks have recharged the area below the test embankment with and without drains, and erased the normal piezometric drawdown which normally existed in the Bangkok subsoils due to deep well pumping, as can be seen in the area which was not influenced by the test embankment location installed with sand wick drains. This recharging effect was somehow not envisaged in the original planning and design of the test embankment. However, it gave valuable insight into the extensive deep well pumping in the Bangkok plain, and the piezometric drawdown that has resulted in the Bangkok subsoils as a consequence of this ground water withdrawal.

1.2.1 Description of test embankment and soil profile

The performance of sand drains (sand wick type of drains) at the Naval Dockyard site, Pom Prachul, Thailand was investigated in 1975 by constructing an instrumented test embankment. The test site is situated at the mouth of the Chao Phraya River in Samut Prakarn province, approximately 20 km south of the Bangkok city. The embankment, which was built in two stages, was 90 m long, 33 m wide, 2.35 m high and consisted of three sections, namely a section with no drains, a section with 2.5 m spacing, and a section with drains of 1.5 m spacing (as shown in Figure 2a and Figure 2b). The soil profile is shown in Figure 2c. The sand drains consisted of small diameter (0.05 m) sand wicks and were installed to a depth of 17 m by the displacement method. These sand wicks were constructed at the site by pouring sand inside a permeable membrane. First a closed end steel casing 75 mm internal diameter was driven into the ground and the sand wick was lowered into the casing and the casing was subsequently withdrawn. A total of 166 piezometers were installed below the test fill area and outside of it. Surface and subsurface settlement points were installed to monitor the settlement along the centre line and the edges of the test embankment. Three hydrostatic profile gauges were installed, that is, one along each central cross-section of a test section. Also, eleven magnetic movement plates were used to monitor lateral displacements along the gauge. Three inclinometer casings were installed along the centre line of each test section. The typical soil profile at the site is shown in Figure 2c.

1.2.2 Pore pressure measurements below the test embankment

The loading pattern for the three test sections and the pore pressure observations are shown in Figure 4a. The piezometric drawdown is shown in Figure 4b. Before constructing the test embankment a sand blanket of 0.35 m was placed and this corresponded to a surcharge pressure of 5.5 kN/m^2. Then the first stage of loading was carried out in 25 days with a fill height of 1.1 m and a surcharge pressure of 19 kN/m^2. Thus, at the end of the first stage of loading the surcharge pressure was 24.5 kN/m^2. After a waiting period of 60 days, the embankment was raised to 2.35 m (inclusive of the 0.35 m sand blanket). The second stage loading was for a period of one month and the observations were continued for a total period of ten months.

The piezometers P41, P27 and P13 located at 7.5 m depths in the three sections indicated consistent rise during the loading phase and drop in values during the waiting period and under the time observed after the full surcharge. These piezometers measured the absolute values of the pore pressures and thus included the original ground water pressure before loading. As shown in Figure 4a, the static ground water pressure was observed from the observation well with hydrostatic assumptions and no drawdown. The dummy piezometers installed at a location far away from the test embankment and without the influence of the sand wick and the surcharge will give the static water pressure inclusive of any possible drawdown due to deep well pumping. At this site the piezometric drawdown only start at a depth below 7.5 m and as such the hydrostatic water pressure indicated by the observation well and the dummy piezometers located at 7.5 m depths are more or less coincident, indicating very small drawdown.

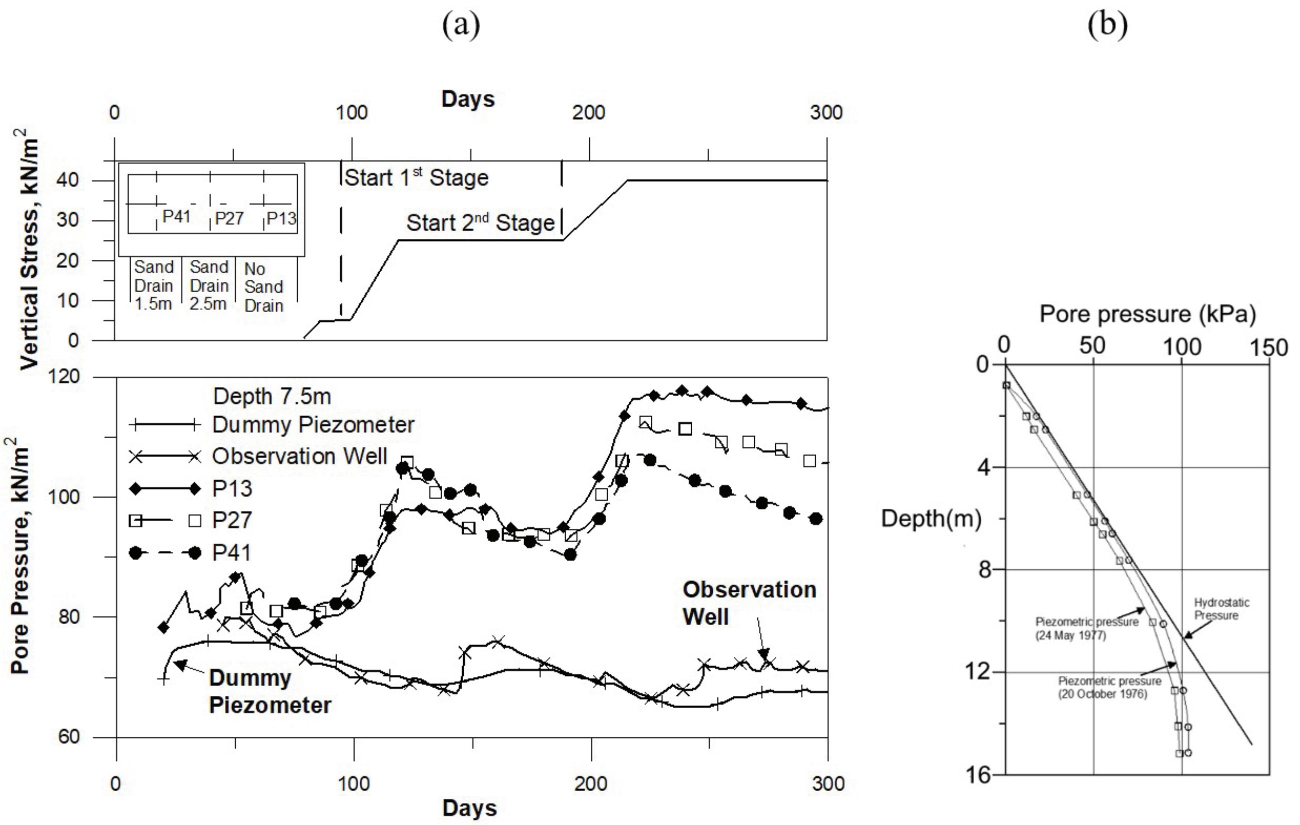

Figure 4. (a) typical piezometer readings at RTN Dockyard site; (b) variation of piezometric pressures with depth at RTN Dockyard site.

All the 166 piezometers were indicating consistent values of the pore pressures. However, the active piezometers installed at depths of 10 to 15 m indicated that the piezometric drawdown below the embankment is more or less erased by the sand drains which have recharged the drawdown area back to its hydrostatic conditions. Thus at deeper depths the absolute values of the piezometer readings under the embankments will be a sum of the static water pressure without any drawdown and the excess pore pressure induced by the surcharge loading. In order to clarify the situation, additional piezometers were installed along the centre line of the longitudinal section of the test embankment from the northern edge corresponding to the closely spaced sand drain section and also along the edge of the eastern boundary of the test embankment. Figure 5 shows the distance from the edge of the embankment in the east direction, up to which the drains have influenced in erasing the drawdown. A similar phenomenon is noted in the north direction along the centre line. In both directions the full draw down was only realized at distances of about 15 to 20 m away from the edges of the embankment. This would indicate that having the three sections side by side without any space in between them was a grave mistake in planning the overall testing program. Ideally speaking the three sections must be separated from each other with substantial allowance for the zone of influence of the drains in recharging the draw down area below the embankment. This was observed in the final planning of the test embankment with PVD at the Second Bangkok International Airport (SBIA) site in the 1994-1995 studies. The three test embankments at the SBIA site were separated from each other with substantial space between them.

1.2.3 Measured and computed settlements at the Dockyard site

Settlement records from 47 active settlement plates have been studied and typical cases are plotted in Figure 6. In this figure the surface settlement at the centre line of the three test sections are plotted with respect to time. Also shown in this figure is the loading pattern with time in terms of the surcharge stress (vertical stress increment). These settlement records are in accordance with the pore pressure dissipation, shown in Figure 4a. The section with closer drain spacing showed higher settlements than the one with wider spacing and the one with no drain. It has already been discussed that the wider spaced drain section was interfering with the no drain section. Thus substantial lateral drainage would have taken place in the no drain section, due to the influence of the nearby adjoining drain section with wider spacing.

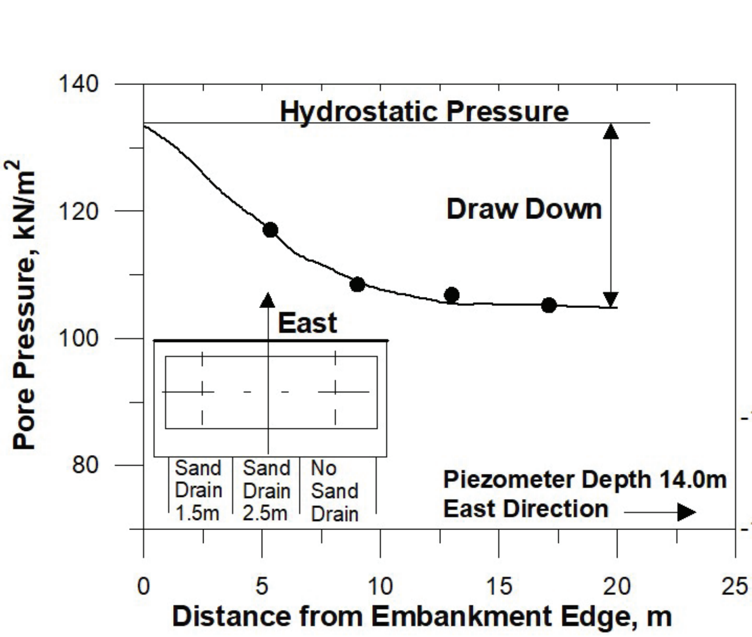

Figure 5. Piezometric pressure vs. distance from the edge of the embankment at RTN Dockyard site (East direction).

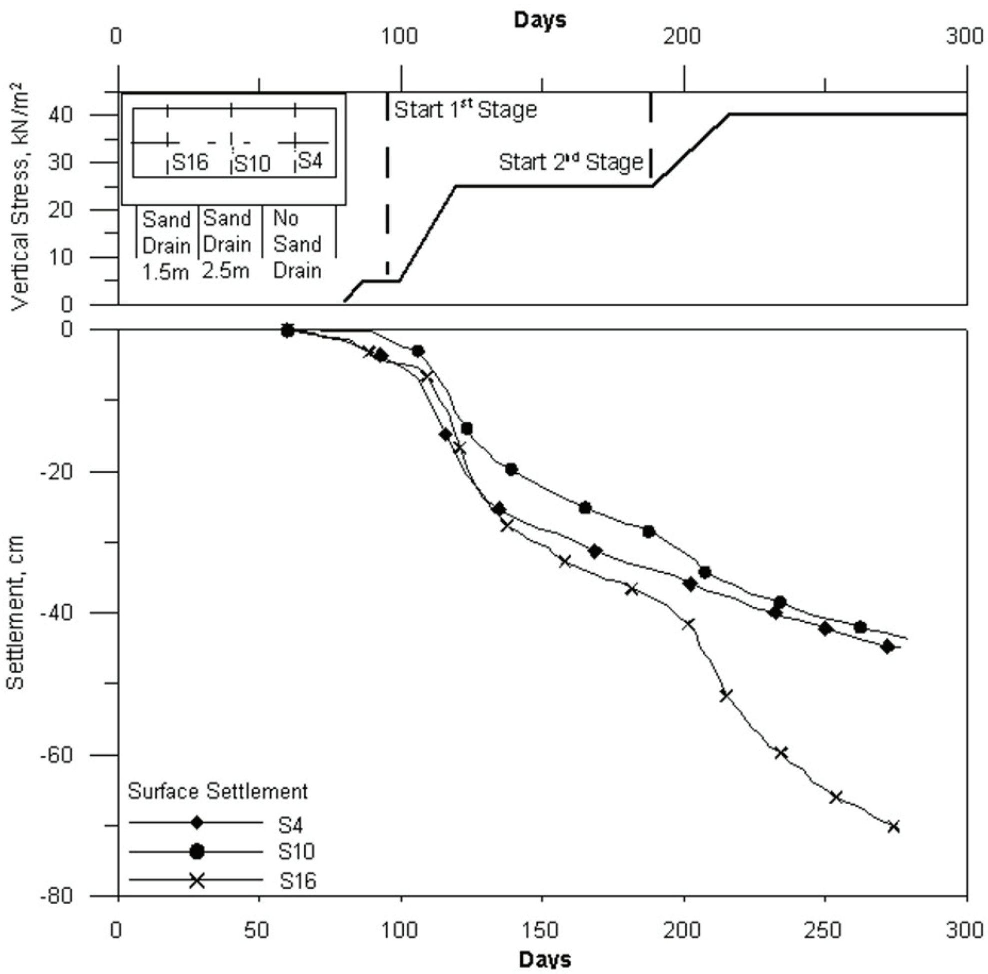

Figure 6. Typical settlement point readings at RTN Dockyard.

Using the elastic theory for increment in stresses below the test sections and the undrained modulus from CK_0U triaxial tests immediate settlements were computed and plotted in Figure 7. It can be seen that very little immediate settlement occurs below a depth of 11 m. The immediate surface settlement under the first stage loading and the second stage loading was computed to be 36 mm and 115 mm respectively. The total primary consolidation settlement under the embankment loading was calculated using the stress strain curves from Oedometer tests. Figure 8 shows the variation of the primary consolidation settlement with depth. In Figure 8, the consolidation settlements were computed from six series of consolidation tests performed with the Lever Arm Consolidometer, Anteus Consolidometer and Bishop Consolidometer. In Series SC seven tests were conducted from 1 to 16 m with 24-hour load increment duration and load increment duration of one. Similar series of tests were conducted in the Anteus Consolidometer as Test Series AC.

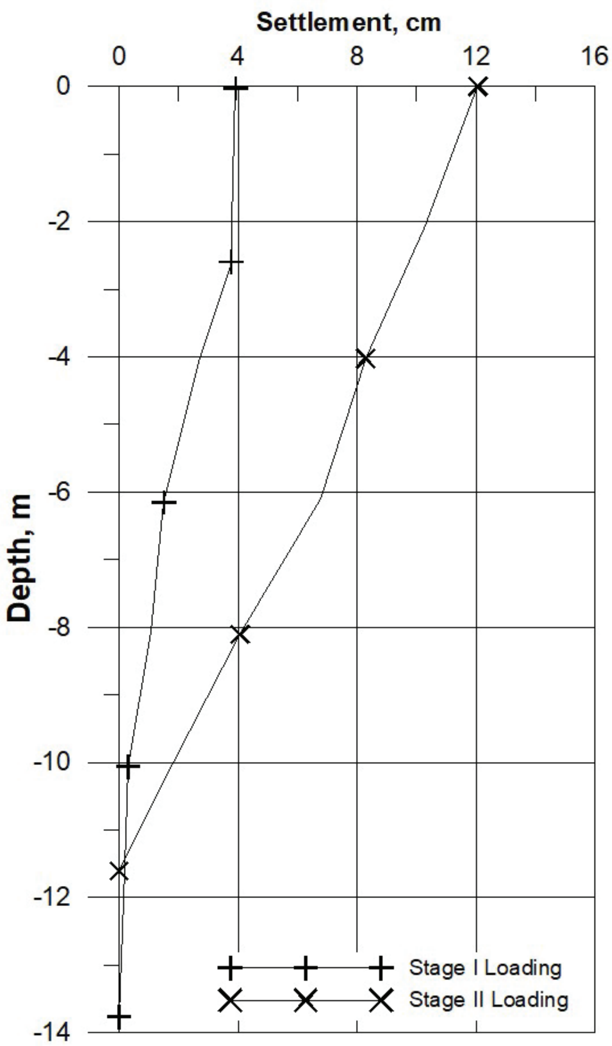

Figure 7. Immediate settlement below embankment at RTN Dockyard site.

Bishop Consolidometer was used in Test Series BC and the load increment duration and ratio were similar to the SC and AC series. In Test Series SI, small load increments were used in the Lever Arm Consolidometer to determine the accurate determination of the pre-consolidation pressure. The measured settlements were in the drained section with 1.5 m drain spacing. These data indicate that even in the 1.5 m-drained section, the primary consolidation is not yet completed.

The major lesson learnt from this trial embankment was that, the sand wick drains have recharged the zone that was originally under piezometric drawdown. Thus, for the bottom later of the soft clay the recharging would have resulted in a decrease in the effective stress and this is the reason why the settlements were smaller below the upper 5 m where there was no drawdown before. Also, the recharging zone seems to extend laterally up to a distance of about 15 m or so, as such the no-drain section would have been influenced by the drained section. It was therefore better to have had three separate sections spaced out in such a manner that there is minimum interference, and the data from each embankment truly represents a no-drain section and the sections with the wider and narrower spacing of drains.

2. Muar clay test embankments

Several lessons were learnt from the analysis of the Muar clay test embankments. The well documented publications

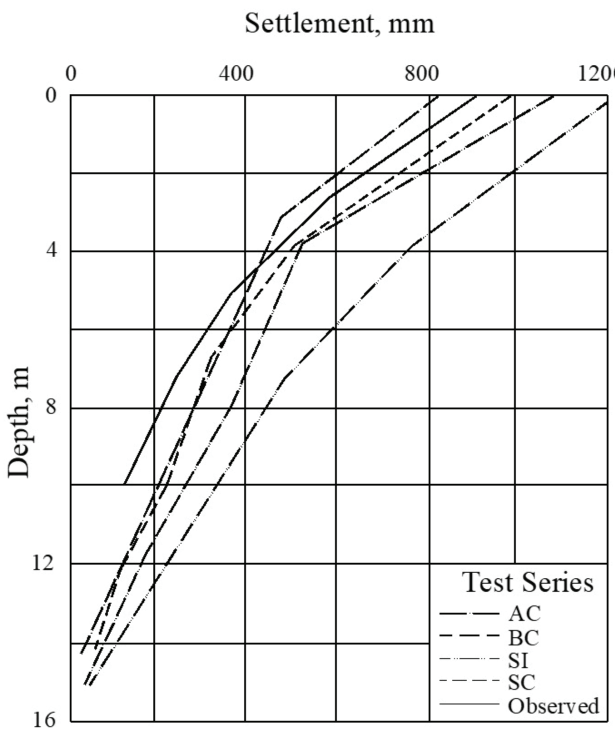

Figure 8. Consolidation settlement below embankment as calculated at RTN Dockyard site.

on the behaviour of the residual soil test embankment built to failure indicated how the performance of such a simple field problem can deviate from the known behaviour of sandfill test embankments. The inclusions of the strength of well compacted residual soil fill material, seem to offer good tensile strength characteristics and prevented the formation of tensile cracks at the base of the embankment. The performance of this embankment, especially pore pressure pattern, stability, settlement, and lateral deformation, were predicted by four predictors, namely, Prof. A. S. Balasubramaniam (Thailand), Prof. J. P. Magnan (France), Prof. A. Nakase (Japan) and Prof. H. G. Poulos (Australia). Their predictions were presented in the "International Symposium on Trial Embankments on Malaysian Muar Clays," in November 1989, held in Kuala Lumpur, Malaysia. All predictors were given the same soil properties and field instrumentation results (Brand & Premchitt, 1989). Most experts also made poor predictions of settlements pore pressures and lateral movements.

The CRISP program as based on the critical state soil mechanics is superior in predicting the coupled behaviour of undrained and consolidation phenomenon in these embankments. The Muar clay test embankments also illustrated that the Pads available in the market for accelerating the dissipation of pore pressures are not 100 percent effective as expected by classical theories of Barron and others. Hansbo in particular considered the non-Darcian flow of water during consolidation with drains in clays and also several other authors studied the effect of smear and possible well resistance in the drains. The Muar clay test embankments also showed the defects in using sand compaction piles, piled embankments and the use of electro-osmosis.

Further studies conducted at AIT on the creep behaviour of the Muar clay test embankments in which continuous undrained creep occurred with the increase in lateral deformation indicate that undrained creep in soft clays due to high embankments is quite substantial. In places where high embankments are constructed with residual soils such undrained creep plays an important role. Loganathan (1992) used the field deformation analysis to separate the immediate settlement from the consolidation settlement during the loading stage and to separate the consolidation settlement and the creep settlement during the performance stage. This method was different from the Asoka technique used to estimate the consolidation settlement especially under one dimensional consolidation. When high embankments are built in soft clays creep is a major factor and this makes it difficult to estimate the so-called residual settlements during the maintenance period in most road works and other projects. Table 1, Figure 3 and Figure 9b contain details of the test embankments built at the Muar Plain. Details of the soil profile at the Muar test embankment site is shown in Figure 9a.

The total settlement observed beneath an embankment subjected to step loading, is basically a combination of different components, namely, immediate settlement, consolidation settlement, and creep settlement. Establishing relationships among these settlements components, upon separating them from the total settlement observed in the field, will facilitate settlement predictions from relatively simple numerical computations. The separation of settlement components provides better understanding of settlement mechanism and thus far better design of step loading. Time-dependent deformations due to undrained creep can be quite large in both normally, consolidated and highly over-consolidated clays. Creep effects are more important for horizontal than for vertical deformations (Christian & Watt, 1972). However, coupling of drained creep with the undrained one could be analytically more cumbersome and would require soil data that are difficult to obtain. A new methodology, termed as field deformation analysis (FDA), based on the changes in volume of foundation soil under embankment loading, is proposed by Loganathan (1992) to separate and quantify settlement components. Shibata (1987) observed that significant volume changes occur during embankment construction and that the behavior of the embankment deviated significantly from undrained conditions. Ting et al. (1989) and Toh et al. (1989) used a similar concept, considering volumetric deformation of embankment foundation under loading, to separate settlement components for Malaysian embankments.

The total settlement observed during loading is a combination of immediate and consolidation settlement components. Figure 10 shows the subsoil deformation pattern due to undrained deformation, which causes the immediate settlement. Since this occurs in an undrained manner, the magnitude of settlement deformation volume, designated as *AOC,* should be equal to the lateral deformation volume, designated as *APM.* Due to dissipation of excess pore pressures, the process of consolidation takes place simultaneously. Figure 10 also shows the ultimate deformation pattern of the embankment foundation at the end of loading, where the volume changes vertically *(ABC)* and laterally *(APMQA)* are due to consolidation. It should be noted that the volumes referred to here are for the unit length of the embankment.

The observed settlement volume in the field from settlement gauge readings, for half the embankment is defined as V_{vL} (volume OAB). The settlement volume V_{vL}(volume OAB) at the end of each loading stage is the resultant of the volume change due to the immediate settlement (V_{iL}= volume OAC) and the consolidation settlement (V_{cL} = volume CAB) as shown in Figure 10. Since the loading period is comparatively small the creep settlement is ignored. The lateral volume increase (= volume APM) due to undrained deformation (immediate settlement) decreases during consolidation due to the dissipation of excess pore pressures (Christian & Watt, 1972). Let α be the ratio of the lateral volume reduction to the consolidation settlement volume. Then

$$\alpha = \frac{Lateral\ Consolidation\ Volume}{Consolidation\ Settlement\ Volume\ (V_{cL})} \quad (1)$$

(a)

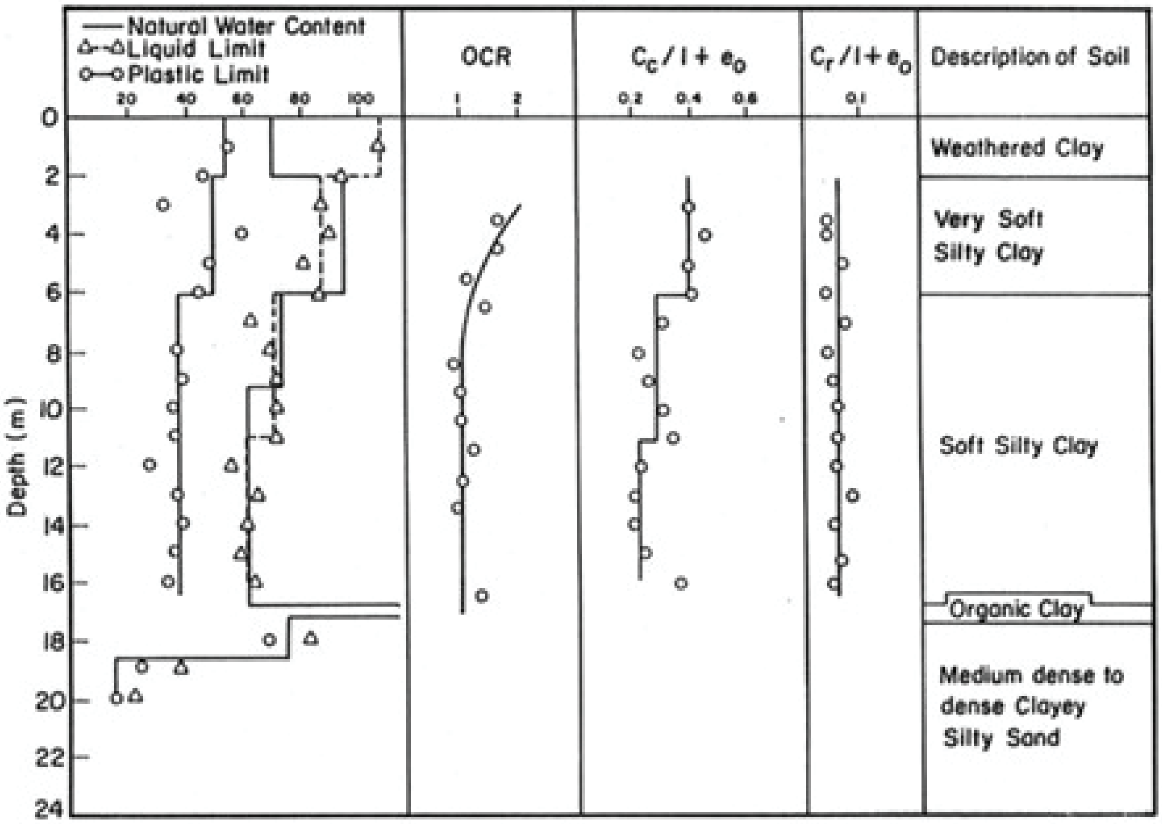

Elevation	Description	Liquid Limit w_L (%)	Plastic Limit w_p (%)	Natural Water Content w_n (%)	Plasticity Index	Grain Size (%) Clay	Silt	Sand	$\frac{C_c}{1+e_0}$	$\frac{C}{1+e_0}$	Preconsolidation Pressure P_c (KPa)
+2.5 mRL											
+0.5	Weathered Crust	108	55	70		42	57	1	.24	.04	110
	Very Soft Silty Clay with Decated Leaves and Roots	90	40	100	50	48	52	0	.48	.04	40
-5.5											
	Soft Silty Clay with Traces of Shell Fragments Occasionally Sand Lenses	80	30	60	50	40	60	0	.31	.04	60
-15.3	Peaty Soil										
-15.9	Sandy silt / clay with Organic Matters					22	43	35			
-19.9	Dense Medium to Coarse Sand with Gravels SPT N = 21 to 37										

Figure 9. (a) soil profile at Muar test embankment site; (b) schematic diagram of ground improvement scheme at the Muar flat site, Malaysia.

(b)

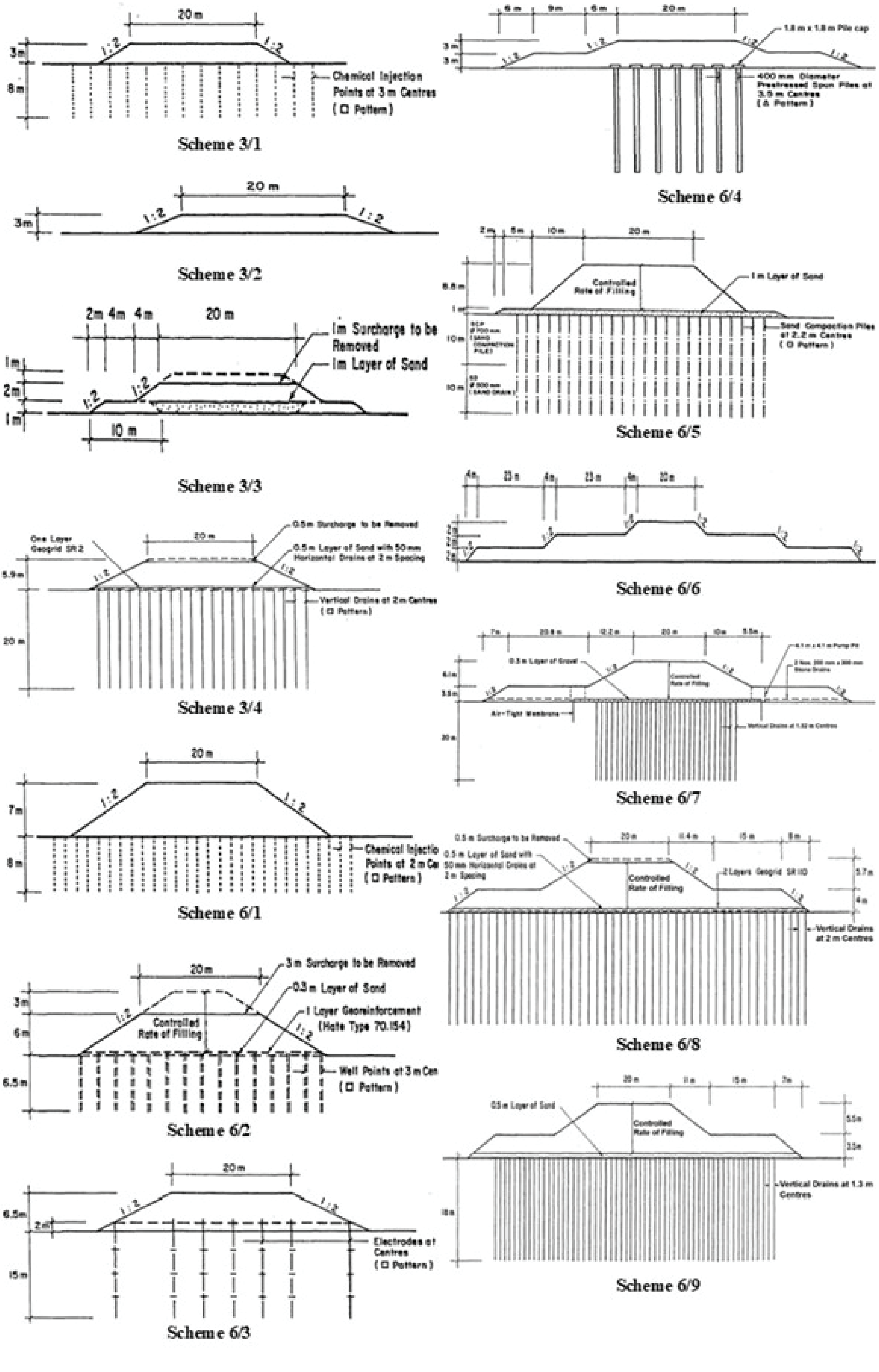

Scheme 3/1
20 m
1:2
3m
8m
Chemical Injection Points at 3 m Centres (□ Pattern)
Scheme 3/2
20 m
3m
Scheme 3/3
2m 4m 4m
20 m
1m Surcharge to be Removed
1m Layer of Sand
10 m
Scheme 3/4
One Layer Geogrid SR 2
0.5m Surcharge to be Removed
0.5m Layer of Sand with 50 mm Horizontal Drains at 2 m Spacing
Vertical Drains at 2m Centres (□ Pattern)
5.9m
20 m
Scheme 6/1
7m
8m
Chemical Injection Points at 2 m Ce (□ Pattern)
Scheme 6/2
3m Surcharge to be Removed
0.3m Layer of Sand
1 Layer Georeinforcement (Hate Type 70.154)
Controlled Rate of Filling
Well Points at 3m Cen (□ Pattern)
6m
6.5m
Scheme 6/3
6.5m
2m
15m
Electrodes at Centres (□ Pattern)
Scheme 6/4
6 m
9m
1.8 m x 1.8 m Pile cap
400 mm Diameter Prestressed Spun Piles at 3.5 m Centres (Δ Pattern)
Scheme 6/5
1 m Layer of Sand
Controlled Rate of Filling
Sand Compaction Piles at 2.2 m Centres (□ Pattern)
10m
6.8m
Scheme 6/6
4m
23 m
Scheme 6/7
0.3 m Layer of Gravel
Controlled Rate of Filling
Air-Tight Membrane
Scheme 6/8
0.5 m Surcharge to be Removed
0.5 m Layer of Sand with 50 mm Horizontal Drains at 2 m Spacing
Controlled Rate of Filling
2 Layers Geogrid SR 110
Vertical Drains at 2 m Centres
5.7 m
4 m
Scheme 6/9
0.5 m Layer of Sand
Controlled Rate of Filling
Vertical Drains at 1.3 m Centres
5.5m
3.5m

In Figure 10, V_{hL} = the observed lateral volume change in the field from inclinometer measurements. The volume V_{hL} measured at the end of loading, is the resultant of lateral volume increase due to undrained deformation (V_{iL} due to immediate settlement) and the lateral volume reduction during consolidation αV_{cL}). If H_j and H_{j+1} correspond to the height of loading at two stages j and j+1, the α can be determined from

$$\alpha = \frac{\left[\dfrac{(V_{hL})_{j+1}}{H_{j+1}} - \dfrac{(V_{hL})_j}{H_j}\right]}{\left[\dfrac{(V_{vL})_j}{H_j} - \dfrac{(V_{vL})_{j+1}}{H_{j+1}}\right]} \tag{2}$$

Similarly at two time stages t_j and t_{j+1}, the α factor during the consolidation stage (Figure 10) can be obtained from:

$$\alpha = \frac{\left[\dfrac{(V_{hL})_{j+1}}{t^{\gamma}_{j+1}} - \dfrac{(V_{hL})_j}{t^{\gamma}_j}\right]}{\left[\dfrac{(V_{vC})_j}{t^{\gamma}_j} - \dfrac{(V_{vC})_{j+1}}{t^{\gamma}_{j+1}}\right]} \tag{3}$$

Where V_{vc} and V_{hc} correspond to the settlement volume and lateral volume during the consolidation stage.

Loganathan (1992) also defined a β factor during consolidation to describe the creep.

$$\beta = \frac{Lateral\ Creep\ Volume}{Creep\ Settlement\ Volume\ (V_{crC})} \tag{4}$$

V_{cC} during the loading stage can be calculated as

$$V_{cC} = \frac{\beta V_{vC} - V_{hC}}{\alpha + \beta} \tag{5}$$

Similarly, V_{crC} during the loading stage can be calculated from

$$V_{crC} = \frac{\alpha V_{vC} + V_{hC}}{\alpha + \beta} \tag{6}$$

Further details of these derivations can be found in Loganathan et al. (1993). In Figure 11 the creep settlement volume (V_{crC}) is denoted as volume EFAE. Similarly the lateral creep volume is represented as volume ARMSA.

The normalised settlement with maximum settlement at the surface is presented in Figures 12a and 12b. The actual settlement with time is presented in Figures 13a and 13b. The percentage contribution from each layer is also tabulated in Table 2. The empirical formulation for the 6 m and 3 m high embankments were respectively:

$$S = -0.02z^3 + 0.75z^2 - 14.11z + 102.83 \text{ with } r^2 = 0.98 \tag{7}$$

$$S = 0.02z^3 + 0.86z^2 - 15.02z + 103.74 \text{ with } r^2 = 0.97 \tag{8}$$

If the two sets of embankment data are combined then the combined relationship is

$$S = -0.02z^3 + 0.86z^2 - 14.68z + 103.38 \text{ with } r^2 = 0.97 \tag{9}$$

The normalised lateral deformations are presented in Figures 14a-c. Tavenas & Leroueil (1980) suggested that irrespective of the depth at which it occurs, the maximum lateral deformation developed during construction and consolidation can be expressed as a function of the settlement of the embankment. The α-values as calculated by Loganathan (1992) are given in Table 3. Also, the α-values determined for the Scheme 3/2 and 6/6 which are the control

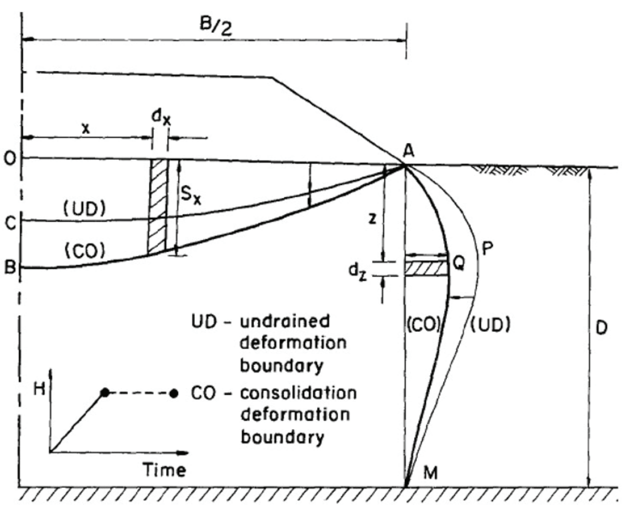

Figure 10. Deformation pattern of embankment foundation at end of loading stage.

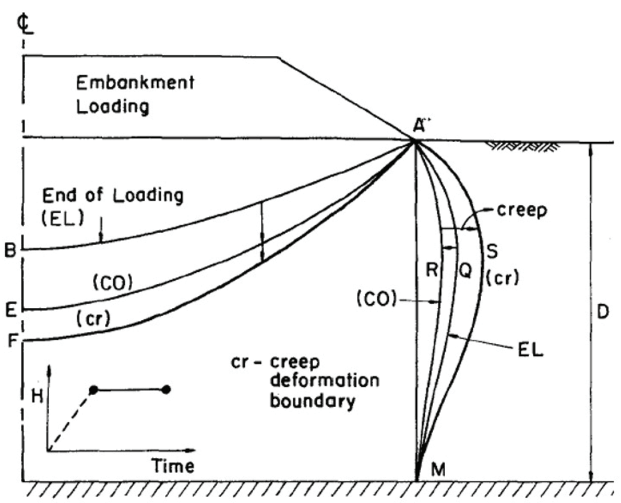

Figure 11. Deformation pattern of embankment foundation at end of consolidation stage.

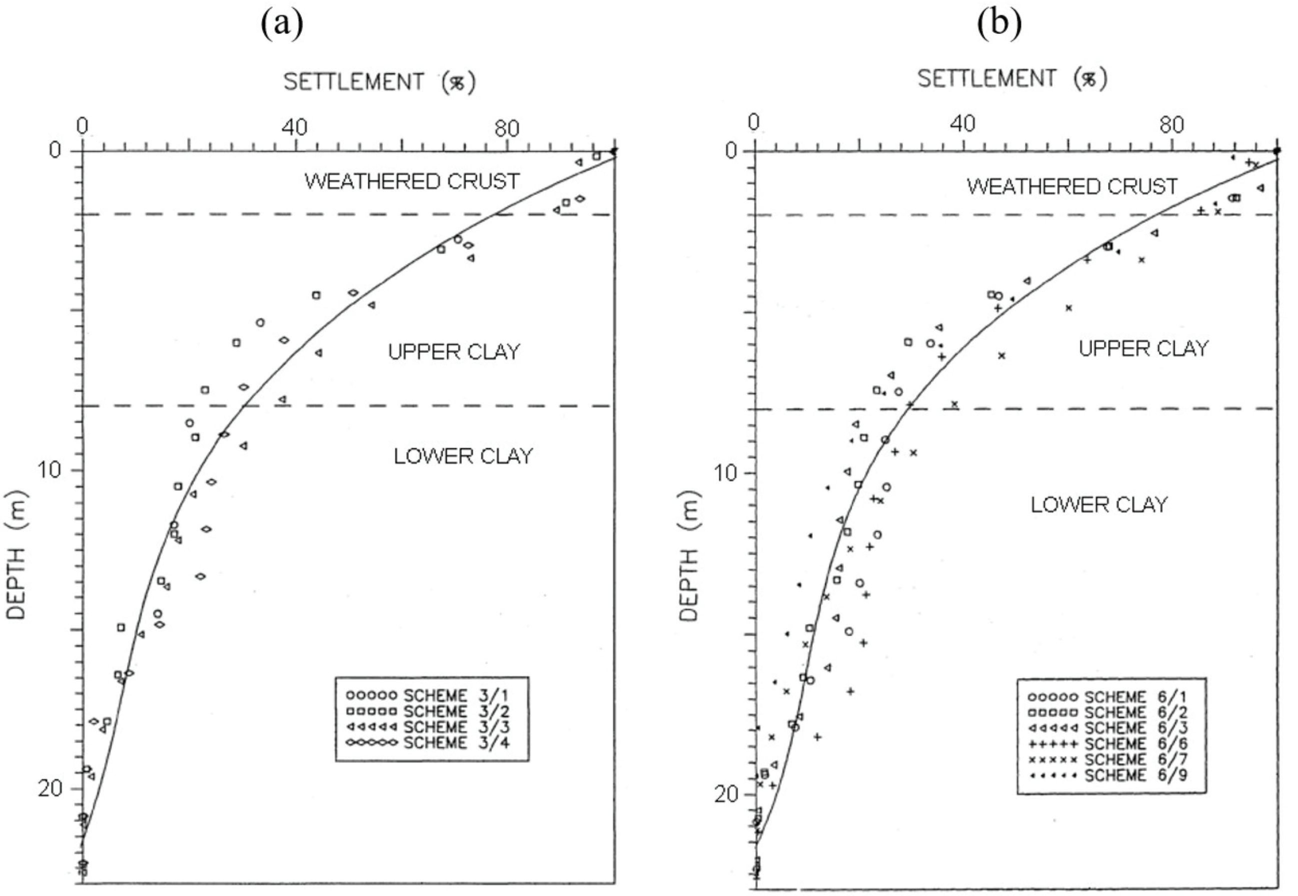

Figure 12. (a) variation of percentage settlement with depth for 3 m high dmbankments; (b) variation of percentage settlement with embankments depth for 6 m high.

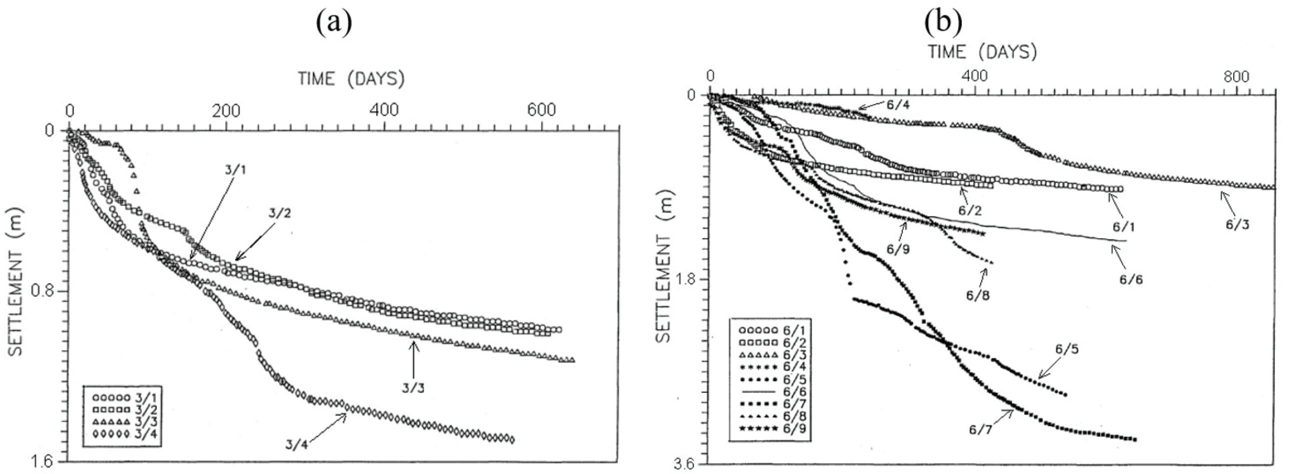

Figure 13. (a) comparison of maximum settlement profiles with time for 3 m-high embankments; (b) comparison of maximum settlement profiles with time for 6 m-high embankments.

embankments are shown in Figure 15. Then the variation of the consolidation settlement with immediate settlement for the other nine schemes is shown in Figure 16 during the loading stage. The corresponding data during the consolidation stage between the consolidation settlement and the creep settlement are given in Figure 17. Substantial creep settlement takes place as evidenced in the lateral movements as well as presented in Figure 18.

Table 2. Settlements (%) contributed by each layer for fifferently treated embankments.

Scheme	Percentage Settlement		
	Weathered Crust	Upper Clay	Lower Clay
3/1	21	57	22
3/2	20	61	19
3/3	15	54	31
3/4	12	51	37
6/1	15	58	27
6/2	14	64	22
6/3	13	68	19
6/6	16	55	29
6/7	11	51	38
6/9	14	64	22

Table 3. Ratio of Maximum lateral deformation to maximum settlement, α-value for all embankment schemes.

Scheme	Ground Improvement	α
3/1	Electro Chemical Injection	0.200
3/2	Control	0.240
3/3	Sand Sandwich Method	0.212
3/4	Preloading, Geogrid & Prefabricated Vertical Drain	0.210
6/1	Electro Chemical Injection	0.342
6/2	Well Point Preloading	0.173
6/3	Electro Osmosis	0.194
6/6	Control	0.240
6/7	Vacuum Preloading & Prefabricated Vertical drain	0.203
6/8	Preloading, Geogrid & Prefabricated Vertical Drain	0.275
6/9	Preloading & Vertical Drain	0.167

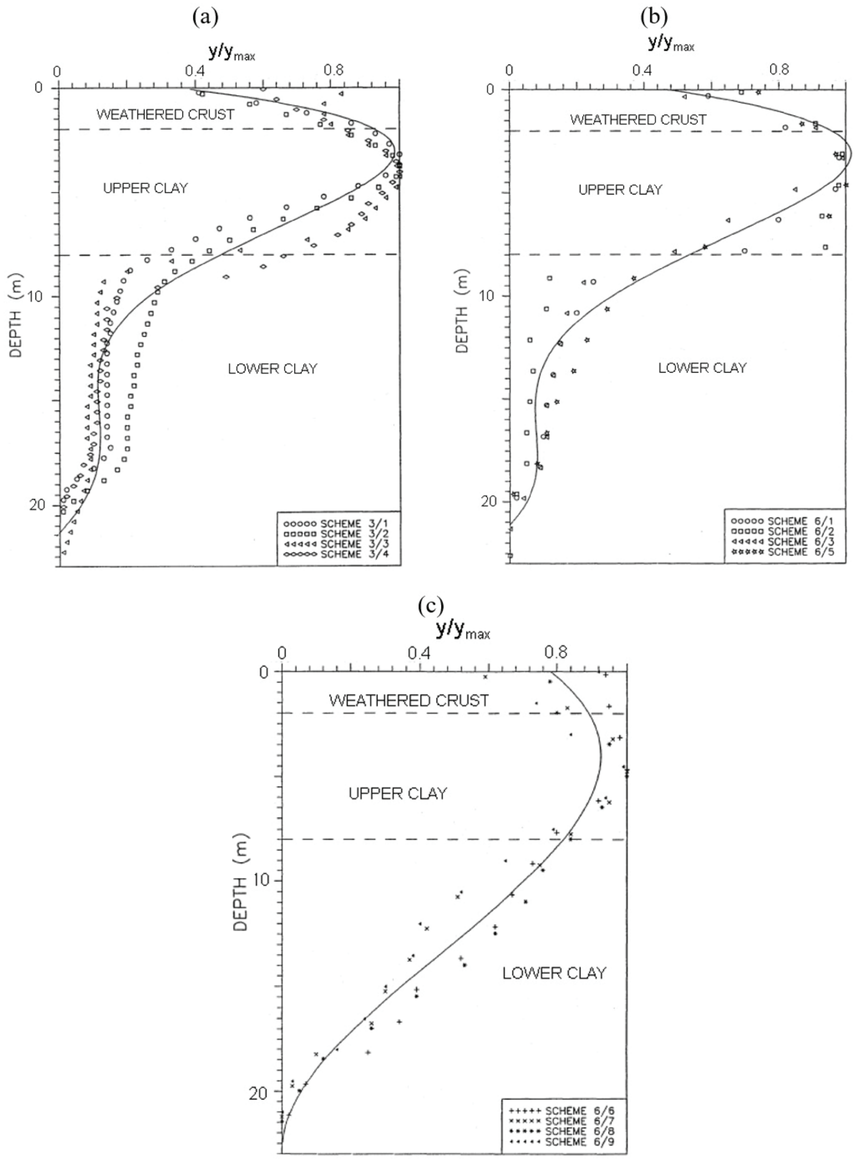

Figure 14. Variation of ratio of lateral deformation to maximum lateral deformation with depth for (a) 3 m-high embankments, (b) and (c) 6 m-high embankments.

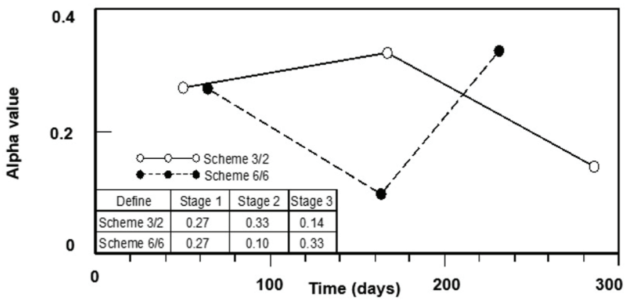

Figure 15. α-values for different stages of construction.

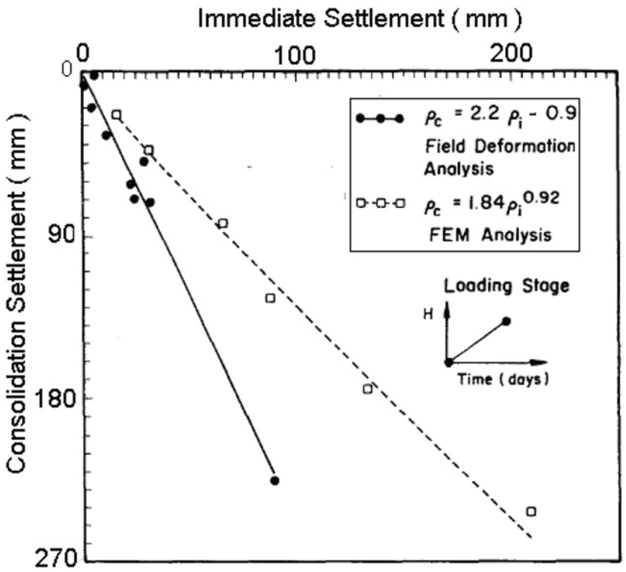

Figure 16. Variation of consolidation settlement with respect to immediate settlement.

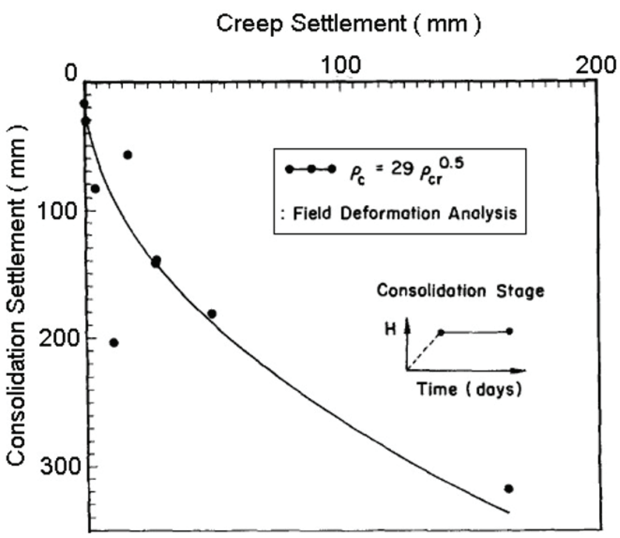

Figure 17. Variation of consolidation settlement with respect to creep settlement.

3. Test embankments at the Sbia site in Bangkok

The history of geotechnical investigations at this site included a test embankment with settlement measurement and without any form of drains and a test embankment conducted to failure, both were conducted in 1973 in the first phase of study. These results indicated that without any form of accelerated consolidation, the maximum fill height at the site can only be 3.4 m corresponding to a surcharge of 61 kPa. This is the failure height and a factor of safety of 1.5 is generally desired when PVD is used perhaps with a lower value of 1.38. The embankment raised to 2.7 m showed 0.48 m of settlement in 6 months of which 0.2 m is estimated as the immediate settlement and 0.28 m of consolidation settlement with in-situ values of coefficient of consolidation.

At the SBIA site in Nong Ngu Hao, the most extensive sand drain studies on test embankments were performed in 1983 (Moh et al., 1987) as part of the ground improvement scheme for the runway pavement and other sections of the taxiways and landside roads. Sand drains of minimum diameter 0.26 m was installed to a depth of 14.5 m by water jetting. The test program included three test areas, one with surcharge fill, the second with vacuum loading, and a third with ground water lowering. Test Section 1 was 40 m × 40 m in plan and sand drains were installed at 2 m spacing in a triangular pattern. The vacuum load was not successful as several leakages developed and finally the section was covered with a plastic shield. Test Section 3 was similar to Test Section 1, except that the spacing of the drain was increased to 2.4 m. Due to similar problem as in Section 1, the loading was not successful. The test Section 2 was slightly larger than test Section 1 and pre-loading of 60 kN/m^2 was applied in three stages. While difficulties were encountered in maintaining the vacuum load as well as the ground water lowering, the embankment surcharge was found to be a reliable technique when compared to vacuum loading in accelerating the consolidation with sand drains. The field trial was not successful in the sense that: (i) there was a settlement of 0.4 m under a sand blanket of 0.7 m after a five-month period, and (ii) the settlement across the section was remarkably asymmetric. The observations indicate the possibility of hydraulic connections between the sand drains and the first sand layer located at 25 m depths with a piezometric drawdown of 120 kN/m^2. It appears sand wicks (as used at the Naval Dockyard site) recharged the piezometric drawdown in the clay layer; while the large diameter sand drains (as those used in the airport site in 1983) tend to form hydraulic connections with the underlying aquifer and caused additional settlements due to the piezometric drawdown.

From the previous trials, it become evident that the engineers in Bangkok were rather cautious of the potential use of vertical drains in the Bangkok plain and the client that is, the Airport Authority of Thailand, insisted that

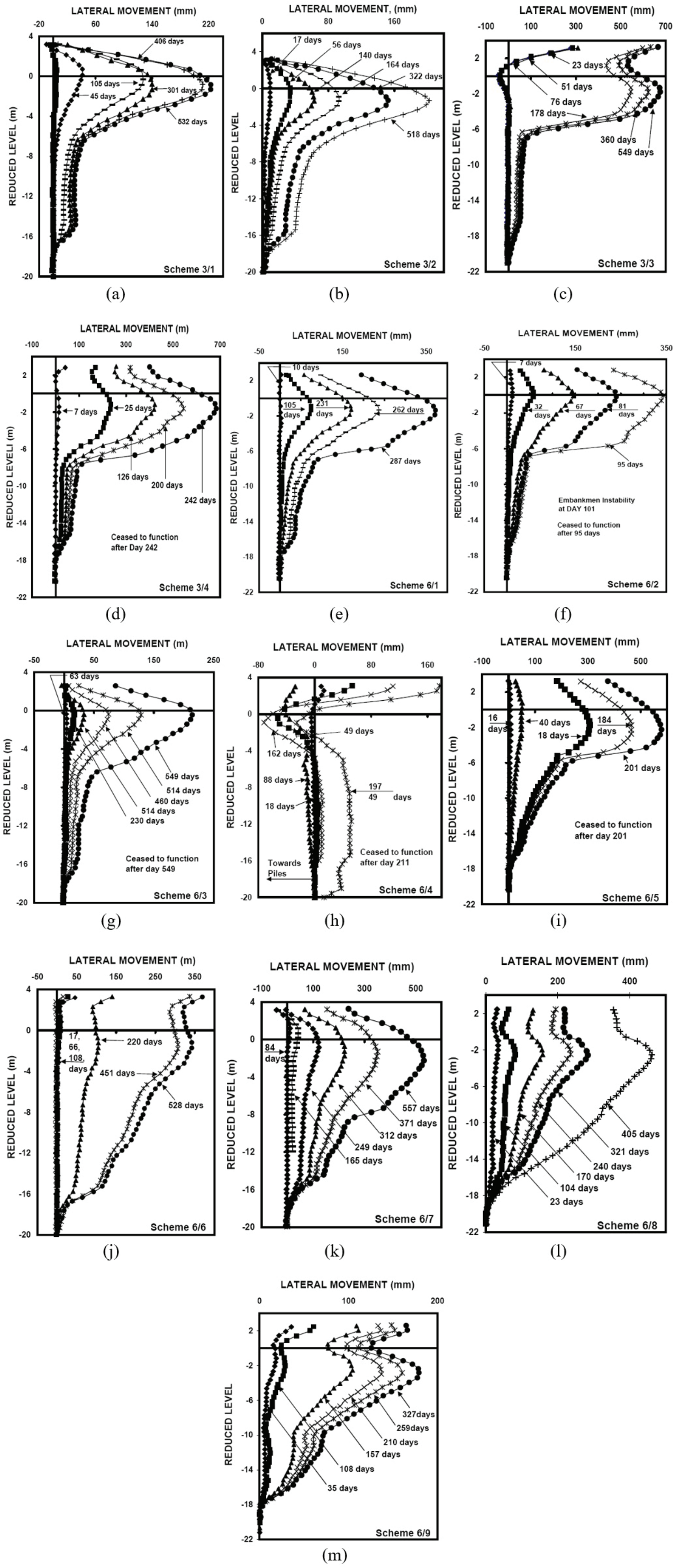

Figure 18. (a) to (m) lateral deformation profile for the ground improvement scheme at the Muar flat site, Malaysia.

the 1994-1995 study must indicate beyond all doubts that the majority of the settlement experienced in the trial embankment must be consolidation type of settlement to indicate the removal of water from the soft clay to improve its strength characteristics as well as to ensure that there is no possible hydraulic connections between the PVD used and the underlying sand strata which is experiencing substantial piezometric drawdown. These objectives are to be met by the estimation of the degree of consolidation, both from direct measurement of the settlements as well as from observation of the pore pressure dissipation in the field. Further, in-situ tests are conducted with vane apparatus to measure the in-situ strength increase with the water content reduction from the consolidation due to the use of PVD and surcharge. Additionally, the rate of settlement with time needs to be plotted to indicate that the final settlement rate is somewhat comparable to that, which one would consider acceptable at a rate similar to those experienced in secondary consolidation and not of higher values corresponding to hydraulic connections.

The plan dimensions of the embankments were the same as the earlier study. The locations of the test embankments and the cross-section of embankment TS3 with PVD are shown in Figures 19a-c respectively. These embankments were fully instrumented to measure the surface and subsurface settlements and pore pressures, lateral movements and heave.

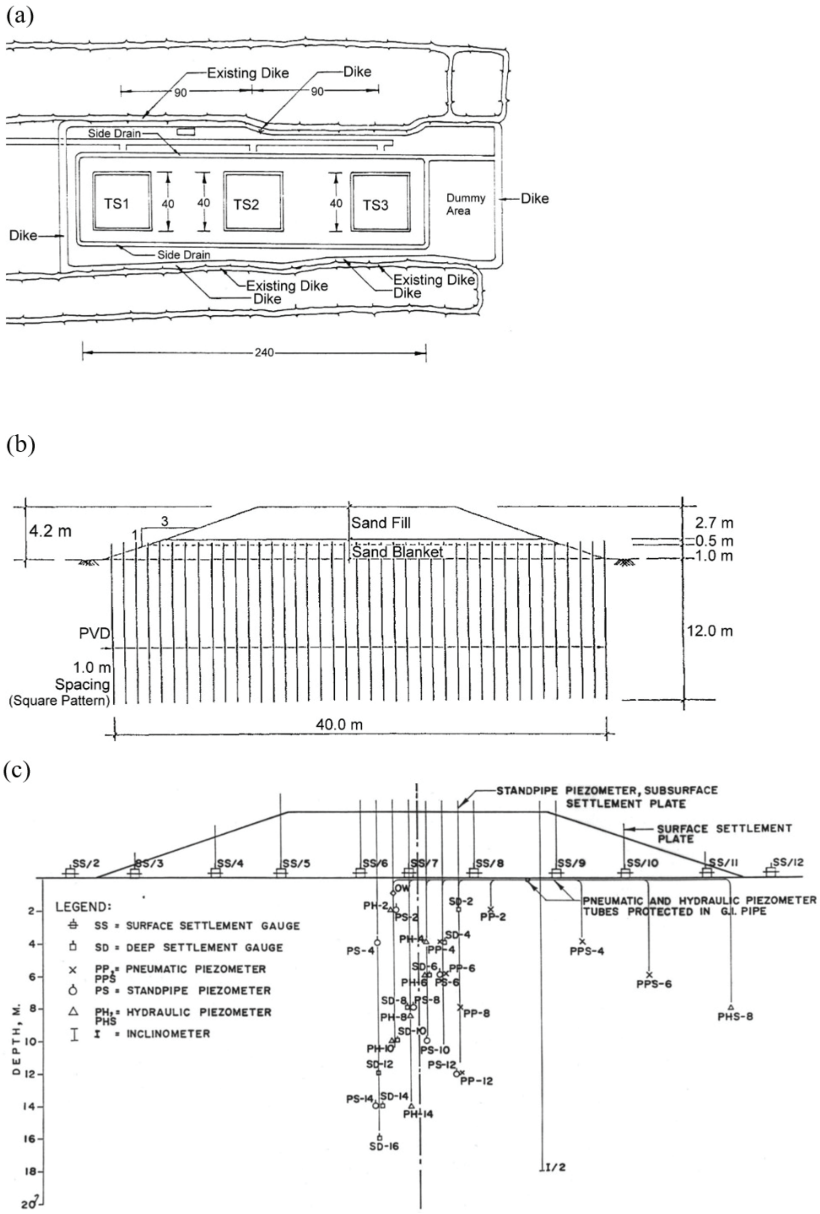

Figure 19. (a) site plan of test embankments TS1, TS2 and TS3 at SBIA site; (b) test section TS3 showing PVD at SBIA site; (c) section view of the test embankment showing the position of instruments at the Second Bangkok International Airport (SBIA).

PVD were installed to 12 m depth and the spacing was 1.5, 1.2 and 1.0 m in the three embankments TS1, TS2 and TS3, respectively.

All three test embankments performed more or less in the same manner and as such detail discussion will only be based on one (Test embankment TS 3 with PVD spacing at 1 m interval). For this embankment the settlement profile with depth, the lateral movement, and the pore pressure plots at various times are shown in Figures 20-25. In Figure 26, settlements were also independently computed from actual pore pressure dissipation. In Figure 26, the dotted curve ABC represents the actual piezometric profile with draw down as observed in September 1994 prior to the construction of the embankment. The full line curve DEF corresponds to the pore pressure profile after the full height of the embankment is reached with a surcharge of 75 kPa and prior to any pore water pressure dissipation. The end of construction pore pressure profile is also shown. Similarly the pore pressure profiles in June 95 and in February 1996 are shown. The final pore pressure after the dissipation of the excess pore pressure and the recharged hydrostatic profile is MNPQ (NPQ is the assumed final recharged pore pressure profile, where there are no data points). Settlements were directly computed from these pore pressure dissipation curves.

The degrees of consolidation computed from the pore pressure dissipations are illustrated in Figure 27 and compared with the degree of consolidation as computed from settlement measurements. In Figure 27, the ordinate axis U_p refers to the degree of consolidation as computed from the pore pressure dissipation, while the abscissa axis refers to the degree of consolidation U_s as computed from

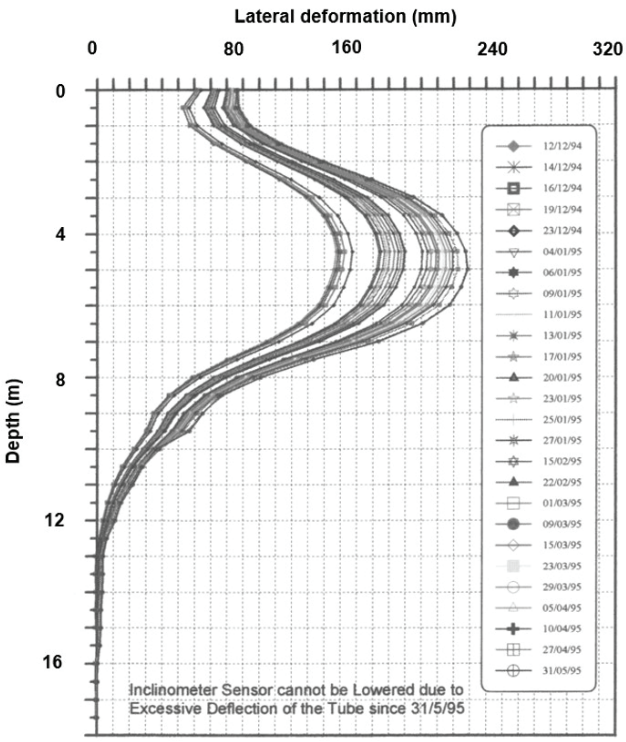

Figure 21. Lateral deformation with depth below embankment TS3 at the SBIA site in Bangkok.

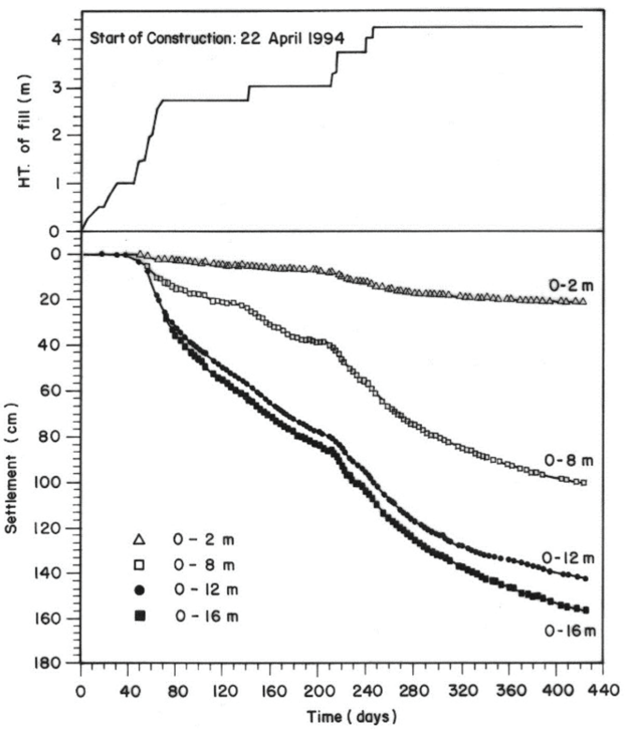

Figure 20. Settlement-time plot of the embankment with PVD at the SBIA site in Bangkok.

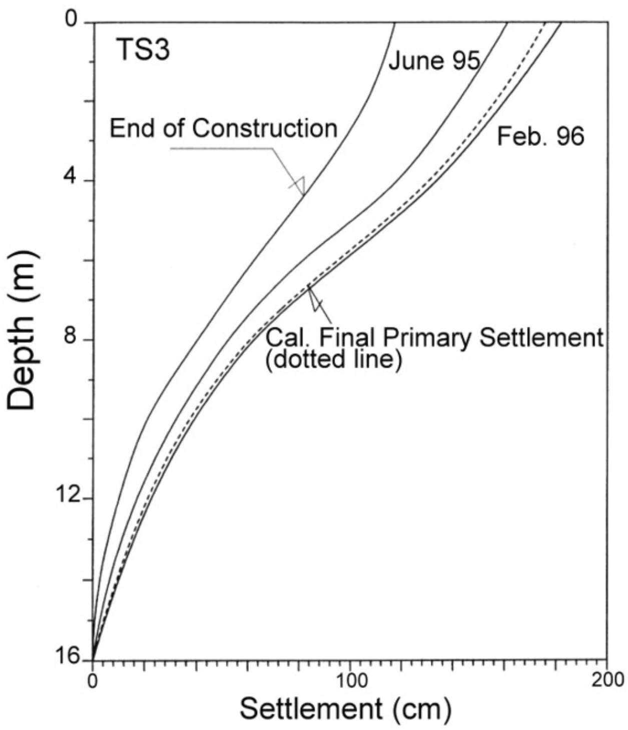

Figure 22. Settlement plot of test embankment with PVD at SBIA site.

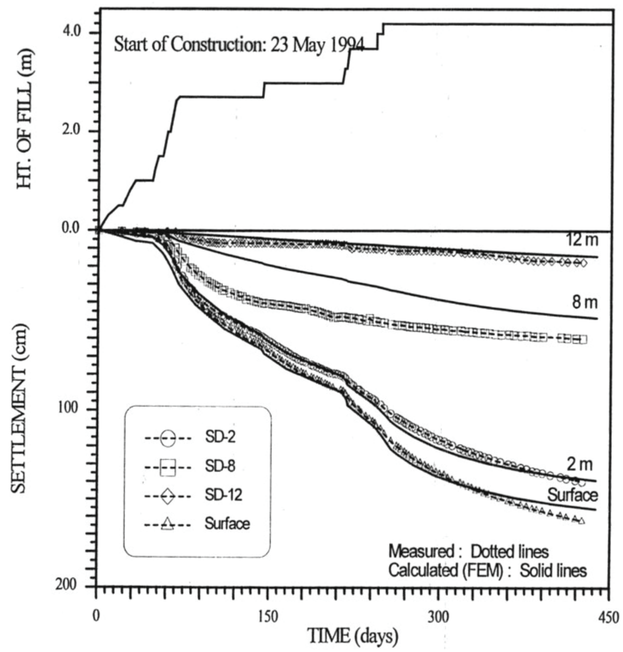

Figure 23. Measured and computed settlement with different depth at the SBIA site in Bangkok.

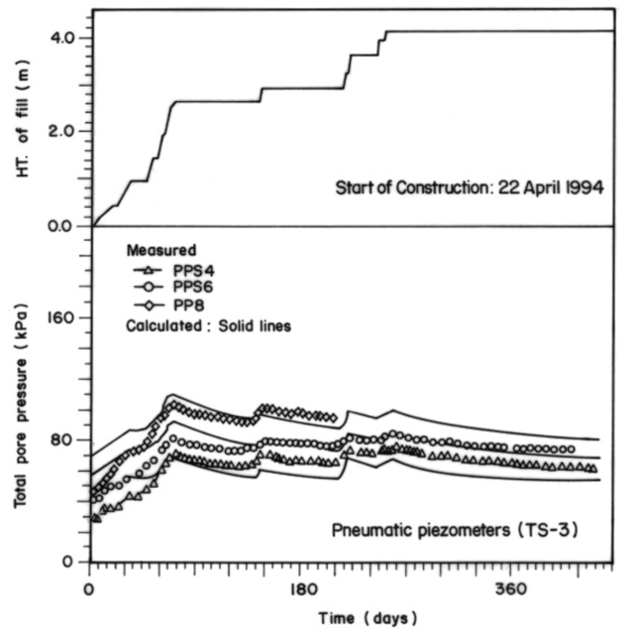

Figure 25. Measured and computed pore pressure dissipation of the embankment at the SBIA site in Bangkok.

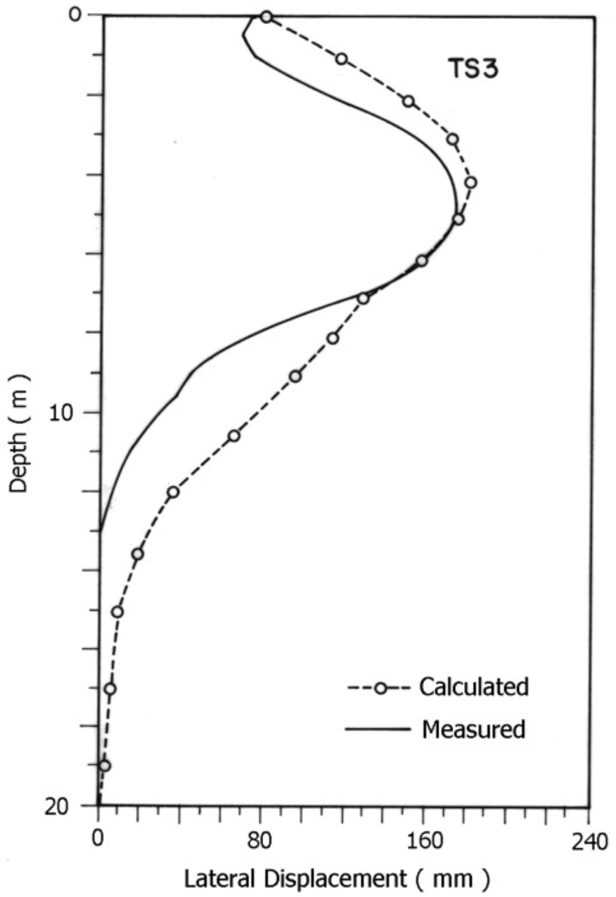

Figure 24. Measured and computed lateral movement of the embankment at the SBIA site in Bangkok.

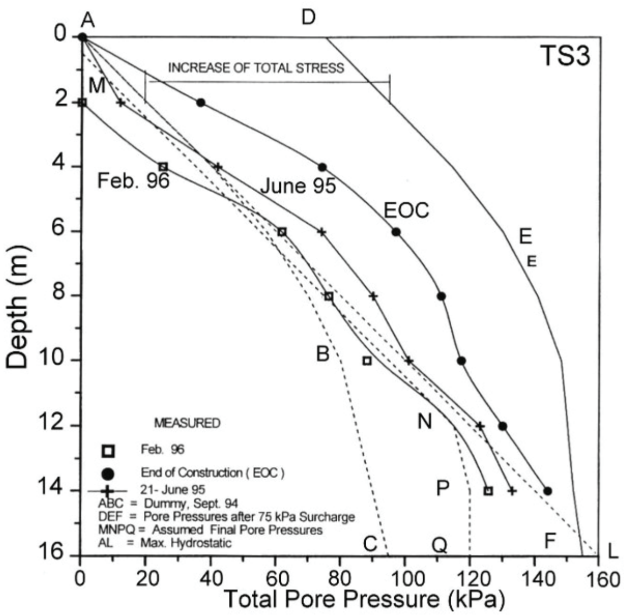

Figure 26. Pore pressure profile of test embankment with PVD at SBIA site.

the settlement measurements. With due allowance for a small percentage of secondary settlement and creep, the two degree of consolidations seem to agree well as they are close to the 45 degree line. The settlement due to the lateral movements was less than 10% as estimated by the method of Loganathan et al. (1993). The immediate settlement computed from the lateral movements as adopted by a method in which the balancing of volume (Loganathan et al., 1993) was within ten percent of the measured vertical settlement. The rate of settlement and the rate of lateral movements were plotted in Figures 28 and 29, and are found to decay with time. Also the settlement log time plots in Figure 30 for the three test embankments were found to be approaching a constant slope. An attempt was made to define the 100% primary consolidation time using Casagrande type of settlement versus log-time plots. The points P and Q (shown in Figure 30) correspond to the 100% primary consolidation for the Test Section TS3 and TS1 respectively. The data for TS2 is not shown, as it will crowd closely with the data from the other two embankments. The final portions of the test data for the two embankments seem to approach the secondary consolidation part as computed from the Casagrande settlement versus log-time plots. These results further confirmed that the PVD did not cause any hydraulic connection with the lower aquifers and the measured final settlement is of the same order as the secondary settlement.

Finally, the increase in the shear strength with time after consolidation in the field is measured with the vane apparatus as plotted in Figure 31.

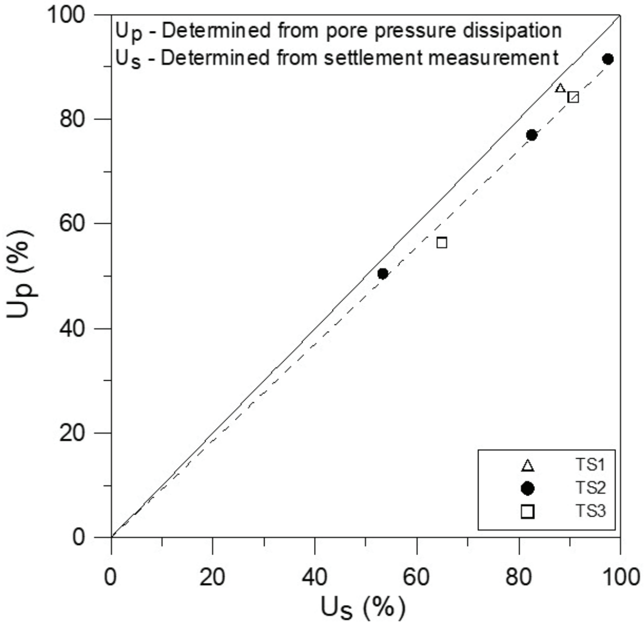

Figure 27. Degree of consolidation computed from pore pressure dissipation and settlement measurements at SBIA site.

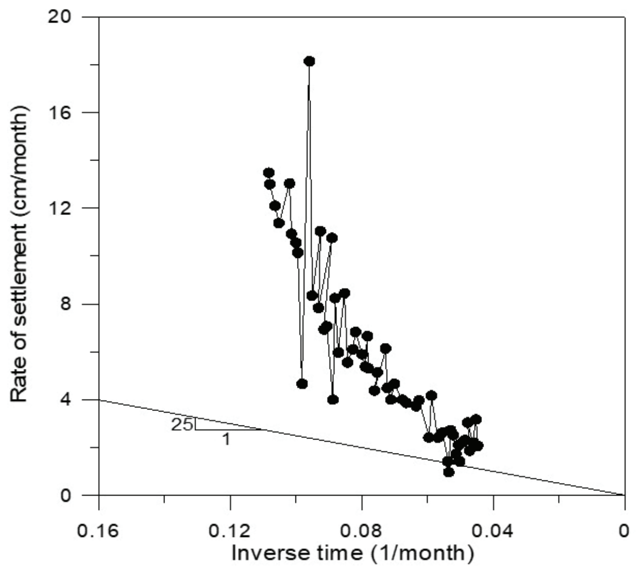

Figure 28. Rate of settlement versus inverse time plot at SBIA site.

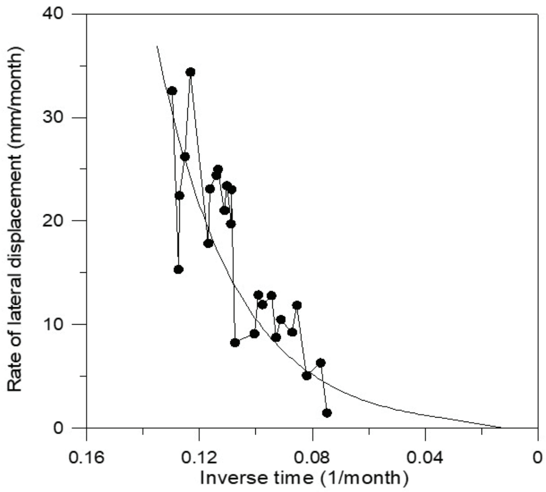

Figure 29. Rate of lateral movement versus inverse time plot at SBIA site.

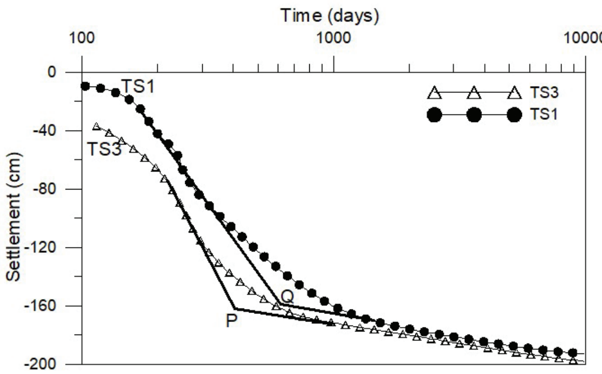

Figure 30. Settlements versus log-time plot for embankments TS1 and TS3 at SBIA site.

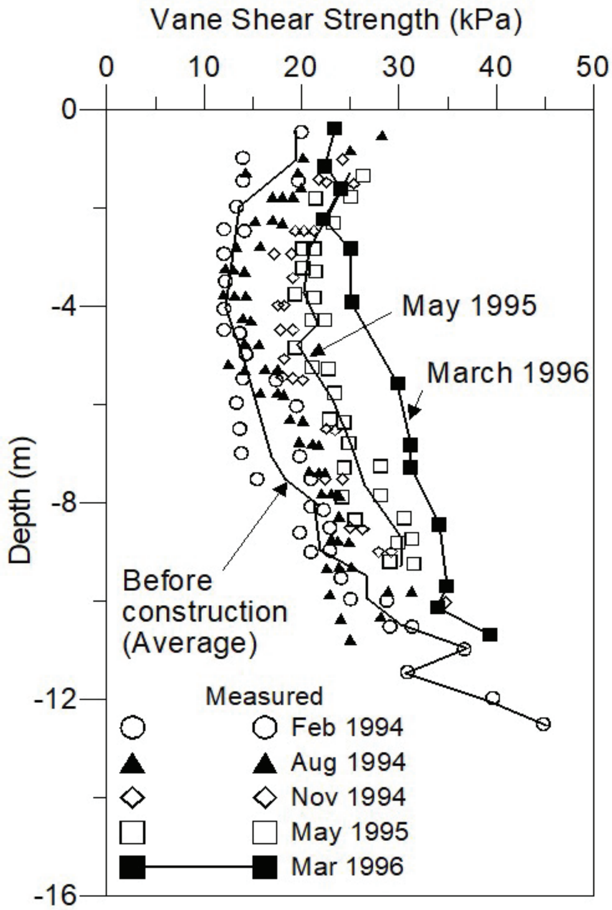

Figure 31. Field vane shear strength as measured in embankment TS3 at SBIA site.

4. Concluding remarks

This lecture is devoted to a study of the role of test embankments as a site investigation, design and construction control aspects related to ground improvement works in soft clays. Test embankments in Bangkok, Thailand and Muar site in Malaysia are used as case studies. The work is more on practical aspects related to the stability and deformation characteristics. Even though research work on this subject has been there now for more than five decades, yet the Case A type of Prediction of the stability and settlement characteristics is still a challenging task.

From the test embankment studies carried out in Bangkok with and without ground improvement, the major experience is with embankments of sand. Without any ground improvement, the failure height of these embankments is very modest and is in the range of 2.5 to 3.5 m. Vane strengths were found to be adequate to determine the stability of these embankments with a total stress analysis and the Bjerrum's correction factor as based on plasticity index is found to be essential. The Authors have no experience in using the subsequent correction as proposed by Aas.

Data from three tests embankments fully instrumented revealed that when vertical drains are used in the Bangkok Plain the piezometric drawdown which naturally exist in the Plain due to deep well pumping is virtually erased in the upper clay layer. Also the presence of sand and silt seams tend to assist lateral drainage and therefore test embankments with and without drains be separated substantially not to have such interference effects. The possibility of such effects also remains in the soft clays of Southeast Queensland and elsewhere. The presence of sand and silt seams and the existence of piezometric drawdown had made it difficult for the vacuum drainage to be implemented successfully. Recent modifications and improvements in the sealing methods together with the use of Bentonite type of cut off walls were not included in the studies made here. Test embankments built on soft clay with pre-fabricated vertical drains have performed successfully in accelerating the consolidation settlement when the PVD spacing is properly designed taking care of smear effect and well resistance as proposed by Hansbo and others. For the soft Bangkok clay this spacing is about 1.5 m. The immediate settlement observed was generally of the order of ten percent. The Asaoka method and the Field Deformation Analysis were also performed to confirm the magnitude of consolidation settlement and immediate settlement respectively. Settlement computations from pore pressure dissipation and direct settlement measurements are found to agree well and the magnitude of long term secondary settlement is also computed from the field data.

The test embankment studies at the Muar site indicated the importance of the fill strength in the stability characteristics when well compacted residual soil is used. Also the Field Deformation Analysis was successful in separating the consolidation settlement, the immediate settlement and the long term creep settlements. The normalised settlement profile and the normalised lateral movement profiles for several ground improvement schemes were found to be similar in shape. The use of sand compaction piles and pre-stressed piles were found to be successful in minimising the lateral deformation at the toe of the embankments.

In all the test embankment studies, prediction of the observed behaviour was found to be possible with the use of CRISP computer program and soft clay models of the type developed at Cambridge University.

Acknowledgements

Impossible to thank all those helped over a lifetime: Mr. Nilan Sachintha Jayasiri for helping with the preparation, old colleagues: Profs. Prinya Nutalaya, Dennes Bergado, Za Chieh Moh, Edward Brand and then Luiz de Mello, Madhav, Purnanand, many colleagues at AIT, NGI, formerly and now Prof. Erwin Oh etc. The Southeast Asian Geotechnical Society, Drs. Ooi Teik Aun, Ting Wen Hui, Chung Tien Chin and many others, Dr. Geoff Chao, Boonjira Intradoot, Chanidaporn Chaymonkoln and so on. Last but not least, I would like to acknowledge the help received from my son, Sasitharan Balasubramaniam and my wife, Chandrika.

Declaration of interest

The author declares that are no conflicting interests that could inappropriately bias this paper.

References

Asaoka, A. (1978). Observational procedure of settlement prediction. *Soils and Foundations*, 18(4), 87-101. https://doi.org/10.3208/sandf1972.18.4_87

Balachandran, S. (1990). *Simulation of a test embankment failure (Muar flood plain, Malaysia) using finite element techniques coupled with critical state soil mechanics*. Bangkok, Thailand: Asian Institute of Technology.

Brand, E.W., & Premchitt, J. (1989). Moderator's report for the predicted performance of the Muar test embankment. In R. R. Hudson, C. T. Toh, S. F. Chan (Eds.), *Proc. International Symposium on Trial Embankment on Malysian Marine Clays* (pp. 31-32). Kuala Lumpur: Malaysian Highway Authority.

Christian, J.T., & Watt, B.J. (1972). Undrained visco-elastic analysis of soil deformations. In C.S. Desai (Ed.), *Proc. Symp. Applications of the Finite Element Method in Geotechnical Engineering* (pp. 533-580). Vicksburg: Army Engineer Waterways.

Cox, J.B. (1968). *A review of the engineering characteristics of the recent marine clays in South East Asia*. Bangkok: Asian Institute of Technology.

Eide, O. (1977). Exploration, sampling and insitu testing of soft clay in the Bangkok area. In E.W. Brand & R.P. Brenner (Eds.), *Proc. International Symposium on Soft Clay* (pp. 122-137). Bangkok: Elsevier.

Loganathan, N. (1992). *Analysis of test embankment on Malaysian Muar clays* [Unpublished thesis]. Asian Institute of Technology.

Loganathan, N., Balasubramaniam, A.S., & Bergado, D.T. (1993). Deformation analysis of embankments. *Journal of Geotechnical Engineering*, 119(8), 1185-1206. http://dx.doi.org/10.1061/(ASCE)0733-9410(1993)119:8(1185).

Moh, Z.C., Brand, E.W., & Nelson, J.D. (1973). Performance of test sections for new Bangkok Airport at nong Ngoo Hao. AIT Research Report to Northrop Airport Development Corporation.

Moh, Z.C., Woo, S.M., VanWeele, A.F., Chotivittayathanin, R., & Trangkarahart, K. (1987). Preconsolidation of soft Bangkok clay by non-displacement sand drains and surcharge. In A. S. Balasubramaniam, P. Nutalaya, G. Rantucci, N. Phienweja, J. Kuwano, S. Saran, S. Kvijitjaru, V. Wijeyakulasuriya, M. Sritharan, S. J. D. Demafeliz, B. M. Lekhak, T. Sivakumar. (Eds.), *Proc. 9th Southeast Asian Geotechnical Conference* (pp. 8-171). Bangkok: SEAGS.

Ratnayake, A.M.P. (1991). *Performance of test embankment with and without vertical drains at Muar Clays, Malaysia* [Unpublished thesis]. Asian Institute of Technology.

Shibata, T. (1987). Lateral deformation of clay foundations, Discussion 6. In K. Akai (Ed.), *Proc. 8th Asian Regional Conference on Soil Mechanics and Foundation Engineering* (pp. 390-391). Kyoto: Geotechnical Society.

Sivaneswaran, N. (1993). *Performance of trial embankments on treated and untreated soft clay at the Muar Site* [Unpublished thesis]. Asian Institute of Technology.

Tavenas, F., & Leroueil, S. (1980). The behaviour of embankments on clay foundations. *Canadian Geotechnical Journal*, 17(2), 236-260. http://dx.doi.org/10.1139/t80-025.

Ting, W.H., Chan, S.F., & Kassim, K. (1989). Embankments with geogrid and vertical drains. In R. R. Hudson, C. T. Toh, S. F. Chan (Eds.), *Proc. International Symposium on*

Trial Embankments on Malaysian Marine Clays. Kuala Lumpur: Malaysian Highway Authority, 21/1-21/13.

Toh, C.T., Chee, S.K., Hudson, R.R., Loh, M.H., & Gue, S.S. (1989). 3m high control embankment on untreated soft ground, MHA. In R. R. Hudson, C. T. Toh, S. F. Chan (Eds.), *Proc. International Symposium on Trial Embankments on Malaysian Marine Clays*. Kuala Lumpur: Malaysian Highway Authority.

ARTICLES

Soils and Rocks
An International Journal of Geotechnical and Geoenvironmental Engineering
www.soilsandrocks.com
ISSN 1980-9743
ISSN-e 2675-5475

The effect of pH and electrical conductivity of the soaking fluid on the collapse of a silty clay

Renan F. B. Zanin[1#], Ana C. C. Padilha[1], Flávia G. P. Pelaquim[1], Nelcí H. M. Gutierrez[2], Raquel S. Teixeira[1]

Article

Keywords
Soil collapse
Soaking fluids
Physical-chemical interactions
PH
Plectrical conductivity

Abstract

Different fluids can permeate the soil collapsing at various levels of severity depending on their physicochemical characteristics. This work evaluated the effect of pH and electrical conductivity (EC_f) of different soaking fluids on the collapsible behavior of a lateritic silty clay. Double and single oedometer tests were performed using four chemically distinct soaking fluids (water, leachate and two laboratory solutions, one alkaline and one acid). The collapse index (I) was evaluated according to two criteria. In addition, physical-chemical analysis of the soil and measurements of pH and EC_f were done. According to the results, the soil is collapsible for the four soaking fluids. No single relationship was found between fluid pH and collapse index, although, the highest values of collapse index were found in the tests soaked with alkaline and acid solutions. Finally, a unique direct relationship was found between the collapse index and the EC_f, that is, the higher this parameter, the higher the collapse index value.

1. Introduction

Leaks in reservoirs and pipes of industrial or domestic effluents can contaminate soils and groundwater. The environmental bias for this context is widely studied. However, the geotechnical implications of these occurrences are sometimes neglected, even though it is known the chemical characteristics of these substances influence the tension versus deformation behavior, due to the interaction between liquid and soil (Mitchell, 1976; Carvalho et al., 1987; Chen et al., 2000; Rodrigues et al., 2010; Futai et al., 2015).

According to Oliveira (2002), who studied the soil of the city of Ilha Solteira, in the state of São Paulo, Brazil, one third of the soil collapse cases occur due to domestic sewage leakage. Réthati (1961) analyzed 57 landfill collapse occurrences in Hungary and identified that the fluids causing such volume reductions were: sewage pipe breakdown (36% of cases), rainwater from the roof (25%), surface water (15%), break in supply line tubes (10%), reflux due to sewage clogging (8%), and processed water (5%).

Soil collapse is the abrupt reduction of volume due to saturation increase, with or without additional load application (Dudley, 1970; Jennings & Knight, 1975; Rezaei et al., 2012). The collapsible soils are characterized by high porosity ($\eta >$ 40%) and low saturation degree ($Sr < 60\%$), resulting in a metastable structure (Feda, 1966; Mariz & Casanova, 1994).

The collapsible condition can occur when the soil has at least one of the following characteristics (Larionov, 1965; Dudley, 1970; Barden et al., 1973):

a) Open, partially saturated and potentially unstable structure, susceptible to volume reductions;

b) High suction value or presence of cementing agents that stabilize the structure;

c) High stress state.

The chemical cementing agents, such as iron or aluminum oxides and carbonates, help to structure the particles. These bonds tend to disappear by chemical attack of certain soaking fluids (Agnelli & Albiero, 1997; Garcia et al., 2004; Gutierrez et al., 2008; Collares & Vilar, 2017).

In general, parameters such as alkaline and acid pH as well as high electrical conductivity, can potentiate the occurrence of the collapse phenomenon, in case the ions present in the solution generate greater structure disaggregation (Reginatto & Ferrero, 1973; Carvalho et al., 1987; Fang, 1997; Olgun & Yildiz, 2010; Motta & Ferreira, 2013; Koupai et al., 2020). Sodium-rich liquids, for example, act as dispersants

#Corresponding author. E-mail adress: renanzanin@uel.br
[1]Universidade Estadual de Londrina, Departamento de Construção Civil, Londrina, PR, Brazil.
[2]Universidade Estadual de Maringá, Departamento de Engenharia Civil, Maringá, PR, Brazil.

Submitted on December 23, 2020; Final Acceptance on June 29, 2021; Discussion open until February 28, 20222.
https://doi.org/10.28927/SR.2021.061620

breaking the cementitious bonds, increasing the magnitude of the collapse (Abdullah et al., 1997; Rodrigues & Lollo, 2007; Conciani & Barbosa, 2013; Motta & Ferreira, 2013; Collares & Vilar, 2017).

The Gouy-Chapman Diffuse Double Layer (DDL) theory can also help to explain compressible soil behavior due to percolation of different fluids (Mitchell, 1976; Van Olphen, 1991). According to this theory, the presence of higher valence ions in the soil solution causes greater reductions in DDL thickness, reducing soil compressibility. (Sridharan et al., 1986; Sposito, 2008; Meurer, 2004).

The present work aims to evaluate the collapsible behavior of a laterite silty clay through double and single oedometer tests using different soaking fluids (water, leachate, alkaline solution and acid solution), in order to find a relation between collapse index, pH and electrical conductivity of these liquids.

2. Materials and methods

2.1 Materials

2.1.1 Soil

The study was accomplished using soil from the Experimental Campus of Geotechnical Engineering (ECGE) surface layer of the State University of Londrina, latitude 23º19.6'S, longitude 51º12.1'W, altitude of 585.7 m under subtropical climate. Originated from basalt, it is a highly weathered soil, where the clay fraction is composed of 1:1 silicate minerals, such as kaolinite, hematite and gibbsite, and also amounts of Fe, Al and Mn oxides and hydroxides, belonging to the rocky basement located in the Third Parana Plateau (Gonçalves et al., 2018). The surface soil on the city of Londrina (up to 2 m) is denominated as a Dystrophic Purple Latosol, characterized as lateritic porous silty clay, with void ratio close to 2, solid specific gravity around 30 kN/m^3 and micro aggregation with collapsible potential (Teixeira et al., 2008; Teixeira et al., 2010; Teixeira et al., 2016; Gonçalves et al., 2018). According to the same authors, this high solid specific gravity is due to the intense presence of iron in the soil constitution, originated from basalt rocky basement. In addition, the soil composition carries no sodium content (Melo et al., 2019; Melo et al., 2020).

2.1.2 Soaking fluids

In order to evaluate how soaking fluids influence on soil collapse, four liquids were used: water (pH 7.2), leachate (pH 8.4), alkaline solution (pH 12) and acid solution (pH 2.4). For the two latter, a solution of sodium hexametaphosphate – $(NaPO_3)_6$ (pH = 5.7) – was used as base in the proportion of 45.7 g of salt to 1 liter of distilled water. For the alkaline solution, 10.3 ml of sodium hydroxide (NaOH (6N)) was added in 500 ml of the solution of $(NaPO_3)_6$ until pH = 12 was reached. For the acid solution, 1.8 ml of phosphoric acid (H_3PO_4) was added in 500 ml of solution of $(NaPO_3)_6$ until pH = 2.4 was reached. Alkaline and acid solutions, for instance, are respectively similar to those found in detergents and effluents from food industries.

The leachate came from the former disposing of Londrina urban solid waste, currently deactivated. It is in the methanogenic phase (Felici et al., 2013), with high levels of alkalinity and ammoniacal nitrogen (5,900.2 mg $CaCO_3.L^{-1}$ and 1,048.4 mg $N\text{-}NH_3.L^{-1}$, respectively) and low BOD/COD ratio (0.05).

2.2 Methods

2.2.1 Physical-chemical analysis of soil and soaking fluids

For the soil physical-chemical characterization, deformed samples were collected at 2 m depth in the ECGE, as recommended by NBR 9604-86 standard (ABNT, 1986b) and prepared according to NBR 6457-86 standard (ABNT, 1986a). Two portions of 50 g each were submitted to physical-chemical analysis according to the methodology described in the Manual of Soil Analysis Methods (Teixeira et al., 1997). Phosphorus (P), calcium (Ca), magnesium (Mg), potassium (K) and aluminum (Al) contents, as well as pH (H_2O), pH (KCl), ΔpH and cation exchange capacity (CEC) were determined.

The electrical conductivity for the soaking fluids was determined in accordance with the methodology described by Rice et al. (2005). The equipment was calibrated with the HI 7031 standard (KCl 0.1g.L – 1,413 $\mu S.cm^{-1}$). Lastly, the fluid electrical conductivity was taken as the average value of three direct readings.

2.2.2 Oedometer tests

For the soil collapse index evaluation, double and single oedometer tests were performed in undisturbed samples, also collected at ECGE at 2 m depth. The procedure was performed according to the method D2435-11 (ASTM, 2011) with the aid of a unidirectional press. The loading stages, with 24 hours duration each, were taken at 6, 12, 25, 50, 100, 200 and 400 kPa. The readings intervals were 8, 15 and 30 seconds, then, 1, 2, 4, 8, 15 and 30 minutes, and ultimately, 1, 2, 4, 8 and 24 hours. There were three unloading stages (200, 100 and 6 kPa) at the same time intervals for the previous readings, however, lasting 2 hours each. The specimens tested were carved in a metal ring, with diameter of 8 cm and height of 3.2 cm.

In the double oedometer tests two specimens were tested, one in the field natural moisture content, and the other soaked since the very beginning of the test. Therefore, it was possible to predict the collapse index (I) for the intended stress values, i.e., 25, 50 and 100 kPa, as from the difference between the curves through the Equation 1, according to

Jennings & Knight (1957), reformulated by Gutierrez (2005) to adapt the parameters to normalized curves:

$$\boldsymbol{I} = \frac{\Delta \boldsymbol{e_c}}{\left[1+\left(\frac{\boldsymbol{e_{nat}}}{\boldsymbol{e_{0(nat)}}}\right)*\boldsymbol{e_{0(aver)}}\right]}*100\% \quad (1)$$

Where:

$$\Delta e_c = \left[\left(\frac{e_{nat}}{e_{0(nat)}}\right)-\left(\frac{e_{soak}}{e_{0(soak)}}\right)\right]*e_{0(aver)} \quad (2)$$

$$e_{0(aver)} = \frac{e_{0(nat)}+e_{0(soak)}}{2} \quad (3)$$

In the single oedometer tests, each specimen was subjected to loading stages up to an interest stress, and maintaining the field moisture content. After stabilization of stress deformations, the chamber was filled with fluid, and a new loading stage was applied only 24 hours after soaking. The stress values of 25, 50 and 100 kPa were adopted for the soaking stages.

The collapse index values for each soaking stress can be found from the curves through the Equation 4, according to Jennings & Knight (1975):

$$\boldsymbol{I} = \frac{\Delta \boldsymbol{e_c}}{1+\boldsymbol{e_b}}*100\% \quad (4)$$

Where:

$$\Delta e_c = e_b - e_a \quad (5)$$

From the collapse index values, for both double and single tests, the soil was analyzed taking into account two criteria: one presented by the standard D533-03 (ASTM, 2003) and another showed by Jennings & Knight (1975). Both criteria classifies the soil according to its collapse severity, as it can be seen in Table 1.

3. Results and discussions

3.1 Characterization of soil and soaking fluids

Table 2 presents the soil chemical analysis run before and after the oedometer tests. The pH values obtained for the natural soil through both H_2O and KCl solutions were low, indicating acidity. This condition, when associated with low sodium content, favors the formation of a flocculated structure (Agnelli & Albiero, 1997; Garcia et al., 2004; Rodrigues & Lollo, 2007; Rodrigues et al., 2010), typical of potentially collapsible soils. The observed difference between pH values in water and in potassium chloride indicates the presence of negative charges on the soil surface (Mendonça et al., 2002).

Phosphorus is the main chemical compound used to prepare alkaline and acid solutions, and its content went through a substantial increase after the oedometer tests. According to Sposito (2008), the specific adsorption of phosphorus by the soil tends to decrease positive active sites available on its

Table 1. Classification of the collapse index by its severity (Jennings & Knight, 1975; ASTM, 2003).

Jennings & Knight (1975)		D5333-03 (ASTM, 2003)	
I	Severity of the problem	*I*	Severity of the problem
0 – 1%	None	0%	None
1 – 5%	Moderate	0.1 – 2%	Slight
5 – 10%	Problematic	2.1 – 6%	Moderate
10 – 20%	Serious	6.1 – 10%	Moderately Severe
> 20%	Very Serious	> 10%	Severe

Table 2. Parameters of chemical analysis of the soil.

Parameters	Before the Test	After the Test			
	Natural	Soaked with Water	Soaked with Leachate	Soaked with Alkaline Solution	Soaked with Acid Solution
pH (H_2O)	5.10	4.50	4.40	6.60	6.00
pH (KCl)	4.40	4.50	4.50	4.80	4.40
ΔpH*	-0.70	0.00	0.10	-2.20	-1.60
P (mg/dm^3)	1.85	2.75	2.55	771.85	2327.25
Al^{3+} (cmol$_c$/dm^3)	0.12	0.19	0.07	0.14	1.06
H+Al (cmol$_c$/dm^3)	5.76	5.34	5.34	7.20	10.45
Ca^{2+} (cmol$_c$/dm^3)	0.79	0.57	0.91	0.35	0.25
Mg^{2+} (cmol$_c$/dm^3)	0.18	0.16	0.76	0.20	0.20
K^+ (cmol$_c$/dm^3)	0.12	0.06	2.50	0.10	0.10
CEC (cmol$_c$/dm^3)	6.84	6.13	9.51	7.85	11.00

Note: ΔpH = pH (KCl) – pH (H_2O)

surface, which justifies the pH (H_2O) increase and consequent decrease of ΔpH for soils soaked with such fluids.

The CEC value found for natural soil was characteristic of lateritic soils (less than 17 $cmol_c/dm^3$) (Agnelli & Albiero, 1997; Meurer, 2004). The observed increase on this parameter for the soils soaked with leachate and alkaline and acid solutions, can be partially explained by the addition of ions to the soil solution (Sposito, 2008; Meurer, 2004). In the sample soaked with leachate, exchangeable bases – calcium (Ca^{2+}), magnesium (Mg^{2+}) and potassium (K^+) – could be retained more expressively on the soil surface, which explains a substantial increase in CEC, as well as observed by Frempong & Yanful (2006) and Teixeira et al. (2010). In the samples soaked with alkaline and acid solutions, the retention of phosphorus anion (P) was significant, contributing to increase the CEC value.

According to Collares (2002), the reactions between soil particles and soaking fluid occur due to colloidal instability under the influence of some liquid characteristics, such as electrolyte concentration, pH and temperature. Soil pH and CEC vary when exposed to such fluids, interfering on the collapse potential.

As for the soaking fluids characterization, it was observed that the solutions prepared in the laboratory presented the highest values of electrical conductivity, according to Table 3, indicating that these liquids have a higher amount of soluble ions in their composition (Sposito, 2008).

3.2 Oedometer tests

Tables 4 and 5 show the properties and statistical study for the specimens before and after the double and single oedometer tests, respectively.

Table 3. Electrical conductivity of soaking fluids.

Soaking Fluid	EC_f ($\mu S.cm^{-1}$)
Water	0.07642 x 10^3
Leachate	4.910 x 10^3
Alkaline Solution	15.20 x 10^3
Acid Solution	23.10 x 10^3

In general, according to the coefficient of variation values (CV), the specimens were similar to each other. Since undisturbed samples were collected in different days and climatic conditions, high CV values were obtained for the initial moisture content and degree of saturation. The observed variability for the void ratio after the tests can be justified by the different physical-chemical interactions between the different fluids and the soil. Finally, the saturation degree values after the soaked tests were close or equal to 100%, indicating that the specimens reached the maximum saturation.

3.2.1 Double oedometer tests

Figure 1 shows the normalized curves resulting from the double tests for the four soaking fluids.

From Equation 1 and the data displayed in Table 6, it was possible to predict the collapse indexes and to classify them according to the criteria of Jennings & Knight (1975) and ASTM (2003), as shown in Table 7.

The highest collapse index values were noticed in soakings by alkaline and acid solutions. This can be explained through the high sodium content in the composition of these liquids, since the cation of sodium acts as a dispersant in soils with flocculated structure, rearranging the colloidal particles (Abdullah et al., 1997; Agnelli & Albiero, 1997; Garcia et al., 2004; Rodrigues et al., 2010; Futai et al., 2015). Due to these reasons, it is also highlighted the fact that, even for the soaking stress of 25 kPa, below the pre-consolidation stress of this saturated soil, the collapse was quite pronounced when the soil was soaked with these two liquids.

In relation to soakings with leachate and water, it was observed lower collapse indexes when compared to soakings with alkaline and acid solutions, considered as sodium-based dispersants. This behavior corroborates the results obtained by Collares & Vilar (2017). Oztoprak & Pisirici (2011) affirmed that leachate-permeated soil voids can be clogged by suspended solids present in the liquid, decreasing compressibility, which could be observed in this work, once the lowest collapse indexes, in general, were found for soaked samples with such fluid.

Table 4. Specimens properties before and after the double tests.

Condition	Moisture Content (%)		Dry Density (kN/m^3)		Void Ratio		Degree of Saturation (%)	
	Before	After	Before	After	Before	After	Before	After
No Soaking	28.3	22.1	9.5	10.8	2.15	1.77	39.6	37.4
Soaked with Water	28.4	42.5	10.1	14.9	1.98	0.99	43.2	100.0
Soaked with Leachate	31.6	38.9	12.5	18.9	2.16	1.19	43.8	97.9
Soaked with Alkaline Solution	20.7	30.9	11.0	17.3	1.73	0.75	35.9	100.0
Soaked with Acid Solution	20.7	28.8	10.0	17.0	2.00	0.86	31.1	100.0
Average	25.3	35.3	10.9	17.0	2.0	0.9	38.5	99.5
Standard Deviation	5.5	6.5	1.2	1.6	0.2	0.2	6.1	1.0
CV (%)	21.9	18.4	10.6	9.7	9.0	20.0	16.0	1.0

Note: Average, Standard Deviation and CV only for the soaked specimens.

Table 5. Specimens properties before and after the single tests.

Condition Before		Moisture Content (%)		Dry Density (kN/m³)		Void Ratio		Degree of Saturation (%)	
		After	Before	After	Before	After	Before	After	
Soaked with Water	Soaked at 25 kPa	35.9	37.2	10.2	13.3	1.95	1.24	55.3	90.2
	Soaked at 50 kPa	31.0	37.1	9.6	13.4	2.13	1.23	43.8	90.1
	Soaked at 100 kPa	31.4	38.6	10.0	14.6	1.99	1.02	47.3	100.0
Soaked with Leachate	Soaked at 25 kPa	30.9	37.6	10.4	14.0	1.88	1.10	49.4	100.0
	Soaked at 50 kPa	29.5	38.9	11.1	14.9	1.69	0.97	52.2	100.0
	Soaked at 100 kPa	32.1	40.5	10.3	14.5	1.92	1.06	50.1	100.0
Soaked with Alkaline Solution	Soaked at 25 kPa	18.1	34.2	10.2	15.5	1.93	0.91	29.2	100.0
	Soaked at 50 kPa	20.2	32.8	10.3	16.6	1.91	0.90	31.7	100.0
	Soaked at 100 kPa	20.8	31.2	10.0	15.7	2.00	0.93	31.3	100.0
Soaked with Acid Solution	Soaked at 25 kPa	21.0	33.8	10.0	18.4	2.00	0.64	31.5	100.0
	Soaked at 50 kPa	20.1	34.6	9.9	16.4	2.03	0.87	29.8	100.0
	Soaked at 100 kPa	32.1	40.5	10.3	14.5	1.92	1.06	50.1	100.0
Average		26.9	36.4	10.2	15.2	1.9	1.0	41.8	98.4
Standard Deviation		6.3	3.0	0.4	1.5	0.1	0.2	10.2	3.8
CV (%)		23.3	8.3	3.6	9.7	5.4	16.6	24.4	3.9

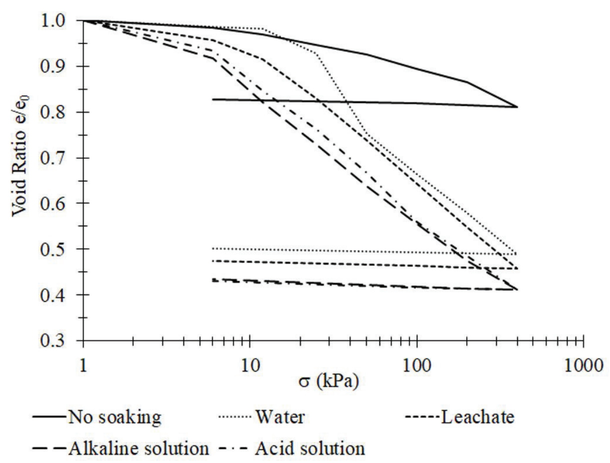

Figure 1. Normalized curves of the double oedometer tests.

3.2.2 Single oedometer tests

Figure 2 below shows the curves obtained from the single oedometer tests for soaking under the stress values of 25, 50 and 100 kPa for the four fluids.

From Equation 4 and the data contained in Table 8, it was possible to obtain the collapse indexes and classify them according to the criteria of Jennings & Knight (1975) and ASTM (2003), as shown in Table 9.

From Figure 2a and Table 9, it is possible to observe for the soaked tests with water that the collapse index was higher at 50 kPa of soaking stress. This is justified by the fact that this specimen has a higher void ratio ($e = 2.13$) than the test specimen soaked at 100 kPa ($e = 1.99$).

Vargas (1978) states that high values of void ratios indicate porous soil structure, favoring an increase of collapse magnitude. With the soaking the pore sizes decrease, which generates an abrupt volume reduction.

Regarding the remaining specimens soaked with leached and the alkaline and acid solutions, the observed behavior was the expected, where higher soaking stresses caused higher collapse rates, since the specimens presented similar physical characteristics (Dudley, 1970; Ferreira, 1995).

The highest collapse indexes occurred in the soaking with alkaline and acid solutions, being, in general, more significant in the second condition. The compositions of these liquids were rich in sodium, which contributed to the greater dispersion of the soil, thus, increasing the collapse

Table 6. Void ratios used to calculate the collapse index from double oedometer tests.

Stress of Interest (kPa)	No Soaking		Soaked with Water		Soaked with Leachate		Soaked with Alkaline Solution		Soaked with Acid Solution	
	$e_{0(nat)}$	e_{nat}	$e_{0(soak)}$	e_{soak}	$e_{0(soak)}$	e_{soak}	$e_{0(soak)}$	e_{soak}	$e_{0(soak)}$	e_{soak}
25	2.15	2.03	1.98	1.83	2.16	1.85	1.73	1.26	2.00	1.52
50		1.98		1.49		1.68		1.10		1.33
100		1.92		1.31		1.50		0.96		1.12

Table 7. Evaluation of collapse from double oedometer tests.

Conditions		Collapse Index - I (%)	Classification Criteria	
Soaking Fluid	Stress of Interest (kPa)		Jennings & Knight (1975)	ASTM (2003)
Water	25	1.40	Moderate	Slight
	50	11.98	Serious	Severe
	100	16.80	Serious	Severe
Leachate	25	6.23	Problematic	Moderately Severe
	50	10.34	Serious	Severe
	100	14.63	Serious	Severe
Alkaline Solution	25	14.79	Serious	Severe
	50	19.85	Serious	Severe
	100	24.01	Very Serious	Severe
Acid Solution	25	12.92	Serious	Severe
	50	18.24	Serious	Severe
	100	24.22	Very Serious	Severe

Table 8. Void ratios used to calculate the collapse index from single oedometer tests.

Soaking Stress (kPa)	Soaked with Water		Soaked with Leachate		Soaked with Alkaline Solution		Soaked with Acid Solution	
	e_b	e_a	e_b	e_a	e_b	e_a	e_b	e_a
25	1.90	1.85	1.81	1.72	1.88	1.51	1.96	1.53
50	2.08	1.87	1.58	1.42	1.86	1.42	1.96	1.43
100	1.69	1.57	1.74	1.41	1.91	1.32	1.79	1.25

Table 9. Evaluation of collapse from single oedometer tests.

Conditions		Collapse Index - I (%)	Classification Criteria	
Soaking Fluid	Soaking Stress (kPa)		Jennings & Knight (1975)	ASTM (2003)
Water	25	1.79	Moderate	Slight
	50	6.86	Problematic	Moderately Severe
	100	4.45	Moderate	Moderate
Leachate	25	3.34	Moderate	Moderate
	50	6.24	Problematic	Moderately Severe
	100	11.98	Serious	Severe
Alkaline Solution	25	12.66	Serious	Severe
	50	15.37	Serious	Severe
	100	20.23	Very Serious	Severe
Acid Solution	25	14.45	Serious	Severe
	50	17.77	Serious	Severe
	100	19.54	Serious	Severe

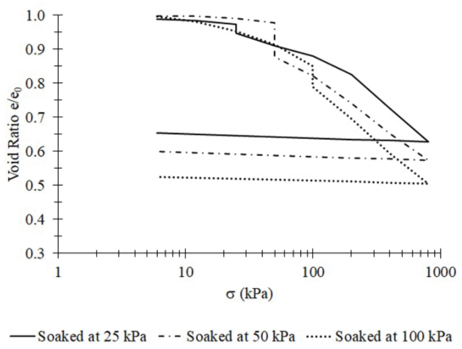

(a)

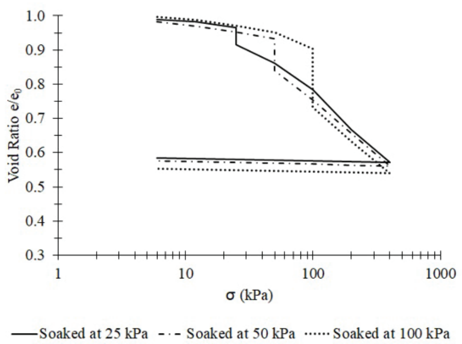

(b)

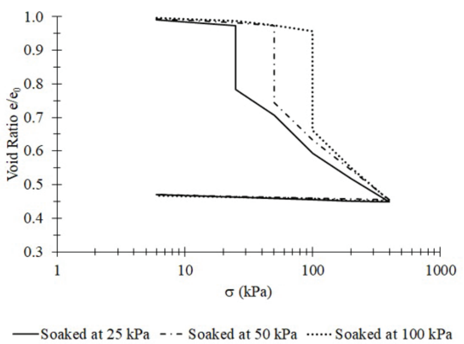

(c)

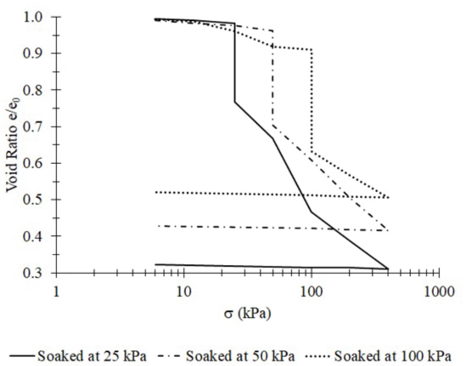

Figure 2. Curves of the single oedometer tests - (a) soaked with water, (b) soaked with leachate, (c) soaked with alkaline solution and (d) soaked with acid solution.

magnitude, even under stresses below that of pre-consolidation saturated, as previously seen in the double test results (Abdullah et al., 1997; Agnelli & Albiero, 1997; Garcia et al., 2004; Rodrigues et al., 2010; Futai et al., 2015).

3.3 Collapse index correlation with pH and electrical conductivity of the soaking fluids

The following Figure 3 shows the variation of (a) total collapse index – I_{total} (%) and (b) partial collapse index – $I_{partial}$ (%) related to pH and EC_f of the soaking fluids at 25, 50 and 100 kPa of soaking stresses (σ_{soak}) for the single oedometer tests. The total collapse index was obtained by the simple difference between the void indexes before and after the soaking for each liquid and soaking stress, according to Equation 4 and shown in Tables 8 and 9. The partial collapse index was obtained by the difference between the normalized final void index after soaking with water and the normalized final void index after soaking with leachate and alkaline and acid solutions, for each soaking stress.

As is already known, matric suction has an important role in the magnitude of soil collapse (Rao & Revanasiddappa, 2000; Jotisankasa et al., 2007; Vilar & Rodrigues, 2011; Benatti & Miguel, 2013; Li and Vanapalli, 2018), and each liquid influences this phenomenon differently. Since the suction analysis was not the focus of this paper, Figure 3b shows the collapse only due to the influence of the composition of the soaking fluid, since the void indexes considered were of the soil already saturated, with matric suction close to zero.

For the Figure 3a and regarding the pH, water and leachate had a proportional relationship, in general – the higher the pH, the higher the collapse index, whereas for the alkaline and acid solutions the relation was inversely proportional – the lower the pH, the higher the collapse index. There were small discrepancies on the collapses at 50 kPa of soaking stress for water and leachate, and at 100 kPa for alkaline and acid solutions. These differences can be explained by the initial void ratio values of the samples (e_0). For the specimen soaked with leachate, the e_0 was smaller (1.69) than that soaked with water (2.13); and for the sample soaked with the alkaline solution, the specimen had a higher value of e_0 (2.00) than the one soaked with the acid solution (1.92). These discrepancies for the alkaline and acid solutions are eliminated when analyzing Figure 3b, where the void indexes were normalized and the influence of the matric suction was almost zero.

This divergence of correlations corroborates the fact that pH alone cannot be an indicative parameter of the collapse behavior, which is, therefore, dependent on other characteristics, such as chemical composition, electrical conductivity and soil structure (Reginatto & Ferrero, 1973; Carvalho et al., 1987; Fang, 1997; Garcia et al., 2004; Olgun & Yildiz, 2010; Collares & Vilar, 2017; Choudhury & Bharat, 2018).

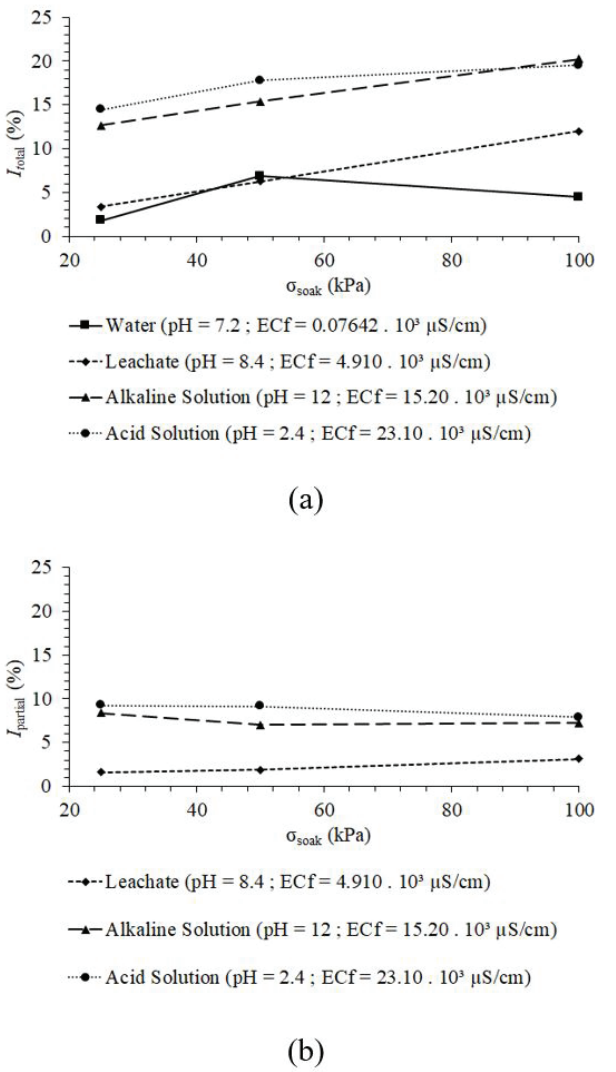

Figure 3. Correlation between (a) the total collapse index and (b) partial collapse index with pH and EC_f of the soaking fluids.

Still considering the trends observed, the soil soaked with the acid solution indicates a higher collapse index compared to the other three fluids, which is in agreement with Imai et al. (2006), Gratchev & Towhata (2011), Gratchev & Towhata (2016), Zhang et al. (2018), Khodabandeh et al. (2020) and Siddiqua et al. (2020), who affirmed that acid fluids could contribute to the dissolution of carbonates, one of those responsible for stabilizing the soil structure. Moreover, Wang & Siu (2006a) and Wang & Siu, (2006b) showed that, in an acidic environment, kaolinite – the main mineral of this soil – tends to form more open arrangements that might result in greater soil compressibility.

Sunil et al. (2006), Motta & Ferreira (2013) and Siddiqua et al. (2020) pointed out that alkaline solutions also tend to cause significant values of collapse index (I), a behavior verified in this study when comparing the alkaline solution with the water and the leachate, with lower pH. This shows that alkaline and acid solutions tend to cause higher collapse indexes when compared to liquids with pH close to neutrality.

In this study it was also observed a direct relationship between collapse index (I) and electrical conductivity (EC_f) that is, the higher the electrical conductivity, the higher the collapse index. According to Motta & Ferreira (2011) and Khan et al. (2017), liquids with higher electrical conductivities tend to cause greater collapses, since the higher this parameter, the greater the ions mobility induced in the soil.

In addition, the soaking with acid solution, whose EC_f value is the highest, presented the highest collapse index. According to Sridharan et al. (1986) and Van Olphen (1991), in acidic environments, H^+ ions tend to change positions with higher valence cations from the diffuse double layer of soil particles, leading to an increase in DDL thickness and, consequently, a higher soil compressibility.

Similar to the correlation with pH, the correlation with EC_f and I_{total} also indicated some divergences: for water at 50 kPa of soaking stress, and for acid solutions at 100 kPa. These differences can again be explained by the initial void ratio or matric suction values of the samples. However, when analyzing the $I_{partial}$ at Figure 3b, where the influence of the matric suction was practically canceled and the void indexes were normalized, it is noted that the divergences were eliminated, confirming the trend mentioned above: the higher the EC_f, the greater the collapse index of the soil.

4. Conclusions

It is concluded from this study that the evaluated soil presents collapsible behavior when soaked with the four fluids. The characteristics of such fluids interfere with the collapse magnitude. Sodium-rich liquids tend to be dispersive to soils, destroying the bonds between the particles and generating greater deformations.

In general, the higher the soaking stresses, the higher the collapse indexes (I). However, it is worth mentioning that this behavior depends on the porosity of the soil structure and the moisture and matric suction before the soaking.

It was not found a unique relationship between pH and collapse index, therefore, this characteristic is insufficient for a more accurate evaluation of the soil collapsible behavior. However, a tendency of alkaline and acid liquids to cause higher collapse indexes was found when compared to liquids with pH closer to neutrality.

Finally, the electrical conductivity of the fluid presented a unique and direct relationship with the collapse index. Hence, the greater the electrical conductivity of the fluid, the greater the collapse magnitude generated by the soaking.

Acknowledgements

The authors thank the Coordination of Improvement of Higher Education Personnel (CAPES) for funding the research.

Declaration of interest

The authors guarantee that there are no conflicts of interest in this research.

Authors' contributions

Renan Zanin: data curation, formal analysis, investigation, visualization, writing – original draft, writing – review & editing. Ana Padilha: conceptualization, data curation, investigation. Flávia Pelaquim: data curation, formal analysis, writing – review & editing. Nelcí Gutierrez: data curation, writing – original draft. Raquel Teixeira: conceptualization, data curation, supervision, writing – original draft.

List of symbols

BOD	biological oxygen demand
COD	chemical oxygen demand
CV	coefficient of variation
EC_f	electrical conductivity of the soaking fluid
e_{nat}	final void index for applied stress of the double test without soaking
e_{soak}	final void index for applied stress of the double test with soaking
Δe_c	variation of the void index due to soaking
$e_{0(nat)}$	initial void index of the double test without soaking
$e_{0(soak)}$	initial void index of the double test with soaking
$e_{0(aver)}$	average initial void index of the double test with and without soaking
e_0	initial void index of the single test sample
e_b	void index before soaking of the single test
e_a	void index after soaking of the single test
I	collapse index
NBR	Brazilian Standard
Sr	degree of saturation
w	moisture content
η	porosity
σ	stress
σ_{soak}	soaking stress

References

Abdullah, W.S., Al-Zou'bi, M.S., & Alshibli, K.A. (1997). On the physicochemical aspects of compacted clay compressibility. *Canadian Geotechnical Journal*, 34, 551-559. http://dx.doi.org/10.1139/t97-027.

ABNT NBR 6457. (1986a). *Soil Samples - Preparation for compaction tests and characterization tests*. ABNT – Associação Brasileira de Normas Técnicas, Rio de Janeiro, RJ. (in Portuguese).

ABNT NBR 9604. (1986b). *Well and trench opening and soil inspection, with removal of disturbed and undisturbed samples*. ABNT – Associação Brasileira de Normas Técnicas, Rio de Janeiro, RJ. (in Portuguese)

Agnelli, N., & Albiero, J.H. (1997). Physical, chemical and mechanical aspects of a collapsible soil, soaked with different liquids. *Soils and Rocks*, 20(2), 79-95. (in Portuguese)

ASTM D2435-11. (2011). *Standard practice for one-dimensional consolidation properties of soils using incremental loading*. ASTM International, West Conshohocken, PA. https://doi.org/10.1520/D2435_D2435M-11.

ASTM D5333-03. (2003). *Standard test method for measurement of collapse potential of soils*. ASTM International, West Conshohocken, PA. https://doi.org/10.1520/D5333-03.

Barden, L., Mcgown, A., & Collins, K. (1973). The collapse mechanism in partly saturated soil. *Engineering Geology*, 7(1), 49-60. http://dx.doi.org/10.1016/0013-7952(73)90006-9.

Benatti, J.C.B., & Miguel, M.G. (2013). A proposal of structural models for colluvial and lateritic soil profile from southwestern Brazil on the basis of their collapsible behavior. *Engineering Geology*, 153, 1-11. http://dx.doi.org/10.1016/j.enggeo.2012.11.003.

Carvalho, J.C., Nunes, P.M., Berberian, D., & Ferreira, E.S. (1987). Influence of the pH of the saturation liquid on the collapsibility. In L Beltrán (Ed.), *Proc. 8th Pan American Congress of Soil Mechanics and Foundation Engineering* (pp. 1-8). Cartagena: ISRM. (in Spanish).

Chen, J., Anandarajah, A., & Inyang, H. (2000). Pore fluid properties and compressibility of kaolinite. *Journal of Geotechnical and Geoenvironmental Engineering*, 126(9), 798-807. http://dx.doi.org/10.1061/(ASCE)1090-0241(2000)126:9(798).

Choudhury, C., & Bharat, T.V. (2018). Wetting-induced collapse behavior of kaolinite: influence of fabric and inundation pressure. *Canadian Geotechnical Journal*, 55(7), 956-967. http://dx.doi.org/10.1139/cgj-2017-0297.

Collares, A.C.Z.B. (2002). *Influence of structural and chemical factors on collapse and dispersion of two soils* [Doctoral thesis, University of São Paulo]. University of São Paulo's repository (in Portuguese).

Collares, A.C.Z.B., & Vilar, O.M. (2017). The influence of some chemical properties of soaking liquids on the collapse of tropical soils. In L.R. Hoyos, J.S. McCartney, S.L. Houston, & W.J. Likos (Eds.), *Proc. 2nd Pan-American Conference on Unsaturated Soils* (pp. 398-407). Dallas: ISSMGE.

Conciani, W., & Barbosa, F.M.D.R. (2013). Differential strains caused by soaking of the soil with hot and caustic water. In L.F.M. Ribeiro (Ed.), *Proc. 3rd Symposium on Geotechnical Engineering Practice in the Central-West Region and 6th Symposium on Tropical Soils and Erosive Processes* (pp. 178-186). Cuiabá: KCM Editora. (in Portuguese).

Dudley, J.H. (1970). Review of collapsing soils. *Journal of the Soil Mechanics and Foundations Division*, 96(3), 925-947.

Fang, H. (1997). *Introduction to environmental engineering*. CRC Press.

Feda, J. (1966). Structural stability of subsident loess from Praha-Dejvive. *Engineering Geology*, 1(3), 201-219. http://dx.doi.org/10.1016/0013-7952(66)90032-9.

Felici, E.M., Kuroda, E.K., Yamashita, F., & Silva, S.M.C.P. (2013). Removal of recalcitrant organic load from urban solid waste leachate pretreated by chemical coagulation-flocculation-sedimentation. *Engenharia Sanitária e Ambiental*, 18(2), 177-184. (in Portuguese). https://doi.org/10.1590/S1413-41522013000200010.

Ferreira, S.E.M. (1995). *Collapse and expansion of unsaturated natural soils due to soaking* [Doctoral thesis, Federal University of Rio de Janeiro]. Federal University of Rio de Janeiro's repository (in Portuguese).

Frempong, E.M., & Yanful, E.K. (2006). Chemical and mineralogical transformations in three tropical soils due to permeation with acid mine drainage. *Bulletin of Engineering Geology and the Environment*, 65, 253-271. http://dx.doi.org/10.1007/s10064-005-0029-7.

Futai, M.M., Lacerda, W.A., & Martins, A.P.S. (2015). Influence of physicochemical interactions on the mechanical behavior of tropical residual gneiss soils. *Soils and Rocks*, 38(1), 9-25.

Garcia, J.R., Rodrigues, R.A., & Lollo, J.A. (2004). The influence of different soaking fluids on the structural collapse of lateritic sandy soil. *Civil Engineering Journal*, 21, 49-58. (in Portuguese)

Gonçalves, F., Zanin, R.F.B., Somera, L.F., Oliveira, A.D., Ferreira, J.W.S., Branco, C.J.M.C., & Teixeira, R.S. (2018). Physical-Chemical and Mineralogical Characterization of Three Soils of Paraná State. In L.M.E Lima & H.M. Baptista (Eds.), *Proc.19th Brazilian Congress of Soil Mechanics and Geotechnical Engineering* (pp. 456-464). Salvador: ABMS. (in Portuguese).

Gratchev, I., & Towhata, I. (2011). Compressibility of natural soils subjected to long-term acidic contamination. *Environmental Earth Sciences*, 64, 193-200. http://dx.doi.org/10.1007/s12665-010-0838-2.

Gratchev, I., & Towhata, I. (2016). Compressibility of soils containing kaolinite in acidic environments. *KSCE Journal of Civil Engineering*, 20, 623-630. http://dx.doi.org/10.1007/s12205-015-0141-6.

Gutierrez, N.H.M. (2005). *Influences of structural aspects in the collapse of soils of the north of Paraná* [Doctoral thesis, University of São Paulo]. University of São Paulo's repository (in Portuguese).

Gutierrez, N.H.M., Nóbrega, M.T., & Vilar, O.M. (2008). Influence of the microstructure in the collapse of a residual clayey tropical soil. *Bulletin of Engineering Geology and the Environment*, 68, 107-116. http://dx.doi.org/10.1007/s10064-008-0180-z.

Imai, G., Komatsu, Y., & Fukue, M. (2006). Consolidation yield stress of Osaka-Bay pleistocene clay with reference to calcium carbonate contents. *Journal of ASTM International*, 3(7), 1-9. http://dx.doi.org/10.1520/JAI13325.

Jennings, J.E., & Knight, K. (1957). The additional settlement of foundations due to a collapse of structure of sand subsoils on wetting. In W. H. Glanville (Ed.), *Proc. 4th International Society for Soil Mechanics and Foundation Engineering* (pp. 316-319). London: ISSMGE.

Jennings, J.E., & Knight, K. (1975). A guide to construction on or with materials exhibiting additional settlement due to "collapse" of grain structure. In Regional Conference for Africa on Soil Mechanics and Foundation Engineering (Ed.), *Proc. 7th Regional Conference for Africa on Soil Mechanics and Foundation Engineering* (pp. 99-105). Rotterdam: AA Balkema.

Jotisankasa, A., Ridley, A., & Coop, M. (2007). Collapse behavior of compacted silty clay in suction-monitored oedometer apparatus. *Journal of Geotechnical and Geoenvironmental Engineering*, 133(7), 867-877. http://dx.doi.org/10.1061/(ASCE)1090-0241(2007)133:7(867).

Khan, M.I., Irfan, M., Aziz, M., & Khan, A.H. (2017). Geotechnical characteristics of effluent contaminated cohesive soils. *Journal of Environmental Engineering and Landscape Management*, 25(1), 75-82. http://dx.doi.org/10.3846/16486897.2016.1210155.

Khodabandeh, M.A., Nokande, S., Besharatinezhad, A., Sadeghi, B., & Hosseini, S.M. (2020). The effect of acidic and alkaline chemical solutions on the behavior of collapsible soils. *Periodica Polytechnica. Civil Engineering*, 64(3), 939-950. http://dx.doi.org/10.3311/PPci.15643.

Koupai, J.A., Fatahizadeh, M., & Mosaddeghi, M.R. (2020). Effect of pore water pH on mechanical properties of clay soil. *Bulletin of Engineering Geology and the Environment*, 79, 1461-1469. http://dx.doi.org/10.1007/s10064-019-01611-1.

Larionov, A.K. (1965). Structural characteristics of loess soils for evaluating their constructional properties. In J. McMurdie (Ed.), *Proc. 6th International Conference on Soil Mechanics and Foundation Engineering* (pp. 64-68). Montreal: Soil Science Society of America.

Li, P., & Vanapalli, S.K. (2018). Simple method for prediction of the soil collapse behavior due to wetting. *International Journal of Geomechanics*, 18(11), 1-5. http://dx.doi.org/10.1061/(ASCE)GM.1943-5622.0001285.

Mariz, D.F., & Casanova, F.J. (1994). Some relevant aspects in the mechanism of the collapse of soils of the Central Plateau. In E. E. Alonso & P. Delage (Eds.), *Proc. 1st Symposium on Unsaturated Soils*. (pp. 129-134). Rotterdam: AA Balkema. (in Portuguese).

Melo, T.R., Figueiredo, A., Machado, W., & Tavares Filho, J. (2019). Changes on soil structural stability after in natura and composted chicken manure application. *International Journal of Recycling of Organic Waste in Agriculture*, 8, 333-338. http://dx.doi.org/10.1007/s40093-019-0250-1.

Melo, T.R., Machado, W., & Tavares Filho, J. (2020). Charge sparsity: an index to quantify cation effects on clay dispersion in soils. *Scientia Agrícola*, 77(1), e20170392. http://dx.doi.org/10.1590/1678-992X-2017-0392.

Mendonça, R.M.G., Barbosa, M.C., & Castro, F.J.C.O. (2002). Evaluation of ions retention capacity of a residual soil of Rio de Janeiro, Brazil. In L.G. Mello & M. Almeida (Eds.), *Proc. 4th International Congress on Environmental Geotechnics* (pp. 439-446). Rio de Janeiro: CRC Press.

Meurer, E.J. (2004). *Fundamentos de química do solo*. (2 ed, 290 p.). EVANGRAF.

Mitchell, J.K. (1976). *Fundamentals of soils behavior*. John Wiley & Sons.

Motta, E.Q., & Ferreira, S.E.M. (2013). Influence of percolation of contaminating fluids on the collapsibility of a compacted. In A.S. Messias (Ed.), *Proc. of 7th International Water Meeting* (pp. 1-8). Recife: Fasa. (in Portuguese).

Motta, E.Q., & Ferreira, S.R.M. (2011). Variability of the compressibility and the collapse potential of a soil before different soaking liquids. *REA – Revista de Estudos Ambientais*, 13(1), 28-41 (in Portuguese). http://dx.doi.org/10.7867/1983-1501.2011v13n1p28-41.

Olgun, M., & Yildiz, M. (2010). Effect of organic fluids on the geotechnical behavior of a highly plastic clayey soil. *Applied Clay Science*, 48(4), 615-621. http://dx.doi.org/10.1016/j.clay.2010.03.015.

Oliveira, C.M.G. (2002). *Risk chart of soil collapse for the urban area of Ilha Solteira (SP)* [Mater's dissertation, Paulista State University]. Paulista State University's repository (in Portuguese).

Oztoprak, S., & Pisirici, B. (2011). Effects of micro structure changes on the macro behaviour of Istanbul (Turkey) clays exposed to landfill leachate. *Engineering Geology*, 121(3-4), 110-122. http://dx.doi.org/10.1016/j.enggeo.2011.05.005.

Rao, S.M., & Revanasiddappa, K. (2000). Role of matric suction in collapse of compacted clay soil. *Journal of Geotechnical and Geoenvironmental Engineering*, 126(1), 85-90. http://dx.doi.org/10.1061/(ASCE)1090-0241(2000)126:1(85).

Reginatto, A.R., & Ferrero, J.C. (1973). Collapse potential of soils and soil-water chemistry. In N. A. Tsytovich & N. S. Chetyrkin (Ed.), *Proc. 8th International Conference on Soil Mechanics and Foundation Engineering* (pp. 177-183). Moscow: Soil Science Society of America.

Réthati, L. (1961). Behaviour of buildings founded on embankments. In International Society of Soil Mechanics and Foundation Engineering. (Ed.), *Proc. 5th International Conference on Soil Mechanics and Foundation Engineering* (pp. 781-784). Paris: Soil Science Society of America.

Rezaei, M., Ajalloeian, R., & Ghafoori, M. (2012). Geotechnical properties of problematic soils emphasis on collapsible cases. *International Journal of Geosciences*, 3, 105-110. http://dx.doi.org/10.4236/ijg.2012.31012.

Rice, E.W., Baird, A.D., & Eaton, A.D. (2005). *Standard methods for the examination of water and wastewater* (21st ed). Washington, DC: American Public Health Association.

Rodrigues, R.A., & Lollo, J.A. (2007). Influence of domestic sewage leakage on the collapse of tropical soils. *Bulletin of Engineering Geology and the Environment*, 66, 215-223. http://dx.doi.org/10.1007/s10064-006-0065-y.

Rodrigues, R.A., Molina Junior, V.E., & Lollo, J.A. (2010). The influence of sewage constituents in sandy soil collapse. *Engenharia Sanitária e Ambiental*, 15(1), 29-36. (in Portuguese). https://doi.org/10.1590/S1413-41522010000100004.

Siddiqua, S., Bigdeli, A., & Cherian, C. (2020). Effect of pore fluid pH on the collapse behaviour and microstructural evolution of a loess. *Environmental Geotechnics*, 40, 1-11. http://dx.doi.org/10.1680/jenge.20.00011.

Sposito, G. (2008). *The Chemistry of soils.* Oxford University Press.

Sridharan, A., Rao, S., & Murthy, N. (1986). Compressibility behaviour of homoionized bentonites. *Geotechnique*, 36(4), 551-564. http://dx.doi.org/10.1680/geot.1986.36.4.551.

Sunil, B.M., Nayak, S., & Shrihari, S. (2006). Effect of pH on the geotechnical properties of laterite. *Engineering Geology*, 85, 197-203. http://dx.doi.org/10.1016/j.enggeo.2005.09.039.

Teixeira, P.C., Donagemma, G.K., Fontana, A., & Teixeira, W.G. (1997). Manual of soil analysis methods. Embrapa. (in Portuguese).

Teixeira, R.S., Branco, C.J.M.C., Sobrinho, V.R.M., & Teixeira, S.H.C. (2008). Evaluation of geotechnical parameters through correlations of SPT, CPT and DMT results. In (Ed.), *Proc.14th Brazilian Congress of Soil Mechanics and Geotechnical Engineering*. Búzios: ABMS. (in Portuguese).

Teixeira, R.S., Cambier, P., Dias, R.D., Pinese, J.P.P., & Jaulin-Soubelet, A. (2010). Mobility of potentially harmful metals in latosols impacted by the municipal solid waste deposit of Londrina, Brazil. *Applied Geochemistry*, 25, 1-15. http://dx.doi.org/10.1016/j.apgeochem.2009.09.022.

Teixeira, R.S., Vendrame, P.R.S., Christoni, A.R.F., & Silva, P.R.C. (2016). Chemistry and mineralogy of a soil developed from basalt, collected by standard penetration test. *Boletim de Geografia*, 34(2), 116-126. (in Portuguese). https://doi.org/10.4025/bolgeogr.v34i2.28948.

Van Olphen, H. (1991). An introduction to clay colloid chemistry. Krieger Publishing Company.

Vargas, M. (1978). Introduction to Soil Mechanics. McGraw-Hill do Brasil (in Portuguese).

Vilar, O.M., & Rodrigues, R.A. (2011). Collapse behavior of soil in a Brazilian region affected by a rising water table. *Canadian Geotechnical Journal*, 48(2), 226-233. https://doi.org/10.1139/T10-065.

Wang, Y.-H., & Siu, W.-K. (2006a). Structure characteristics and mechanical properties of kaolinite soils. I. Surface charges and structural characterizations. *Canadian Geotechnical Journal*, 43(6), 587-600. http://dx.doi.org/10.1139/t06-026.

Wang, Y.-H., & Siu, W.-K. (2006b). Structure characteristics and mechanical properties of kaolinite soils. II. Effects of structure on mechanical properties. *Canadian Geotechnical Journal*, 43, 601-617. http://dx.doi.org/10.1139/t06-027.

Zhang, Y., Hu, Z., Chen, H., & Xue, T. (2018). Experimental investigation of the behavior of collapsible loess treated with the acid-addition pre-soaking method. *KSCE Journal of Civil Engineering*, 22, 4373-4384. http://dx.doi.org/10.1007/s12205-017-0170-4.

Soils and Rocks
An International Journal of Geotechnical and Geoenvironmental Engineering
www.soilsandrocks.com
ISSN 1980-9743
ISSN-e 2675-5475

Use of machine learning techniques for predicting the bearing capacity of piles

Yago Ferreira Gomes[1], Filipe Alves Neto Verri[2], Dimas Betioli Ribeiro[1#]

Article

Keywords
Concrete precast piles
Bearing capacity
Semi-empirical methods
Machine learning

Abstract

Geotechnical engineers frequently rely on semi-empirical methods like Décourt-Quaresma and Meyehof's to estimate the bearing capacity of piles. This paper proposes alternatives to these methods, presenting an approach using machine learning models for predicting the bearing capacity of precast concrete piles. It uses data samples including 165 load tests, each one accompanied with a SPT sounding. This study proposes two types of analysis using two separated datasets, one based on the Décourt-Quaresma method and the other based on the Meyerhof method. Six machine learning algorithms of distinct biases are trained and tested with a leave-one-out cross validation procedure and the models' predictive performance is assessed through two metrics: root mean squared error (RMSE) and coefficient of determination (R^2). The best performing technique was random forest (RF) using Décourt-Quaresma dataset, with an RMSE of 642.38. All other machine learning techniques obtained a RMSE below 710, overcoming Meyerhof's and Décourt-Quaresma's semi-empirical methods, which both obtained RMSE values close to 900. This study proposes 95% and 90% confidence intervals for the best technique employing a graphical interpretation, so that geotechnical engineers can choose which level of safety they wish to work with. Finally, the study presents a case study showing that the best performing models achieve a reasonable accuracy, surpassing the semi-empirical methods in two of the three piles considered. The representativity of the new examples within the used datasets explain the accuracy of the techniques.

1. Introduction

Designers need to estimate the load bearing capacity of piles and the most precise way is through static pile load tests. The Brazilian Standard (ABNT 2019) define procedures for this type of test, which basically consists on applying an increasing load to an executed pile and measuring its displacement. Designers can obtain the load bearing capacity by examining the load-displacement graph, using criteria defined by the standard. Nonetheless, they cannot rely only on static pile load tests because they are expensive, time consuming and usually executed when part of the piles of the project are already in place. The most popular approach to estimate pile bearing capacity beforehand is to use semi-empirical methods, like those proposed by Aoki & Velloso (1975), Décourt & Quaresma (1978, 1998) and Meyerhof (1976). Most semi-empirical methods propose two separate estimates: one for the shaft resistance and another for the tip resistance. The total pile bearing capacity given by the sum of them. These methods usually estimate the bearing capacity through results of in situ tests and pile geometric features. In several countries (including Brazil), contractors usually only make available the standard penetration test (SPT). The main reasons are cost and simplicity when compared to methods like the cone penetration test, making the SPT popular in those countries. Even when designers do have access to other in situ tests, they sometimes rely on correlations to convert data into SPT values.

In recent years, machine learning techniques are increasingly gaining space within a wide variety of engineering applications. Their advantages include the capability to deal with large amounts of data and to find complex and highly nonlinear relationships among different parameters. In geotechnics many works have been using these algorithms to solve different kinds of problems with good results over traditional methods. Some of these problems are: soil classification (Bhattacharya & Solomatine, 2006; Kovacevic et al., 2010; Bonini et al., 2017; Carvalho & Ribeiro 2019), soil profiling (Arel, 2012), soil liquefaction (Juang & Chen, 1999; Hanna et al., 2007; Goh & Goh,

[#]Corresponding author. E-mail address: dimasbetioli@gmail.com
[1]Instituto Tecnológico de Aeronáutica, Divisão de Engenharia Civil, São José dos Campos, SP, Brasil.
[2]Divisão de Ciência da Computação, Instituto Tecnológico de Aeronáutica, São José dos Campos, SP, Brasil.

Submitted on September 6, 2021; Final Acceptance on Outubro 27, 2021; Discussion open until February 28, 2022.
https://doi.org/10.28927/SR.2021.074921

2007; Livingston et al., 2008; Kohestani et al., 2015), slope stability (Ferentinou & Sakellariou, 2007; Bui et al., 2019; Maxwell et al., 2020) , foundation settlement (Samui, 2008; Nejad et al., 2009; Nejad & Jaksa, 2017) and bearing capacity. For the latter, authors have used well-known algorithms with different kinds of inputs, such as wave stress data (Lok & Che, 2004; Pal & Deswal, 2008; Maizir & Kassim, 2013; Momeni et al., 2015), soil parameters (Pal & Deswal, 2010; Moayedi & Hayati, 2019; Kardani et al., 2020), CPT results (Ardalan et al., 2009; Shahin, 2010; Kordjazi et al., 2014; Kordjazi et al., 2013; Alkroosh et al., 2015) and SPT measures (Lee & Lee, 1996; Nawari & Liang, 2000; Ismail & Jeng, 2011; Benali et al., 2018; Jesswein & Liu, 2018; Pham et al., 2020). These studies achieved reasonable results for the proposed problems. Nevertheless, most of them include weaknesses like comparing few techniques or using very homogeneous datasets, with all soundings taken from the same construction site.

The main objective of this paper is to propose a new approach for the use of machine learning techniques, using classical semi-empirical methods as a basis for estimating the bearing capacity of piles. It is better than previous machine learning models from the literature concerning generality for tropical soils and ease of use. The used datasets include only static load tests (slow maintained load) of pre-cast concrete piles executed accordingly to the Brazilian standard (see ABNT 2019) and accompanied with SPT soundings. The investigation starts with the training of six machine learning techniques, producing two models for each one: the first using the inputs from the Décourt-Quaresma method and the second the inputs from the Meyerhof method. A multiple linear regression (LR) is also included as a baseline for performance. The authors selected the Décourt-Quaresma method because it is commonly used in Brazilian foundation projects and Meyerhof for being widely used worldwide. Both sets of inputs include pile diameter and length, the mean SPT along the shaft and the mean SPT at the pile tip. The main difference of the two sets is how mean SPT values are calculated.

It is shown in a general application that the precision of all machine learning techniques surpassed both Meyerhof (1976) and Décourt & Quaresma (1978, 1998) semi-empirical methods with respect to RMSE. This work proposes a graphical method to provide 90% and 95% confidence intervals for the results of the best technique. A case study applies the top two machine learning models and the two semi-empirical methods to three new examples, from one site that was not included in the training dataset. The machine learning techniques presented reasonable performance, and were better than the semi-empirical methods in two of the three piles.

2. Semi-empirical methods

Semi-empirical methods work based on empirical correlations of in situ tests data and adjustments with load test results. Results can vary for these methods due to their implicit subjectivity. For the Meyerhof method, little subjectivity was included because it uses N_{SPT} and pile geometry as inputs, which are not sensitive to interpretation. On the other hand, the Décourt-Quaresma method relies on soil types as presented in Table 1, which are sensitive to interpretation.

In these methods, the pile load capacity R_t is usually divided into two parts: lateral friction R_l and tip resistance R_p, as shown in Equation 1. Different expressions are proposed for R_l and R_p in the literature, using information such as soil type, pile type, pile geometry and in situ test results.

$$R_t = R_l + R_p \tag{1}$$

The authors selected two methods for this study: the Décourt-Quaresma method for being popular in Brazil and the Meyerhof method for being widely used around the world. The next sections describe these methods.

2.1. Décourt-Quaresma

This method obtains the tip resistance using a factor related to the soil type, as presented in Table 1. It also uses the tip area A_p and the mean N_{SPT} index around the pile tip SPT_p, considering the value at the tip, the one above and the one below. It obtains the lateral resistance using pile geometry and the mean N_{SPT} index along the pile shaft SPT_l. The latter is subjected to $3 < SPT_p < 15$ and N_{SPT} values used to obtain SPT_p cannot be included. The final expression is

$$R_t = \alpha.K.SPT_p.A_p + U.\beta.10\left(\frac{SPT_l}{3}+1\right)L \tag{2}$$

where α and β refer to soil and pile type, respectively. U is the pile perimeter and L is the pile length.

2.2. Meyerhof

This method uses the N_{SPT} index, pile length L and pile diameter D to estimate the pile bearing capacity. It calculates SPT_l as the mean of the whole pile shaft and SPT_p as the mean including $8D$ above the tip and $3D$ below it (Meyerhof, 1976). The expression proposed by Meyerhof is

Table 1. Values for K (Décourt & Quaresma, 1978, 1998).

Soil type	K (KN/m^2)
Clays	120
Clayey silts	200
Sandy silts	250
Sands	400

$$R_t = A_p.q_p + U.L.q_s \tag{3}$$

where

$$q_p = 40.L\frac{SPT_p}{D} \leq 400.SPT_p \tag{4}$$

and

$$q_s = 2.SPT_l \tag{5}$$

3. Dataset

The information used in this work includes 165 precast concrete pile load tests and their respective SPT measures collected from many different construction sites in Brazil. It was obtained from the works of Lobo (2005), Vianna (2000) and Santos (1988) and all load tests were performed according to the Brazilian Standard (ABNT, 2019). When the maximum applied load was not achieved, the load-settlement curve was extrapolated using the Van der Veen method (Van Der Veen, 1953). Interested readers can find further detail about these load tests in Lobo (2005), Vianna (2000) and Santos (1988). In specific cases, information about pile rupture and comparisons between applied and ultimate loads is available.

Figure 1 presents the location of the soundings, most of them from the south and southeast regions of Brazil. The country presents a predominant tropical climate and high temperatures, with 65% of its territory covered by non-homogeneous lateritic soils. The clay-ferruginous soil is the most common type (Morais et al., 2020). The authors had access to some details about the set provided by Vianna (2000), which is composed by soundings taken from the city of Curitiba, in Paraná state. The geology of this region can be divided into three groups: a metamorphic rock complex from the Precambian; sedimentary deposits from Tertiary; and a more recent sedimentary deposit (Holocene), as a result of a partial removal of older sediments (Cenozoic). This entire sequence of Cenozoic sediments in the Curitiba Basin is named Guabirotuba Formation in the literature (Bigarella & Salamuni, 1962).

After assembly, raw data was preprocessed into two datasets. The first, named Décourt dataset, uses SPT_p, SPT_l, D (in cm) and L (in m) as calculated in the Décourt-Quaresma method. The second uses the same inputs, but defined accordingly to the Meyerhof method. Notice that the difference is how each method calculates SPT_p and SPT_l, as presented in previous sections. The authors did not include soil type among the inputs because, based on their previous experience, these variables do not contribute to improve accuracy and include too much human error. Thus, although the authors consider the position of the water table relevant for the problem, they decided not to include it because many of the used soundings did not include this information. Figure 2 illustrates the variables used in each set. The target feature is the pile bearing load capacity Q_u

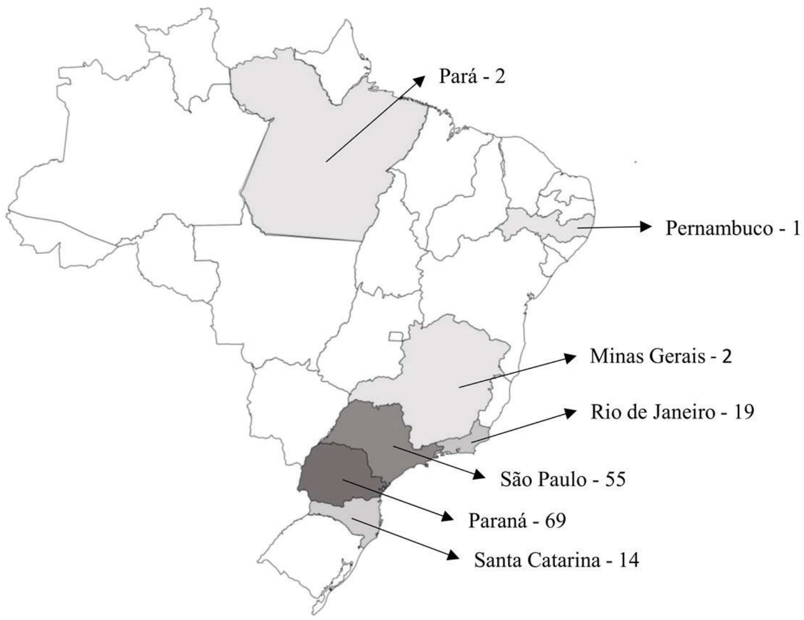

Figure 1. Number of soundings at each Brazilian state.

in kN, obtained from the load test. Tables 2 and 3 present a sample of each dataset. Unity b refers to the number of blows needed for the sampler to penetrate 30 cm into the soil (Salgado, 2008).

Tables 4 and 5 present correlation matrices generated for each dataset. Inputs are not severely correlated, with all values within the interval $[-0.7, 0.7]$. This indicates that they can be all considered informative, occurring few redundancies between them. Notice that the correlation between SPT_l and SPT_p is only 0.35 for the Décourt dataset, while it rises to 0.7 for the Meyerhof dataset. This can be explained by the way each method obtains these variables, with completely separated soil layers considered for the Décourt dataset and an intersection of common soil layers considered for the Meyerhof dataset (see Figure 2). D and L are the ones with stronger correlation to the output Q_u, which was expected.

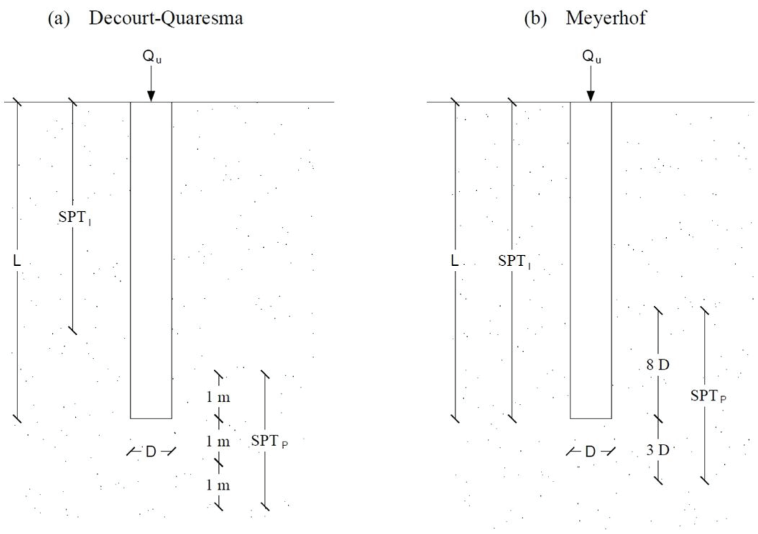

Figure 2. a) Décourt-Quaresma parameters. b) Meyerhof parameters.

Table 2. Sample from Décourt dataset.

N	SPT_l (b)	SPT_p (b)	L (m)	D (cm)	Q_u (kN)
1	6.46	27.33	18.90	26	1115
2	7.94	27.33	21.12	26	1005
...	...	...	...	...	...
165	22.71	42.25	7.00	40	1800

Table 3. Sample from Meyerhof dataset.

N	SPT_l (b)	SPT_p (b)	L (m)	D (cm)	Q_u (kN)
1	4.16	27.33	18.90	26	1115
2	6.04	27.33	21.12	26	1005
...	...	...	...	...	...
165	12.80	51.67	7.00	40	1800

Table 4. Correlation matrix for Meyerhof dataset.

	SPT_l (b)	SPT_p (b)	L (m)	D (m)	Q_u (KN)
SPT_l (b)	1	0.70	-0.25	0.11	0.13
SPT_p (b)	0.70	1	0.11	0.33	0.39
L (m)	-0.25	0.11	1	0.62	0.66
D (m)	0.11	0.33	0.62	1	0.84
Q_u (KN)	0.13	0.39	0.66	0.84	1

Table 5. Correlation matrix for Décourt dataset.

	SPT_l (b)	SPT_p (b)	L (m)	D (m)	Q_u (kN)
SPT_l (b)	1	0.35	-0.15	0.06	0.09
SPT_p (b)	0.35	1	0.28	0.51	0.56
L (m)	-0.15	0.28	1	0.62	0.66
D (m)	0.06	0.51	0.62	1	0.84
Q_u (kN)	0.09	0.56	0.66	0.84	1

4. Model description

After pre-processing, this study uses both datasets to train a set of selected machine learning algorithms. First step is organizing each dataset as a matrix, where each column represents an input or the output and each line represents an example. In other words, each dataset becomes a 165×5 matrix. Next, it divides the examples (lines) of each dataset into two portions: the training set and the test set. This work uses the leave-one-out cross validation approach, using the full dataset for training except for one example kept apart for test. The procedure tests all examples and the final accuracy is given by the mean (Wong, 2015).

The coefficient of determination $R^2 \in [0,1]$ is one metric used in this work to evaluate the performance of the algorithms. It is obtained using Equation 6, where $\hat{y}_i$ is a predicted value obtained from the model, y_i is an observed value from dataset, $\overline{y}$ the mean of all observed values and ne is the number of examples. In this work, y_i is the pile bearing load capacity (Q_u) of a specific pile i. R^2 values close to 1 imply that the target variable is completely explained by the used model. 0 means no connection between predicted and observed values. The literature considers this metric a meaningful indicator of accuracy (Draper & Smith, 1998).

$$R^2 = \frac{\sum_{i=1}^{ne} \left(\hat{y}_i - \overline{y} \right)^2}{\sum_{i=1}^{ne} \left(y_i - \overline{y} \right)^2} \tag{6}$$

Other performance metric adopted in this work is the root mean square error (RMSE). It is calculated for all machine learning models and is given by Equation 7.

$$RMSE = \sqrt{\sum_{i=1}^{ne} \frac{\left(\hat{y}_i - \overline{y} \right)^2}{ne}} \tag{7}$$

The machine learning techniques used in this work are k-nearest neighbor (KNN), kernel-KNN (KKNN), decision tree (DT), random forest (RF), artificial neural networks (ANN) and support vector machines (SVM). The following subsections present them, with a brief overview of its functionality. They were chosen considering their popularity within machine learning applications, their different biases and their reasonable results towards this work dataset. Multiple linear regression (LR) is also included as a baseline for the performance of the techniques.

4.1 KNN and KKNN

The KNN technique understands each example as a point whose coordinates are the inputs. It expects that a new example would have an output similar to those that are close in this input space. The regression problem can use Equation 8, which defines the output of the new example as the average value of its k nearest neighbors.

$$\hat{y}_i = \frac{1}{k} \sum_{j=1}^{k} y_j \tag{8}$$

This work weights the output of each neighbor with respect to its distance to the new example, giving more weight to closer ones to improve accuracy (Dudani, 1976). It calculates the distance using the Minkowski metric, as presented in Equation 9. In this work $p = 2$, which leads to the Euclidian metrics. Equation 9 gives the distance between arbitrary points represented by vectors $\boldsymbol{a}$ and $\boldsymbol{b}$, with components $\left(a_1, \cdots, a_n\right)$ and $\left(b_1, \cdots, b_n\right)$, considering an n-dimensional space.

$$d\left(\boldsymbol{a}, \boldsymbol{b}\right) = \left(\sum_{i=1}^{n} \left| a_i - b_i \right|^p \right)^{1/p} \tag{9}$$

KNN has the disadvantage of poor performance for some type of complex problems (Kuo et al., 2008). The KKNN technique solves this problem by changing the distribution of samples, mapping them into a higher dimensional input space. The objective is to obtain a linear problem in this new space, equivalent to the nonlinear problem of the original space. Equation 10 presents an example of mapping a n-dimensional input space into a m-dimensional space:

$$\begin{gathered} \boldsymbol{a} = \left(a_1, \cdots, a_n\right) \xrightarrow{mapping} \psi\left(\boldsymbol{a}\right) = \left(\varphi_1\left(\boldsymbol{a}\right), \cdots, \varphi_m\left(\boldsymbol{a}\right)\right), \\ \boldsymbol{a} \in S_1, \psi\left(\boldsymbol{a}\right) \in S_2 \end{gathered} \tag{10}$$

S_1 is the original n-dimension space and S_2 the new m-dimension space. $\boldsymbol{a}$ is a vector in S_1 and $\psi(\boldsymbol{a})$ is its corresponding vector in S_2. ψ defines the mapping from S_1 to S_2 and $\varphi_i, i = 1, \cdots, m$, are input mapping functions. One problem in this approach is that finding ψ is usually impracticable. Nevertheless, the mapping does not require ψ if the internal product $\psi(\boldsymbol{a}).\psi(\boldsymbol{b})$ is known for arbitrary vectors $\boldsymbol{a}$ and $\boldsymbol{b}$. This inner product is called kernel (Yu et al., 2002).

The most commonly used kernel functions are: polynomial, radial basis and sigmoid, as shown in Equations 11, 12 and 13, respectively:

$$K(\boldsymbol{a},\boldsymbol{b}) = (1+\boldsymbol{a}.\boldsymbol{b})^{\rho} \tag{11}$$

$$K(\boldsymbol{a},\boldsymbol{b}) = exp\left(-\frac{\boldsymbol{a}-\boldsymbol{b}^2}{\sigma^2}\right) \tag{12}$$

$$K(\boldsymbol{a},\boldsymbol{b}) = tanh(\gamma.\boldsymbol{a}.\boldsymbol{b}+\omega) \tag{13}$$

where ρ, σ, γ and ω are adjustable parameters and $\boldsymbol{a}.\boldsymbol{b}$ is the inner product between vectors $\boldsymbol{a}$ and $\boldsymbol{b}$. This work uses the radial basis kernel based on preliminary tests.

4.2 DT and RF

A DT model is a flow-chart-like structure, with nodes that create ramifications dividing the dataset. It starts with a single root node that receives the complete dataset and distributes it to other nodes using a rule, which is usually an inequality applied to one of the inputs. New nodes receive portions of the dataset, subjects them to their rules and distributes them to other nodes, forming the branches of the tree. The last nodes, called leafs, assign outputs to the examples. Figure 3 presents a scheme of a DT.

One disadvantage of DTs is that they tend to become overspecialized in the dataset used for training, which prejudices performance for new examples. This behavior is called overfitting. RF is a technique based on DTs that minimizes this problem by using a collection of different DTs built randomly. The algorithm selects a subset of examples for each tree and node, ensuring that they are different. After RF creates the trees, each one make a separate prediction and the mean gives the final value (Ho, 1995).

4.3 ANN

The interaction of neurons in the human brain inspires the ANN algorithm. Its structure consists of a number of processing elements or nodes that are arranged in layers: an input layer, an output layer and one or more hidden layers. Each node from the first layer receives an input x_i, which is multiplied by an adjustable connection weight w_{ij}. These values are inputs for the neurons of the next layer, that sum them and add a threshold value θ_j to obtain a combined input I_j. Then, the algorithm applies an activation function $f(I_j)$ to produce the output o_j, as expressed in Equations 14 and 15.

$$I_j = \sum w_{ij} x_i + \theta_j \tag{14}$$

$$o_j = f(I_j) \tag{15}$$

This work uses a sigmoid function for activation, which is expressed as:

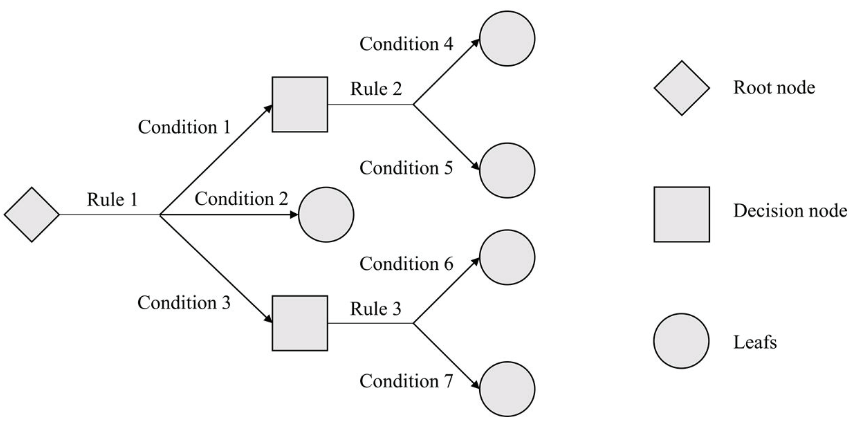

Figure 3. Example of a decision tree.

$$f\left(I_j\right) = \frac{1}{1 + e^{-\lambda I_j}} \tag{16}$$

where λ is a calibration parameter.

4.4 SVM

SVMs use statistical learning principles as a basis. Their main objectives are minimizing errors associated with the training dataset and maximizing the generalization of the model (Vapnik, 1999). The algorithm uses a set of functions for its regression model that can have a solution as given in Equation 17:

$$\boldsymbol{y} = \boldsymbol{w}.\boldsymbol{x} + \boldsymbol{\imath} \tag{17}$$

where $\boldsymbol{x} = \left(x_1, y_1\right), \cdots, \left(x_l, y_l\right) \boldsymbol{x} \in R^m$ is the input of l samples and m dimensions, $\boldsymbol{y} \in R^m$ is the output, $\boldsymbol{w}$ is the weight vector and $\boldsymbol{\imath}$ is the bias. The margin is a distance from the hyperplane which is set to contain all points, as illustrated in Figure 4. This distance is the error $\in$ to be minimized, included in Equation 18 as follows:

$$\boldsymbol{y} = \boldsymbol{w}.\boldsymbol{x} + \boldsymbol{\imath} \pm \in \tag{18}$$

Equation 19 presents the function to be minimized. ξ_i and ξ_i^* are parameters introduced to penalize points outside the margins and parameter C controls these penalties (Smola & Scholkopf, 2004). The algorithm solves this optimization problem using Lagrange multipliers (Vapnik, 1998).

$$\frac{1}{2}\boldsymbol{w}^2 + C\sum_{i=1}^{l}\left(\xi_i + \xi_i^*\right) \tag{19}$$

This procedure is valid for linear problems. One can extend it to nonlinear problems using kernels to map the input data into a higher dimensional space. It is the same approach described for the KKNN. The authors chose radial basis functions after observing better accuracy in preliminary tests.

4.5 LR

A LR seeks a linear relationship between the input variables and the output. Equation 20 represents the model generated by this kind of regression:

$$\hat{y}_i = \beta_0 + \beta_1 x_1 + \beta_2 x_2 + \cdots + \beta_n x_n \tag{20}$$

where $\hat{y}_i$ is the predicted variable, β_j are the coefficients determined by the model and x_j are the input values for the problem.

This technique has the advantage of being simple and widely used in geotechnical engineering practice, but it cannot reproduce non-linear behavior. Although it is not expected to obtain good results from this technique, it is included in this work as one of the baselines for the performance of the machine learning techniques.

5. Results and discussion

5.1 General application

The objective of this example is to apply the six machine learning techniques to Décourt and Meyerhof datasets, using RMSE and R^2 metrics to evaluate performance. The baselines for performance are the original semi-empirical methods and LR.

Tables 6 and 7 present the performance obtained using the Décourt and Meyerhof datasets, respectively. RF was the technique with best accuracy, presenting the lowest RMSE in both tables. The second best was KNN for Décourt, followed

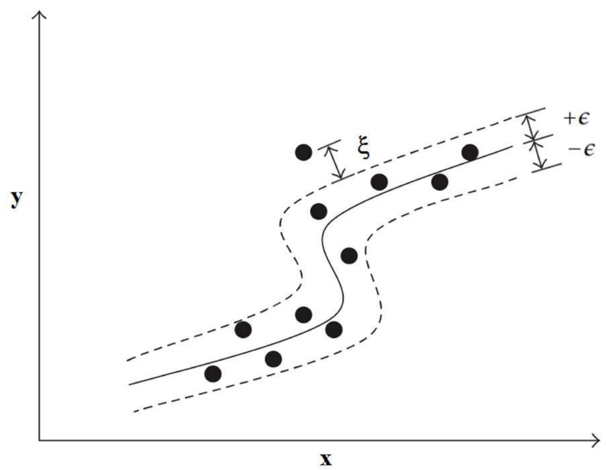

Figure 4. Graphical representation of Support Vector Machines.

Table 6. Performance metrics using Décourt dataset.

Algorithm	RMSE (kN)	R^2
RF	642.38	0.765
KNN	651.24	0.762
ANN	659.08	0.752
KKNN	665.37	0.750
LR	684.22	0.732
SVM	686.24	0.744
DT	704.40	0.717

by ANN and KKNN. For Meyerhof, the second best was ANN followed by KKNN and KNN. DT presented the worst performance, which can be explained by the tendency of this technique to overfit. SVM presented poor performance as well, worse than LR which is the baseline.

Table 8 presents a comparison between the performance of the semi-empirical methods (Décourt-Quaresma and Meyerhof), the LR and the RF algorithms. The subscript Dq indicates the use of the Décourt dataset for training. One can observe that even LR surpass the semi-empirical method of Meyerhof, encouraging the use of machine learning techniques for this type of problem. This conclusion is corroborated by other studies (Lee & Lee, 1996; Pham et al., 2020).

Figure 5 complements the comparisons presented in Table 8, with abscissas representing measured values and ordinates representing predicted values. This study uses logarithm scale to better represent the wide range of values. A predicted value equal to the observed one produces a point at the black line, while poor predictions tend to produce points far from it. Note that the cloud of white circles, that represents RF_{Mey}, is clearly more concentrated around the black line than black squares and triangles, which represent semi-empirical methods. It is also shown that the semi-empirical methods tend to underestimate the load bearing capacity, while points from RF_{Mey} tend to be split in half by the black line.

In order to present a complementary analysis, Table 9 presents predicted values using RF_{Dq}, the corresponding measured values Q_u and the ratio between them. This ratio is organized in ascending order including all 165 load tests, with a range from 0.340 to 4.62. The objective is to produce confidence intervals for the RF_{Dq}/Q_u values, allowing a better understanding of the accuracy of the algorithm.

The authors first verify whether the RF_{Dq}/Q_u results follow a normal distribution using the Shapiro-Wilk test.

Table 7. Performance metrics using Meyerhof dataset.

Algorithm	RMSE (kN)	R^2
RF	651.16	0.758
ANN	660.44	0.751
KKNN	676.31	0.742
KNN	679.90	0.741
LR	694.52	0.724
SVM	704.65	0.728
DT	706.02	0.715

Table 8. Performance results by method.

Method	RMSE (kN)	R^2
RF_{Dq}	642.38	0.765
LR_{Dq}	684.22	0.732
Meyerhof	896.08	0.662
Décourt-Quaresma	909.98	0.748

Table 9. Relation between predicted and measured values.

RF_{Dq} (kN)	Q_u (kN)	RF_{Dq}/Q_u
1803	5300	0.340
1203	2720	0.442
...	...	...
2770	600	4.62

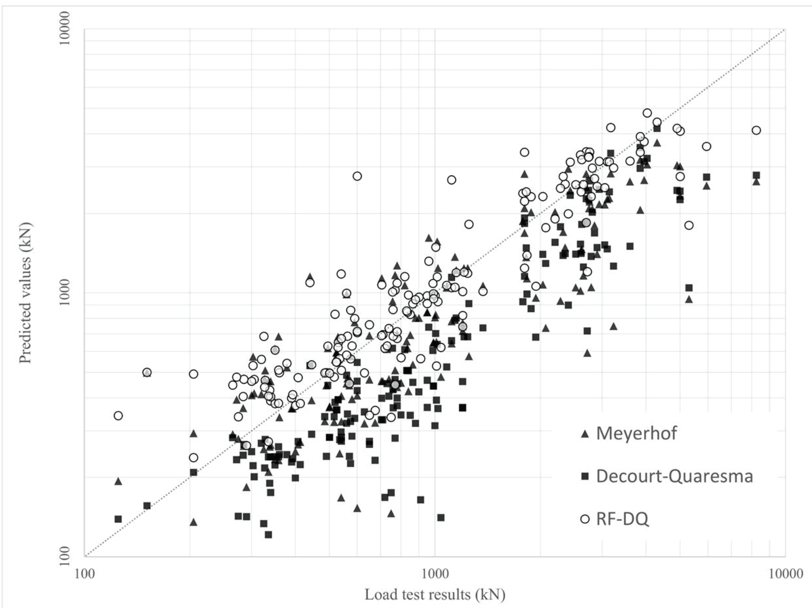

Figure 5. Graphical comparison between methods studied in this work.

The procedure uses a significance level of 5% and a starting null hypothesis H_0 that data follows a normal distribution. However, when calculating the p-value, the result was far below 5%, indicating that the data does not have a normal behavior. This means that it is not possible to apply the confidence level theory for this distribution.

To solve this problem, this study proposes a less rigorous approach using the concept of percentiles. The n^{th} percentile is a value greater than n percent of all values in the list. The authors use the RF_{Dq}/Q_u ordered list from Table 9 to estimate the confidence interval, considering that it must be centralized in the list with respect to the percentiles. The analysis proposes two confidence intervals: one of 90%, that must be limited by the 5^{th} and 95^{th} percentiles, and one of 95%, that must be limited by the 2.5^{th} and 97.5^{th} percentiles. This procedure resulted $[0.603, 2.185]$ for the 90% confidence interval of RF_{Dq}/Q_u and $[0.559, 2.170]$ for its 95% confidence interval.

Figure 6 illustrates these results. Abscissa axis represents measured values, the ordinate axis represents predicted values and each point represents a RF_{Dq}/Q_u value. The continuous line is the locus of points with $RF_{Dq} = Q_u$, while the other lines represent the limits of the confidence intervals. Considering engineering practice, this graph can give to geotechnical engineers a sense of which confidence interval would suit better their specific case.

5.2 Case study

This section presents a case study with new examples to validate the generated models. The analysis uses results taken from three SPT soundings and load tests of precast concrete piles located in a construction site in Monte Largo, Paraná state, Brazil. These examples came from Lobo (2005) and were not used to train the machine learning techniques. The objective is to evaluate what would be the accuracy of the models if applied in the future to a completely new site. Figure 7 presents the SPT values and load test information.

The study starts calculating the results obtained with the original semi-empirical methods of Décourt-Quaresma and Meyerhof, as well as for the best performing techniques for each dataset. To facilitate comparisons, Table 10 presents all relative errors. For a predicted value $\hat{y}_i$ and an observed value y_i, the relative error is $RE_i = |\hat{y}_i - y_i| / y_i$.

Note that the first example seems to be more difficult than the other two. One possible explanation for this disparity is the soil of this examples, with the first underrepresented within the training datasets. This issue is investigated incorporating

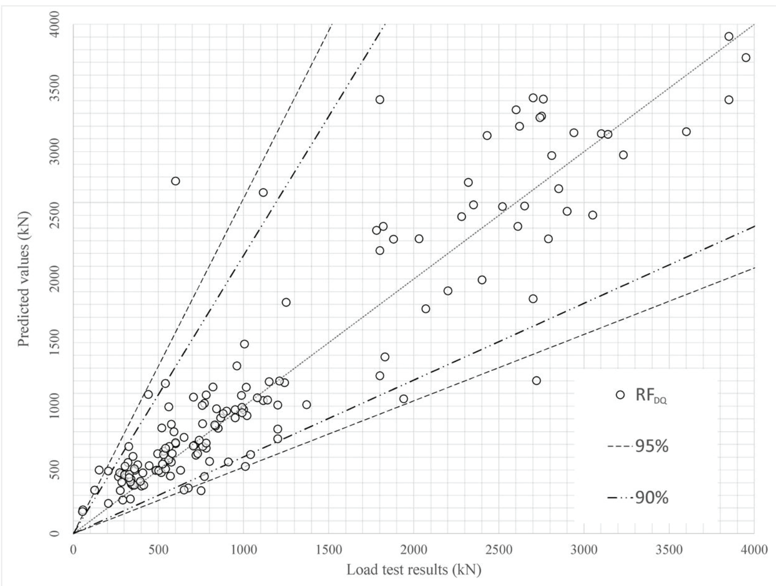

Figure 6. Confidence intervals for ratio between observed and predicted values.

Table 10. Relative errors for the load tests from Monte Largo.

Relative error					
Décourt-Quaresma			Meyerhof		
Déc	RF_{Dq}	KNN_{Dq}	Mey	RF_{Mey}	ANN_{Mey}
6.48	26.26	24.12	35.60	33.62	53.94
40.04	10.50	19.39	31.50	14.44	1.24
43.81	2.46	8.45	32.71	11.50	0.41

Pile A		
D = 25 cm L = 16.2 m		
Depth (m)	**NSPT**	**Soil type**
1	8	
2	7	
3	5	
4	6	Silty Clay
5	5	
6	4	
7	5	
8	6	
9	7	
10	14	
11	8	
12	7	Sandy Clay
13	9	
14	14	
15	19	
16	35	
17	40	Sandy Clay
18	40	

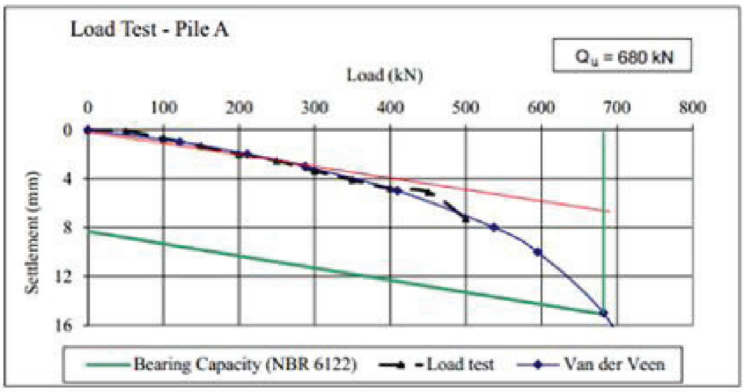

Pile B		
D = 25 cm L = 16.8 m		
Depth (m)	**NSPT**	**Soil type**
1	8	
2	7	
3	6	Silty Clay
4	13	
5	12	
6	9	
7	8	Silty Sand
8	4	
9	5	
10	5	
11	7	Silty Clay
12	6	
13	8	
14	13	
15	12	
16	14	
17	10	Clayey Silt
18	17	
19	15	
20	18	

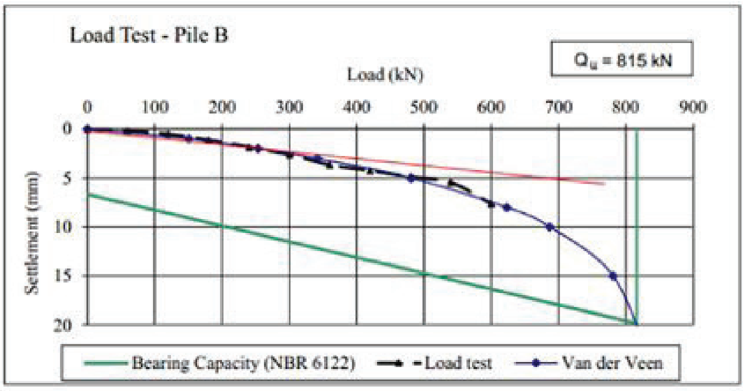

Pile C		
D = 25 cm L = 15.35 m		
Depth (m)	**NSPT**	**Soil type**
1	16	
2	12	
3	15	Slity Clay
4	8	
5	6	
6	2	
7	2	Silty-sandy Clay
8	2	
9	15	
10	10	
11	9	Silty Clay
12	7	
13	10	
14	11	
15	7	
16	8	Clayey Silt
17	19	
18	20	

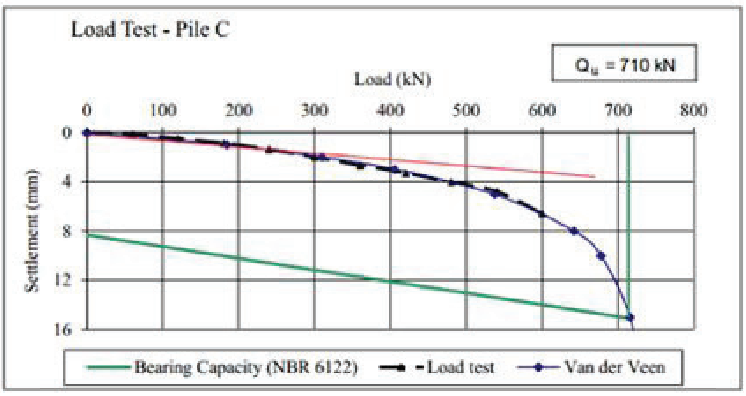

Figure 7. SPT sounding and load test for the pile tests. Adapted from Lobo (2005).

Table 11. Relative error for predictions made with the updated datasets.

Relative error			
Décourt-Quaresma		Meyerhof	
RF_{Dq}	KNN_{Dq}	RF_{Mey}	ANN_{Mey}
25.62	24.12	31.72	53.94
9.25	20.65	6.55	1.55
2.59	3.47	11.64	0.61

these piles to the datasets, to verify if performance changes. The objective is verifying if the inclusion of two of the load tests of this construction site helps predicting the third one, as performed in the leave-one-out methodology. Table 11 presents the result.

One can observe that most machine learning techniques presented some improvement for the first example, which is still the most difficult. For the other two, although some specific values increased, the overall performance of the techniques can be considered better. This allows concluding that the inclusion of information from the same construction site helped improving performance. In other words, the performance of the techniques for new examples depends on its representativity within the training dataset.

6. Conclusions

This work applies machine learning techniques to predict the bearing capacity of concrete precast piles. It presents two examples, the first with a general application and the second with a case study. The results obtained in the first example, considering all techniques applied to both datasets, allows concluding that RF is the best algorithm for this problem, with lower RMSE values. KNN and ANN also detached from the others, presenting the second best performance for Décourt-Quaresma and Meyerhof datasets, respectively. The semi-empirical methods of Décourt-Quaresma and Meyerhof presented a relatively poor performance in this example with an RMSE close to 900, being surpassed by all other techniques including LR. These results demonstrate that machine learning algorithms are a good alternative for predicting the ultimate bearing capacity of piles. The analysis proposed an approximation of the confidence intervals using the concept of percentile. A graph presented two intervals, 90% and 95%, to give engineers choices for the desired accuracy.

The second example presented a study to evaluate the effect of the representativity of the dataset. Results confirm that performance depends on representativity and also reveal the limits of these models, which tend to present poor accuracy for examples very different from the ones contained in the used datasets.

Acknowledgements

To the Coordination of Improvement of Higher Education Personnel (CAPES) for granting the first author's scholarship.

Declaration of interest

The authors have no conflicts of interest to declare. All co-authors have observed and affirmed the contents of the paper and there is no financial interest to report.

Authors' contributions

Yago Ferreira Gomes: conceptualization, data curation, formal analysis, investigation, methodology, visualization, writing – original draft. Filipe Alves Neto Verri: conceptualization, methodology, supervision, validation, visualization, writing – review & editing. Dimas Betioli Ribeiro: conceptualization, data curation, funding acquisition, methodology, project administration, supervision, validation, writing – review & editing.

List of symbols

a,b: Arbitrary vectors
a_i,b_i: Vector components
b: Number of blows needed for the sampler to penetrate 30 cm into the soil
A_p: Area of the pile tip
f: Activation function
I_j: Combined input of a neuron
k: Number of nearest neighbors
K: Soil type factor
$K(\boldsymbol{a},\boldsymbol{b})$: Kernel
l: Number of samples for a SVM
L: Pile length
n,m: Space dimensions
ne: Number of examples
o_j: Output of a neuron
p: Exponent of Minowsky equation
q_p,q_s: Parameters of Meyerhof´s method
Q_u: Pile bearing load capacity
R^2: Coefficient of determination
RE_i: Relative error
R_l: Lateral friction
RMSE: Root mean square error
R_p: Tip resistance
R_t: Pile load capacity
S_1,S_2: Spaces of dimension n and m, respectfully
SPT_l: Mean N_{SPT} index along the pile shaft

SPT_p: Mean N_{SPT} index around the pile tip
U: Pile perimeter
$\boldsymbol{w}$: Weight vector
w_{ij}: Adjustable connection weight
$\boldsymbol{x}$: Input of a SVM
x_i: Input of a neuron
x_i, y_i: Components of $\boldsymbol{x}$ and $\boldsymbol{y}$, respectfully
$\boldsymbol{y}$: Output of a SVM
y_i: Observed value
$\hat{y}_i$: Predicted value
$\overline{y}$: Mean of all observed values
ξ_i, ξ_i^*, C: Parameters of a SVM
α, β: Parameters of Décourt-Quaresma method
θ_j: Threshold value
$\rho, \sigma, \gamma, \omega$: Kernel parameters
φ_i: Component of ψ
β_j: Coefficients to be determined for a LR
ι : Bias of a SVM
λ: Calibration parameter
ψ: Mapping vector
ϵ: Error to be minimized

References

Alkroosh, I., Bahadori, M., Nikraz, H., & Bahadori, A. (2015). Regressive approach for predicting bearing capacity of bored piles from cone penetration test data. *Journal of Rock Mechanics and Geotechnical Engineering*, 7(5), 584-592. http://dx.doi.org/10.1016/j.jrmge.2015.06.011.

Aoki, N., & Velloso, D. (1975). An approximate method to estimate the bearing capacity of piles. In *Proc., 5th Pan-American Conf. of Soil Mechanics and Foundation Engineering* (pp. 367-376) Buenos Aires: International Society of Soil Mechanics and Geotechnical Engineering.

Ardalan, H., Eslami, A., & Nariman-Zadeh, N. (2009). Piles shaft capacity from CPT and CPTu data by polynomial neural networks and genetic algorithms. *Computers and Geotechnics*, 36(4), 616-625. http://dx.doi.org/10.1016/j.compgeo.2008.09.003.

Arel, E. (2012). Predicting the spatial distribution of soil profile in Adapazari/Turkey by artificial neural networks using CPT data. *Computers & Geosciences*, 43, 90-100. http://dx.doi.org/10.1016/j.cageo.2012.01.021.

Associação Brasileira de Normas Técnicas – ABNT (2019). *Projeto e execução de fundações*. Associação Brasileira de Normas Técnicas, Rio de Janeiro.

Benali, A., Nechnech, A., Boukhatem, B., Hussein, M.N., & Karry, M. (2018). Neural networks and principle component analysis approaches to predict pile capacity in sand. In MATEC Web of Conference (Org.), *2nd International Congress on Materials & Structural Stability*. Les Ulis: EDP Sciences. https://doi.org/10.1051/matecconf/201814902025

Bhattacharya, B., & Solomatine, D.P. (2006). Machine learning in soil classification. *Neural Networks*, 19(2), 186-195. http://dx.doi.org/10.1016/j.neunet.2006.01.005.

Bigarella, J.J., & Salamuni, R. (1962). *Caracteres texturais dos sedimentos da bacia de Curitiba*. Instituto de Geologia.

Bonini Neto, A., Bonini, C.S.B., Bisi, B.S., Reis, A.R., & Coletta, L.F.S. (2017). Artificial neural network for classification and analysis of degraded soils. *IEEE Latin America Transactions*, 15(3), 503-509.

Bui, D.T., Moayedi, H., Gör, M., Jaafari, A., & Foong, L.K. (2019). Predicting slope stability failure through machine learning paradigms. *ISPRS International Journal of Geo-Information*, 8(9), 395. http://dx.doi.org/10.3390/ijgi8090395.

Carvalho, L.O., & Ribeiro, D.B. (2019). Soil classification system from cone penetration test data applying distance-based machine learning algorithms. *Soils and Rocks*, 42(2), 167-178. http://dx.doi.org/10.28927/SR.422167.

Décourt, L., & Quaresma, A. (1978). Capacidade de carga de estacas a partir de valores de SPT. In *Congresso Brasileiro de Mecânica dos Solos e Engenharia de Fundações* (pp. 45-53). São Paulo: Associação Brasileira de Mecânica dos Solos e Engenharia Geotécnica.

Décourt, L., & Quaresma, A. (1998). Análise e Projeto de Fundações Profundas. In: W. Hachich (Eds.), *Fundações: teoria e prática* (pp. 275-276). PINI.

Draper, N.R., & Smith, H.K. (1998). *Applied regression analysis* (3rd edition). Wiley.

Dudani, S.A. (1976). The distance-weighted k-nearest-neighbor rule. *IEEE Transactions on Systems, Man, and Cybernetics*, SMC-6(4), 325-327.

Ferentinou, M.D., & Sakellariou, M.G. (2007). Computational intelligence tools for the prediction of slope performance. *Computers and Geotechnics*, 34(5), 362-384. http://dx.doi.org/10.1016/j.compgeo.2007.06.004.

Goh, A.T.C., & Goh, S.H. (2007). Support vector machines: their use in geotechnical engineering as illustrated using seismic liquefaction data. *Computers and Geotechnics*, 34(5), 410-421. http://dx.doi.org/10.1016/j.compgeo.2007.06.001.

Hanna, A.M., Ural, D., & Saygili, G. (2007). Neural network model for liquefaction potential in soil deposits using Turkey and Taiwan earthquake data. *Soil Dynamics and Earthquake Engineering*, 27(6), 521-540. http://dx.doi.org/10.1016/j.soildyn.2006.11.001.

Ho, T.K. (1995). Random decision forests. In International Association for Pattern Recognition. Technical Committee 11 (Org.), *Proceedings of 3rd International Conference on Document Analysis and Recognition* (pp. 278-282). Los Alamitos: IEEE Computer Society Press.

Ismail, A., & Jeng, D. (2011). Modelling load–settlement behavior of piles using high-order neural network (HON-PILE model). *Engineering Applications of Artificial Intelligence*, 24(5), 813-821. http://dx.doi.org/10.1016/j.engappai.2011.02.008.

Jesswein, M., & Liu, J. (2018). Predicting the side resistance of piles using a genetic algorithm and SPT n-values. In Canadian Geotechnical Society (Org.), *Proceedings of the 71st Canadian Geotechnical Conference and the 13th Joint CGS/IAH-CNC Groundwater Conference - GeoEdmonton 2018 : moving forward* (pp. 1-8). Richmond: Canadian Geotechnical Society.

Juang, C.H., & Chen, C.J. (1999). CPT-based liquefaction evaluation using artificial neural networks. *Computer-Aided Civil and Infrastructure Engineering*, 14(3), 221-229. http://dx.doi.org/10.1111/0885-9507.00143.

Kardani, N., Zhou, A., Nazem, M., & Shen, S. (2020). Estimation of bearing capacity of piles in cohesionless soil using optimised machine learning approaches. *Geotechnical and Geological Engineering*, 38(2), 2271-2291. http://dx.doi.org/10.1007/s10706-019-01085-8.

Kohestani, V.R., Hassanlourad, M., & Ardakani, A. (2015). Evaluation of liquefaction potential based on CPT data using random forest. *Natural Hazards*, 79(2), 1079-1089. http://dx.doi.org/10.1007/s11069-015-1893-5.

Kordjazi, A., Nejad, F.P., & Jaksa, M.B. (2013). Prediction of load-carrying capacity of piles using a support vector machine and improved data collection. In G. Cassidy (Ed.), *Proceedings of the 12th Australia New Zealand conference on geomechanics: the changing face of the earth - geomechanics & human influence* (pp. 1-8). Wellington: Opus.

Kordjazi, A., Nejad, F.P., & Jaksa, M.B. (2014). Prediction of ultimate axial load-carrying capacity of piles using a support vector machine based on CPT data. *Computers and Geotechnics*, 55, 91-102. http://dx.doi.org/10.1016/j.compgeo.2013.08.001.

Kovacevic, M., Bajat, B., & Gajic, B. (2010). Soil type classification and estimation of soil properties using support vector machines. *Geoderma*, 154(3-4), 340-347. http://dx.doi.org/10.1016/j.geoderma.2009.11.005.

Kuo, B., Yang, J., Sheu, T., & Yang, S. (2008). Kernel-based KNN and gaussian classifiers for hyperspectral image classification. In Geoscience and Remote Sensing Society (Org.), *2008 International Geoscience and Remote Sensing Symposium* (pp. 1006-1008). Piscataway: IEEE.

Lee, I., & Lee, J. (1996). Prediction of pile bearing capacity using artificial neural networks. *Computers and Geotechnics*, 18(3), 189-200. http://dx.doi.org/10.1016/0266-352X(95)00027-8.

Livingston, G., Piantedosi, M., Kurup, P., & Sitharam, T.G. (2008). An approximate method to estimate the bearing capacity of piles. In X. Zeng, M.T. Manzari, & D.R. Hiltunen (Eds.), *Geotechnical Earthquake Engineering and Soil Dynamics IV Congress* (pp. 1-10). Reston: American Society of Civil Engineers.

Lobo, B. (2005). *Método de previsão de capacidade de carga de estacas: aplicação dos conceitos de energia do ensaio SPT* [Doctoral thesis]. Universidade Federal do Rio Grande do Sul.

Lok, T.M.H., & Che, W.F. (2004). Axial capacity prediction for driven piles using ANN: model comparison. In M.K. Yegian, & E. Kavazanjian (Eds.), *Geotechnical Engineering for Transportation Projects* (pp. 697-704). Reston: American Society of Civil Engineers. https://doi.org/10.1061/40744(154)56.

Maizir, H., & Kassim, K.A. (2013). Neural network application in prediction of axial bearing capacity of driven piles. In O. Castillo, C. Douglas, D.D. Feng & J. Lee (Eds.), *Proc of the International MultiConference of Engineers and Computer Scientists*. Hong Kong: Newswood Limited.

Maxwell, A.E., Sharma, M., Kite, J.S., Donaldson, K.A., Thompson, J.A., Bell, M.L., & Maynard, S.M. (2020). Slope failure prediction using random forest machine learning and lidar in an eroded folded mountain belt. *Remote Sensing*, 12(3), 486. http://dx.doi.org/10.3390/rs12030486.

Meyerhof, G. (1976). Bearing capacity and settlements of pile foundations. *Journal of Geotechnical Engineering*, 102, 197-228. http://dx.doi.org/10.1061/AJGEB6.0000243.

Moayedi, H., & Hayati, S. (2019). Artificial intelligence design charts for predicting friction capacity of driven pile in clay. *Neural Computing & Applications*, 31(11), 7429-7445. http://dx.doi.org/10.1007/s00521-018-3555-5.

Momeni, E., Nazir, R., Armaghani, D., & Maizir, H. (2015). Application of artificial neural network for predicting shaft and tip resistances of concrete piles. *Earth Sciences Research Journal*, 19(1), 85-93.

Morais, T.S.O., Tsuha, C.H.C., Bandeira Neto, L.A., & Singh, R.M. (2020). Effects of seasonal variations on the thermal response of energy piles in an unsaturated Brazilian tropical soil. *Energy and Building*, 216, 1-19. http://dx.doi.org/10.1016/j.enbuild.2020.109971.

Nawari, N.O., & Liang, R. (2000). Intelligent hybrid system for the design of pile foundations. In N.D. Dennis, R. Castelli, & M.W. O'Neill (Eds.), *New Technological and Design Developments in Deep Foundations* (pp. 312-326). Reston: American Society of Civil Engineers. https://doi.org/10.1061/40511(288)22.

Nejad, F.P., & Jaksa, M.B. (2017). Load-settlement behavior modeling of single piles using artificial neural networks and CPT data. *Computers and Geotechnics*, 89, 9-21. http://dx.doi.org/10.1016/j.compgeo.2017.04.003.

Nejad, F.P., Kakhi, M.B., & McCabe, B.A. (2009). Prediction of pile settlement using artificial neural networks based on standard penetration test data. *Computers and Geotechnics*, 36(7), 1125-1133. http://dx.doi.org/10.1016/j.compgeo.2009.04.003.

Pal, M., & Deswal, S. (2008). Modeling pile capacity using support vector machines and generalized regressions neural network. *Journal of Geotechnical and Geoenvironmental Engineering*, 134(7), 1021-1024. http://dx.doi.org/10.1061/(ASCE)1090-0241(2008)134:7(1021).

Pal, M., & Deswal, S. (2010). Modelling pile capacity using Gaussian process regression. *Computers and*

Geotechnics, 37(7), 924-947. http://dx.doi.org/10.1016/j.compgeo.2010.07.012.

Pham, T., Ly, H., Tran, V., Giap, L., Vu, H., & Duong, H. (2020). Prediction of pile axial bearing capacity using artificial neural network and random forest. *Applied Sciences*, 10(5), 1871. http://dx.doi.org/10.3390/app10051871.

Salgado, R. (2008). *The engineering of foundations*. McGraw Hill.

Samui, P. (2008). Support vector machine applied to settlement of shallow foundations on cohesionless soils. *Computers and Geotechnics*, 35(3), 419-427. http://dx.doi.org/10.1016/j.compgeo.2007.06.014.

Santos Junior, O. (1988). *Previsão do comportamento carga-recalque de estacas pré-moldadas de concreto* [Masters thesis]. Universidade de São Paulo.

Shahin, M.A. (2010). Intelligent computing for modeling axial capacity of pile foundations. *Canadian Geotechnical Journal*, 47(2), 230-243. http://dx.doi.org/10.1139/T09-094.

Smola, A.J., & Scholkopf, B. (2004). A tutorial on support vector regression. *Statistics and Computing*, 14(3), 199-222. http://dx.doi.org/10.1023/B:STCO.0000035301.49549.88.

Van Der Veen, C. (1953). The bearing capacity of a pile. In International Conference on Soil Mechanics and Foundation Engineering (Org.), *International Conference on Soil Mechanics and Foundation Engineering* (pp. 367-376). Zurich: ICOSOMEF.

Vapnik, V.N. (1998). Statistical learning theory. Wiley.

Vapnik, V.N. (1999). An overview of statistical learning theory. *IEEE Transactions on Neural Networks*, 10(5), 988-999.

Vianna, A. (2000). *Análise de provas de carga estática em estacas pré-moldadas cravadas na cidade de Curitiba e região metropolitana* [Masters thesis]. Universidade de São Paulo. https://doi.org/10.11606/D.18.2000.tde-18102006-101542

Wong, T. (2015). Performance evaluation of classification algorithms by k-fold and leave-one-outcross validation. *Pattern Recognition*, 48(9), 2839-2846. http://dx.doi.org/10.1016/j.patcog.2015.03.009.

Yu, K., Ji, L., & Zhang, X. (2002). Kernel nearest-neighbor algorithm. *Neural Processing Letters*, 15(2), 147-156. http://dx.doi.org/10.1023/A:1015244902967.

Soils and Rocks
An International Journal of Geotechnical and Geoenvironmental Engineering
www.soilsandrocks.com
ISSN 1980-9743
ISSN-e 2675-5475

Tridimensional geotechnical database modeling as a subsidy to the standardization of geospatial geotechnical data

Bruno Rodrigues de Oliveira[1#], Newton Moreira de Souza[1], Rafael Cerqueira Silva[1], Eleudo Esteves de Araújo Silva Júnior[1]

Article

Keywords
Geotechnical data model
OMT-G
Geospatial database modeling
Geotechnical data standard

Abstract
Geotechnical data is often produced and managed by several producers in isolation, in their own formats and standards, which aim to meet the unique needs of specific users, because there is not a defined geospatial geotechnical data storage standard. This article presents the physical implementation of a three-dimensional geotechnical database, based on a data model generated using the Object Modeling Technique for Geographic Applications, composed of information produced by the academy and various administrative institutions of the Federal District Government. More than four thousand quantitative e qualitative geotechnical investigations are available in this structured database that can be accessed by anyone with some geographic information system knowledge using QGIS. Considering that the compiled information was stored by their producers in distinct formats and most of them in a non-digital and without locational information, this work reinforces the need to adoption a standardization of geospatial geotechnical data storage on a unified basis compatible with the National Spatial Data Bank to disseminate this information.

1. Introduction

The demand for geospatial information today has grown exponentially and given the multiplicity of existing geotechnologies in the market, the production and distribution of geospatial data became more agile every day. To ensure the quality, interoperability, and data sharing between producers and users of geospatial data and information, it is important that there is a geospatial geotechnical data storage standard.

A large amount of geotechnical data has been produced to support the elaboration of geotechnical maps in view of the obligation established by the Federal Government and, when associated with public and private sectors data results in a large volume of unstandardized and restricted access geotechnical data. This fact is reinforced because the National Spatial Data Bank does not have a geospatial geotechnical data standard.

There are data format that provides a standard way to transfer geotechnical or geoenvironmental data between the contributing parties of a project like Association of Geotechnical & Geoenvironmental Specialists (AGS) Format and Geography Markup Language (GML), but this does not guarantee that the consistency of the information that originated the file in the standard format. When standardization occurs at the data modeling level, all stored information follows the rules defined in the model, and the added information is automatically subjected to a check of all integrity constraints.

The use of a database in geotechnics has been discussed by several authors since the 2000s (Priya & Dodagoudar, 2018), which point to several advantages for the adoption of this practice such as allowing information quality control, availability in a single place, low risk of information loss and provide structured information to subsidiary the most diverse analyses.

In general, all databases are built based on a data model, even if implicit, but few authors approach the conceptual model and commonly develop solutions that meet only a specific need as can be observed in (Bozio & Reginato, 2020; Priya & Dodagoudar, 2018; Moura et al., 2017; Ribeiro et al., 2016; Santos et al., 2018). Therefore, this work aims to present a proposal for a conceptual model of geographic database using the Object Modeling Technique for Geographic Applications (OMT-G) for the theme geotechnics and its implementation in a free database management system (DBMS), PostgreSQL / PostGIS.

[1]Universidade de Brasília, Faculdade de Tecnologia, Distrito Federal, Brasil.
#Corresponding author. E-mail address: brunorodriguesoli@gmail.com.

Submitted on July 25, 2021; Final Acceptance on October 7, 2021; Discussion open until February 28, 2022.
https://doi.org/10.28927/SR.2021.073321

2. Object Modeling Technique for Geographic Application (OMT-G)

A data model is a set of concepts that can be used to describe data, its relationships, and constraints (Silberschatz et al., 2020). Among the existing models, the OMT-G expands the Unified Modeling Language (UML) by introducing bidimensional geographical primitives like points, polygons, and lines, which increase its semantic representation capacity.

The structure of OMT-G model is based in three mains concepts, the class, which is responsible for data representation in geographic applications, relationships that explains how a class is related with other classes and constraints which are the rules that need to be followed in the database to ensure data integrity. The model allows space to be modeled and represented as non-spatial, continuous and discrete data, last one with different types of geometry and topological relations (Borges et al., 2001, 2005) providing an integrated view of the modeled space (Figure 1).

As for the relationships between the classes, the OMT-G model allows simple associations represented by continuous lines and spatial associations by dashed lines, generalization, which allows defining more generic classes (superclass) from classes with similar characteristics (subclass), and specialization, which is the reverse process (Figure 1). Relationships are characterized by their cardinality that represents the number of instances of a class that can be associated with instances of the other class. More information about OMT-G can be obtained from (Borges et al., 2001, 2005; Davis, 2000; Queiroz & Ferreira, 2006; SPUGeo, 2021).

3. Materials and methods

Conceptual modeling was performed using the Star UML 5.0 free code (Lee et al., 2005) which has an OMT-G module for visualization and modeling of class and transformation diagrams. For the logical schema was used pgModeler 0.93 (Silva, 2021) which is a free code database modeling program. The physical implementation was done via pgAdmin version 5.4 (PostgreSQL Global Development Group, 2021) in the chosen database, PostgreSQL Version 11.17 (PostgreSQL Global Development Group, 2021) with the spatial extension PostGIS Version 3.0 (POSTGIS, 2021) which, supports 2D and 3D geographic objects and queries. 3D Data visualization and analysis were performed using QGIS GIS in version 3.16 (QGIS, 2021), which allows direct connection to the database.

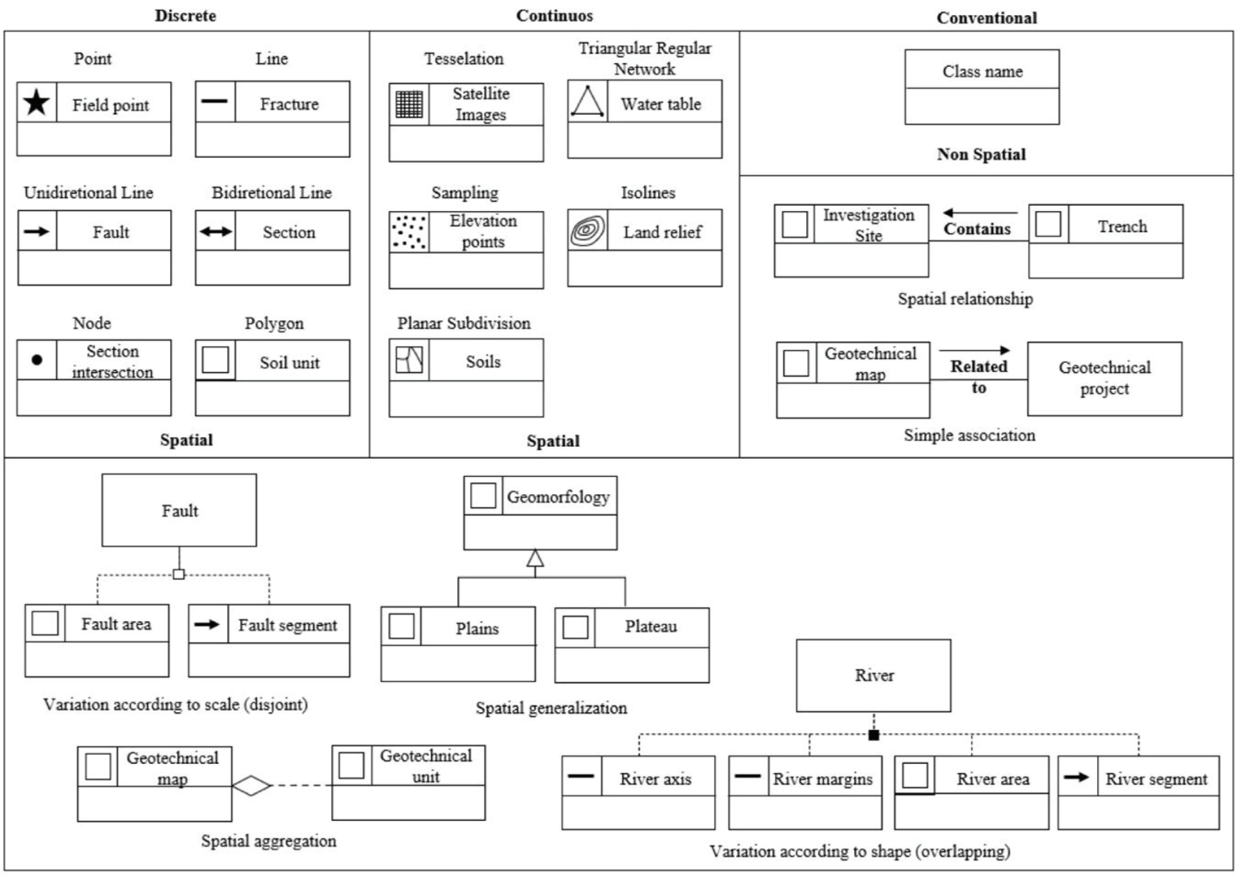

Figure 1. Graphical notation for the OMT-G model classes and relationships.

As all the manipulation and visualization of the data inserted in the database is done by a geographic information system that can visualize the information two or three dimensions using the tools available in the program itself and import and export various data formats such as vectorial, matrix, tabular, text, images, among others. Other thematic information such as topography, geology, pedology, geomorphology, among others, can be inserted in the database or in the GIS itself and analyzed together with the geotechnical data.

3.1 Compiling pre-existing data

Approximately 4.850 quantitative and qualitative geotechnical data from mappings, laboratory tests and field investigations conducted in academic research and by government agencies of the Federal District Government (GDF) were compiled, whose spatial distribution is presented in Figure 2. All compiled data were submitted to pre-processing routine consisting of georeferencing, and data quality analysis.

3.2 Requirements gathering

The process begins by choosing the objects that will be represented by conventional or georeferenced classes during abstraction process to elaborate the conceptual model, which will later be implemented on the database. In this step, the requirements of the information itself and the spatial representation of the chosen objects are defined.

The requirements consist of the definition of the concepts of the different laboratory tests and geotechnical field investigations that define the scope of the proposed data model and semantic constraints, also known as business rules, which are inherent to geotechnical data. For example, the spatial constraint that two laboratory tests represented as tridimensional points, which alter the arrangement of the soil particles, cannot overlap spatially is linked to a semantic constraint that when we want to know any geotechnical property of a soil in an in-situ condition, both tests cannot be performed on the same sample. However, the execution of particle size with sedimentation using the material resulting from the test is possible then, in this case, the spatial overlap is allowed.

3.3 Conceptual modeling

In this stage, the class diagram containing the conventional and georeferenced classes was elaborated with the spatial representation defined during the requirements gathering step, followed by the definition of the relationships between classes whether simple, topological, semantic, or user-defined, and finally the cardinality of the relationships between the classes.

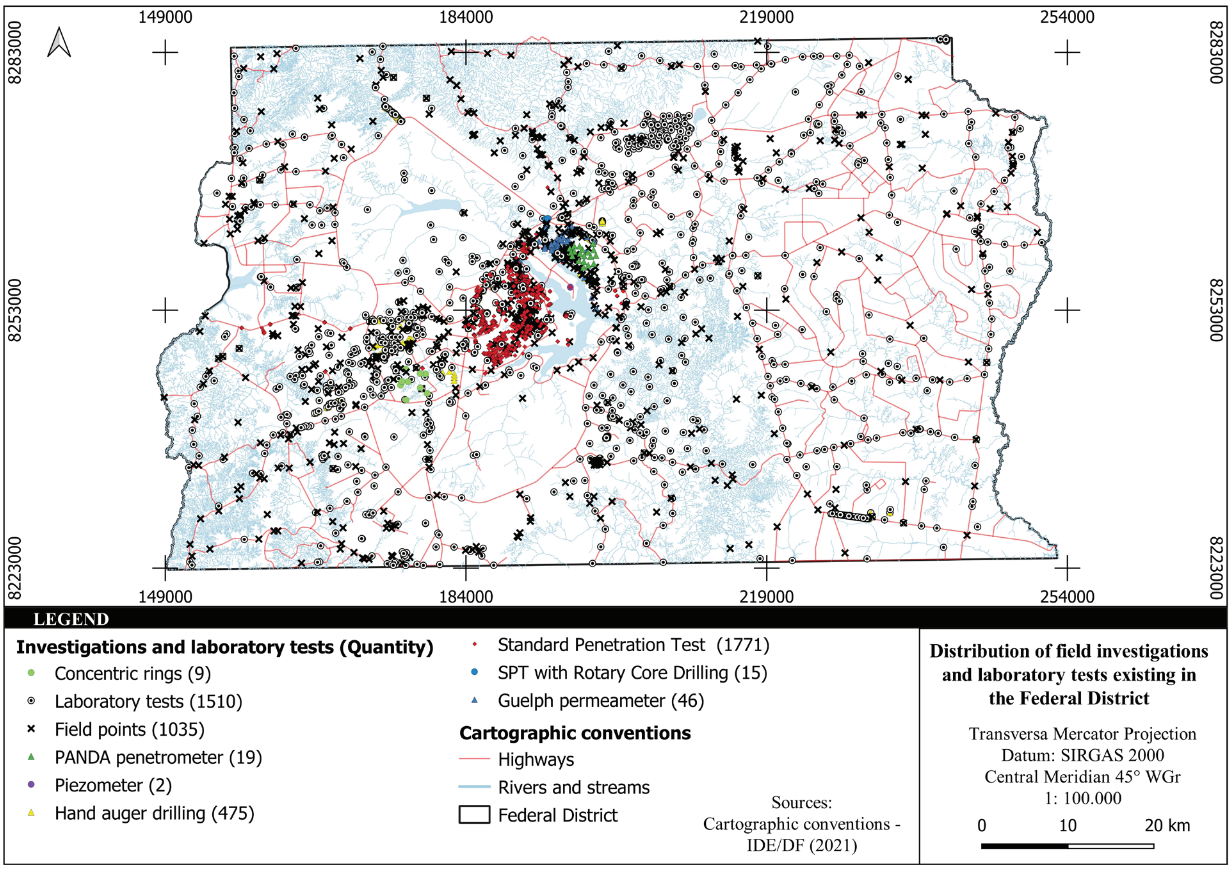

Figure 2. Spatial distribution of the compiled field investigations and laboratory tests.

The proposed model was based on previous experiences with geological and geotechnical databases and data models (Gao, 2007; OGC, 2017; Ribeiro et al., 2016; Santos et al., 2018; Silva, 2005; Silva, 2007; Tegtmeier et al., 2014; Zand, 2011). Of the above-mentioned articles, implementations and models are restricted to only one type of field investigation or laboratory test, especially standard penetrations tests.

Since OMT-G does not specify 3D geometric primitives, the transformation diagram, routines for the construction of 3D geometries were defined the based on computational geometry transformations such as buffer construction, extrusion and expand using the locational information of the data and the dimensions of the three-dimensional object to be constructed by database. This article does not include the presentation diagram since the focus is on storing information within the database although an example of graphical representation of three-dimensional geotechnical data is presented.

3.4 Logical schema and physical implementation

In the logical schema, data was organized in the way that it will be stored in the database and is where the primary and foreign keys, normalization, and referential integrity are defined. All information contained in the logical schema is recorded in the data dictionaries and metadata that follows the Geospatial Metadata Profile of Brazil specification (IBGE, 2021).

The database is composed of tables, visualizations, and spatial and non-spatial indexes that were implemented through Structured Query Language (SQL) code which are being compiled in a PostgreSQL extension that will be available at the https://github.com/bro-geo/geotechnical_database.

4. Analysis and results

4.1 Compiled requirements

The main objects of interest of the model are field investigations, laboratory tests, samples, and geotechnical units. The main types of laboratory tests and field investigations conducted by academic research and government agencies of the GDF were chosen to compose the proposed conceptual model but ensuring the possibility of expanding the model if necessary.

Field investigation is a method of obtaining information in the field, on the surface or subsurface, in which the researcher may or may not have contact with the sampled material to obtain its physical properties (Marrano et al., 2018).

Field investigations are represented by point or volume geo-objects, which can overlap spatially if they are not executed in the same period but does not apply to field point subclass that can overlap other subclasses in any period or piezometer subclass that cannot be overlapped spatially by other types of field investigations except field points. The geometry of investigations superclass must be constructed using latitude, longitude, point elevation and any information related to the shape of the investigation like diameter, and it is essential that all investigations share the same horizontal and vertical reference system. This superclass does not need to be related to the sample class or the laboratory tests superclass.

Laboratory tests consist of tests carried out within a laboratory on soil or rock samples, to obtain the physical, mineralogical, mechanical, and hydraulic properties of the materials and/or categorize the tested materials by their geotechnical properties (Head, 2006).

The laboratory tests are represented by point-type geo-objects or volumes which cannot overlap spatially, regardless of the execution date, except for the rules presented below. Two laboratory tests geometries can overlap spatially when we are not interested in an in-situ condition of any geotechnical property. The geometries of the subclasses compression and California bearing ratio (CBR) can overlap each other because CBR the test is executed on a compacted soil cylinder. Two geometries of laboratory tests that are executed on deformed samples can overlap each other. A laboratory test executed on deformed sample can overlap a laboratory test executed on undeformed sample if it was executed after the undeformed sample test.

The geometry of a laboratory tests superclass must be constructed using the latitude and longitude coordinates and the elevation of the point and any shape-related information, and it is essential that all laboratory tests share the same horizontal and vertical reference system. Laboratory tests superclass needs to be spatial related with a sample class and a field investigation superclass.

Table 1 presents the subclasses of the field investigations and their respective descriptions and spatial and semantic restrictions which were based on Marrano et al. (2018), ABNT (2018), ABNT (2016) and ABNT (2020).

The Table 2 and Table 3 presents the subclasses of laboratory tests and their respective descriptions and spatial, semantic, and user-defined restrictions which were based on ABNT (2018), Head (2006), Head & Epps, (2011, 2014).

As every test comes from a sample, it is necessary to compile the requirements of this class. The sample can be defined as a material, rock or soil, collected through field investigations that can be used for performing laboratory tests. For soils, the sample is said to be disturbed when its natural structure was modified by breaking the structure of a soil without variation of its moisture content. The deformed sample is the one that does not maintain all the characteristics that occur in-situ and the undeformed sample is obtained in order to preserve the soil characteristics that occur in-situ (ABNT, 1995).

Samples are represented by point-type geo-objects on small scales and polygon and/or volume on large scales and cannot overlap itself regardless of period. The sample should always be related to the investigation in which the collection was performed but does not necessarily need to be related

Table 1. Subclasses of the superclass investigations and their respective descriptions and constraints.

Subclass of investigations	Description	Spatial and semantic constraints
Field Points	Any point on the earth's surface or subsoil that contains information relevant to an engineering project.	The geometries of this subclass can overlap independently of the period or overlap geometries from other subclasses of the superclass independent of the period investigations.
Concentric rings	Field test to determine the speed of water infiltration into the soil.	Geometries of this subclass can overlap geometries of other subclasses of the superclass independent of the period-independent investigations with the exception of the piezometer and can overlap geometries of this class at different periods. Geometries of this subclass cannot be related to sample and laboratory test classes. Relationship with conventional tables with measurement values.
Piezometer	Field test that allows to check the water pressures and the position of the groundwater level in the rock mass respectively.	Geometries of this subclass cannot be overlapped by geometries of other subclasses of the investigation superclass with a period after the piezometer is installed except for field points.
Drilling	Field test to collect deformed soil or rock samples depending on the driling type. The borehole is commonly used to perform soil infiltration tests or pressure water loss in rocks.	Geometries of this class can overlap geometries from other subclasses of the superclass investigations at different times, with the exception of the piezometer.
Inspection trenches and pits	Vertical excavation (circular, square or rectangular section) that allows access of a researcher to make visual inspection of the walls and bottom and the removal of representative samples (undeformed and/or deformed).	Polygon and/or volume geometry at large scales and point on small scales The superclass investigations must contain a geometry with the same geociu originating from this class.
All subclasses		Inherits the constraints, geometry, and relationships of the investigations superclass unless otherwise specified.

Table 2. Subclasses of the superclass laboratory tests that are executed in disturb samples and their respective descriptions and constraints.

Subclass of laboratory tests	Description	Spatial and semantic constraints
Moisture	Laboratory test performed to determine the amount of water present in the soil structure.	Inherits the constraints, geometry, and unique identifier code of the superclass tests unless otherwise specified. Geometries related to this subclass can overlap geometries from other subclasses of the laboratory tests superclass. Relationship with conventional tables with measurement values.
Atterberg limits	Laboratory test carried out for the measurement and description of the soil plasticity interval in numerical terms.	
Physical Indexes	Stores minimum, maximum, natural, critical, porosity, saturation, humidity, and volumetric humidity content in addition to information of specific mass and weight, dry, in optimum humidity, saturated, submerged and solids.	
MCT classification tests	Mini-MCV composite laboratory tests, mass loss by immersion and quick classification.	
Particle size test	Laboratory test to obtain the distribution of soil particles.	

to laboratory tests because it may not have been subjected to any type of test, i.e., the geometries of this class must be contained in the field investigations superclass and contain the laboratory tests that have the same identifier code.

The geotechnical units are defined by lithological, pedological, hydrogeological and geomorphological conditions that present a homologous geotechnical behavior and are represented in geo-objects of the polygon or volume type. In this article it proposes a third form of abstraction of geotechnical units consisting of their subdivision of the volume of the geographical feature into a regular mesh of representative elementary volumes, represented by their

Table 3. Subclasses of the superclass laboratory tests that are executed in undisturbed samples and their respective descriptions and constraints.

Subclass of laboratory tests	Description	Spatial and semantic constraints
Compaction	Laboratory test to determine the soil compaction.	Cannot overlap other subclasses if the sample is supposed to be in-situ conditions. Inherits the constraints, geometry, and unique identifier code of the superclass tests unless otherwise specified. Relationship with conventional tables with measurement values.
Permeability Test with Constant Load Permeameter	Laboratory test to measure the ability to flow a fluid through its structure. Used in non-cohesive soils.	
Permeability Test with Variable Load Permeameter	Laboratory test to measure the ability to flow a fluid through its structure. Used in cohesive soils.	
Simple Compression	Laboratory test to measure unconfined compressive strength of cohesive soils.	
Direct Shear	Laboratory test to determine soil shear strength parameters (cohesion and friction angle).	
Consolidation	Determines the compressibility characteristics of soils under the condition of lateral confinement.	
Triaxial	Laboratory tests to determine soil resistance and deformability parameters.	
California Bearing Ratio	Laboratory test to measure the support capacity of the sub-base and subbed.	All constrains established for other subclasses. Geometries related to this subclass can overlap geometries from the compaction subclass as long as they have the same identifier code.

Table 4. Subclasses of the geotechnical unit superclass and their respective descriptions and constraints.

Subclass of the geotechnical unit	Description	Spatial and semantic constraints
Soil Unit	Mapping units defined by pedological conditions presenting homologous geotechnical behavior or soils categorized by a soil classification system for engineering purposes.	Inherits constraints, representation, and geometry unless otherwise specified. Units related to the same geotechnical map, cannot overlap, cannot have gaps and must be contained within the boundary of the geotechnical map. Gaps and inner rings are allowed because rock units or other soil units can occur between or within the unit.
Rock Unit	Mapping units defined by lithological conditions that present homologous geotechnical behavior.	All constrains established for soil units. For rock unit, there is an intersection relationship with geological structures of the type alignment and with structures of the plane type.

respective centroids. Geotechnical units related to the same geotechnical map cannot overlap, cannot have gaps, and must be contained within the boundary of the geotechnical map.

Related to the rock unit, we have the class of the rock mass that is composed by the intact rock discontinuities, water, and the stress state. The rock mass is represented by point-type geo-objects on small scales and by a polygon or volume type geo-object or large-scale. This separation of the rock mass is important because depending on the scale that addresses the problem the same rock unit can present distinct geomechanical behaviors.

The geotechnical unit also relates topologically to the geotechnical sections and the boundary of geotechnical maps. Geotechnical sections can be represented by a line-type geo-object, which corresponds to the alignment of the section, and by polygon-type geo-objects corresponding to a 2D section that is a simplified two-dimensional representation of 3D geotechnical reality or the three-dimensional section itself. Table 4 presents the subclasses of the geotechnical units and their descriptions and spatial and semantic constraints.

The boundary of geotechnical maps consists of the polygons of the areas in which geotechnical maps have been drawn and must be represented by a polygon-type geo-object and overlap and gaps between geometries are allowed. All topological relationships between the geo-objects of the model, regardless of the geometric primitive, are specified in the class diagram and spatial-time relationship is made based on the execution date of a field investigation or laboratory test.

4.2 Proposed conceptual model

Based on the analyses performed regarding the topological and semantic characteristics of the classes, a conceptual model that represents the geotechnical field investigations and laboratory tests in an objective and coherent manner is proposed (Figure 3). The terminology "ge" in the diagram classes means large scales while "pe" means small scales.

The subclasses of field investigations and laboratory tests inherit the common information from their respective superclass's while the sample class is responsible for relating investigations and laboratory test spatially and through the unique identifier code. The superclass field investigations is responsible for generating the unique identifier code, here called geociu, of geotechnical data whose construction was based on the articulation of charts of systematic mapping of the Federal District and a point on the surface of the geometry of the field investigation.

From the superclass investigations, any number of subclasses can be derived if it meets their specifications. In the proposed model, the superclass field investigation through specialization, using the type of investigation attribute, we obtain the subclasses Field Points, Concentric Rings, Piezometer, Trench and Drilling. Each of these objects is responsible for storing information related to geotechnical investigation of the type of the subclass.

In the relationship between the superclass investigations and their respective subclasses, the partial overlap specialization relationship was adopted, overlap because it defines that, two investigations can be conducted in the same place and partial because the subclasses presented do not constitute all the possibilities of field investigations. This relationship validates situations such as a drilling followed by the installation of a piezometer, but it does not prevent the overlap of drilling, whose problem would be that the soil would no longer be in the in-situ conditions. Time could be a variable that makes the second example feasible if the execution of the tests were not in the same period.

In the case of the laboratory test superclass, any number of subclasses may be derived if it meets the definition of the superclass. In the proposed model, the superclass laboratory test, through specialization using the attribute type of derive subclasses moisture, atterberg, physical indexes, particle size test, permeability test with variable or constant load permeameter, california bearing ratio, direct shear, simple compression, consolidation, characterization tests of MCT and triaxial.

In the relationship between the superclass laboratory test and their respective subclasses, the partial disjoining specialization relationship was adopted, because two tests cannot be performed in the same undeformed sample and partial sample because the subclasses presented do not constitute all the possibilities of geotechnical tests. Although the partial disjoining specialization relationship was adopted there are some exceptions for this rule as defined in the requirements section that need to be implemented in the database. The other conventional tables are intended to store the results of the measurements of the tests.

The transformations that involve the classes mentioned above are presented in Figure 4. Regarding the transformations that occur in the database for the generation of 3D geometries, three routines of two-dimensional to three-dimensional data transformations were proposed. For investigations and tests that collect or use cylindrical samples, a buffer is created with the radius of the sample followed by extrusion with its respective height. In the case of a square or rectangular sample, an expansion is made on the X and Y axes followed by extrusion by the height of the sample. For classes that have a polygon or multi-polygon geometry it is only necessary to extrude by the depth that is the case of samples and trenches.

4.3 Logical schema e physical implementation of database

During the elaboration of the logical schema and the physical implementation of the database it was necessary to consider the storage of historical series, measurement results and information related to the execution of tests. Conventional tables were created during the implementation to store the results of measurements during the execution of tests as the concentric rings and information of laboratory test measurements and historical series, for example, water level in piezometer. Because the database user will not open multiple tables to obtain information, selections have been created through materialized visualizations to facilitate access to the data.

The Field Points and Concentric Rings classes inherit the geometry of the superclass and were treated as conventional classes during physical implementation. The field points class was segmented into two tables during implementation, one to store soil profiles and the other for rock outcrops.

Rotary, Percussion and auger drilling, PANDA penetrometer, Cone penetrometer, Guelph Permeameter and Vane test are generated from the query of the field investigations superclass, the drilling subclass, responsible for storing the volumes of the subclasses, and the conventional tables "rotary", "percussion", "auger", "panda_penetrometer", "cone_penetrometer", "guelph" e "vane_test" respectively. In the DBMS, this selection was made by creating materialized visualizations.

Considering that a point, for trenches and pits, would not represent the area investigated at larger scales, and that the centroid generation inserted within the polygon that originates it is a simpler procedure than generating a polygon from a point, it was decided to represent them by polygon-type geo-objects and whose centroid should be included in the field investigation superclass.

The target of the generated 3D geometries varies with the class. The investigations superclass stores the 3D point data while the sample class stores the 2D sample projection as a polygon. The laboratory test superclass uses the point registered in this class as a reference, creates the two-dimensional projection based on the radius or length and width depending on the sample shape of the test, which is stored in the sample class. Based on this projection and with the height of the generates the tested volume, which is stored in the test class. The dimensions of the samples evaluated, in 2D or 3D, are represented in the "tests_geom3d" table

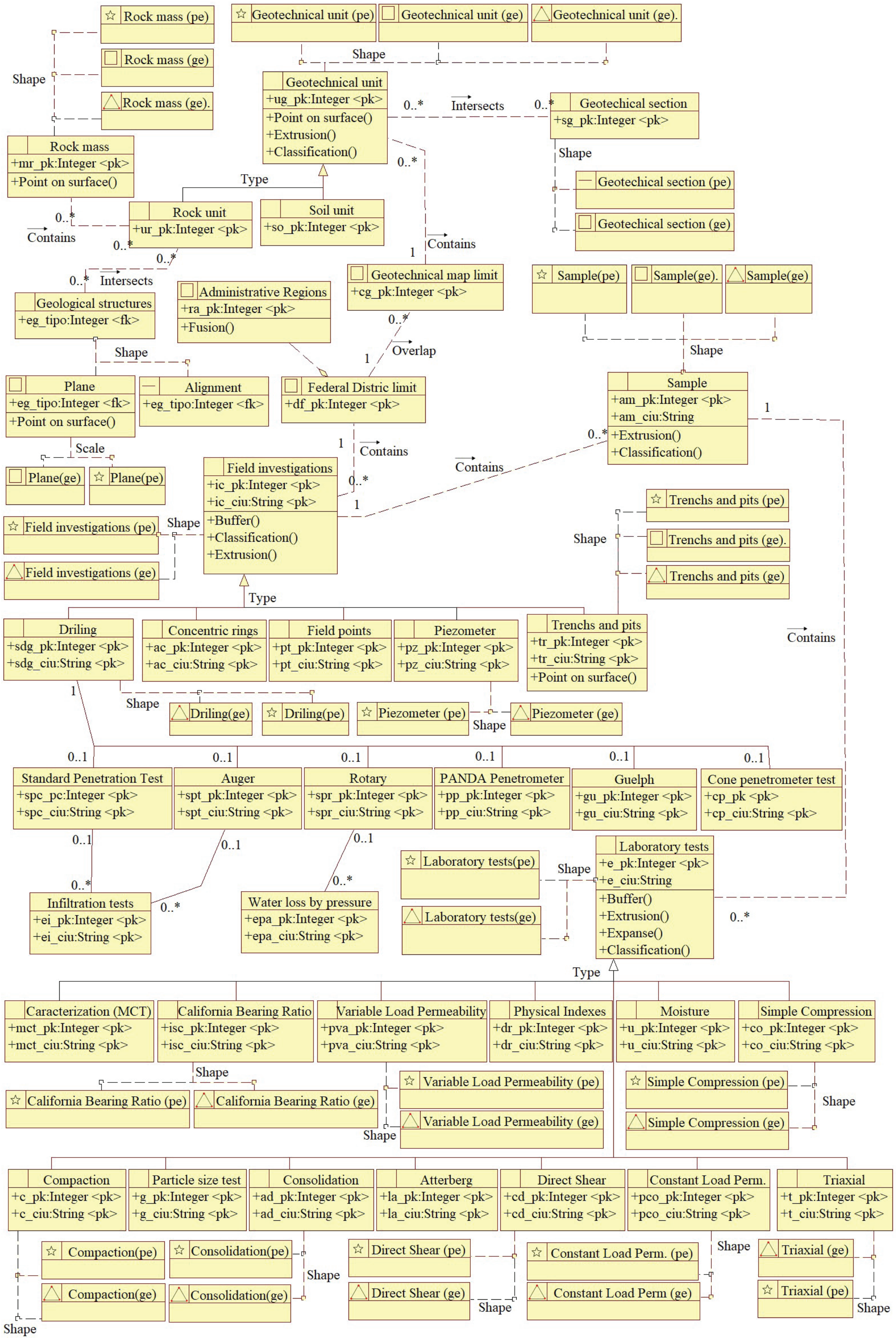

Figure 3. Conceptual model proposed for tridimensional geotechnical data.

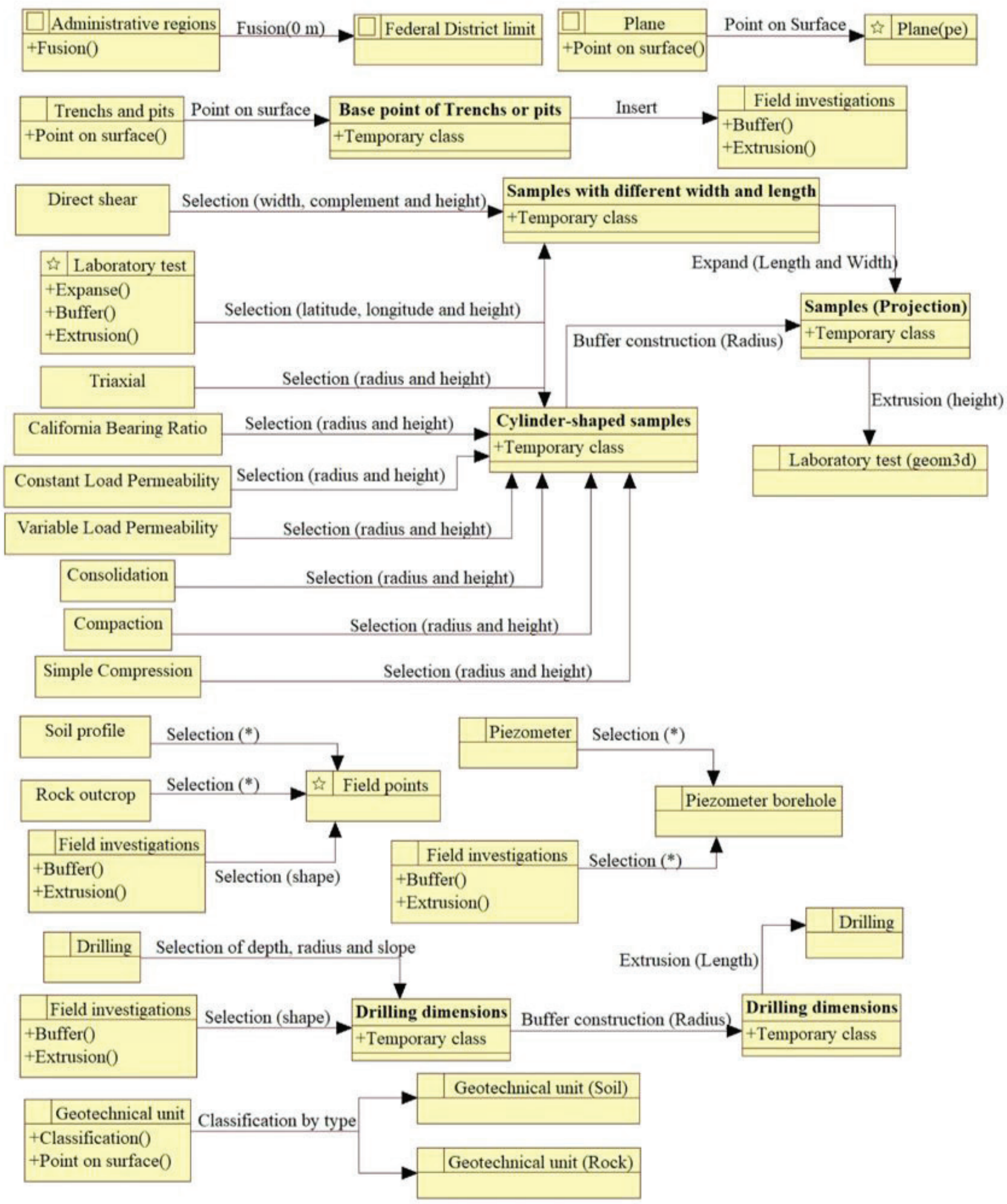

Figure 4. Transformation diagram proposed for tridimensional geotechnical data.

which has the same purpose as the drilling table, which is to store the volumes of the subclasses.

The Figure 5 presents the geometry of field investigations of SPT type and a geotechnical section projected in two dimensions and the original geometries of the section and investigations in three dimensions. QGIS allows to query any information in the database using PL/pgSQL expressions and visualize the data using the 3d viewer.

Figure 5 is just one example of the many possible applications that can be made based on the data inserted into the database. The use of pre-existing geotechnical data in the elaboration of geotechnical maps, for example, facilitates their elaboration and the remaining time, previously invested in the compilation and compatibility of information, can be reallocated to other activities. Besides geotechnical cartography, we can mention the importance of a geotechnical database as a preliminary source of information for engineering projects such as foundations and excavations for example.

The sections were prepared based on information of number of blows and geological origin of the soils available from boreholes. To include more information in the section, or any other information together with the geotechnical data, it is only necessary to perform a spatial analysis between the section and the other information available in the database or insert the data in the GIS together with the section in the same project, since all the information shares the same reference system. Figure 6 shows in detail the sections shown in Figure 5. Other types of information are not displayed in

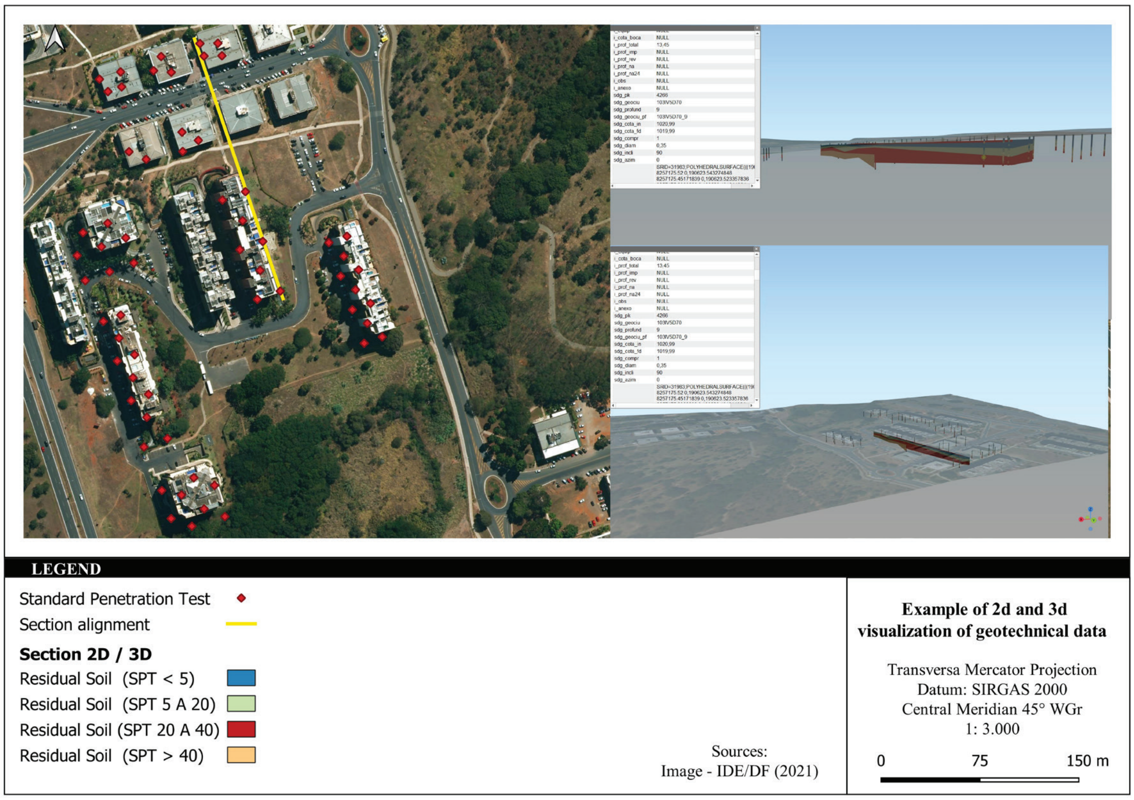

Figure 5. Boreholes and geotechnical section presented in two and three dimensions using QGIS to access the database and view the data.

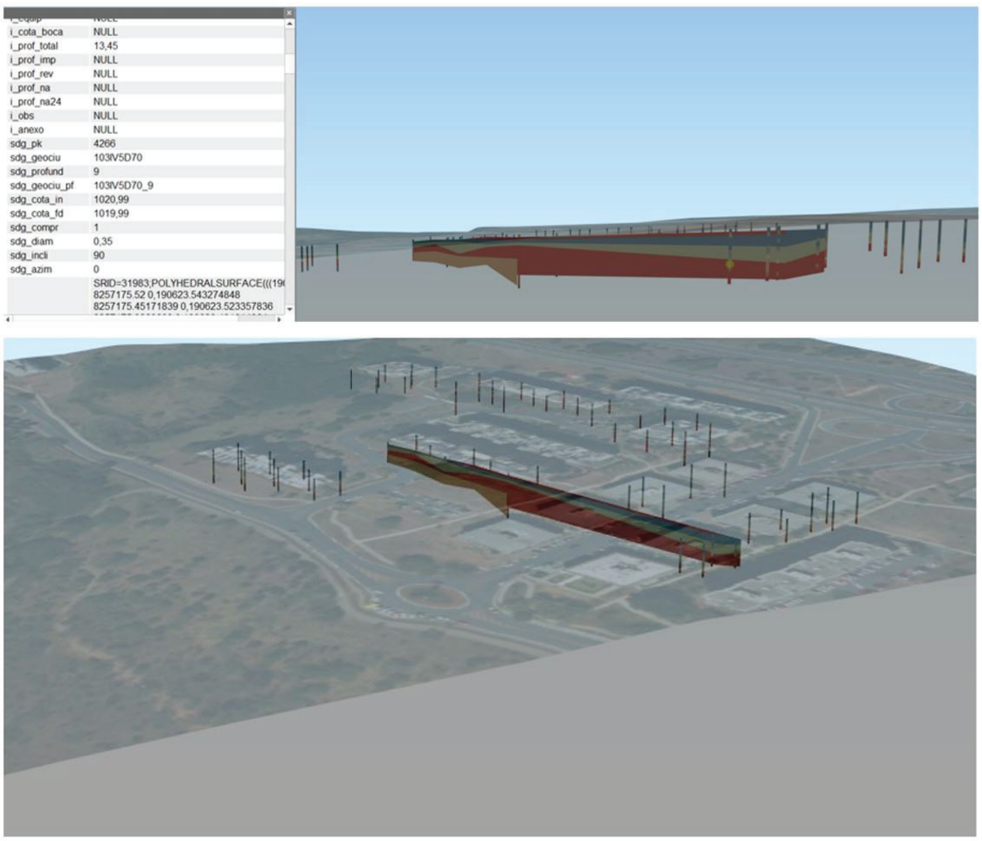

Figure 6. Detail of the sections shown in the figure 5 with image projected on terrain.

the section because there is no information available in the same place. As this information is compiled from several sources, there are no cases with overlaps of different types of field investigations and laboratory tests.

5. Conclusion

Considering the reality of the Federal District, in which more than four thousand geotechnical investigations were compiled the auto to make up this database were restricted in their respective sources, it is observed the real need to build a geospatial database that is compatible with the Spatial Data Infrastructure of Federal District and National Spatial Data Bank to disseminate this information.

The implementation of the proposed model allows, and the systematic and periodic organization of data produced by various agencies or companies, improves the quality of stored data, facilitates the interoperability of geotechnical data between producers and consumers of geoinformation in addition to optimizing investigation plans, improving the planning of investments for geotechnical studies, and optimizing the execution of future construction projects.

In the case of the OMT-G model, it proved appropriate to obtain adequate representations of laboratory tests and field investigations. Relationships such as specialization can define more specific classes from generic classes by adding new properties in the form of attributes, such as field investigations and laboratory tests and their respective subclasses. This type of relationship also allows you to specify that two field tests can be done in the same location as a drilling followed by the installation of a piezometer, but two tests cannot be done in the same sample, such as a triaxial assay followed by a simple compression test.

Despite the OMT-G model was not designed to model data with time property, due to the characteristics of geotechnical data, queries related to the date of execution or registration of an investigation are easily constructed and are sufficient to retrieve information related to the temporal issue.

The OMT-G was also satisfactory in modeling three-dimensional data, when associating the class and transformation diagrams. All the operations required for the construction of the three-dimensional geometries are available in the chosen DBMS and the available topological relationships meet those specified in the class diagram.

The DBMS PostgreSQL proved to be extremely robust and stable to serve as the basis for the geotechnical three-dimensional database and its integration with GIS such as Quantum GIS creates the possibility to use all its functionalities to analyze the data in question. All the structures and relationships mentioned during conceptual modeling and the structures presented in the logical schema have been successfully implemented in the PostgreSQL database and are being compiled in the PostgreSQL extension that will be available in the https://github.com/bro-geo/geotechnical_database.

Finally, this model will serve as the basis for the development of an application for geotechnical database management in Quantum GIS. Later the model will be expanded to include more objects of interest of the Geotechnics theme, and greater interoperability with other databases such as the Multifinalitary Technical Cadastre of the Federal District.

Declaration of interest

The authors have no conflicts of interest to declare. All co-authors have observed and affirmed the contents of the paper and there is no financial interest to report.

Authors' contributions

Bruno Rodrigues de Oliveira: conceptualization, data compilation, methodology, visualization, writing – original draft and writing – review & editing. Newton Moreira de Souza: supervision, writing – review & editing. Rafael Cerqueira Silva: supervision, writing – review & editing. Eleudo Esteves de Araújo Silva Júnior: supervision, writing – review & editing.

List of symbols

AGS:	Association of Geotechnical & Geoenvironmental Specialists
CBR:	California Bearing Ratio
DBMS:	Database Management System
GDF:	Federal District Government
GIS:	Geographical Information System
GML:	Geography Markup Language
MCT:	Miniature, Compacted, Tropical
OMT-G:	Object Modeling Technique for Geographic Applications
UML:	Unified Modeling Language
SQL:	Structured Query Language

References

ABNT NBR 6484. (2020). *Soil - Standard penetration test - SPT - Soil sampling and classification - Test method*. Associação Brasileira de Normas Técnicas, Rio de Janeiro.

ABNT NBR 6502. (1995). *Rocks and soils - Terminology*. Associação Brasileira de Normas Técnicas, Rio de Janeiro.

ABNT NBR 8044. (2018). *Geotechnical design - Procedure*. Associação Brasileira de Normas Técnicas, Rio de Janeiro.

ABNT NBR 9604. (2016). *Well opening and soil profile inspection trench, with removal of disturbed and undisturbed soil samples — Procedure*. Associação Brasileira de Normas Técnicas, Rio de Janeiro.

Borges, K.A.V., Davis Junior, C.A., & Laender, A.H. (2005). Modelagem conceitual de dados geográficos. In M. A. Casanova, G. Câmara, C. A. Davis Junior, L. Vinhas, &

G. R. Queiroz (Eds.), Banco de dados geográficos (1. ed., pp. 93-146). INPE.

Borges, K.A.V., Davis, C.A., & Laender, A.H.F. (2001). OMT-G: an object-oriented data model for geographic applications. *GeoInformatica*, 5(3), 221-260. http://dx.doi.org/10.1023/A:1011482030093.

Bozio, A.F., & Reginato, V.S.C. (2020). Modelagem conceitual de banco de dados para mapeamento geotécnico. In H. Fonseca Filho (Eds.), *2o Simpósio Brasileiro de Infraestrutura de Dados Espaciais* (pp. 1-13). Rio de Janeiro: INDE.

Davis Junior, C.A. (2000). *Múltiplas Representações em Sistemas de Informação Geográficos* [Doctoral thesis]. Universidade Federal de Minas Gerais.

Gao, S. (2007). *Development of a 3D GIS database model for geotechnical analysis incorporating geostatistics* [Doctoral thesis]. Nanyang Technological University. https://doi.org/10.32657/10356/39359.

Head, K.H. (2006). Manual of soil laboratory testing. Volume 1. Soil classification and compaction tests. *International Journal of Rock Mechanics and Mining Sciences & Geomechanics Abstracts*, 18(3), 43. https://doi.org/10.1016/0148-9062(81)90992-x.

Head, K.H., & Epps, R.J. (2011). Manual of soil laboratory testing. *Environmental and Engineering Geoscience*, 21(3), 247-248. https://doi.org/10.2113/gseegeosci.21.3.247.

Head, K.H., & Epps, R.J. (2014). Manual of soil laboratory testing - Volume 2: Permeability, Shear Strength and Compressibility Tests. (3rd ed.).

Instituto Brasileiro de Geografia e Estatística – IBGE (2021). Perfil de Metadados Geoespaciais do Brasil: perfil MGB 2.0. IBGE.

Lee, M., Kim, H., Kim, J, Lee, J. (2005). *StarUML – The Open-Source UML /MDA Plataform (5.0.2)*. Retrieved in November 11, 2021, from http://www.dpi.inpe.br/cursos/ser300/Softwares/staruml-5.0-with-cm.exe.

Marrano, A., Iyosama, W.S., & Miyashiro, N. (2018). Investigações geotécnicas e geoambientais. In A.M.S. Oliveira, & J.J. Monticeli (Eds.), *Geologia de Engenharia e ambiental* (1st ed., 912 p.). ABGE.

Moura, A.R.L.U., Gusmão, A.D., & Alves, F. (2017). Modelagem conceitual de banco de dados espaciais para análise geotécnica. In D. Gherardi (Ed.), *Proc. Simpósio Brasileiro de Sensoriamento Remoto* (pp. 4032-4039). Santos: Galoá.

OGC (2017). *Geoscience Markup Language (GeoSciML)*. GeoSciML Modeling Team.

POSTGIS. (2021). *PostGIS - spatial database extender for PostgreSQL object-relational database (3.0.3)*. PostGIS. Retrieved in November 11, 2021, from https://postgis.net/install/

PostgreSQL Global Development Group. (2021). *PostgreSQL (11.17)*. PostgreSQL. Retrieved in July 15, 2021, from https://www.postgresql.org/about/

Priya, B.D., & Dodagoudar, G.R. (2018). An integrated geotechnical database and GIS for 3D subsurface modelling: application to Chennai City, India. *Applied Geomatics*, 10, 47-64. https://doi.org/https://doi.org/10.1007/s12518-018-0202-x.

QGIS. (2021). *Quantum Geographical Information System Software (3.16)*. QGIS. Retrieved in July 15, 2021, from https://www.qgis.org/pt_BR/site/

Queiroz, G.R., & Ferreira, K.R. (2006). Tutorial sobre bancos de dados geográficos (1. ed.). INPE.

Ribeiro, A.J.A., Silva, C.A.U., & Barroso, S.H. (2016). Metodologia para criação de um banco de dados georeferenciado a partir de dados geotécnicos obtidos em "as built" e projetos rodoviários. *REEC – Revista Eletrônica de Engenharia Civil*, 12(2), 1-13. https://doi.org/10.5216/reec.V12i2.39413.

Santos, J. V., Thiesen, S., & Higashi, R.A.R. (2018). Geological-Geotechnical database from standard penetration test investigations using geographic information systems. In M. Pomffyova (Eds.), *Management of Information Systems*. IntechOpen. https://doi.org/10.5772/intechopen.74208.

Silberschatz, A., Korth, H.F., & Sudarshan, S. (2020). Database System Concepts (Seventh ed). McGraw-Hill.

Silva, A.M. (2005). *Banco de dados de curvas de retenção de água de solos brasileiros* [Master's dissertation]. Universidade de São Paulo.

Silva, C.P.L. (2007). *Cartografia geotécnica de grande escala: estudo de caso Brasília - área tombada pela UNESCO* [Master's dissertation]. Universidade de Brasília.

Silva, R.A. (2021). *pgModeler - PostgreSQL Database Modeler (0.93)*. PostgreSQL. Retrieved in July 15, 2021, from https://pgmodeler.io/

SPUGeo. (2021). Modelagem de dados geográficos no contexto de infraestruturas de dados espaciais SPU. In SPUGeo (Org.), *Geoinformação na SPU – conceitos, fundamentos e tecnologias*. SPUGeo.

Tegtmeier, W., Zlatanova, S., Oosterom, P.J.M., & Hack, H.R.G.K. (2014). 3D-GEM: geo-technical extension towards an integrated 3D information model for infrastructural development. *Computers & Geosciences*, 64, 126-135. http://dx.doi.org/10.1016/j.cageo.2013.11.003.

Zand, A.G. (2011). *Enabling geotechnical data for broader use by the spatial data infrastructures* [Doctoral thesis] University of Southern California.

Soils and Rocks
www.soilsandrocks.com
An International Journal of Geotechnical and Geoenvironmental Engineering
ISSN 1980-9743
ISSN-e 2675-5475

Geosynthetic Encased Column: comparison between numerical and experimental results

Nima Rostami Alkhorshid[1#], Gregório Luís Silva Araújo[2], Ennio Marques Palmeira[2]

Article

Keywords
Geosynthetic
Embankment
Granular column
Soft soil
Finite element method
Laboratory test

Abstract

The use of granular column is one of the ground improvement methods used for soft soils. This method improves the foundation soils mechanical properties by displacing the soft soil with the compacted granular columns. The columns have high permeability that can accelerate the excess pore water pressure produced in soft soils and increase the undrained shear strength. When it comes to very soft soils, the use of granular columns is not of interest since these soils present no significant confinement to the columns. Here comes the encased columns that receive the confinement from the encasement materials. In this study, the influence of the column installation method on the surrounding soil and the encasement effect on the granular column performance were investigated using numerical analyses and experimental tests. The results show that numerical simulations can reasonably predict the behavior of both the encased column and the surrounding soil.

1. Introduction

Construction on soft soils is one of the most significant challenges for geotechnical engineers. One of the solutions is the use of granular columns to improve the composite foundation soil overall shear strength. The performance of granular columns is highly dependent on the confinement provided by the surrounding soil. This technique is not recommended in very soft soils (S_u < 15 kPa), since these soils present low shear strength and high compressibility. In this context, the lack of confinement around the column can be overcome using geosynthetic encasement. In recent years, many projects used geosynthetic encased columns to stabilize the soft soil foundation (De Mello et al., 2008; Araujo et al., 2009; Gniel & Bouazza, 2009; Alexiew & Raithel, 2015; Xue et al., 2019; Chen et al., 2020). Encased granular columns act like semi-rigid piles that transfer the loads to the soil layers at specific depths capable of bearing them. Moreover, they function like vertical drains and provide radial drainage to the soft soils and accelerate the consolidation process. Besides providing lateral confinement to the column, geotextiles protect them from the clogging of the granular infill material (Castro & Sagaseta, 2011; Zhang et al., 2012; Pulko & Logar, 2017; Li et al., 2020; Chen et al., 2020).

The influence of encasement on the granular column performance was appraised in various experimental studies. In these studies, partial and full encasement of the granular columns were investigated. The results showed that the encasement could increase the bearing capacity and reduce the settlement of the column (Yoo & Lee, 2012; Ali et al., 2012; Xue et al., 2019; Alkhorshid, 2017; Zhang et al., 2020; Cengiz & Guler, 2020; Chen et al., 2020; Alkhorshid et al., 2020).

The Finite Element Method (FEM) is a powerful tool to investigate geotechnical problems and can be calibrated using laboratory and field data and, consequently, be utilized for large-scale projects (Alkhorshid, 2012; Keykhosropur et al., 2012; Castro & Sagaseta, 2013; Alkhorshid et al., 2014; Mohapatra et al., 2017; Nagula et al., 2018, Alkhorshid et al., 2021). Despite various studies that have been done to investigate encased granular columns, the current knowledge on their performance still needs improvement. In this study, the displacement installation method's effect on the surrounding soil and the encasement influence on the granular column behavior were evaluated using laboratory tests and numerical analyzes. Laboratory tests were analyzed using PLAXIS 3D and 2D to evaluate the numerical analysis capability in predicting soft soil and column behavior.

[#]Corresponding author. E-mail address: nimara@unifei.edu.br
[1]Universidade Federal de Itajubá, Institute of Integrated Engineering, Itabira, MG, Brasil.
[2]Universidade de Brasília, Department of Civil and Environmental Engineering, Brasília, DF, Brasil.

Submitted on July 9, 2021; Final Acceptance on October 26, 2021; Discussion open until February 28, 2022.
https://doi.org/10.28927/SR.2021.073121

2. Model test

2.1 Test setup

The test tank, with dimensions 1.6 m × 1.6 m × 1.2 m (Figure 1), was covered internally by lubricated plastic sheets to make it impermeable before placing the soft soil inside the tank and reduce friction along the internal faces of the tank. A scale factor (λ = prototype diameter/model diameter) of 4 (Alkhorshid et al., 2019) was used to reach the desired soil undrained shear strength (S_u < 5 kPa), column diameter (d_c = 0.15 m) and geotextile tensile stiffness (J < 125 kN/m) for laboratory modeling. The soft soil was allowed to consolidate under self-weight before the column installation. Four piezometers were installed in the soft soil to monitor the effects of column installation on the soil pore water pressures during the tests, as shown in Figure 1.

2.2 Installation method

The displacement method was adopted to install the column. The encased column was prepared outside of the test tank using vibration to reach a target relative density of 85%. The column infill was placed and vibrated inside a closed-tip (by a non-woven geotextile) geotextile encasement in layers 20 cm thick. Then, the column was placed inside a PVC pipe closed at the tip. A wooden casing (Figure 2) was used to keep the column perpendicular to the tank base during installation. By driving the column inside the soft soil, the surrounding soil displaces laterally and influences the soil mechanical and physical properties.

2.3 Boundary conditions and numerical modeling

To simulate the model tests in PLAXIS 2D and 3D (Figure 3), roller and pinned supports were applied to the lateral and base boundaries, respectively. Thus, the soft soil was able to displace vertically at the tank sides, but horizontal and vertical displacements were restrained at the base. Undrained conditions were adopted for the lateral and base boundaries to avoid water flow, since the tank was internally covered with plastic sheets.

The Soft Soil model is an appropriate model for normally consolidated clay, which was the case in this study. The Mohr-Coulomb model was adopted to simulate sand, gravel and recycled construction and demolition waste (RCDW – composed of broken bricks, concrete, and gravel) used as column infill materials (Khabbazian et al., 2010; Keykhosropur et al., 2012; Alkhorshid, 2012; Almeida et al., 2013; Alkhorshid et al., 2014, 2018). The properties of materials used in the numerical simulations, obtained from laboratory tests and back analysis, are given in Table 1 (Alkhorshid, 2017; Alkhorshid et al., 2019). The model geotextile encasement with the desired diameter (d_c = 0.15 m) and tensile stiffness (J < 125 kN/m) was not commercially available. Therefore, three types of geotextile encasements, G1 (J = 120 kN/m), G2 (J = 107 kN/m) and G3 (J = 53.4 kN/m), were used in this study to account for the scale factor (λ). Seam was used along the column length, which made it an anisotropic material, with different tensile stiffness along vertical and circumferential directions. Consequently, the geotextile encasements were simulated using elastic material with two different values of tensile stiffness in these directions (Table 2). Interface elements were applied to simulate the interactions between

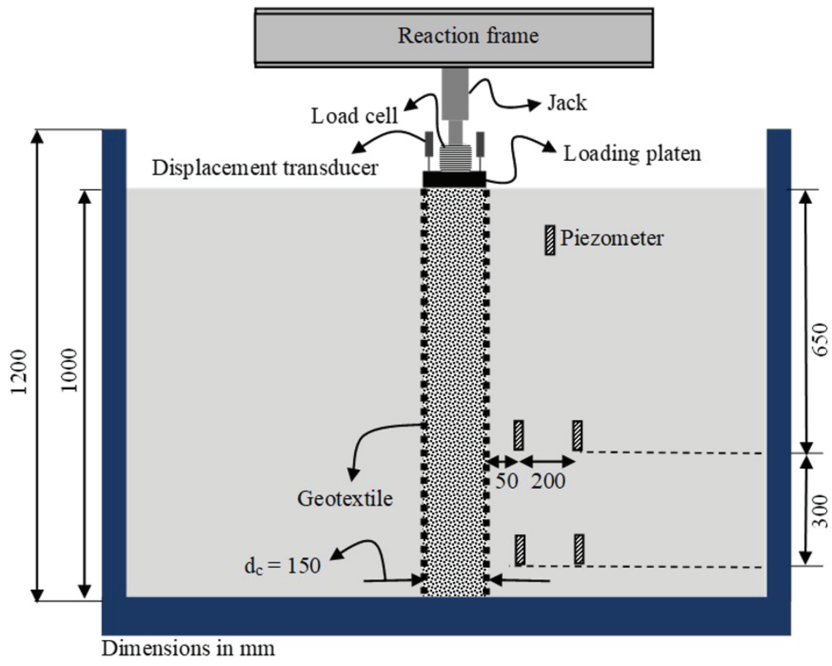

Figure 1. Schematic view of the equipment.

the geotextile encasement and the adjacent materials (soft soil and column infill), and the strength reduction factor (R_{int} – see Table 1) was assigned to specify these interactions.

An axisymmetric model (6-noded elements) in PLAXIS 2D was analyzed using consolidation analysis to evaluate the installation effects (excess pore water pressure, undrained shear strength and soil heave) on the surrounding soil. A cylindrical cavity with a radius of 0.02 m was applied to the soil to enable lateral prescribed displacement (equal to the column radius, 0.075 m). Actually, the column is driven into the soil, and during penetration the soil is displaced laterally. However, in this numerical analysis, the cavity approach (Castro & Karstunen, 2010) was required to apply lateral displacements. Results of laboratory column bearing capacity tests were back analyzed using PLAXIS 3D (Alkhorshid, 2017; Alkhorshid et al., 2019). Hence, the prescribed settlements and their corresponding loads were compared to the laboratory results.

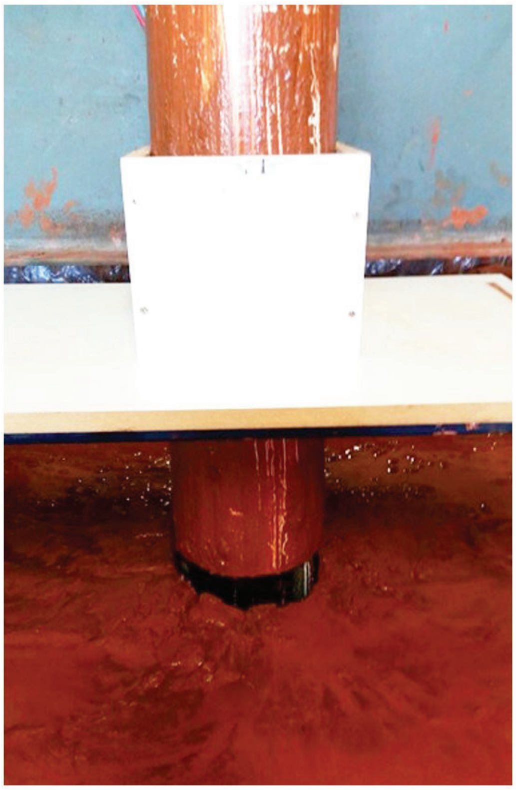

Figure 2. Installation of the column using a wooden casing.

3. Numerical and model tests results

3.1 Load-settlement curves

The results obtained from the laboratory tests (Figure 4a) show conventional (uncased) column inability to bear significant loads. The differences between the load capacities carried by the three different columns (sand, gravel, and RCDW) are negligible, which was predictable since these columns received no significant confinement from the surrounding soft soil. The numerical results are in satisfactory agreement with those from the tests. The numerical prediction for RCDW compared better with the test results.

Figures 4b and 4c show the importance of the geotextile encasement in improving the column bearing capacity and show that the numerical results compare well with those from the tests. Still, the numerical results obtained for G3 (Figure 4b) show some differences as the load increases, leading to an overestimation of 8.5% at the end of the test. Figure 4c shows that the numerical results for G2 do not perfectly fit those from the tests at the early stages of the test. Thus, the numerical predictions underestimated the load values by as much as 10% in these stages.

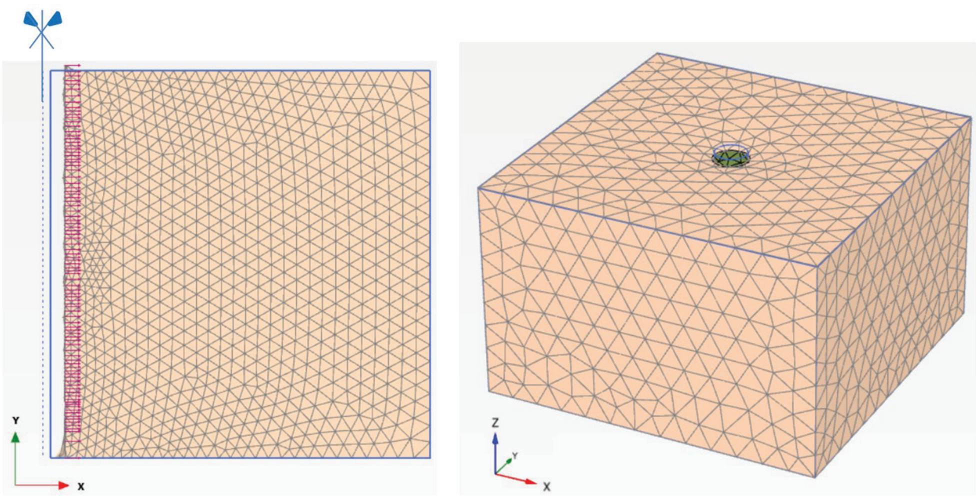

(a) (b)

Figure 3. Numerical simulations: (a) axisymmetric model; (b) three-dimensional model.

Table 1. Material parameters used in FEM simulations.

Material Properties	Soft clay	Sand column	Gravel column	RCDW column
	Soft Soil (SS)	Mohr-Coulomb (MC)	Mohr-Coulomb (MC)	Mohr-Coulomb (MC)
Saturated unit weight, $\gamma_{sat}\left(\mathrm{kN}/m^3\right)$	17	20	20	19
Effective Young's modulus, $E'\left(\mathrm{kPa}\right)$	-	80000	80000	35000
Effective friction angle, $\phi'(^o)$	25	40.5	43	42
Dilatancy angle, $\Psi(^o)$	0	10	12	10
Effective cohesion, $c'\left(\mathrm{kPa}\right)$	3	0.1	0.1	0.1
Effective Poisson's ratio, ν'	0.15	0.3	0.3	0.3
Modified compression index, λ*	0.2	-	-	-
Modified swelling index, κ*	0.12	-	-	-
Lateral earth pressure coefficient, K_0	0.57	0.35	0.32	0.33
Hydraulic conductivity in x direction, K_x (m/day)	1.39×10^{-3}	7	7	7
Hydraulic conductivity in y direction, K_y (m/day)	1.39×10^{-3}	7	7	7
Hydraulic conductivity in z direction, K_z (m/day)	1.39×10^{-3}	7	7	7
Interface coefficient (R_{int})	0.4	0.9	0.9	0.9

Table 2. Geotextile encasement parameters used in FEM simulation.

Properties	Seam (circumferential direction)		No seam (vertical direction)
	Maximum tensile strength of seam (kN/m)	Tensile stiffness at 5% strain (kN/m)	Tensile stiffness (kN/m)
G1	30	120	950
G2	16	107	366
G3	8	53.4	160

The encased RCDW numerical prediction (Figure 4d) was the least accurate regarding the results obtained in the tests. The predicted variation of settlement with load is quite linear, whereas the experimental variation is a curve, resulting in a difference of 26% at the final loading stage for G3. The RCDW grains were broken bricks, concrete, and gravel that may significantly influence the column mechanical properties.

3.2 Excess pore water pressure

The piezometers installed show the excess pore water pressure produced during the column installation. The column loading tests started after the excess pore pressure was dissipated, which took approximately 45 hours. The numerical results compare rather well with those from the tests (Figure 5). The excess pore pressures reached a pick value during column installation and dropped down as time went by for all piezometers. However, the predicted reductions of pore pressures are steeper, showing a difference of approximately 200% at 18 hours of dissipation for P1. When it comes to the time needed for the full dissipation, the difference between predicted and measured results is between 1.5 to 2 hours. P3 and P4 show better comparisons between predicted and observed results than P1 and P2. During the loading stages, small values of excess pore water pressure were obtained by the piezometers. Piezometer P1, located at the bottom, close to the column, showed higher values of excess pore water pressure, as shown in Figure 6.

3.3 Soft soil undrained shear strength

Predicted and observed results in Figure 7 show some improvements in the undrained shear strength of the surrounding soil after the column was installed and the excess pore pressure dissipated. The undrained shear strength (S_u) in laboratory tests and numerical analysis was obtained from the vane shear tests and principal stresses, respectively. The test results show that values of S_u at the depths of 20 cm, 40 cm, 60 cm, and 80 cm increased by approximately 200% at 30 mm from the column. No increase in undrained strength was observed at 70 mm from the column. Hence, the diameter of the region (d_s, smear zone) disturbed by the column installations was 1.8 to 1.9 times the column diameter (d_c). However, the numerical analysis predicted values of ds greater than $1.9d_c$ as the soil

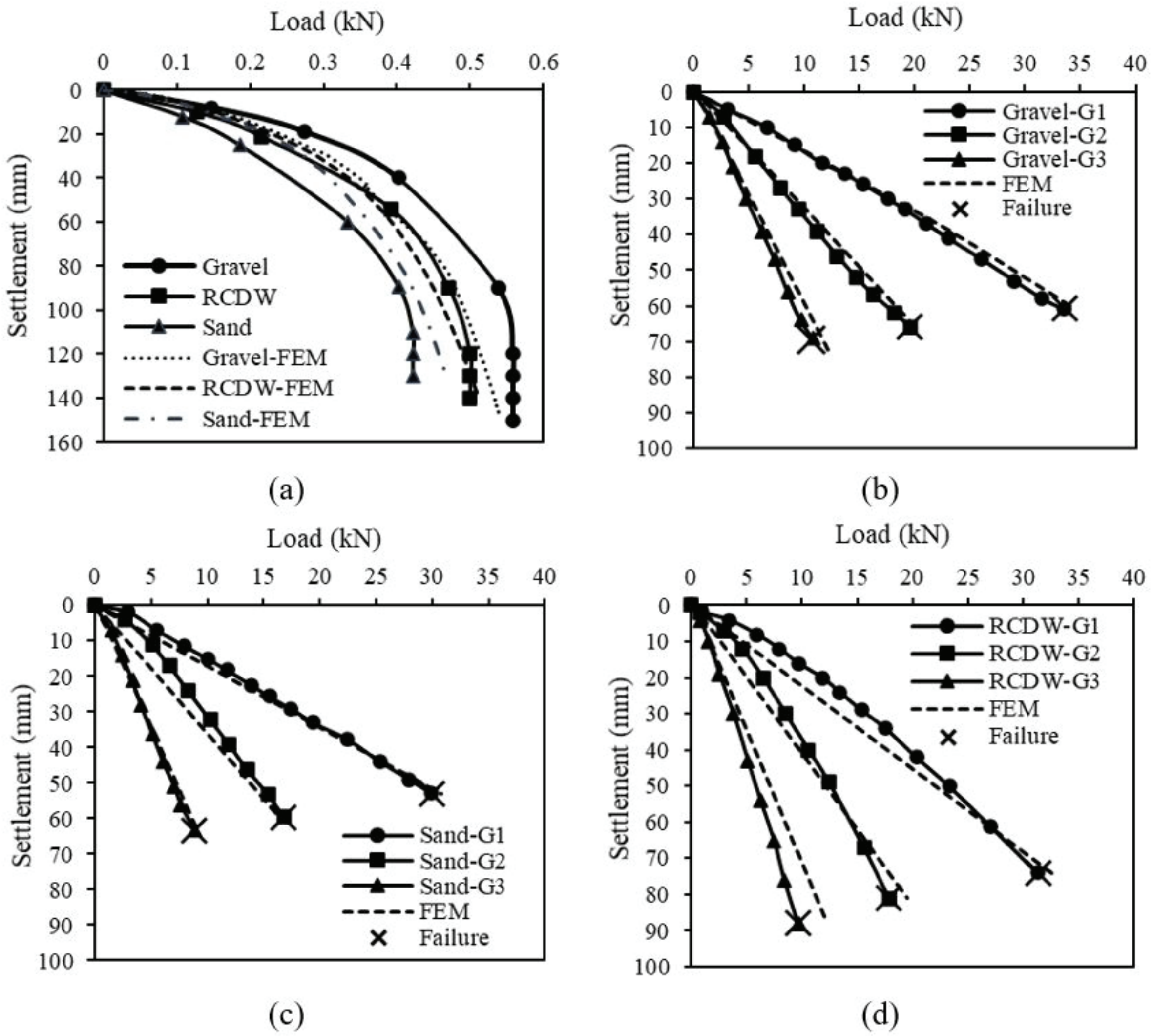

Figure 4. Load-settlement curves: (a) conventional columns; (b) encased gravel column; (c) encased sand column; (d) encased RCDW column.

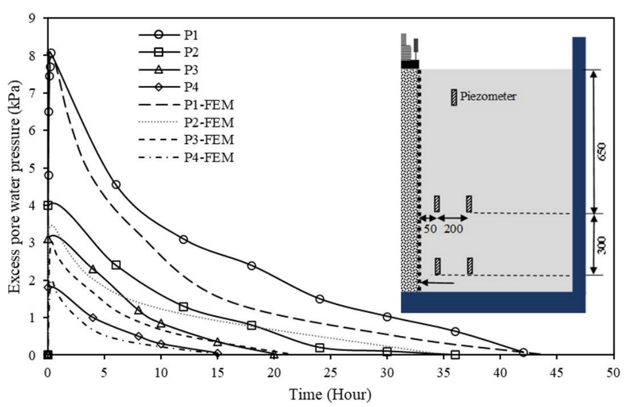

Figure 5. Excess pore water pressure during the column installation (dimensions in mm).

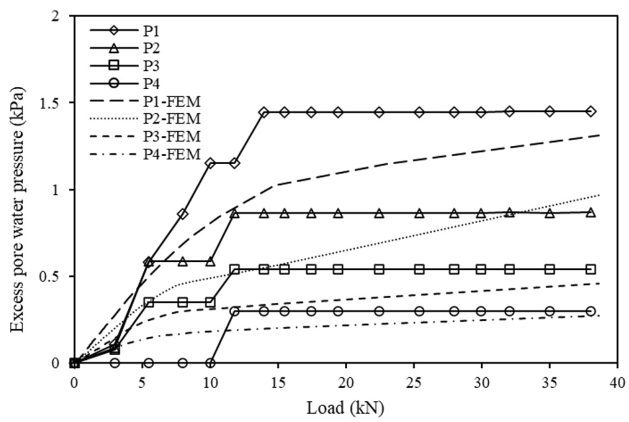

Figure 6. Excess pore water pressure during loading.

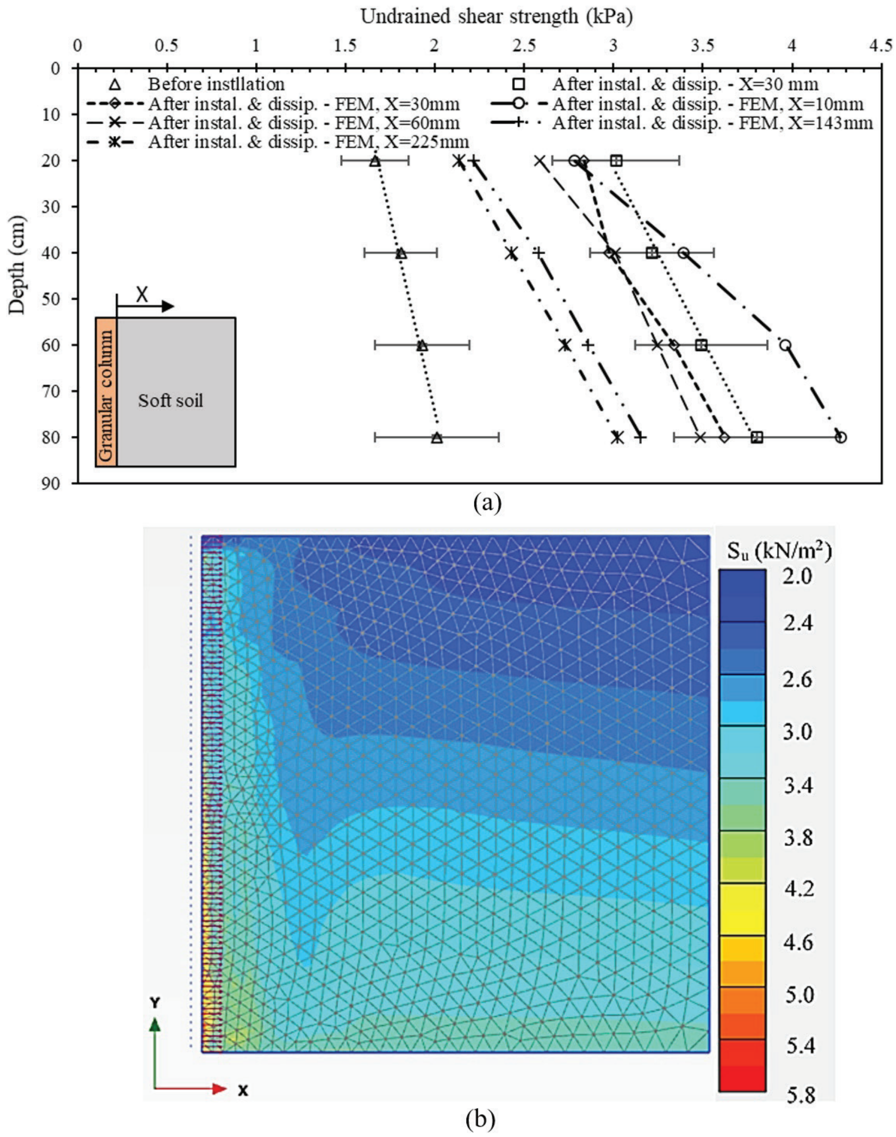

Figure 7. Changes of undrained shear strength with depth: (a) comparison between numerical and measured results and (b) numerical results.

undrained shear strength increases when it consolidates. The numerical results at 30 mm from the column depict reasonable agreements with those from the tests. These results show that at 10 mm, the values of S_u were approximately 3 times greater than the initial values (before column installation) at the depths of 60 cm and 80 cm.

3.4 Soil heave

The predicted and measured results show that the column installation displaces the soil circumferentially (Figure 8), leading to soil surface heave. These results show that the soil experienced a heave displacement approximately equal to half the column radius along the column perimeter. However, regarding the diameter of the region around the column that underwent heave (d_h), a significant difference can be noted between predicted and observed results so that the former is half the latter one.

3.5 Failure and deformation mechanisms

The loading tests were carried out to obtain the column's maximum loading capacity. As shown in Figures 9a and 9b, the column failed at a depth of 0.15 to 0.18 m (from the column top). The load on the column top caused it to bulge, leading to geotextile encasement failure. The numerical analyses indicated that the column experienced excessive bulging at the same depths, as shown in Figure 9c. Figure 10 shows that the tensile forces developed in the geotextile encasement slightly exceeded or were close to the encasement maximum tensile strength

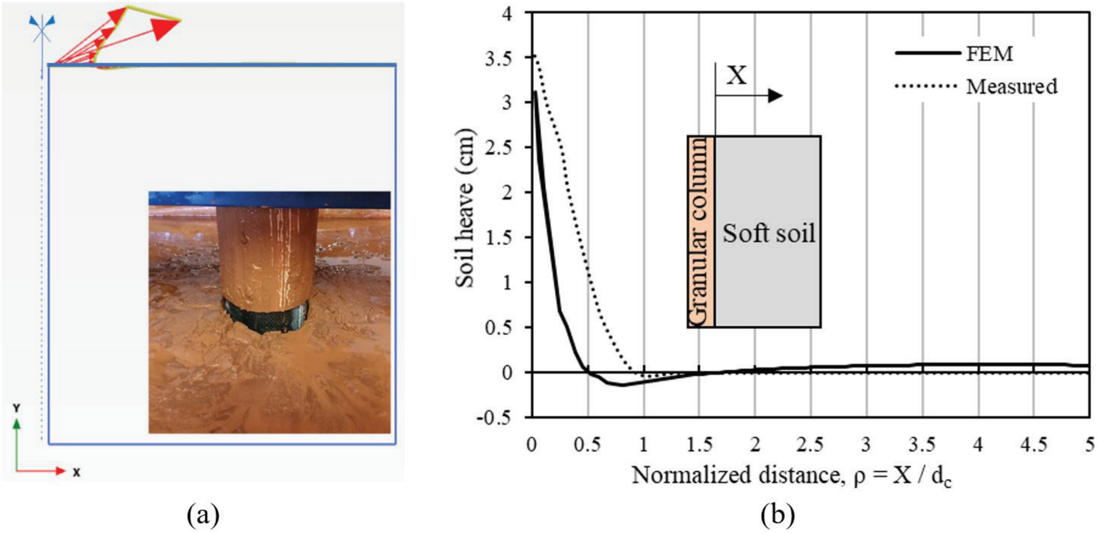

Figure 8. Soil heave after column installation: (a) soil surface; (b) predicted and measured results.

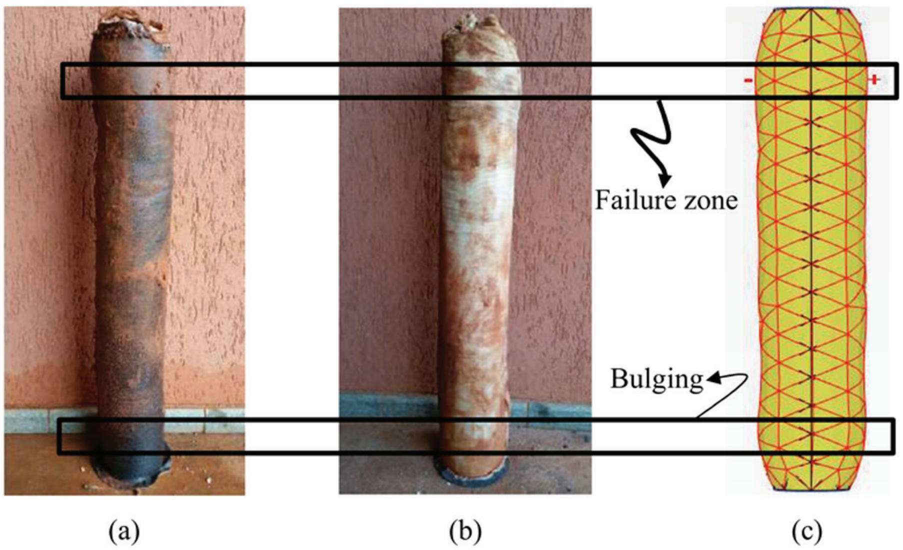

Figure 9. Columns after loading: (a) and (b) exhumed columns after testing; (c) column shape obtained from numerical analyses.

(marked with red circles in Figure 10) between elevations 0.07 m and 0.15 m and between elevations 0.8 m and 0.94 m.

3.6 Breakage of the granular column particles

The gravel and RCDW columns were divided into five sections to evaluate the breakage (B_g) of particles of the column infill material using Marsal's (1967) procedure, as shown in Figure 11. The results (Table 3) show that the gravel and RCDW columns (encased with G1) underwent particle breakage of as much as 15.89% and 20.94%, within sections 1 and 2 ($2d_c$), respectively. The numerical results predicted that within these sections the column experienced significant shear strains (Figure 12) and confinement (from the encasement, Figure 13), which can be the reason for the column infill breakage. Sieving tests on the infill material did not show any significant level of particle breakage in sections 3, 4, and 5.

At the end of every test, the region around the column top experienced an active state of stresses resulting in tension cracks development up to a radius (R_{TC}) of 22.5 cm (Figure 14a). It can also be verified by checking the tension cut-off points in the numerical analyses that show the region in which the soil fails in tension. The predicted results (Figure 14b) show that R_{TC} extended up to a radius of 22.7 cm, which compares well with the test results.

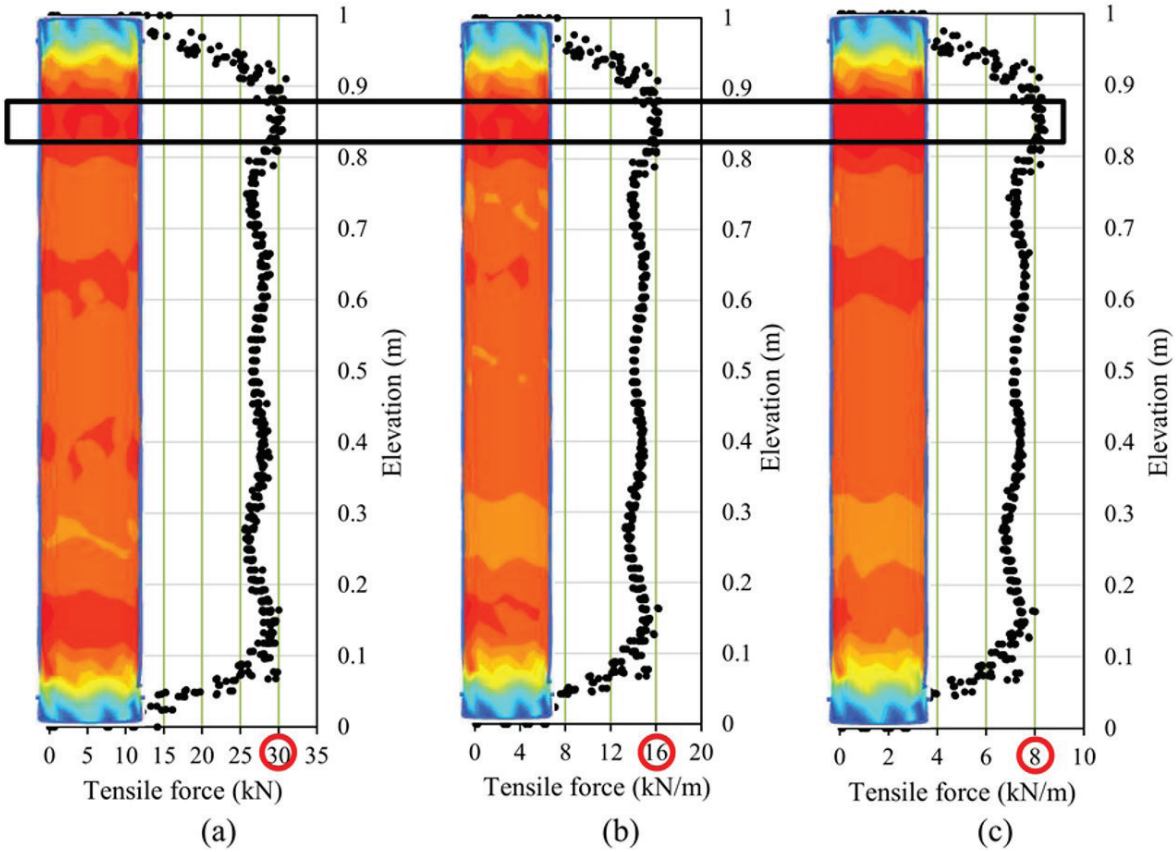

Figure 10. The tensile force along the column height (a) G1; (b) G2; (c) G3.

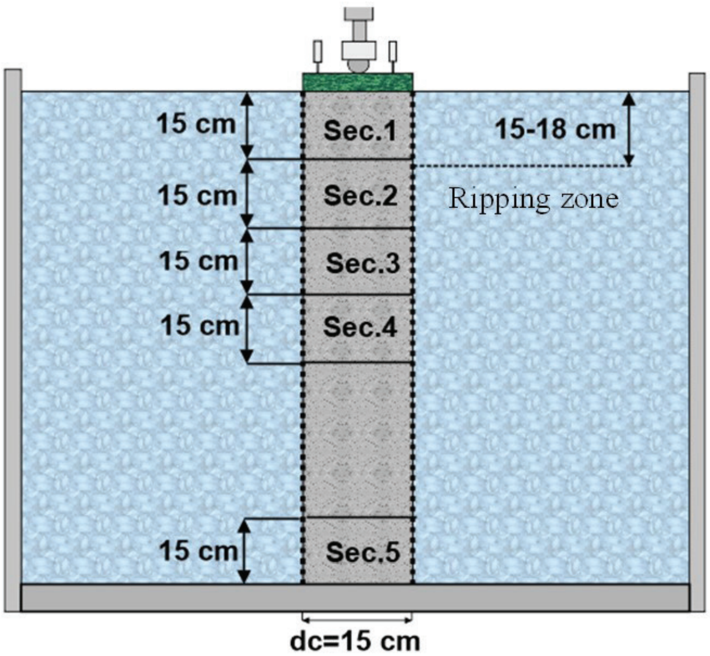

Figure 11. Column sections used to measure particle breakage.

Table 3. Particle breakage index for the encased gravel and CW column.

Geotextile	Column type	Section	Particle breakage index – B_g (%)	Average of B_g (%)
G-1	Gravel column	Sec.1	14.11	15.89
		Sec.2	17.67	
	RCDW column	Sec.1	17.18	20.94
		Sec.2	24.7	
G-2	Gravel column	Sec.1	6.82	7.04
		Sec.2	7.27	
	RCDW column	Sec.1	8.11	9.34
		Sec.2	10.58	
G-3	Gravel column	Sec.1	1.34	1.55
		Sec.2	1.77	
	RCDW column	Sec.1	2.65	3.3
		Sec.2	3.95	

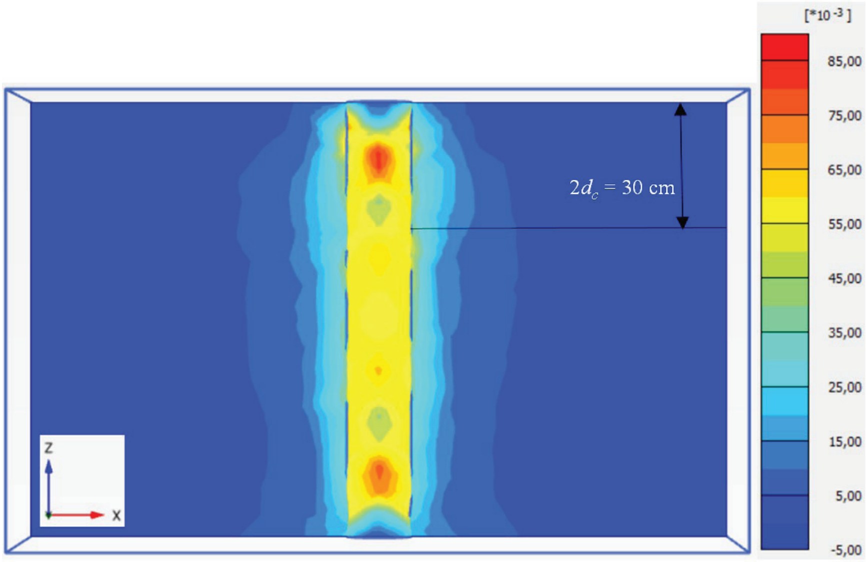

Figure 12. Shear strains along the column.

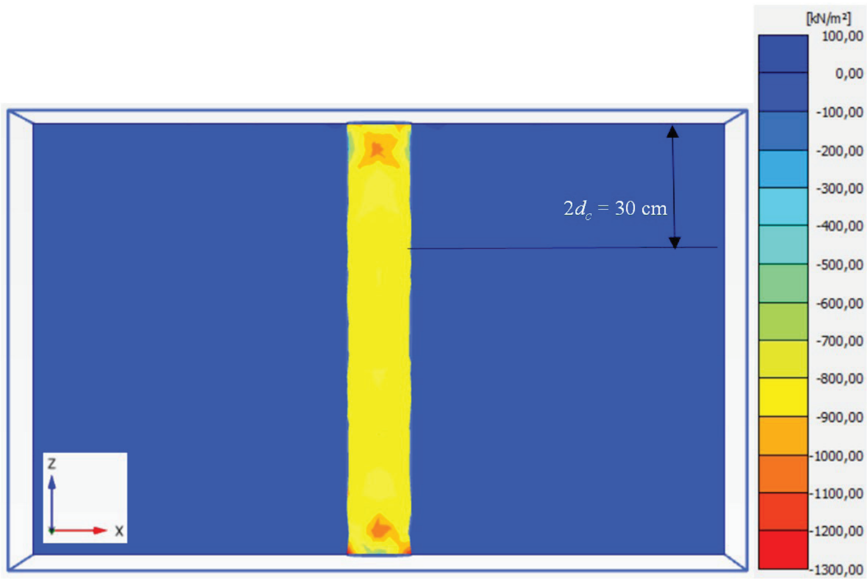

Figure 13. Total mean stress along the column.

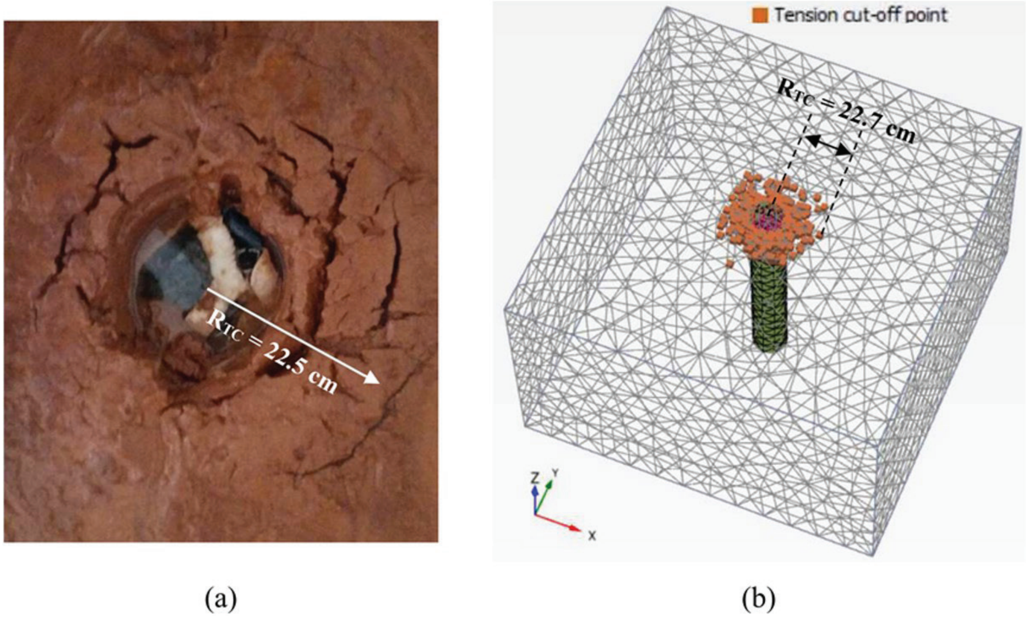

Figure 14. Tension cracks at the soil surface: (a) test result; (b) numerical result.

4. Conclusions

This study compared finite element predictions with results from large scale laboratory tests for a better understanding on the behavior of geosynthetic encased columns in soft soils. The main conclusions of the study are summarized below:

- The column infill type (sand, gravel, and RCDW) did not contribute significantly to the bearing capacity of the conventional (uncased) column. On the other hand, the bearing capacity of the encased column was influenced by the type of infill material, with greater value for the gravel column;
- The predicted load-settlement results for the conventional and encased sand and gravel columns compared satisfactorily with the experimental results, except for the case of RCDW infill, which can be a consequence of higher particle breakage of RCDW;
- The results obtained by the numerical analyses and laboratory tests showed the contribution of the granular column in the dissipation of the excess pore water pressures;
- The experimental results showed that the undrained strength of the soft soil (S_u) was increased up to a radial distance of 1.9 times the column diameter (d_c), after pore pressure dissipation. On the other hand, the numerical results predicted S_u increases even beyond $1.9d_c$;
- The soil heave displacement predicted by the numerical analyses compared well with that measured in the laboratory tests. Nevertheless, the radius of the region that underwent heave in the tests was twice that predicted by the numerical analysis;
- The numerical results accurately predicted the depths where the geotextile encasement failed. Furthermore, the results showed that the encasement experienced the highest tensile forces within regions with lengths equal to two times the column diameter at the column top and bottom.

Acknowledgments

The authors would like to thank the following institutions for their support in the research activities described in this paper: Brazilian National Council for Scientific and Technological Development (CNPq), CAPES-Brazilian Ministry of Education, University of Brasília and Federal University of Itajubá.

Declaration of interest

The authors have no conflicts of interest to declare. All co-authors have observed and affirmed the contents of the paper and there is no financial interest to report.

Authors' contributions

Nima Rostami Alkhorshid: conceptualization, Methodology, Data curation, Software, Writing – original draft. Gregório Luís Silva Araújo: funding acquisition, Supervision, Validation, Writing – review & editing. Ennio Marques Palmeira: supervision, Validation, Writing – review & editing.

List of symbols

γ_{sat} Saturated unit weight
E' Effective Young's modulus
ϕ' Effective friction angle
Ψ Dilatancy angle
c' Effective cohesion
ν' Effective Poisson's ratio
λ^* Modified compression index
κ^* Modified swelling index
K_0 Lateral earth pressure coefficient
K_x Hydraulic conductivity in x direction
K_y Hydraulic conductivity in y direction
K_z Hydraulic conductivity in z direction
R_{int} Interface coefficient

References

Alexiew, D., & Raithel, M. (2015). Geotextile-encased columns: case studies over twenty years. In B. Indraratna, J. Chu & C. Rujikiatkamjorn (Eds.), *Ground improvement case histories* (pp. 451-477). Kidlington: Elsevier. https://doi.org/10.1016/B978-0-08-100192-9.00017-X.

Ali, K., Shahu, J.T., & Sharma, K.G. (2012). Model tests on geosynthetic-reinforced stone columns: a comparative study. *Geosynthetics International*, 19(4), 292-305. http://dx.doi.org/10.1680/gein.12.00016.

Alkhorshid, N.R. (2012). *Numerical analysis of soft clay reinforced with stone columns* [MSc thesis, Eastern Mediterranean University]. Eastern Mediterranean University's repository. Retrieved in July 9, 2021, from http://hdl.handle.net/11129/1259

Alkhorshid, N.R. (2017). *Analysis of geosynthetic encased columns in very soft soil* [PhD thesis, University of Brasília]. University of Brasília's repository. Retrieved in July 9, 2021, from https://repositorio.unb.br/handle/10482/32033.

Alkhorshid, N.R., Araujo, G.L., & Palmeira, E.M. (2018). Behavior of geosynthetic-encased stone columns in soft clay: numerical and analytical evaluations. *Soils and Rocks*, 41(3), 333-343. http://dx.doi.org/10.28927/SR.413333.

Alkhorshid, N.R., Araujo, G.L., & Palmeira, E.M. (2019). Large-scale load capacity tests on a geosynthetic encased column. *Geotextiles and Geomembranes*, 47(5), 632-641. http://dx.doi.org/10.1016/j.geotexmem.2019.103458.

Alkhorshid, N.R., Araujo, G.L., & Palmeira, E.M. (2020). Large scale tests on geotextile encased stone columns. In *Proc. 4th Pan American Conference on Geosynthetics* (pp. 1-7). Rio de Janeiro: IGS.

Alkhorshid, N.R., Araujo, G.L., & Palmeira, E.M. (2021). Consolidation of soft clay foundation improved by geosynthetic-reinforced granular columns: numerical evaluation. *Journal of Rock Mechanics and Geotechnical Engineering*, 13(5), 1173-1181. http://dx.doi.org/10.1016/j.jrmge.2021.03.004.

Alkhorshid, N.R., Nalbantoglu, Z., & Araujo, G.L. (2014). 3D analysis of full scale stone column reinforced soft clay: numerical evaluation. In *Proc. XVII Congresso Brasileiro de Mecânica dos Solos* (pp. 1-6). Goiânia: ABMS.

Almeida, M.S., Hosseinpour, I., & Riccio, M. (2013). Performance of a geosynthetic-encased column (GEC) in soft ground: numerical and analytical studies. *Geosynthetics International*, 20(4), 252-262. http://dx.doi.org/10.1680/gein.13.00015.

Araujo, G.L., Palmeira, E.M., & Cunha, R.P. (2009). Behaviour of geosynthetic-encased granular columns in porous collapsible soil. *Geosynthetics International*, 16(6), 433-451. http://dx.doi.org/10.1680/gein.2009.16.6.433.

Castro, J., & Karstunen, M. (2010). Numerical simulations of stone column installation. *Canadian Geotechnical Journal*, 47(10), 1127-1138. http://dx.doi.org/10.1139/T10-019.

Castro, J., & Sagaseta, C. (2011). Deformation and consolidation around encased stone columns. *Geotextiles and Geomembranes*, 29(3), 268-276. http://dx.doi.org/10.1016/j.geotexmem.2010.12.001.

Castro, J., & Sagaseta, C. (2013). Influence of elastic strains during plastic deformation of encased stone columns. *Geotextiles and Geomembranes*, 37, 45-53. http://dx.doi.org/10.1016/j.geotexmem.2013.01.005.

Cengiz, C., & Guler, E. (2020). Load bearing and settlement characteristics of Geosynthetic Encased Columns under seismic loads. *Soil Dynamics and Earthquake Engineering*, 136, 106244. http://dx.doi.org/10.1016/j.soildyn.2020.106244.

Chen, J.F., Li, L.Y., Zhang, Z., Zhang, X., Xu, C., Rajesh, S., & Feng, S.Z. (2020). Centrifuge modeling of geosynthetic-encased stone column-supported embankment over soft clay. *Geotextiles and Geomembranes*, 49(1), 210-221. http://dx.doi.org/10.1016/j.geotexmem.2020.10.021.

De Mello, L.G., Mondolfo, M., Montez, F., Tsukahara, C.N., & Bilfinger, W. (2008). First use of geosynthetic encased sand columns in South America. In *Proc. 1st Pan-American Geosynthetics Conference* (pp. 1332-1341), Cancun, Mexico.

Gniel, J., & Bouazza, A. (2009). Improvement of soft soils using geogrid encased stone columns. *Geotextiles and Geomembranes*, 27(3), 167-175. http://dx.doi.org/10.1016/j.geotexmem.2008.11.001.

Keykhosropur, L., Soroush, A., & Imam, R. (2012). 3D numerical analyses of geosynthetic encased stone columns. *Geotextiles and Geomembranes*, 35, 61-68. http://dx.doi.org/10.1016/j.geotexmem.2012.07.005.

Khabbazian, M., Kaliakin, V.N., & Meehan, C.L. (2010). Numerical study of the effect of geosynthetic encasement on the behaviour of granular columns. *Geosynthetics International*, 17(3), 132-143. http://dx.doi.org/10.1680/gein.2010.17.3.132.

Li, L.Y., Rajesh, S., & Chen, J.F. (2020). Centrifuge model tests on the deformation behavior of geosynthetic-encased stone column supported embankment under undrained condition. *Geotextiles and Geomembranes*, http://dx.doi.org/10.1016/j.geotexmem.2020.11.003.

Marsal, R.J. (1967). Large scale testing of rockfill materials. *Journal of the Soil Mechanics and Foundations Division*, 93(2), 27-43. http://dx.doi.org/10.1061/JSFEAQ.0000958.

Mohapatra, S.R., Rajagopal, R., & Sharma, J. (2017). 3-Dimensional numerical modeling of geosynthetic-encased granular columns. *Geotextiles and Geomembranes*, 45(3), 131-141. http://dx.doi.org/10.1016/j.geotexmem.2017.01.004.

Nagula, S.S., Nguyen, D.M., & Grabe, J. (2018). Numerical modelling and validation of geosynthetic encased columns in soft soils with installation effect. *Geotextiles and Geomembranes*, 46(6), 790-800. http://dx.doi.org/10.1016/j.geotexmem.2018.07.011.

Pulko, B., & Logar, J. (2017). Fully coupled solution for the consolidation of poroelastic soil around geosynthetic encased stone columns. *Geotextiles and Geomembranes*, 45(6), 616-626. http://dx.doi.org/10.1016/j.geotexmem.2017.08.003.

Xue, J., Liu, Z., & Chen, J. (2019). Triaxial compressive behaviour of geotextile encased stone columns. *Computers and Geotechnics*, 108, 53-60. http://dx.doi.org/10.1016/j.compgeo.2018.12.010.

Yoo, C., & Lee, D. (2012). Performance of geogrid-encased stone columns in soft ground: full-scale load tests. *Geosynthetics International*, 19(6), 480-490. http://dx.doi.org/10.1680/gein.12.00033.

Zhang, L., Xu, Z., & Zhou, S. (2020). Vertical cyclic loading response of geosynthetic-encased stone column in soft clay. *Geotextiles and Geomembranes*, 48(6), 897-911. http://dx.doi.org/10.1016/j.geotexmem.2020.07.006.

Zhang, Y., Chan, D., & Wang, Y. (2012). Consolidation of composite foundation improved by geosynthetic-encased stone columns. *Geotextiles and Geomembranes*, 32, 10-17. http://dx.doi.org/10.1016/j.geotexmem.2011.10.006.

Soils and Rocks
An International Journal of Geotechnical and Geoenvironmental Engineering
www.soilsandrocks.com
ISSN 1980-9743
ISSN-e 2675-5475

A multiple model machine learning approach for soil classification from cone penetration test data

Lucas O. Carvalho[1] Dimas B. Ribeiro[1#]

Article

Keywords
Robertson
Charts
Tropical soil
Pore
Pressure
Budget constraints

Abstract

The most popular methods for soil classification from cone penetration test (CPT) data are based on examining two-dimensional charts. In the last years, several authors have dedicated efforts on replicating and discussing these methods using machine learning techniques. Nonetheless, most of them apply few techniques, include only one dataset and do not explore more than three input features. This work circumvents these issues by: (i) comparing five different machine learning techniques, which are also combined in an ensemble; (ii) using three distinct CPT datasets, one composed of 111 soundings from different countries, one composed of 38 soundings with information of soil age and the third composed of 64 soundings taken from the city of São Paulo, Brazil; and (iii) testing combinations of five input features. Results show that, in most cases, the ensemble of multiple models achieves better predictive performance than any technique isolated. Accuracies close to the maximum were obtained in some cases without the need of pore pressure information, which is costly to measure in geotechnical practice.

1. Introduction

The classical approach for soil classification from CPT data is based on examining two-dimensional charts, with pioneer studies pursuing to predict the soil granulometrical distribution from two raw CPT measurements (Begemann, 1965). Later work stated that predicting soil behavior would be more useful for real engineering projects than predicting soil granulometry (Douglas & Olsen, 1981). As a result, the well-known Robertson classification methods were proposed, using two charts obtained from three raw CPT measurements (Robertson et al.,1986; Robertson,1990). These charts became particularly popular due to the proposed input transformations, capable of better separating soil classes. Nonetheless, further investigations exposed limitations in those methods (Jefferies & Davies, 1991), associated with overconsolidated clays with dilative behavior. Although these methods evolved to minimize these problems (Robertson, 1991), other studies have shown that similar limitations remained (Ramsey, 2002; Schneider et al., 2008). To overcome these limitations two new charts were proposed (Schneider et al., 2008, 2012). In recent work, these charts were modified to create a full behavior-based classification method (Robertson, 2016).

Many recent works from the literature have also applied machine learning (ML) techniques to different geotechnical problems and most of them use artificial neural networks (ANN) to predict soil characteristics (Goh, 1995, 1996; Schaap et al., 1998; Juang & Chen, 1999; Kumar et al., 2000; Juang et al., 2002; Juang et al., 2003; Hanna et. al., 2007). On the other hand, Livingston et al. (2008) used decision trees (DT) models, Kohestani et al. (2015) employed random forests (RF), whilst Goh & Goh (2007) induced support vector machine (SVM) models. In addition, most studies dedicated to soil classification from CPT data seek for new soil classes using data clustering (Hegazy & Mayne, 2002; Facciorusso & Uzielli, 2004; Liao & Mayne, 2007; Das & Basudhar, 2009; Rogiers et al., 2017; Carvalho & Ribeiro, 2020). But another possible approach, which is relatively unexplored in the literature, is using ML techniques to replicate predefined soil classification systems, like classical soil classification methods based on charts (Arel, 2012). Most work adopting this approach use only ANN models (Kurup & Griffin, 2006; Arel, 2012; Reale et al., 2018) and, when more ML techniques are used, applications are restricted to small CPT datasets, with all soundings taken at the same location (Bhattacharya & Solomtine, 2006). Recent work has explored the additional potentialities of ML techniques to prospect and discuss alternative geotechnical aspects of soil classification, using the k-nearest neighbor ML technique (Carvalho & Ribeiro, 2019). Expanding this study with a larger

#Corresponding author. E-mail address: dimasbetioli@gmail.com
[1]Instituto Tecnológico de Aeronáutica, Divisão de Engenharia Civil, São José dos Campos, SP, Brasil.

Submitted on May 26, 2021; Final Acceptance on August 24, 2021; Discussion open until February 28, 2022.
https://doi.org/10.28927/SR.2021.072121

and more diverse dataset, comparing more ML techniques and investigating different combinations of input features are the main objectives of this work.

Herewith, several ML techniques are trained to classify soil from CPT data, aiming to replicate classification systems generated with a student version of the CPeT-IT v2.0.2.5 software. First, CPeT-IT is used to classify all examples from three datasets: one composed of 111 CPT soundings taken from different countries; one composed of 38 soundings including soil age information; and the third composed of 64 CPT soundings taken from the city of São Paulo, Brazil. The authors believe that using more diverse data samples is important to reveal general properties of the problem and to assess the competence of the ML models more properly. Next, the collected soil samples are used to train the following ML techniques: distance-weighted nearest neighbors (DWNN), boosted DT, RF, ANN, SVM and a multiple model predictor (MMP), which is a combination of the previous models, aka a heterogeneous ensemble of classification techniques. In addition, the combination of different input features is tested, including the original inputs required by CPeT-IT. This allows to investigate and discuss novel geotechnical aspects related to soil classification. As a result, this work has achieved the following original contributions:

- This is a first attempt to apply and compare multiple ML techniques of distinct biases (namely, DWNN, DT, RF, ANN, SVM) in a geotechnical application. In addition, their outputs are combined in an ensemble (MMP), resulting in higher predictive accuracies for soil classification;
- Discussing the utility and application of Robertson charts for classifying tropical soil, as their usage is more common in the analysis of soil data from temperate countries;
- Making possible to approximate Robertson soil classes without the need of pore pressure information, which is costly to measure in geotechnical practice. This is particularly important for the analysis of data from developing countries, which usually have severe budget constraints imposed on the engineering practice.

Although the results that sustain the last contribution, presented in Section 5.4, are not enough to dismiss measuring pore pressure in real engineering projects, they are important to motivate discussions concerning novel methods for soil classification that may be especially appealing for underdeveloped and developing countries.

2. Classification methods used in CPeT-IT

This section describes the two soil classification methods replicated in this work using ML techniques. For both cases, class 0 denotes a misclassified soil.

2.1. Method influenced by soil granulometry (ISG)

One of the chart-based classification methods replicated in this work was proposed by Robertson (1991), which is referred as ISG throughout this text. In this reference, the author intended to include soil behavior within the classification system, nonetheless the defined classes refer to granulometrical soil composition only. Furthermore, borehole samples were used to make soil classes compatible with real soil types. The ISG soil classes are:

- Sensitive, fine grained.
- Organic soils - peats.
- Clays - clay to silty clay.
- Silt mixtures - clayey silt to silty clay.
  - Sand mixtures - silty sand to sandy silt.
  - Sands - clean sand to silty sand.
  - Gravelly sand to sand.
  - Very stiff sand to clayey sand.
  - Very stiff, fine grained.

The four basic parameters measured in CPT are depth (z), uncorrected cone resistance (q_c), lateral friction (f_s) and pore pressure in a disturbed state (u_2), usually measured behind the cone tip. In the method proposed by Robertson (1991), these parameters are combined to obtain normalized versions.

First, q_c is corrected to discount the water pressure aiding cone penetration, resulting the total cone resistance q_t. Next, the equilibrium pore pressure u_0 is needed to calculate the excess pore pressure $u_2 - u_0$. The u_0 value can be obtained by drawing a straight line through the u_2 value in the graphic.

The effective σ'_{v0} and total $\sigma_{v0} = \sigma'_{v0} + u_0$ overburden stresses are then obtained, enabling to calculate the net cone resistance $q_n = q_t - \sigma_{v0}$. In order to eliminate correlations, Robertson (1990) proposed that q_n should be divided by σ'_{v0} to discount overburden and that f_s and $u_2 - u_0$ should be divided by q_n, resulting in the normalizations presented in Equations 1 to 3:

$$Q_{t1} = \frac{q_n}{\sigma'_{v0}} \tag{1}$$

$$F_r = \frac{f_s}{q_n} \tag{2}$$

$$B_q = \frac{u_2 - u_0}{q_n} \tag{3}$$

Later work (Robertson & Wride, 1998) found that the exponent n of σ'_{v0} in the Q_{t1} expression should be 1 only for pure sands, 0.5 only for pure clays and intermediary for mixtures of them. The result is presented in Equation 4:

$$Q_{tn} = \left(\frac{q_n}{pa}\right)\left(\frac{pa}{\sigma'_{v0}}\right)^n \tag{4}$$

where pa is a reference pressure of 0.1 MPa. The exponent n can be obtained with the Equation 5:

$$n = 0.381 I_c + 0.05\left(\frac{\sigma'_{v0}}{pa}\right) - 0.15 \tag{5}$$

The parameter I_c can be calculated as presented in Equation 6 (Robertson, 2009):

$$I_c = \left[\left(3.47 - log\, Q_{tn}\right)^2 + \left(log\, F_r + 1.22\right)^2\right]^{0.5} \tag{6}$$

Based on the previous equations, two charts are proposed by Robertson (1991) for soil classification. After obtaining raw CPT values and performing all procedures defined previously, a point can be placed in these charts, resulting in an attribution to each soil example. That is, the area to which the point belongs gives the class of the corresponding collected soil. If the obtained point is located outside the ranges defined within these charts, the soil is considered misclassified, receiving class 0.

2.2. Method focused on soil behavior (FSB)

The second soil classification method replicated in this work was proposed by Robertson (2016) and is referred as FSB throughout this text. It includes, as a new application, a method to identify if soil contains microstructure. In this method, considered fully behavioral in the literature, soil classes are divided into three main blocks: clay-like, sand-like and transitional. One advantage of this division is that the behavior of sands and clays is clearly separable. Sands usually present high strength, low compressibility and high permeability, while clays usually present low strength, high compressibility and low permeability. Each soil group is subdivided as pursuing dilative or contractive behavior, according to the consolidation state. A separate class was created for contractive clays that are sensitive to disturbance. The FSB classes are:

- CCS: Clay-like - Contractive – Sensitive.
- CC: Clay-like – Contractive.
- CD: Clay-like – Dilative.
- TC: Transitional – Contractive.
- TD: Transitional – Dilative.
- SC: Sand-like – Contractive.
- SD: Sand-like – Dilative.

One problem of the ISG method, described in the previous section, is that B_q has strong negative correlation with Q_{tn}, which makes highly overconsolidated clays indistinguishable from very dense sands (Schneider et al., 2008). To solve this problem, a new normalized excess pore pressure was proposed (Robertson, 2016) as:

$$U_2 = B_q Q_{t1} = \frac{u_2 - u_0}{\sigma'_{v0}} \tag{7}$$

The FSB method then employs two charts, one using F_r and Q_{tn} and the other using U_2 and Q_{tn}. The first is similar to the chart proposed in Schneider et al. (2008), while the second uses the hyperbolic curves presented in Schneider et al. (2012). New curves are also added to the $F_r \times Q_{tn}$ chart to separate dilative and contractive behaviors, as well as for separating the contractive sensitive behavior.

The values obtained for Q_{tn}, F_r and U_2 enable obtaining one point in each of the charts. If classes given in both charts do not agree, the soil is considered misclassified (class 0). In addition to that, a soil sample is attributed to class 0 if the point is located outside the ranges of Q_{tn}, F_r and U_2 of the charts and if a modified normalized small-strain rigidity index is greater than 330.

Robertson (2016) highlights that the FSB method is inaccurate for aged or cemented soils, which contain microstructure.

3. Machine learning (ML) techniques employed

In this work, six ML techniques of distinct biases are used to replicate the soil classification methods described in Section 2. In this Section, a brief theoretical description is given for DWNN, DT, RF, ANN and SVM. In the MMP model, all previous five ML models have their outputs combined in the classification of new samples by a majority voting strategy. Table 1 presents the main advantages and disadvantages experienced by the authors, applying these ML techniques to soil classification problems.

3.1. Distance-weighted nearest neighbors (DWNN)

The DWNN technique (Dudani, 1976) is a distance-based technique, meaning that it uses distances to evaluate if two objects x and y are similar. In this work, the Euclidean distance is used, which can be written as:

$$d\left(x, y\right) = \sqrt{\Sigma \left|x_i - y_i\right|^2} \tag{8}$$

In DWNN, all known examples (composing the training dataset) can be regarded as a cloud of points within the input space. A new point can be classified according to its proximity to the known examples. For instance, it can be classified into the same class of its nearest neighbor. Or a

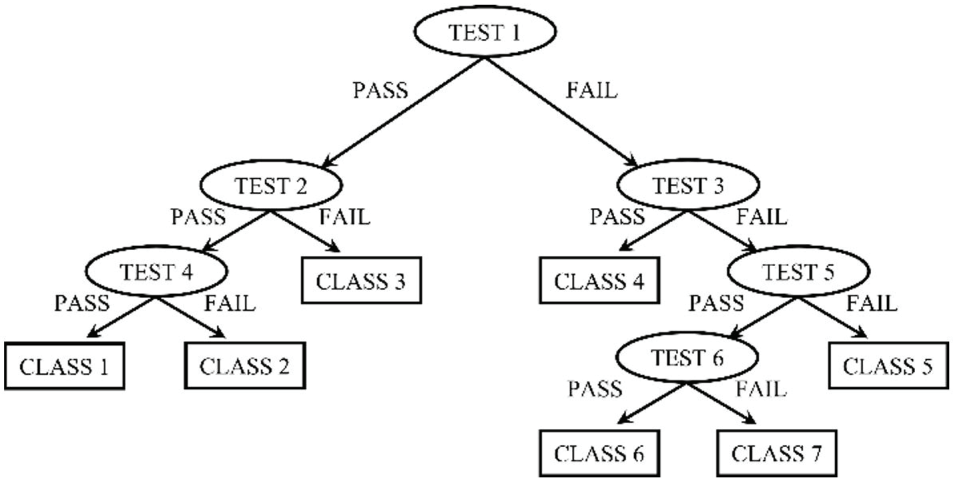

Figure 1. Example of DT.

Table 1. Advantages and disadvantages of each technique.

Technique	Advantages	Disadvantages
DWNN	Flexible and easy to program	Sensitive to outliers, not so accurate
DT	Can lead to an interpretable model	Tends to overfit to training data
RF	Accurate in most cases	The model becomes too complex to be interpreted
ANN	Can be replicated with simple spreadsheets	Not interpretable and difficult to calibrate
SVM	Leads to a globally optimal solution	Difficult to tune the hyper-parameter values
MMP	In general, more accurate than the isolated techniques	Can combine disadvantages of isolated techniques

majority voting of the classes of the *k* nearest neighbors can be employed instead. Weights can also be assigned to the votes of the nearest neighbors, proportional to the inverse of their distance to the new data point. This results in the DWNN technique. A Gaussian DWNN weighting is used in this work, which is given by:

$$w\left(d\left(x,y\right)\right)=\frac{1}{\sqrt{2\pi}}e^{-\frac{1}{2}d\left(x,y\right)^{2}} \tag{9}$$

where $d\left(x,y\right)$ is the Euclidean distance between two data items expressed in Equation 8. A recent work has shown that Gaussian weighting leads to better predictive performance in soil classification than attributing the same weights to all nearest neighbors (Carvalho & Ribeiro, 2019).

3.2. Decision trees (DT) and random forest (RF)

A DT can be defined as a graph with a tree structure, containing decision and leaf nodes (Quinlan, 1986). The decision nodes perform tests on the feature values of the data points, whilst leaf nodes output a class. Starting from the root node, the feature values of an example are used to decide to each branch of the tree the example will proceed until a leaf node is reached, giving the final classification of the object. Figure 1 illustrates a DT with six decision nodes (tests) and seven leaf nodes (classes).

The test performed by each decision node is usually chosen to maximize a goodness of split criterion, that is, the ability of distinguishing the classes. One problem of DTs is that they tend to overfit if they are induced to classify all training points correctly, meaning that the obtained solution can achieve good results only when applied to the same dataset that was used for its training. Overfitting can be avoided by DTs in multiple ways. One of them is pruning branches of the DT. Other strategy, employed in this work, is to join multiple trees trained using bootstrapping samples from the original dataset. From this point of this text, DT associated with the bootstrapping method is referred simply as DT. RF is another ensemble of tree-based models (Ho, 1995) which also randomly chooses subsets of input features from the original dataset in the bootstrapping procedure.

3.3. Artificial neural networks (ANN)

ANN are based on the brain structure and processing. Their fundamental units, the neurons, communicate to each other using weighted signals that usually belong to the [0,1] interval. The output of a neuron can be an input of another neuron, so that multiple layers of neurons can be combined. The neuron model presented in Figure 2 is called McCulloch

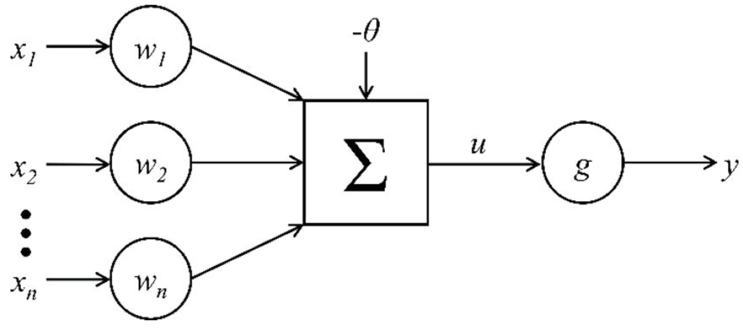

Figure 2. ANN neuron. Adapted from Carvalho et al. (2019).

& Pitts (MCP) model and is used in the perceptron ANN (McCulloch & Pitts, 1943).

The MCP neuron receives input signals x_i, which are multiplied by weights w_i and summed up. After an excitation threshold θ is discounted, a signal u is produced. This signal is input to an activation function g, generating an output signal y. In the original MCP model, the activation function is a stepwise or signal function. Alternative functions, including non-linear functions, can provide more representative power to the ANN models.

If many artificial neurons are combined in layers, the model is called multi-layer perceptron neural network (Rumelhart et al., 1986). In this work, ANN architectures using up to two hidden layers were tested. The output layer has one neuron representing each class. The neuron outputting the highest value defines the final classification.

One can demonstrate that a network with a single hidden layer of neurons with non-linear activation functions can reproduce any continuous function, and that a network with two hidden layers of such neurons can reproduce any function (Hornik et al., 1989). Considering that a limit must be imposed to select among infinite possible architectures, in this work networks with three or more hidden layers are not tested.

3.4. Support vector machines (SVM)

In its simplest version, the SVM technique divides the input space with a hyperplane and assigns one class to each side. The optimal hyperplane seeks to maximize the margin of separation between both classes, as illustrated in Figure 3.

The support vectors correspond to examples that are placed over the margin limits after the hyperplane is defined. In Figure 3, for example, four support vectors are represented, two white circles and two white squares. In this work a soft-margin version of SVM is used, being possible that points remain within the margins or even on the wrong side of the decision border.

One limitation of this version of SVM is that it admits only linear separations between the classes. One way

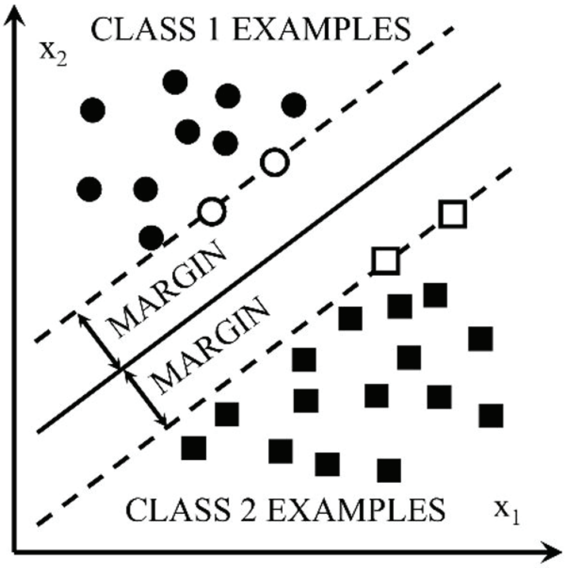

Figure 3. Hyperplane dividing the input space.

of extending the SVM to solve non-linear classification problems is by mapping the original input space into a higher dimension space, using a function called kernel. After preliminary tests, the polynomial kernel was chosen here due to its better predictive performance compared to other types of kernel functions. Considering x and y two points in input space, the polynomial kernel can be written as:

$$k(x, y) = \left(\delta(x \bullet y) + \kappa\right)^{\alpha} \tag{10}$$

where δ, κ and α are calibration parameters.

Although the described version of SVM is defined only for separating two classes, it is possible to extend it to multi-class problems by simply combining two or more binary classifiers. In this procedure, all classes must be evaluated in pairs, generating $(c\,2)$ classifiers for c classes.

4. Data analysis

The analysis performed in this paper use the following parameters from CPT soundings:

- : Dimensionless pore pressure normalization used by Robertson (1991).
- F_r: Dimensionless lateral friction normalization used by Robertson (2016).
- f_s: Lateral friction, measured in kPa.
- q_c: Uncorrected cone resistance, measured in MPa.
- q_t: Total cone resistance, calculated in MPa.
- Q_{t1}: Dimensionless cone resistance normalization used by Robertson (1990).
- Q_{tn}: Dimensionless cone resistance normalization used by Robertson (2016).
- SA: Soil age, represented by a dimensionless discrete number related to the geological epoch when the soil was deposited.
- u_2: Pore pressure in a disturbed state, measured in kPa.
- U_2: Dimensionless pore pressure normalization used by Robertson (2016).
- z : Depth measured from the surface in m.

4.1. Description of the used datasets

Professor P. K. Robertson provided the 38 soundings described in Table 2 and Professor P. W. Mayne provided the 73 soundings described in Table 3. The information given by these 111 soundings compose the dataset used in the main studies of this work; therefore, it is hereafter named Main dataset.

A second dataset, here named Geological dataset, is gathered to investigate the influence of soil age within soil classification. The motivation for its usage is the difficulty reported in the literature for classifying aged soil (Robertson, 2016). A variable called soil age (*SA*) is then proposed, which is represented by a number related to the geological age when the soil was deposited. The Geological dataset, which is described in Table 4, uses information only from the 38 soundings provided by Robertson because no information about soil age was available for the other soundings.

The third dataset used in this work is composed of 64 CPT soundings from the metropolitan area of São Paulo, Brazil, being here named Tropical dataset. Measurements were taken at each 2 cm of depth and included more than forty thousand soil examples. These soundings were provided by the São Paulo Metropolitan Company under a confidentiality term, so most information about it cannot be exposed here.

Robertson charts were produced using samples taken from temperate regions, which can lead to uncertainty when applied to tropical soil. To discuss this issue, in section 5.2 the Tropical dataset is used to test if the performance of the ML techniques remains accurate. The study is divided in two parts, in the first the Main dataset is used for training the ML techniques and the Tropical dataset is used for testing. The objective of this first part is discussing if Brazilian soil can be accurately classified using soil information from other countries. In the second part, the Tropical dataset is used for both training and testing, aiming to observe if accuracy raises when compared to the first part. Figure 4 presents data of one of the CPT soundings to illustrate the used data.

Table 2. Dataset from P. K. Robertson. Adapted from Carvalho & Ribeiro (2019).

Soil type	Location	Soundings
Mixed Soils	Canada	3
	Italy	1
	USA	6
	Switzerland	1
Soft Clay	UK	1
	Australia	1
	Norway	1
	USA	3
	Canada	2
	Sweden	2
	North Sea	1
	Very soft offshore	1
Soft Rock	USA	4
Stiff Clay	UK	3
	USA	4
	Italy	1
	France	1
	Ireland	1
	Alaska (USA)	1
Total		38

Table 3. Dataset from P. W. Mayne. Adapted from Carvalho & Ribeiro (2019).

Location in USA	Soundings
Gosnell, Arkansas	1
Lenox, Tennessee	1
Memphis, Tennessee	16
Dexter, Missouri	6
Mooring, Tennessee	6
Marked Tree, Arkansas	19
Collierville, Tennessee	1
Meramec, Missouri	4
Opelika, Alabama	4
Wilson, Arkansas	4
Wolf, Wyoming	7
Wyatt, Missouri	4
Total	73

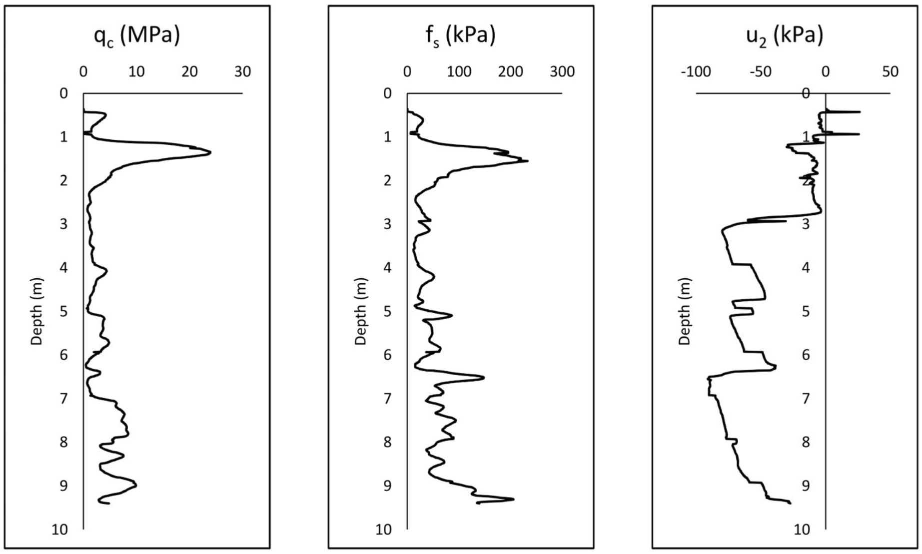

Figure 4. Illustration of the data recovered from one of the CPT soundings.

Table 4. Geological dataset. Adapted from Carvalho & Ribeiro (2019).

Soil type	Identification	Geological age	SA
Mixed Soils	UBC, Canada	Holocene	2
	Venetian Lagoon, Italy	Holocene	2
	Ford Center, USA	Pleistocene	4
	San Francisco, USA	Late Pleistocene	3
	Tailings, USA	Recent	1
	UBC KIDD, Canada	Holocene	2
	UBC KIDD, Canada (2)	Holocene	2
Soft Clay	Bothkennar, RU	Holocene	2
	Burswood, Perth, Australia	Holocene	2
	Onsoy, Norway	Holocene	2
	Amherst, USA	Late Pleistocene	3
	San Francisco Bay, USA	Holocene	2
	San Francisco Bay, USA (2)	Holocene	2
Soft Rock	Newport Beach, USA	Miocene	5
	LA Downtown, USA	Miocene	5
	Newport Beach, USA (2)	Miocene	5
Stiff Clay	Madingley, UK	Cretaceous	6
	Houston, USA	Pleistocene	4

4.2. Data preprocessing

As data-driven techniques, ensuring data quality is important when ML techniques are concerned. The identification and treatment of outliers, which are inputs with discrepant values, is one of the important steps for a proper data cleansing. One way of automatically detecting potential outliers is by the use of boxplots. Nonetheless, preliminary tests have shown that removing all potential outliers severely reduces accuracy. In this work, this problem is avoided by applying the Edit Nearest Neighbor technique (Wilson, 1972). It compares the classes of the potential outlier and its nearest neighbors, removing it only if their labels do not match.

Another problem is an imbalance within classes, which can bias the ML techniques towards the majority class in detriment of classes with less examples. An evaluation based on histograms allowed identifying some issues, solved as listed next:

1) There were too few ISG class 0 examples, therefore they were completely removed from the datasets. FSB class 0 examples were maintained;
2) ISG classes were very imbalanced within the Geological dataset, therefore all analysis with this dataset were restricted to the FSB method;
3) Random sampling was applied to reduce majority classes, considering that CPT data contains several redundancies due to many measurements taken within each soil layer;
4) Minority classes were incremented applying the SMOTE oversampling technique (Chawla et al., 2002).

After procedures 3 and 4, all classes have the same number of examples. A second data transformation is applied for the ANN, SVM and MMP analyses, imposing a logarithmic scale to each input feature. This procedure was adopted because the original charts from Robertson use logarithmic scale and preliminary tests showed that better performance is achieved with this transformation. Figure 5 shows an example of the logarithmic scale effect.

4.3. General methodology

The 10-fold cross-validation procedure is applied for each dataset and input combination. In this process, the original dataset is divided into 10 partitions called folds, in which the class proportion is kept the same as in the original dataset. Among these 10 folds, one is used for testing, one is used for validation and the remaining compose the training set. The training set is the only one subject to all preprocessing procedures and is used as a reference for all predictions. The validation fold is used to calibrate the parameters of each technique and the testing fold is used to measure predictive performance for new data points previously unseen by the ML techniques. At each step of the 10-step procedure a different testing fold is selected, and the final predictive performance is given by the average and standard deviation of the ten values obtained.

The most common performance metric adopted in multi-class problems is accuracy, which is given by the total number of correct predictions divided by the total number of objects. Nevertheless, majority classes can bias this measurement once the testing and validation folds are not balanced. To solve this problem, the predictive performance measure used in this work is obtained by calculating accuracy for each class separately and then calculating their mean value. This value would be the accuracy if the classes were balanced and had the same number of objects. For simplicity, this performance measure is called accuracy here, although it is commonly referred as balanced accuracy in the ML literature.

The calibration process performed for each technique is described in Section 3.

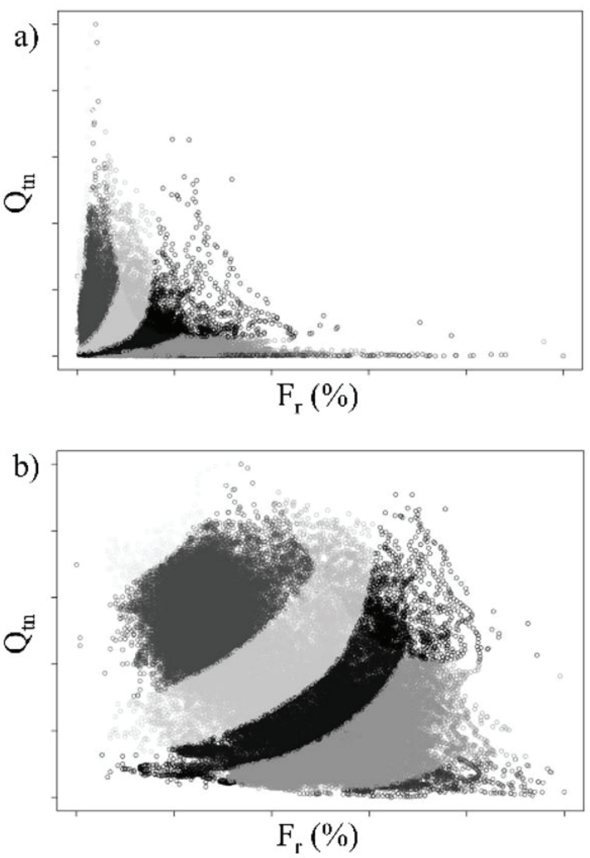

Figure 5. Example of logarithmic scale effect: (a) without logarithmic scale; (b) with logarithmic scale.

4.4. Comments about the inputs

Many variables mentioned in previous sections can be used as inputs for the ML techniques. Specific combinations are selected here considering previous work from the authors (Carvalho & Ribeiro, 2019; Carvalho et al., 2019) and the objectives of the present study. These combinations are:

1) z, q_t, f_s and u_2: Raw CPT measurements, except for the correction of the cone tip resistance from q_c to q_t;
2) z, Q_{t1}, F_r and B_q: Depth plus normalizations proposed by Robertson (1990);
3) z, Q_{tn}, F_r and U_2: Depth plus normalizations proposed by Robertson (2016);
4) Q_{tn}, F_r: Inputs used by the ISG method;
5) Q_{tn}, F_r and U_2: Inputs used by the FSB method;
6) z, Q_{t1}, F_r, B_q and SA: Depth plus normalizations proposed by Robertson (1990) plus soil age;
7) z, Q_{tn}, F_r, U_2 and SA: Depth plus normalizations proposed by Robertson (2016) plus soil age;
8) z, q_c and f_s: Raw CPT measurements, excluding u_2 and not correcting q_c to q_t.

The use of combination 1 has the objective of evaluating how accurately ISG and FSB can be replicated without using the normalizations proposed by Robertson. Combinations 2 and 3 aim to test predictive performance when such normalizations are combined to depth. The original input combinations 4 and 5 are used as a reference, while combinations 6 and 7 aim to evaluate if soil age improves predictive performance. The last combination 8 refers to CPT equipment which cannot measure pore pressure, making impossible to correct q_c to q_t.

5. Results and discussion

5.1. General performance for replicating ISG and FSB

Results in this section refer to the general performance of the ML techniques when applied to the Main and Geological datasets. These results are summarized in Table 5, where each

Table 5. MA results obtained with all techniques (%).

Input	Output	DWNN	DT	RF	ANN	SVM	MMP
$z\ q_t f_s u_2$	ISG	90.23	91.71	91.53	91.57	92.63	93.17
$z\ Q_{t1}\ F_r\ B_q$		89.40	95.81	96.09	93.59	96.47	96.64
$z\ Q_{tn}\ F_r\ U_2$		93.13	97.60	97.44	96.56	97.97	98.25
$Q_{tn}\ F_r$		96.58	96.97	97.31	96.48	98.03	97.95
$z\ q_t f_s u_2$	FSB	90.28	91.32	91.43	85.88	87.57	91.82
$z\ Q_{t1}\ F_r\ B_q$		88.82	96.40	96.38	84.39	91.24	96.15
$z\ Q_{tn}\ F_r\ U_2$		93.77	97.31	97.27	86.18	92.77	97.08
$Q_{tn}\ F_r\ U_2$		93.06	94.69	94.63	82.85	89.24	94.66
$z\ q_t f_s u_2\ SA$		91.03	91.66	91.78	87.79	89.75	93.23
$z\ Q_{tn}\ F_r\ U_2\ SA$		94.73	97.01	97.31	89.96	94.44	97.42

line represents a 10-fold cross validation test (see Section 4.3). The first column presents the used inputs, and the second column represents the replicated method, ISG (Section 2.1) or FSB (Section 2.2). Considering that 10 tests (one for each fold) are made for each line, resulting in 10 separated accuracy measurements, other columns represent their mean value (MA stands for mean accuracy) for each technique. One can calculate MA from the individual accuracies Ac_i using the expression:

$$MA = \frac{\sum_{i=1}^{10} Ac_i}{10} \tag{11}$$

One can observe that MA is above 91% in all lines for MMP, which can be considered a good predictive performance for soil profiling. In most cases MMP presents best performance, in others it presents a performance close to the best one. Results obtained with z, q_t, f_s and u_2 show that accurate soil classification is possible without the data transformations proposed by Robertson. As expected, high accuracies are obtained when the original inputs are used for each method, Q_{tn} and F_r for ISG and Q_{tn}, F_r and U_2 for FSB. Nonetheless, the highest accuracy for ISG was obtained when z, Q_{tn}, F_r and U_2 were used as inputs for MMP and the highest accuracy for FSB was achieved when z, Q_{tn}, F_r, U_2 and SA were used for MMP. This suggests that including depth as an input brings relevant information to soil classification.

Table 6. Results obtained with MMP without the FSB class 0 (%).

Input	Output	MA	SD
$z\ q_t f_s u_2$	FSB	92.62	0.39
$z\ Q_{t1}\ F_r\ B_q$		98.55	0.18
$z\ Q_{tn}\ F_r\ U_2$		99.41	0.15
$Q_{tn}\ F_r\ U_2$		99.60	0.12
$z\ q_t f_s u_2\ SA$		92.37	1.19
$z\ Q_{tn}\ F_r\ U_2\ SA$		98.35	0.63

Reasonable accuracy was obtained for ANN and SVM only after applying logarithmic scale, as presented in Figure 5.

Preliminary tests have shown that objects assigned to class 0 in FSB prejudice the predictive performance of ANN and SVM. In order to quantify this influence, additional experiments were performed removing these objects from the training and test sets, resulting the values presented in Table 6. SD stands for standard deviation and, for a sake of conciseness, only results for MMP are presented. As the proposal is to focus on the FSB method, results from the ISG method are omitted. One can observe that a higher MA is achieved for most of the cases, including values close to

100%. This suggests that objects assigned to the class 0 of the FSB method do not form a homogeneous region within input space, making the classification problem harder.

In order to complement the application of ML techniques for soil profiling, the MMP was employed to determine the soil profile according to the ISG method for a sounding taken in Vancouver, Canada and provided by Professor Renato da Cunha (Cunha, 1994). The Main dataset was used for training. Comparing the result obtained with CPeT-IT v2.0.2.5 to the one obtained with the MMP they are almost the same, with an accuracy of 95.4%.

5.2. Study with the Tropical dataset

Once the DWNN technique did not present good performance its results are omitted, as well as some input combinations tested in Section 5.2, to avoid redundancy.

Results from the first part of the study are shown in Table 7. One can observe that, even though the multiple model is not the best performing technique for all testing combinations, its performance is in general close to the best one. This shows that MMP is stable, while larger variations can be observed for the other techniques. Comparing Table 7 to Table 5, one can observe that accuracy drops in all cases.

Results from the second part of the study are presented in Table 8. The general behavior of the MMP is maintained, presenting stability and good performance when compared to other techniques. In some cases, accuracies close to 100% were obtained, showing that the information of the Tropical dataset is substantially different from the information of the Main dataset. This suggests that it is justifiable to develop new soil classification methods specific for tropical soil.

5.3. Soil classification without measuring the pore pressure

Once not all CPT equipment available in the market measure the pore pressure u_2, one could question if this variable

Table 7. MA results for the first part (%).

Input	Output	DT	RF	ANN	SVM	MMP
$z\ q_t f_s u_2$	ISG	68.70	62.92	74.68	77.20	71.29
$z\ Q_{t1} F_r B_q$		88.03	88.27	85.55	85.84	87.94
$z\ Q_{tn} F_r U_2$		89.94	89.80	92.98	89.86	91.50
$z\ q_t f_s u_2$	FSB	79.50	79.49	82.82	82.68	82.01
$z\ Q_{t1} F_r B_q$		92.98	92.76	88.68	92.86	92.99
$z\ Q_{tn} F_r U_2$		95.87	95.78	92.41	95.78	95.87

Table 8. MA results for the second part (%).

Input	Output	DT	RF	ANN	SVM	MMP
$z\ q_t f_s u_2$	ISG	86.82	87.94	84.64	85.36	89.42
$z\ Q_{t1} F_r B_q$		95.00	95.17	76.83	92.97	95.34
$z\ Q_{tn} F_r U_2$		97.02	96.78	84.88	96.08	96.66
$z\ q_t f_s u_2$	FSB	89.42	89.71	80.57	84.52	90.67
$z\ Q_{t1} F_r B_q$		96.86	96.85	27.61	69.89	90.47
$z\ Q_{tn} F_r U_2$		98.67	98.60	40.43	86.24	96.70

Table 9. Results using z , q_c and f_s as inputs (%).

Technique	ISG		FSB		FSB (no 0)	
	MA	SD	MA	SD	MA	SD
DWNN	90.30	0.65	86.79	0.47	88.12	0.72
DT	90.13	0.56	87.35	0.45	88.99	0.40
RF	90.31	0.60	87.84	0.35	89.37	0.32
ANN	90.18	0.85	82.86	0.64	85.82	1.08
SVM	91.04	0.70	82.44	0.48	85.58	0.82
MMP	91.83	0.56	87.58	0.32	89.15	0.30

is really needed for soil classification. Consulting Section 2 one quickly concludes that, without u_2, classifying soil within the original ISG and FSB methods is not possible. Pore pressure u_2 plays a fundamental role throughout the methodology proposed, not only for correcting cone resistance but also for calculating stresses and obtaining the final normalizations. Therefore, since the approach presented here simply replicates those charts, one should not conclude from this study that measuring u_2 could be neglected for soil classification in real engineering projects. Nonetheless, the aim here is to start a discussion in this direction, possibly leading to further studies with conclusions that are more consistent.

In this context, additional experiments were performed to verify if the friction penetrometer without the pore pressure filter could provide enough information for obtaining a rough approximation of the soil classes. Therefore, all techniques plus the MMP were tested with the Main dataset using only z, q_c and f_s as inputs, resulting the values presented in Table 9. This study was replicated for the ISG method, for the FSB method with class 0 objects and for the FSB method without class 0 objects.

One can notice that all techniques achieved accuracy higher than 90% for the ISG method, which can be considered reasonable for soil profiling. Although lower accuracies were obtained for the FSB method, the accuracy values can also be considered practicable, especially when objects assigned to the class 0 are removed. These results show that, for this specific dataset, soil can be classified within reasonable accuracy with CPT data that do not include pore pressure filter measurements.

6. Conclusions and recommendations

A general methodology for the application of ML techniques for soil classification from CPT data is presented in this paper, including six ML techniques of distinct biases: DWNN, DT, RF, ANN, SVM and MMP, which is a combination of the previous techniques. MMP joins the predictions of the multiple individual models by majority voting, producing a heterogeneous ensemble of classifiers. All techniques are applied initially to a dataset composed of 111 CPT soundings, testing different input combinations within a 10-fold cross-validation procedure. Training data is also subject to a preprocessing procedure within each 10-fold cross-validation step for improving data quality, including data transformation, cleaning and balancing. Tests are also performed with two other datasets, one containing soil age information and the other with tropical soil information. The original CPT measurements included within the analysis are depth z, cone resistance q_c and corrected cone resistance q_t, lateral friction f_s and pore pressure u_2. Included normalizations are the cone resistances Q_{t1} and Q_{tn}, the lateral friction F_r and the pore pressures B_q and U_2. A soil age SA parameter was also included, representing the geological age when the soil was deposited.

The machine learning techniques were successfully compared and combined in an ensemble that produces more accurate results that any isolated technique. MMP can be also considered the most stable technique, with accuracies above 93% in most cases. The predictive results in the classification of soil samples from tropical areas are in general inferior to those recorded for soil from temperate areas, especially when the models built from temperate areas are employed in the classification of soil from tropical areas. This indicates the need to develop classification methods specific for tropical soil, which the authors suggest as future work. Another important observation is that accuracy remains reasonable for all techniques even if pore pressure information is omitted during training. These results can encourage future work pursuing soil classification methods that do not use pore pressure information, which can be costly to measure and requires specialized equipment. The results do not allow concluding that pore pressure measurements can be dismissed in real engineering projects, but that soil classes can be roughly approximated without this information. This can become an alternative for initial geotechnical studies in underdeveloped and developing countries, where budget constrains limit engineering practice.

It is important to notice that none of these discussions would be possible by using the original Robertson charts alone, once these methods do not allow changing inputs or using incomplete data.

Acknowledgements

To Peter K. Robertson, Paul W. Mayne, Renato da Cunha and São Paulo Metropolitan Company for making available the CPT soundings used in this work. This research received no external funding.

Declaration of interest

The authors declare no conflict of interest.

Authors' contributions

Lucas Orbolato Carvalho: formal analysis, methodology, writing – original draft, validation. Dimas Betioli Ribeiro: investigation, project administration, supervision, writing – review & editing.

List of symbols

ANN	Artificial neural networks.
CPT	Cone penetration test.
DT	Decision trees.
DWNN	Distance-weighted nearest neighbors.
FSB	Focused on soil behavior.
ISG	Influenced by soil granulometry.
MA	Mean accuracy.
ML	Machine learning.
MMP	Multiple model predictor.
MCP	McCulloch & Pitts model.
RF	Random forests.
SA	Soil age.
SD	Standard deviation.
SMOTE	Synthetic minority over-sampling technique.
SPT	Standard penetration test.
SVM	Support vector machines.
z	Depth.
q_c	Uncorrected cone resistance.
f_s	Lateral friction.
u_2	Pore pressure in a disturbed state.
q_t	Total cone resistance.
u_0	Equilibrium pore pressure.
σ'_{v0}	Effective overburden stress.
σ_{v0}	Total overburden stress.
q_n	Net cone resistance.
Q_{t1}, F_r, B_q	Normalizations proposed by Robertson (1990).
Q_{tn}, U_2	Normalizations used by Robertson (2016).
n	Exponent used to calculate Q_{tn}.
pa	Reference pressure of 0.1 MPa.
I_c	Parameter used to calculate n.
x, y	Objects at the input space.
d	Distance between two points.
w	Gaussian weighting.
w_i, θ, u, g, y	Parameters used in the perceptron neuron.
δ, κ,	Calibration parameters of the polynomial kernel.
c	Number of classes.
SA	Soil age.

References

Arel, E. (2012). Predicting the spatial distribution of soil profile in Adapazari/Turkey by artificial neural networks using CPT data. *Computers & Geosciences*, 43, 90-100. http://dx.doi.org/10.1016/j.cageo.2012.01.021.

Begemann, H.K.S.P. (1965). The friction jacket cone as an aid in determining the soil profile. In *Proceedings of the 6th International Conference on Soil Mechanics and Foundation Engineering* (pp. 17-20).

Bhattacharya, B., & Solomtine, D.P. (2006). Machine learning in soil classification. *Neural Networks*, 19(2), 186-195. http://dx.doi.org/10.1016/j.neunet.2006.01.005.

Carvalho, L.O., & Ribeiro, D.B. (2019). Soil classification system from cone penetration test data applying distance-based machine learning algorithms. *Soils and Rocks*, 42(2), 167-178. http://dx.doi.org/10.28927/SR.422167.

Carvalho, L.O., & Ribeiro, D.B. (2020). Application of kernel k-means and kernel x-means clustering to obtain soil classes from cone penetration test data. *Soils and Rocks*, 43(4), 607-618. http://dx.doi.org/10.28927/SR.434607.

Carvalho, L.O., Ribeiro, D.B., & Monteiro, F.A.C. (2019). Comparing artificial neural networks with support vector machines for soil classification. In *Proceedings of the XL Ibero-latin american congress on computational methods in engineering* (pp. 11-14). Natal/RN, Brazil.

Chawla, N.V., Bowyer, K.W., Hall, L.O., & Kegelmeyer, W.P. (2002). SMOTE: synthetic minority over-sampling technique. *Journal of Artificial Intelligence Research*, 16, 321-357. http://dx.doi.org/10.1613/jair.953.

Cunha, R.P. (1994). *Interpretation of selfboring pressuremeter tests in sand* [Doctoral thesis, University of British Columbia]. University of British Columbia's repository. http://dx.doi.org/10.14288/1.0050418.

Das, S.K., & Basudhar, P.K. (2009). Utilization of self-organizing map and fuzzy clustering for site characterization using piezocone data. *Computers and Geotechnics*, 36(1-2), 241-248. http://dx.doi.org/10.1016/j.compgeo.2008.02.005.

Douglas, B.J., & Olsen, R.S. (1981). Soil classification using electric cone penetrometer. In *Proceedings of the Symposium on Cone Penetration Testing and Experience* (pp. 209-227). Reston: ASCE.

Dudani, S.A. (1976). The distance-weighted k-nearest-neighbor rule. *IEEE Transactions on Systems, Man, and Cybernetics*, SMC-6(4), 325-327. http://dx.doi.org/10.1109/TSMC.1976.5408784.

Facciorusso, J., & Uzielli, M. (2004). Stratigraphic profiling by cluster analysis and fuzzy soil classification from mechanical cone penetration tests. In *Proceedings of the ISC-2 on Geotechnical and Geophysical Site Characterization* (pp. 905-912). Porto.

Goh, A.T., & Goh, S. (2007). Support vector machines: their use in geotechnical engineering as illustrated using seismic liquefaction data. *Computers and Geotechnics*, 34(5), 410-421. http://dx.doi.org/10.1016/j.compgeo.2007.06.001.

Goh, A.T.C. (1995). Modeling soil correlations using neural networks. *Journal of Computing in Civil Engineering*, 9(4), 275-278. http://dx.doi.org/10.1061/(ASCE)0887-3801(1995)9:4(275).

Goh, A.T.C. (1996). Neural-network modeling of CPT seismic liquefaction data. *Journal of Geotechnical Engineering*, 122(1), 70-73. http://dx.doi.org/10.1061/(ASCE)0733-9410(1996)122:1(70).

Hanna, A.M., Ural, D., & Saygili, G. (2007). Neural network model for liquefaction potential in soil deposits using Turkey and Taiwan earthquake data. *Soil Dynamics and Earthquake Engineering*, 27(6), 521-540. http://dx.doi.org/10.1016/j.soildyn.2006.11.001.

Hegazy, Y.A., & Mayne, P.W. (2002). Objective site characterization using clustering of piezocone data. *Journal of Geotechnical and Geoenvironmental Engineering*, 128(12), 986-996. http://dx.doi.org/10.1061/(ASCE)1090-0241(2002)128:12(986).

Ho, T.K. (1995). Random decision forests. In *Proceedings of the 3rd International Conference on Document Analysis and Recognition* (pp. 278-282). USA: IEEE. http://dx.doi.org/10.1109/ICDAR.1995.598929.

Hornik, K., Stinchombe, M., & White, H. (1989). Multilayer feedforward networks are universal approximators. *Neural Networks*, 2(5), 359-366. http://dx.doi.org/10.1016/0893-6080(89)90020-8.

Jefferies, M.G., & Davies, M.P. (1991). Soil classification by the cone penetration test. *Canadian Geotechnical Journal*, 28(1), 173-176. http://dx.doi.org/10.1139/t91-023.

Juang, C.H., & Chen, C.J. (1999). CPT-Based liquefaction evaluation using neural networks. *Computer-Aided Civil and Infrastructure Engineering*, 14(3), 221-229. http://dx.doi.org/10.1111/0885-9507.00143.

Juang, C.H., Lu, P.C., & Chen, C.J. (2002). Predicting geotechnical parameters of sands from CPT measurements using neural networks. *Computer-Aided Civil and Infrastructure Engineering*, 17(1), 31-42. http://dx.doi.org/10.1111/1467-8667.00250.

Juang, C.H., Yuan, H., Lee, D.H., & Lin, P.S. (2003). Simplified cone penetration test-based method for evaluating liquefaction resistance of soils. *Journal of Geotechnical and Geoenvironmental Engineering*, 129(1), 66-80. http://dx.doi.org/10.1061/(ASCE)1090-0241(2003)129:1(66).

Kohestani, V.R., Hassanlourad, M., & Ardakani, A. (2015). Evaluation of liquefaction potential based on CPT data using random forest. *Natural Hazards*, 79, 1079-1089. http://dx.doi.org/10.1007/s11069-015-1893-5.

Kumar, J.K., Konno, M., & Yasuda, N. (2000). Subsurface soil-geology interpolation using fuzzy neural network. *Journal of Geotechnical and Geoenvironmental Engineering*, 126(7), 632-639. http://dx.doi.org/10.1061/(ASCE)1090-0241(2000)126:7(632).

Kurup, P.U., & Griffin, E.P. (2006). Prediction of soil composition from CPT data using general regression neural network. *Journal of Computing in Civil Engineering*, 20(4), 281-289. http://dx.doi.org/10.1061/(ASCE)0887-3801(2006)20:4(281).

Liao, T., & Mayne, P.W. (2007). Stratigraphic delineation by three-dimensional clustering of piezocone data. *Georisk*, 1(2), 102-119. http://dx.doi.org/10.1080/17499510701345175.

Livingston, G., Piantedosi, M., Kurup, P., & Sitharam, T.G. (2008). Using decision-tree learning to assess liquefaction potential from CPT and V_s. *Geotechnical Earthquake Engineering and Soil Dynamics IV Congress*, 2008, 1-10. http://dx.doi.org/10.1061/40975(318)76.

McCulloch, W., & Pitts, W. (1943). A Logical calculus of ideas immanent in nervous activity. *The Bulletin of Mathematical Biophysics*, 5, 115-133. http://dx.doi.org/10.1007/BF02478259.

Quinlan, J.R. (1986). Induction of decision trees. *Machine Learning*, 1, 81-106. http://dx.doi.org/10.1007/BF00116251.

Ramsey, N. (2002). A calibrated model for the interpretation of cone penetration tests (CPTs) in north sea quaternary soils. In *Proceedings of the Offshore site investigation and geotechnics 'Diversity and Sustainability' conference* (pp. 341-356). London. SUT.

Reale, C., Gavin, K., Libric, L., & Juric-Kacunic, D. (2018). Automatic classification of fine-grained soils using CPT measurements and Artificial Neural Networks. *Advanced Engineering Informatics*, 36, 207-215. http://dx.doi.org/10.1016/j.aei.2018.04.003.

Robertson, P.K. (1990). Soil classification using the cone penetration test. *Canadian Geotechnical Journal*, 27(1), 151-158. http://dx.doi.org/10.1139/t90-014.

Robertson, P.K. (1991). Soil classification using the cone penetration test. *Canadian Geotechnical Journal*, 28(1), 176-178. http://dx.doi.org/10.1139/t91-024.

Robertson, P.K. (2009). Interpretation of cone penetration tests – a unified approach. *Canadian Geotechnical*

Journal, 46(11), 1337-1355. http://dx.doi.org/10.1139/T09-065.

Robertson, P.K. (2016). Cone penetration test (CPT)-based soil behaviour type (SBT) classification system – an update. *Canadian Geotechnical Journal*, 53(12), 1910-1927. http://dx.doi.org/10.1139/cgj-2016-0044.

Robertson, P.K., & Wride, C.E. (1998). Evaluating cyclic liquefaction potential using the cone penetration test. *Canadian Geotechnical Journal*, 35(3), 442-459. http://dx.doi.org/10.1139/t98-017.

Robertson, P.K., Campanella, R.G., Gillespie, D., & Greig, J. (1986). Use of piezometer cone data. In *Proceedings of the SITU' 86 Use of In-Situ Testing in Geotechnical Engineering, ASCE Specialty Conference* (pp. 1263-1280).

Rogiers, B., Mallants, D., Batelaan, O., Gedeon, M., Huysmans, M., & Dassargues, A. (2017). Model-based classification of CPT data and automated lithostratigraphic mapping for high-resolution characterization of a heterogeneous sedimentary aquifer. *PLoS One*, 12, e0176656. http://dx.doi.org/10.1371/journal.pone.0176656.

Rumelhart, D.E., Hinton, G.E., & Williams, R.J. (1986). Learning representations by back-propagation errors. *Nature*, 323, 533-536. http://dx.doi.org/10.1038/323533a0.

Schaap, M.G., Leij, F.J., & van Genuchten, M.T. (1998). Neural network analysis for hierarchical prediction of soil hydraulic properties. *Soil Science Society of America Journal*, 62(4), 847-855. http://dx.doi.org/10.2136/sssaj1998.03615995006200040001x.

Schneider, J.A., Hotstream, J.N., Mayne, P.W., & Randolph, M.F. (2012). Comparing CPTU *Q–F* and $Q–\Delta u_2/\sigma_{v0}'$ soil classification charts. *Géotechnique Letters*, 2(4), 209-215. http://dx.doi.org/10.1680/geolett.12.00044.

Schneider, J.A., Randolph, M.F., Wayne, P.W., & Ramsey, N.R. (2008). Analysis of factors influencing soil classification using normalized piezocone tip resistance and pore pressure parameters. *Journal of Geotechnical and Geoenvironmental Engineering*, 134(11), 1569-1586. http://dx.doi.org/10.1061/(ASCE)1090-0241(2008)134:11(1569).

Wilson, D.L. (1972). Asymptotic properties of nearest neighbor rules using edited data. *IEEE Transactions on Systems, Man, and Cybernetics*, SMC-2(3), 408-421. http://dx.doi.org/10.1109/TSMC.1972.4309137.

Soils and Rocks

An International Journal of Geotechnical and Geoenvironmental Engineering

www.soilsandrocks.com

ISSN 1980-9743
ISSN-e 2675-5475

Evaluation of the influence of compaction energy on the resilient behavior of lateritic soil in the field and laboratory

Paula Taiane Pascoal[1#], Amanda Vielmo Sagrilo[1], Magnos Baroni[1], Luciano Pivoto Specht[1], Deividi da Silva Pereira[1]

Article

Keywords
Lateritic soil
Pavement subgrade
Undisturbed samples
Resilient modulus

Abstract

This article presents the study of the resilient behavior of three soil horizons from a deposit of lateritic soil employed in a pavement structure in Rio Grande do Sul, Brazil. The use of lateritic soils in pavement layers is a common practice in Brazil and due to its peculiarities, its behavior must be investigated. The methodology consisted of physical and chemical characterization and resilient modulus determination. Samples from the three horizons, compacted at standard, intermediate and modified energy, were analyzed. In addition, undisturbed samples extracted from the interior and top layer of the embankment were submitted to repeated load triaxial tests for resilient modulus determination. The results indicated that the soil exhibit good behavior for pavement subgrade applications, perhaps as subbase or base course layers. The compound and universal models yielded the best correlation coefficients. Furthermore, the results showed that as the compaction energy increased, the resilient modulus also increased, as long as they are within the optimum water content and compaction degree limit. However, when subjected to immersion in water for four days, the resilient behavior decreased about 73% in relation to unsaturated samples.

1. Introduction

The constant search for improvements in pavement projects has led to the adoption of a mechanistic-empirical approach to flexible pavement design in Brazil. This approach is supported by the development of a software program, new M-E pavement design methodology (MeDiNa), which takes into consideration structural efficiency, employment of materials with known performance characteristics and the impact of environmental and traffic conditions (Medina et al., 2006; Ubaldo et al., 2019; Lima et al., 2019; Souza Júnior et al., 2019; Lima et al., 2020; Franco & Motta, 2020).

To validate a design or structural analysis with MeDiNa, it is necessary to carry out laboratory tests to characterize constituent materials, in addition to considering a set of parameters referring to all materials that comprise the flexible pavement structure (Franco & Motta, 2018). Regarding to the subgrade, the resilient modulus (DNIT, 2018a) and the permanent deformation parameters (DNIT, 2018b) are essential, as well as the characterization of the soil physical properties and Miniature Compaction Tropical (MCT) classification (DNER, 1996) of the constituent material. MCT is a Brazilian classification system which was developed specifically to consider the characteristics of fine tropical soils (Nogami & Villibor, 1995). Soils used in subbase and base course layers must be characterized according to MCT methodology and have their elastic and plastic properties determined, regarding resilient modulus and permanent deformation.

The parameter that describes the elastic behavior of materials submitted to cyclic loading is the resilient modulus (RM). Resilience is the capacity of a material to recover from deformations after loading ceases (Huang, 1993; Medina, 1997; Balbo, 2007). In general, the resilient modulus of soils employed in pavement structures exhibit a non-linear behavior, due the variation in the stress state, such as external load variation, changes in layer thickness and the different specific weights of the constituent materials, among others (Hicks & Monismith, 1971; Uzan, 1985).

Previous research on soil behavior under cyclic loading indicates that the resilient modulus depends on the following: soil origin, particle size distribution (percentage of material passing through sieve #200), physical state (water content and dry unit weight), loading conditions (frequency and amplitude of cyclic loading), stress history and state, number of deviator stress solicitations, density, compaction water content, degree of saturation and compaction method, among others (Seed et al., 1967; Medina & Preussler, 1980; Bayomy & Al-Sanad, 1993; Li & Selig, 1994; Guimarães et al., 2001;

#Corresponding author. E-mail address: ptpascoal@hotmail.com
[1]Universidade Federal de Santa Maria, Department of transportation, Santa Maria, RS, Brasil.

Submitted on May 18, 2021; Final Acceptance on September 18, 2021; Discussion open until February 28, 2022.
https://doi.org/10.28927/SR.2021.071321

Ceratti et al., 2004; Buttanaporamakul et al., 2014; Razouki & Ibrahim, 2017; Rahman & Gassman, 2017; Lima et al., 2018; Venkatesh et al., 2018; Lima et al., 2019; El-Ashwah et al., 2019; Ackah et al., 2020; de Freitas et al., 2020; Zhang et al., 2020; Zago et al., 2021; Silva et al., 2021).

The use of lateritic soils in pavement layers is a common practice in Brazil, however, their nature is not sufficient to assure a good performance, which is associated with peculiarities of formation and location the deposit (Medina, 2006; Guimarães et al., 2018). According to Camapum de Carvalho et al. (2015) it is necessary to verify the chemical, mineralogical, physical and structural characteristics of tropical soils so that they can be used for highway construction.

In this context, this study evaluates the resilient behavior of a lateritic clay soil deposit, used in a highway project in the state of Rio Grande do Sul, Brazil, by: analyzing the influence of the variation in compaction energy on the behavior of this material; comparing samples compacted in the laboratory to undisturbed samples compacted in the field and extracted from the interior and top layer of the road embankment; and, determining the resilient behavior of samples immersed in water for 96 hours. Due the lack of Brazilian studies about the behavior of undisturbed samples of soil, this article seeks to highlight the importance of compaction energy and the technological control of the process with regard to the behavior of soils used in the subgrade of flexible pavements.

2. Materials and methods

The experimental program for this research was divided into the following steps: sample collection, physical and chemical characterization tests, repeated load triaxial tests, and subsequent analysis of the results.

2.1. Materials

Lateritic soils are very common in humid tropical climates, such as Brazil. According to Nogami & Villibor (1991), the material most frequently used in Brazilian road pavements is fine lateritic soil, due to its abundance in most states.

The study area was located in the municipality of Cruz Alta in the northwest mesoregion of Rio Grande do Sul. The pedological and geological aspects of the area present medium textured, dark red clayey latosols. This material is the result of the weathering process at the upper portion of the Paraná Basin basalt effusion, which belongs to Serra Geral formation and was developed in flat and smooth undulated areas.

Soil from the studied deposit was employed/used in the construction of a 14.20-meter-high road embankment, which served as the subgrade for expansion of an intersection of highway RS-342, located near Cruz Alta. Disturbed samples from the deposit were collected from three pedological horizons (A, B and C) located at 28°37’39.40” S and 53°37’30.50” W, as seen in Figure 1A. The three horizons were used to compose the subgrade of the previous pavement structure. The soils from the horizons were extracted from the deposited and transported to the jobsite to be compacted.

The structure of the intersection of highway studied was made up of: the embankment, a 19 cm sub-base course layer granular material, and a 15 cm granular base course layer. Two asphalt layers were also applied, a 5 cm of conventional asphalt mixture and 5 cm of polymer modified asphalt mixture. This structure was designed to support a total of 3.5 x10^7 ESALs (equivalent single axle load of 80 kN – USACE).

Figure 1B presents the compacted embankment before the extraction of the undisturbed samples. The samples were collected at 28°37’54.00” South and 53°37’31.50” West, from the interior of the embankment, compacted at standard energy, and also from the top layer of the embankment, compacted at intermediate energy.

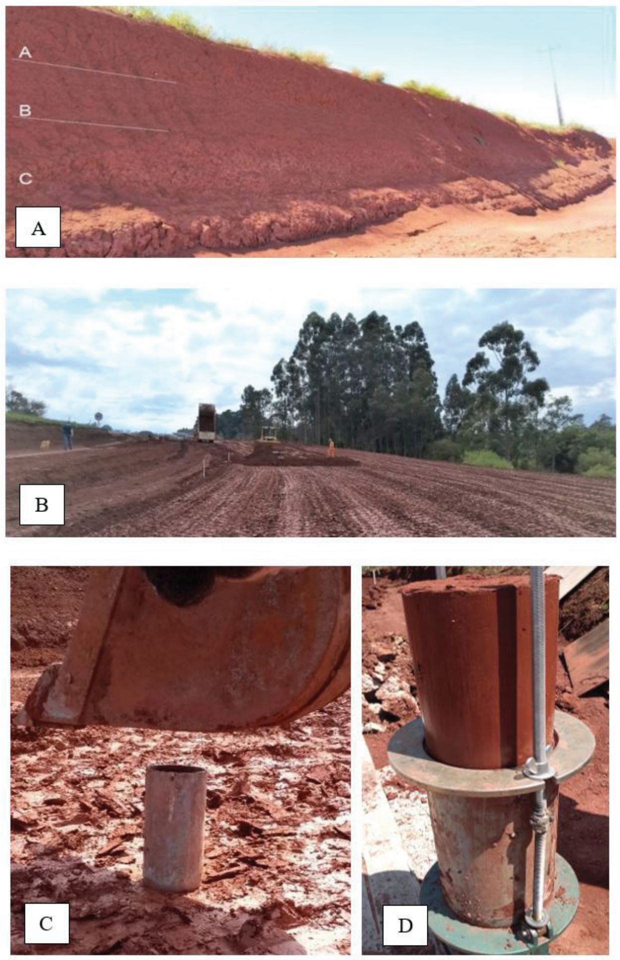

Figure 1. (A) Soil horizons at the Cruz Alta deposit, (B) location of the extraction of undisturbed soil sample, (C) sampler cylinder extraction procedure and (D) undisturbed soil sample.

Cylindrical steel samplers (15 cm diameter x 30 cm height) developed for the extraction of undisturbed samples, were inserted into the subgrade with a backhoe (Figure 1C). The undisturbed samples were extracted with a puller and a hydraulic jack (Figure 1D). Then, they were protected with plastic wrap, aluminum foil and paraffin, to keep the field compaction structure and moisture.

2.2. Physical and chemical characterization

The physical characterization of the soil was developed based on Brazilian national standards and soil mechanics tests (Atterberg limits, grain size analysis and specific gravity of soil grains). In addition, mass loss tests by immersion and Moisture Condition Value Compaction (mini-MCV were performed in order to classify the samples according to the Brazilian MCT methodology (DNER, 1996).

The chemical characterization of the soil was done with energy-dispersive X-Ray Fluorescence (EDXRF), using Bruker S2 Ranger equipment. Energy dispersive X-ray fluorescence provides a qualitative and quantitative analysis to identify elements simultaneously by means of emission detection. Further, a chemical analysis of the horizons was carried out in order to identify the pH, the cation exchange capacity (CEC), the amount of aluminum, magnesium and calcium, the saturation percentage and the percentage of organic matter.

2.3. Mechanical characterization

For the disturbed samples, compaction tests were performed in order to obtain the maximum dry density (MDD) and the optimum moisture content (OMC). A three-part cylindrical mold was employed, as described in the DNIT 134 standard (DNIT, 2018a). For each horizon (A, B and C), compaction curves for standard energy (SE), intermediate energy (IE) and modified energy (ME) were plotted. Then, with the maximum values obtained, three specimens compacted for each horizon, at each compaction energy, were submitted to resilient modulus tests.

Three undisturbed samples from the interior of the embankment (compacted at standard energy) and three undisturbed samples from the top layer (compacted at intermediate energy) were tested. To avoid any change in the structure of the samples due to the contact between the soil and the edge of the sampler, the undisturbed samples were trimmed reducing the extraction dimensions (30 cm in height and 15 cm in diameter) to the test dimensions (10 cm height and 20 cm diameter). The molding procedure for reducing the size of the specimens was done hours before the resilient modulus test, using spatulas and steel lines, controlling the ambient humidity and verifying the moisture content of the specimens every fifteen minutes.

Repeated load triaxial tests were performed on the equipment shown in the Figure 2A and Figure 2B, according to the DNIT 134 (DNIT, 2018a), in order to determine the elastic

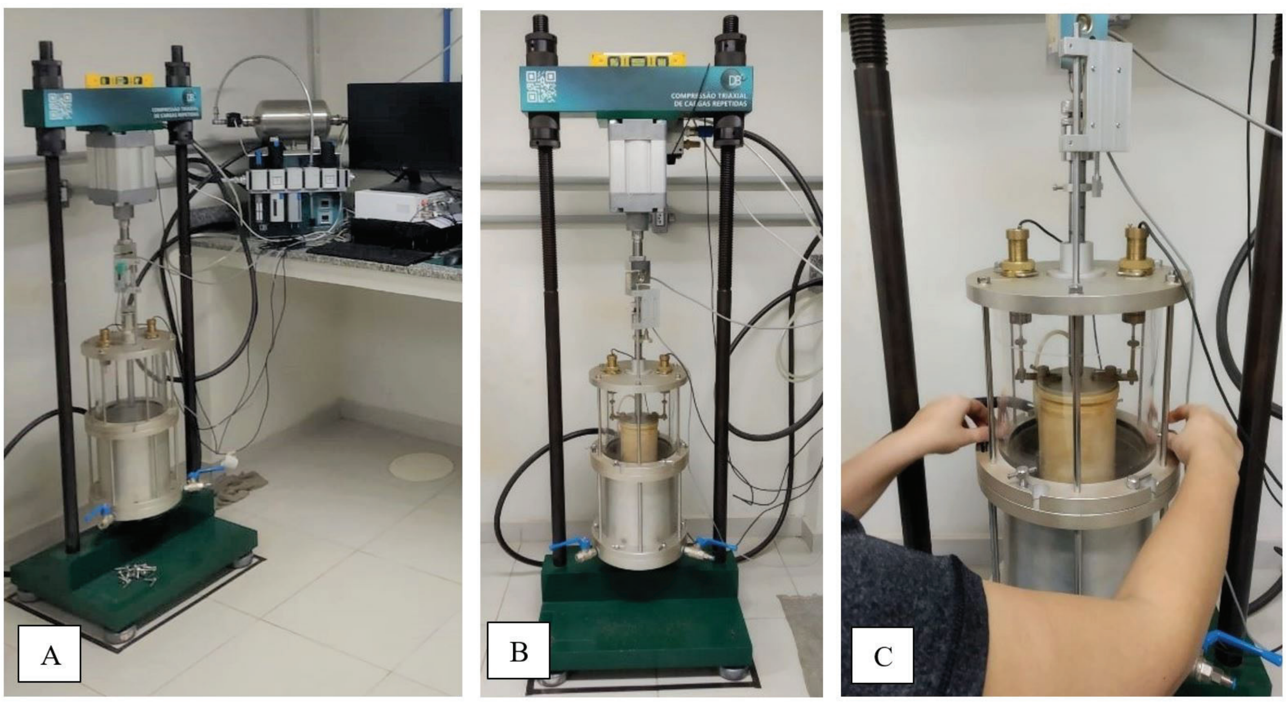

Figure 2. (A) Triaxial equipment of repeated loads, (B) soil sample being positioned on equipment, (C) detail of the two LVDTs inside the triaxial chamber.

properties (resilient modulus test) of both the undisturbed samples, compacted in the field, and the samples taken from the three soil horizons, compacted in the laboratory. In Figure 2C it is possible to observe the two linear variable differential transformers (LVDT) used inside the bipartite triaxial chamber, supported under a top cap that receives the action of the deviator stress through a load cell and a piston. The Brazilian standard DNIT 134 (DNIT, 2018a) presents technical procedures similar to those adopted by American Association of State Highway and Transportation Officials: T 307-99 (AASHTO, 2012) and MEPDG-1 (AASHTO, 2008).

Five hundred cycles were applied for conditioning, with confining stress (σ_3) of 0.07 MPa and deviator stress of (σ_d) 0.07 MPa, at a frequency of 1 Hz. Then, each specimen was submitted to twelve loading sequences, each with 100 cycles, in accordance with the standards, being applied to each sequence of confining stress versus deviator stress: 0.02x0.02 MPa, 0.02x0.04 MPa, 0.02x0.06 MPa, 0.035x0.035 MPa, 0.035x0.070 MPa, 0.035x0.105 MPa, 0.05x0.05 MPa, 0.05x0.10 MPa, 0.05x0.15 MPa, 0.07x0.07 MPa, 0.07x0.14 MPa, 0.07x0.21 MPa.

The determination of the resilient parameters was based on the mathematical models that best describe the behavior of the samples, such as the Biarez model (Biarez, 1962), the Svenson model (Svenson, 1980), the stress invariant model, the Pezo et al. model (Pezo et al., 1992) and the NCHRP 1-37A model (AASHTO, 2004), summarized in Table 1 (Guimarães, 2009; Medina & Motta, 2015; Nguyen & Mohajerani, 2016).

After obtaining the resilient parameters, the relationship between the resilient modulus and soil physical indexes could be identified. For this, the average RM from the model that presented the best fit was correlated with the void ratio, the optimum moisture content and the maximum dry density.

3. Results and analysis

The results of the laboratory tests and analysis of mathematical models are presented here to support the discussions regarding the comparison of the disturbed and undisturbed samples as well as the change in the resilient behavior relative to changes in the compaction energy.

3.1. Physical and chemical characterization

Table 2 shows the average values from the physical and chemical characterization, as well as the soil classification for the three horizons under study. The Atterberg limits and particle size distribution curve are very similar for horizons A and B, however horizon C is different, with a higher Plasticity Index (PI), higher silt content and a lower percentage of sand. Horizon A has a predominance of particles smaller than 0.06 mm and is composed of 64% silt and clay. Horizon B and C exhibit 67% and 72% of the same fractions, respectively.

The particle size distribution sieve analysis for each of the horizons is presented in Figure 3. The tests were performed both with the dispersant sodium hexametaphosphate (WD) and without dispersant (WOD), using only distilled water. The results of the particle size distribution curves without the dispersant shows a tendency for larger particle sizes, in

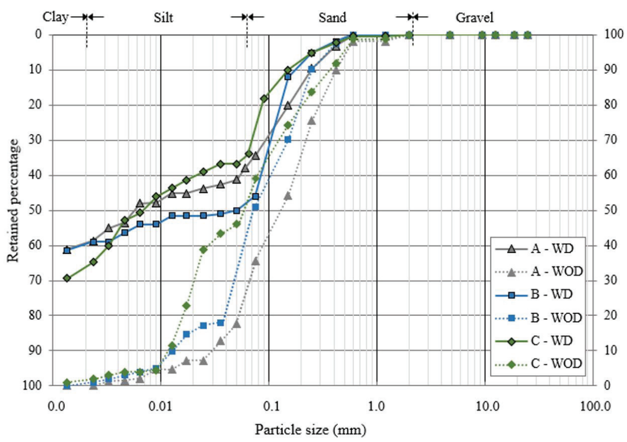

Figure 3. Particle size distribution curves of the horizons.

Table 1. Equations from the models used.

Models	Equation	
Biarez – confining stress	$RM = k_1.\sigma_3^{k_2}$	(1)
Stress invariant	$RM = k_1.\theta^{k_2}$	(2)
Svenson – deviator stress	$RM = k_1.\sigma_d^{k_2}$	(3)
Pezo et al. – compound	$RM = k_1.\sigma_3^{k_2}.\sigma_d^{k_3}$	(4)
NCHRP 1-37A – universal	$RM = k_1.\rho_a\left(\frac{\theta}{\rho a}\right)^{k_2}.\left(\rho\frac{\tau_{oct}}{\rho a}+1\right)^{k_3}$	(5)

Note: RM: resilient modulus; σ_3 : confining stress; σ_d : deviator stress; θ : principal stress; τ_{oct} : octahedral stress; ρ_a : atmospheric pressure; k_1, k_2 e k_3 : resilient parameters experimentally determined.

addition to not showing the clay particles. This difference between the WOD and WD results is due to the adherence of the clay particles to the larger grains when a chemical dispersant is not used.

According to the Brazilian MCT classification of tropical soils (Nogami & Villibor, 1995), the soil belongs to the clayey lateritic behavior (LG') group, which infers good behavior for pavement subgrade, exhibiting high bearing capacity, low expansion and permeability. In comparing the MCT classification with the AASHTO, the importance of classifying the behavior of tropical silts is evident. According to the AASHTO road classification, the studied soil is classified in groups A-7-5 or A-7-6, indicating fair to poor behavior for use in pavement structures. Based on the Unified Soil Classification System (USCS), horizon A is classified as a low compressibility inorganic clay, while horizons B and C are classified as high compressibility silt.

Based on the data summarized in Table 2, silicon dioxide, iron oxide and aluminum oxide were present in all three horizons of from deposit. This is consistent with the MCT classification and the physical characteristics of the deposit.

Horizon A which is closer to the surface, had a higher organic matter content. However, as depth increased, organic matter content decreased, with values of 0.2 and 0.1, for horizon B and C, respectively. Organic matter content values are related to cation exchange capacity (CEC). The CEC of the three horizons is less than 6%, indicating low activity clays and little or no presence of organic matter (OM ≤ 2%). As the amount of aluminum in the material increases, the clay content also increases, which reinforces the hypothesis of the clay mineral kaolinite. The pH values of the three horizons, ranging between 4.6 and 5.8, indicate that the deposit presents acidic soils.

3.2. Mechanical characterization of the laboratory samples

Figure 4 presents the optimum moisture content (OMC) and maximum dry density (MDD) for each of the horizons, compacted at standard (SE), intermediate (IE) and modified energy (ME). As compaction energy increases, there is an increase in maximum dry unit weight and a decrease the optimum moisture content (Lambe & Whitman, 1969). Based on the analysis, as closer is the soil to the surface, the lower are the OMC and specific weight of the grains (see Table 2) and the higher is the MDD. As the soil thickness increases, as in the case of horizon C, lower values of specific weight and OMC are observed, and lower values of MDD.

Based on the standard DNIT 134 (DNIT, 2018a), only the tests in which the compacted specimens of the had a maximum variation of ± 0.5% relative to the OMC were considered valid (DNIT, 2018a). Although the standard does not impose a variation limit for maximum dry density, a variation of ±1.0% was adopted to consider the specimen valid.

Table 2. Physical and chemical characterization and soil horizon classification.

Parameters	Horizon A	Horizon B	Horizon C
Liquid Limit (%)	43	55	77
Plastic Limit (%)	28	44	51
Plasticity Index - PI (%)	16	11	26
Specific weight (kN/m^3)	26.13	27.80	28.75
% gravel (>2.0mm)	0	0	0
% coarse sand (0.6 – 2.0 mm)	0	0	0
% average sand (0.2 – 0.6 mm)	15	8	7
% fine sand (0.06 – 0.2 mm)	21	25	21
% silt (2 μm – 0.06 mm)	24	26	38
% clay (%< 2 μm)	40	41	34
Brazilian MCT - c'	2.29	2.35	1.91
Brazilian MCT - d'	48.78	67.00	21.38
Brazilian MCT - e'	1.02	0.69	1.08
Brazilian MCT	LG'	LG'	LG'
AASHTO	A-7-5	A-7-6	A-7-5
USCS	CL	MH	MH
EDXRF - chemical components that prevail	SiO_2/Fe_2O_3 Al_2O_3/Na_2O	Fe_2O_3/SiO_2 Al_2O_3/TiO_2	Fe_2O_3/SiO_2 Al_2O_3/Na_2O
Chemical analysis - CEC	2.0	1.8	3.7
Chemical analysis - basic cations Ca / K / Mg (Cmol$_c$dm^3)	1.4 / 0.05 / 0.6	0.3 / 0.02 / 0.4	0.2 / 0.02 / 0.3
Chemical analysis - saturation Al / base (%)	50.0 / 15.4	55.6 / 9.2	86.6 / 2.6
Chemical analysis - organic matter (%)	2.0	0.2	0.1
Chemical analysis - pH	4.6	5.8	5.6

Note: Results of particle size distribution analysis were obtained with dispersant; Note: Miniature Compaction Tropical – MCT is a classification for tropical soils developed by Nogami e Villibor (1995); Note: AASHTO - American Association of State Highway and Transportation Officials; Note: USCS - Unified Soil Classification System.

As previously mentioned, five resilient modulus prediction models were used to analyze the data obtained by the resilient modulus test for the twelve pairs of confining and deviator stresses previously mentioned. For this, multiple nonlinear regression was performed using Statistica v.10 software, taking into consideration the compaction conditions for each individual sample and for the set of the three samples (01 + 02 + 03). Table 3 shows the prediction model results for the three-sample sets. The criterion used to evaluate the models was the best fit of the coefficient of determination (R^2), obtained by regression analysis.

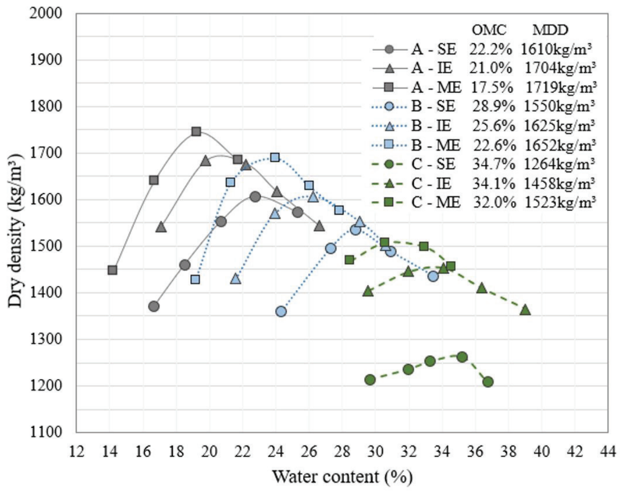

Figure 4. Mechanical characterization of horizons.

Regarding horizon A, in general, the Biarez and stress invariant models presented the worst fit. For the compound model, there was a 57.4% gain in the resilient modulus compacted at intermediate energy, when compared to standard energy. Likewise, the resilient modulus at modified energy was 84.5% higher than the RM at intermediate energy and 190.4% higher than at standard energy.

The universal and compound model, which takes into account deviator stress and confining stress interactions, satisfactorily represented the behavior of horizon A, for the samples compacted at standard and intermediate energy. The Svenson model also showed a good fit based on the nature and particle size distribution curve of the soil, as found in the technical literature (Guimarães et al., 2001; Behak & Núnez, 2017; Bhuvaneshwari et al., 2018; Guimarães et al., 2018).

Table 3. Resilient parameters for the soil horizons for the five models under evaluation.

Models		Horizon A			Horizon B			Horizon C		
		SE	IE	ME	SE	IE	ME	SE	IE	ME
Biarez	k_1	79.72	173.09	736.83	109.76	751.38	1724.20	140.77	523.95	1113.89
	k_2	-0.16	-0.06	0.21	-0.08	0.34	0.50	-0.08	0.30	0.38
	R^2	0.14	0.04	0.61	0.05	0.90	0.91	0.08	0.73	0.90
	RM (MPa)	134.0	211.4	376.4	140.5	250.1	348.7	181.4	202.4	328.3
Svenson	k_1	71.55	143.39	557.70	102.98	387.90	729.83	128.43	302.98	546.45
	k_2	-0.23	-0.15	0.14	-0.15	0.17	0.29	-0.13	0.16	0.20
	R^2	0.62	0.49	0.49	0.41	0.48	0.62	0.43	0.40	0.49
	RM (MPa)	134.2	211.3	391.9	153.4	246.7	349.3	181.4	202.5	328.5
Stress Invariant	k_1	90.21	171.17	541.85	122.03	397.98	721.03	147.27	309.03	559.74
	k_2	-0.24	-0.13	0.20	-0.14	0.30	0.46	-0.13	0.26	0.33
	R^2	0.36	0.21	0.64	0.20	0.80	0.89	0.23	0.66	0.81
	RM (MPa)	134.1	211.3	290.3	153.3	246.8	349.3	181.4	202.5	328.5
Compound	k_1	104.46	208.43	740.80	144.30	739.20	1640.16	163.58	520.12	1105.77
	k_2	0.20	0.20	0.15	0.18	0.34	0.43	0.13	0.29	0.37
	k_3	-0.34	-0.25	0.05	-0.24	0.00	0.08	-0.20	0.01	0.01
	R^2	0.72	0.70	0.65	0.55	0.90	0.93	0.53	0.73	0.90
	RM (MPa)	134.3	211.4	390.1	153.3	246.7	348.4	181.5	202.5	328.1
Universal	k_1	2849.9	3674.9	3245.99	2649.35	2497.19	3016.35	2870.91	1979.15	3271.91
	k_2	0.33	0.33	0.32	0.31	0.54	0.66	0.24	0.43	0.58
	k_3	-0.66	-0.51	-0.006	-0.50	-0.25	-0.21	-0.41	-0.18	-0.26
	R^2	0.81	0.80	0.51	0.64	0.90	0.93	0.64	0.72	0.90
	RM (MPa)	134.1	211.3	368.2	153.4	248.5	350.9	181.9	202.7	330.2

For horizon B, the compound model yielded a RM gain of 60.9% when comparing samples compacted at intermediate energy to those compacted at standard energy. Likewise, due the compaction increase, from standard to modified, there was a gain of 127.3% in stiffness. In comparing intermediate to modified energy compaction, a 41.2% increase was reported. In general, for horizon B, all evaluated models yielded good correlations for samples compacted at IE and ME. However, for SE, the Biarez and stress invariant models did not provide a sufficiently good fit. Therefore, only the compound and universal models presented a good fit.

Among all horizons, horizon C presented the lowest gains in stiffness as the compaction energy increased. For the compound model, an increase in energy from standard to intermediate, yielded a RM gain of 11.6%. In a comparison between intermediate and modified energy, the gain was 62% and between standard and modified it was 80.8%. The precision of fit analysis shows that the behavior of this horizon was similar to horizon B, in terms of the models that best fit each compaction energy. At all energy levels the universal model presented a better fit for this horizon, followed by compound model.

In order to evaluate the resilient behavior of the material under saturation, three specimens from horizon B were compacted at intermediate energy. These specimens remained immersed for 96 hours, according to the procedure performed by Medina et al. (2006) and were subsequently submitted to RM tests. Table 4 presents the specimen properties and the resilient parameters for the set of samples analyzed.

Evaluating the RM obtained from the parameters of the compound model, an average RM of 66.7 MPa was reached, value 72.9% lower than the RM reached in the unsaturated condition of horizon B, compacted at IE (246.7 MPa). This decline in the resilient behavior of the soil is consistent with studies developed by Thadkamalla & George (1995), in which 50-75% reductions in RM were reported depending on the degree of saturation. It therefore follows that if drainage is not designed and executed properly, it can affect the performance of the material, because bearing capacity is drastically compromised on contact with water.

One of the objectives of this article was to determine whether there is a relationship between compaction energy and the coefficient of determination for each model. For the compound and universal model, each sample exhibited different behaviors under the varying compaction conditions, so it was not possible identify any behavior trend for R^2. The Biarez and stress invariant models were the only ones that yielded similar behavior, where, there was not a good fit at low energy levels, whereas at modified energy, the R^2 values were high.

Since the mathematical analysis of horizon B material showed the best fitting, this material was selected to be examined regarding stresses action. Furthermore, this horizon was chosen because it had a lower organic matter content, compared to horizon A, and because it exhibits an absence of sediments from the original rock, unlike horizon C. Figure 5 shows the behavior of the specimens relative to variations in compaction energy levels according to the (A) Biarez, (B) Svenson e (C) stress invariant models.

The resilient behavior at standard compaction energy differs from the other energy levels for the three models under analysis. The samples compacted, at IE and ME energy tests, behaved as follows: as the stresses increased, the RM also increased. The opposite occurred for the samples compacted at SE energy test. The variation of the RM results is higher for samples compacted at standard energy.

3.3. Mechanical characterization of undisturbed samples

After the procedure for reducing the specimen dimensions, three undisturbed soil samples from the interior of the embankment and three from the top layer were subjected to repeated load triaxial test for determination of the resilient

Table 4. Characteristics and resilient parameters of the immersed samples – Horizon B – IE.

Characteristics and parameters	Sample 01	Sample 02	Sample 03
Compaction moisture content (%)	25.20	25.30	25.10
Dry unit weight (kg/m^3)	1630.20	1628.90	1631.50
Compaction degree (%)	100.32	100.24	100.40
Average diameter after compaction (cm)	10.09	10.11	10.11
Average height after immersion (cm)	20.27	20.61	20.40
Moisture content after immersion (%)	31.93	32.38	33.36
Average diameter after tests (cm)	10.20	10.19	10.27
Average height after tests (cm)	20.18	20.37	20.07
Moisture content after tests (%)	30.17	30.04	30.47
Compound model – k_1		116.14	
Compound model – k_2		0.46	
Compound model – k_3		-0.33	
Compound model – R^2		0.84	
RM average (MPa)		66.70	

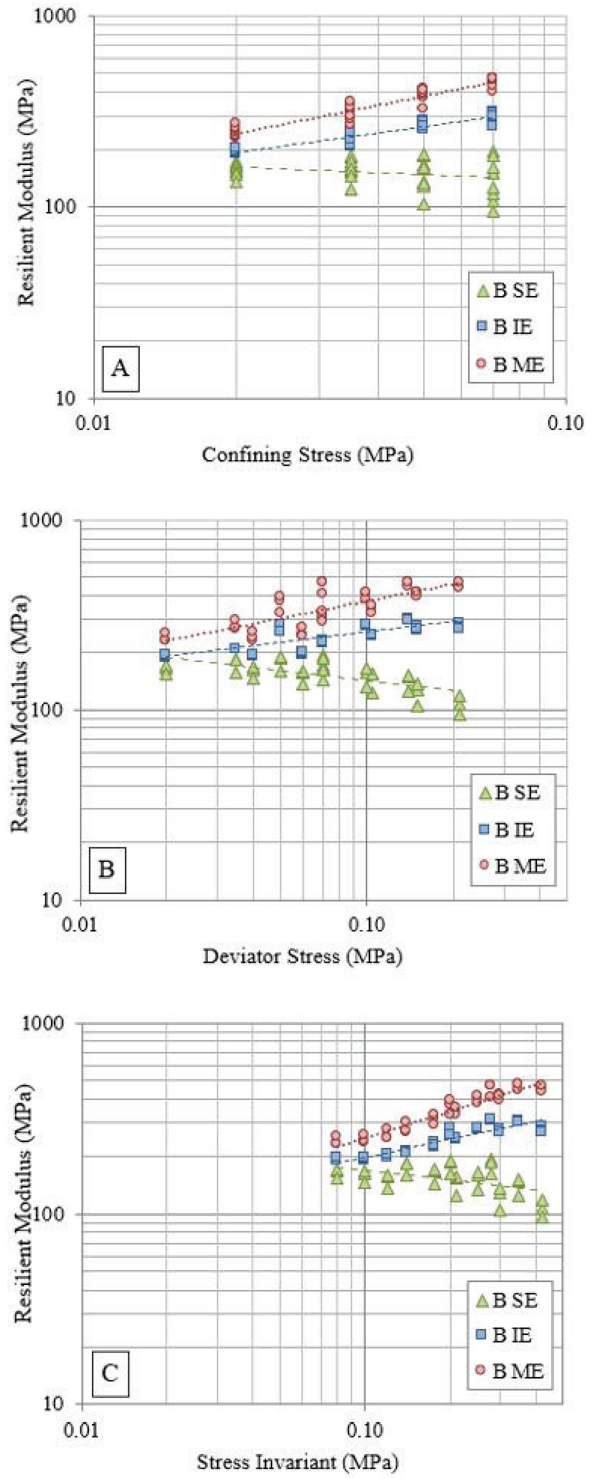

Figure 5. RM behavior for horizon B at three compaction energy levels, based on the (A) Biarez, (B) Svenson and (C) stress invariant models.

modulus. Table 5 presents the quality control for each sample before and after the resilient modulus tests. It is worth noting that the moisture content of the interior of the embankment at the time of collection was 46.07% and the top layer was 21.52%. The maximum dry density of the top layer, obtained with a core-cutter was 1645.30 kg/m^3.

Regarding the measurement of the resilient parameters of the undisturbed soil samples, the results of the 12th pair of stresses from two samples from the interior of the embankment were disregarded. This was due to the interruption of the test at this pair, when the measurement capacity of the linear variable differential transformer (LVDT) had ended. Table 6 presents the parameters of resilience each of the models analyzed, as well as the average resilient modulus.

Note that the moisture contents of the undisturbed field samples, especially those from the interior of the embankment, were 18% to 37.5% higher than the optimum moisture content of the samples from the soil horizons compacted in the laboratory. This may explain the low resilient modulus for the undisturbed samples. In general, for the specimens from the interior of the embankment, the Biarez and stress invariant models presented the worst fit, while other models presented a better fit. The analysis of the parameters obtained from the compound model, for the sample set, reveals a negative value for parameter k3, indicating a decrease in the RM with increases in the deviator stress. The positive values for k2 indicate that increases in confining stress, yields increase in the RM. In order to illustrate the behavior of undisturbed samples taken from the interior of the embankment, Figure 6 A presents a three-dimensional-graph of results from the compound model for these samples. Furthermore, the increase in the deviator stress and confining stresses and the resulting decrease in the resilient modulus values evidence of the non-linear behavior of the material under these specific conditions.

Unlike the undisturbed samples from the interior of the embankment, the samples from the top layer exhibited an improvement in the RM as the stresses increased. In this case, the k2 parameter, for the Biarez, Svenson and stress invariant models produced a positive value, indicating that as the confining, deviator or principal stresses increased, the resilient modulus also increased.

Figure 6 B represents the behavior of undisturbed samples from the top layer using the compound model. As the confining stress increases, the resilient modulus also increases. It is worth mentioning that the universal model presented a better fit than the compound model for the top layer of the embankment.

Based on the parameters obtained from the compound model for undisturbed samples from the top layer of the embankment, this soil presented an average RM of 309.4 MPa, behavior considered satisfactory for the properties of the soil and its application. When compared to the average RM value from the horizon B (246.7 MPa) compacted sample at intermediate energy, the same energy employed in the field, a lower value than the obtained for undisturbed samples from

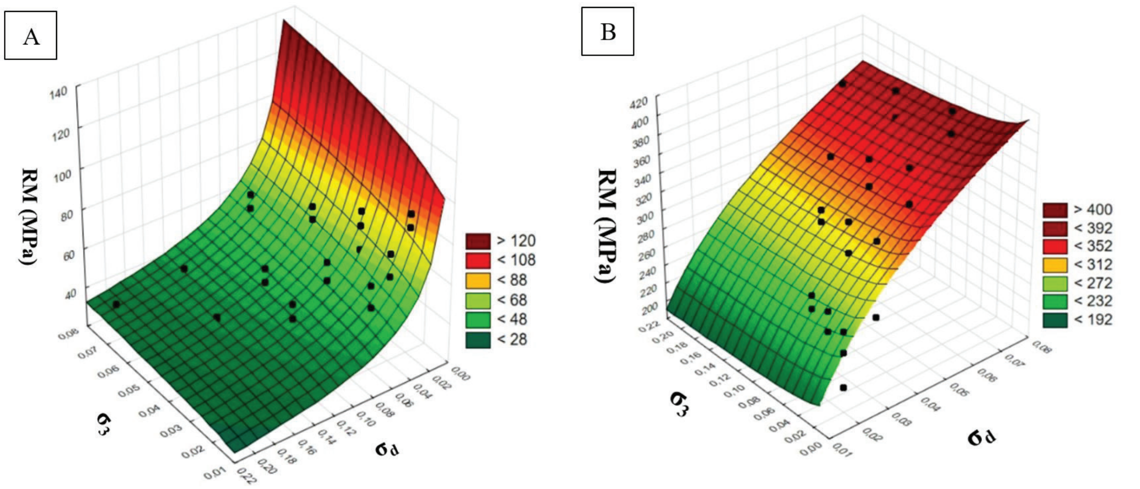

Figure 6. Three-dimensional graph of the undisturbed samples from the (A) interior of embankment and the (B) top layer, using the compound model.

Table 5. Characteristics of the undisturbed samples before and after the RM test.

Sample	Average diameter(cm)	Average height (cm)	Moisture before the test (%)	Average moisture after the test (%)
Interior of Embankment - 01	9.95	19.98	50.25	50.99
Interior of Embankment - 02	10.25	20.21	51.80	51.47
Interior of Embankment - 03	10.02	20.06	51.25	51.36
Top layer – 01	10.03	19.79	20.27	20.03
Top layer – 02	10.00	19.96	20.84	20.08
Top layer – 03	10.05	20.02	20.55	20.15

Table 6. Parameters of resilience for the undisturbed samples.

Models		Interior of Embankment	Top layer
Biarez	k_1	17.70	775.59
	k_2	-0.34	0.29
	R^2	0.26	0.68
	RM (MPa)	53.9	309.5
Svenson	k_1	17.12	433.04
	k_2	-0.42	0.13
	R^2	0.78	0.28
	RM (MPa)	53.4	309.5
Stress Invariant	k_1	24.46	454.16
	k_2	-0.46	0.24
	R^2	0.53	0.55
	RM (MPa)	53.5	309.5
Compound	k_1	21.57	792.87
	k_2	0.12	0.32
	k_3	-0.48	-0.03
	R^2	0.80	0.69
	RM (MPa)	53.4	309.4
Universal	k_1	1476.72	3394.95
	k_2	0.18	0.51
	k_3	-0.78	-0.29
	R^2	0.81	0.71
	RM (MPa)	53.3	310.4

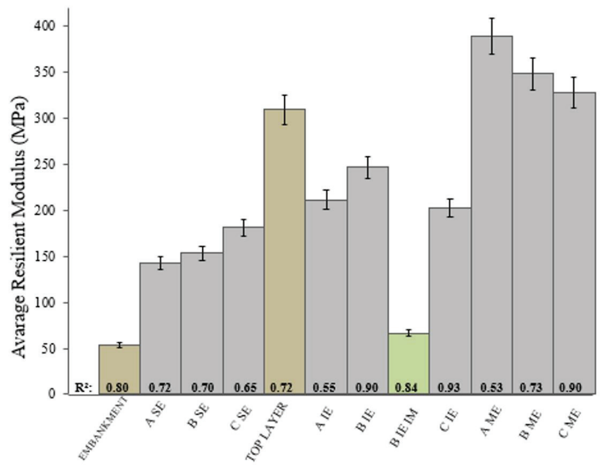

Figure 7. Average Resilient modulus determined by the compound model.

the top layer. This behavior can be explained by the fact that the compaction moisture in the field samples is lower than the optimum moisture content of the laboratory samples for all horizons. The field moisture content of the top layer specimens was near the OMC of the samples compacted at modified energy. Therefore, the resilient modulus values are similar, presenting good performance in terms of resilient behavior.

Figure 7 shows an average resilient modulus for each condition studied, as well as the coefficient of determination, based on the compound model. The values expressed within the bars refers to the R^2 for sample condition. The difference in the average RM for the undisturbed samples from the embankment interior is evident, when compared to the soil horizon specimens compacted at standard energy. Moreover, the loss of resilience in the immersed samples from horizon B, compacted at intermediate energy (B IE IM), can be seen when compared to other compacted samples at the same energy level.

The soil deposit horizons, with varying compaction energy levels, presented average resilient modulus values between 134 and 390 MPa, and the average resilient modulus values for the embankment layers were between 53 and 309 MPa. The variation in the RM for the three horizons of the deposit, with the increase of the compaction energy, tends to show significant impact on the bearing capacity, directly affecting structural design and performance.

In order to determine the influence of the physical indexes on resilient modulus behavior, the relationship between the RM of each sample to its void ratio (e), optimum moisture content (OMC) and maximum dry density (MDD) was investigated. Table 7 presents the data from the samples that were subjected to resilient modulus tests, as well as their respective compaction energy and origin. These relationships are illustrated in Figure 8, the relationship between RM

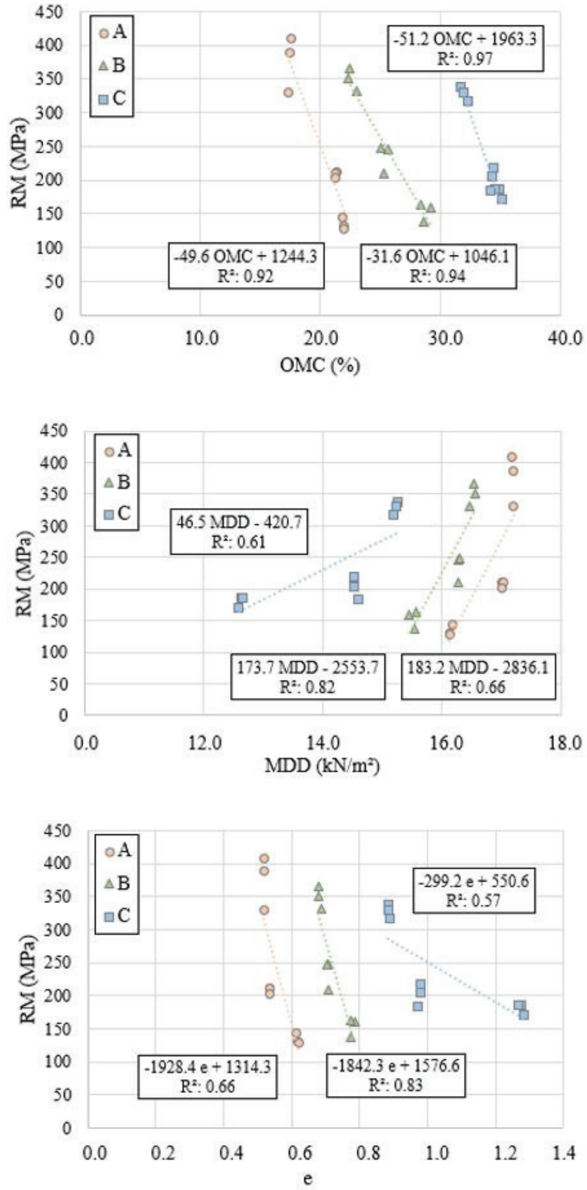

Figure 8. Correlations between the RM and the physical indexes for the samples analyzed with compound model.

and OMC, between RM and MDD and the relationship between RM and void ratio. Note that the RM of each sample corresponds to the average for all of the stresses, based on the compound model.

Among the correlations performed, the relationship between the RM and the OMC yielded the best R^2, indicating that the compaction moisture has a higher influence on the resilient behavior of this deposit, although the density and the void index are related to this physical index. Analyzing simultaneously the three correlations and the three horizons, horizon B presented the strongest relationships and best fit. All of the correlations were considered satisfactory.

Table 7. Physical indices of samples compacted in the laboratory, submitted to RM tests and analyzed with the compound model.

SOIL		Standard Energy			Intermediate Energy			Modified Energy		
Horizon A	RM (MPa)	131.0	128.0	143.6	211.2	210.6	202.4	330.3	408.5	387.7
	e	0.62	0.62	0.61	0.54	0.53	0.54	0.52	0.52	0.52
	OMC (%)	21.94	22.02	21.89	21.43	21.29	21.33	17.35	17.61	17.43
	MDD (kN/m^3)	16.13	16.13	16.19	17.01	17.03	17.02	17.21	17.17	17.20
Horizon B	RM (MPa)	159.6	163.4	137.2	246.5	248.1	209.4	351.3	331.5	366.0
	e	0.79	0.77	0.77	0.71	0.70	0.71	0.68	0.69	0.68
	OMC (%)	29.25	28.42	28.58	25.70	25.10	25.31	22.33	23.01	22.48
	MDD (kN/m^3)	15.46	15.57	15.56	16.27	16.32	16.29	16.55	16.47	16.54
Horizon C	RM (MPa)	187.0	170.9	186.4	218.6	204.5	184.2	338.2	329.8	316.8
	e	1.28	1.28	1.27	0.98	0.98	0.97	0.88	0.89	0.89
	OMC (%)	34.87	35.14	34.55	34.41	34.33	34.20	31.69	32.00	32.26
	MDD (kN/m^3)	12.63	12.60	12.67	14.53	14.53	14.59	15.26	15.24	15.20

Note: void ratio – e.

4. Final considerations

The performance of a pavement is directly correlated with the performance of the materials that compose it. Given that relationship, a new M-E pavement design methodology (MeDiNa) has been developed in Brazil, aimed at analyzing materials under a mechanistic-empirical approach, ensuring durability and quality parameters. For materials that compose the base, sub-base, subgrade and subgrade reinforcement for pavement layers, this analysis is performed by tests and modeling of the resilient modulus. The present study aimed to evaluate the physical and chemical properties and the resilient behavior of a soil deposit used as subgrade in an embankment for a stretch of highway RS 342, in Cruz Alta, using disturbed and undisturbed samples.

The MCT classification and the chemical analyses showed that the deposit under study is composed of lateritic soils, rich in silicon, iron and aluminum oxides, which offers a good behavior as pavement subgrade. The MCT classification is more suitable for tropical soils, since according to the traditional classifications, USCS and AASHTO, the soil in question would be classified as having fair to poor behavior for use in pavement structures.

The mechanical characterization was carried out by means of resilient modulus tests, for compacted specimens at standard, intermediate and modified compaction energies for three horizons of a soil deposit, and then fitted according to the Biarez, Svenson, compound, universal and stress invariant models. As expected, the resilient behavior increases with the increase in compaction energy, although it is not proportional for all horizons. Based on analysis with the compound model, soil Horizon B had the highest percentage increase in RM from standard energy to intermediate energy; and the smallest increase from intermediate to modified energy. The material from this horizon was used to study of resilience loss after sample saturation, demonstrating the behavior of subgrades subject to poor drainage. The RM declined considerably, showing that, sometimes, the material completely loses its bearing capacity, leading to total rupture.

For the undisturbed samples, the top layer of the embankment, which exhibited a degree of compaction of 100%, presented good resilient modulus values, while the values from the interior of the embankment were not as satisfactory. This behavior can be attributed to the moisture content of the extracted samples, considerably different from the optimum wet content found in laboratory tests. Thus, it is evident the need to control the compaction.

Based on these findings, the compound or universal models are the best options when working with a variety compaction energies and materials; and when it is important to use a standardized model.

The gain in RM, as compaction energy increases, can directly affect the distribution of internal stress of a pavement and it can be correlated with the parameters of compaction curves and soil physical indices. This fact reinforces the need for executive control and influences the design of the structure as well as its performance over its service life.

Finally, the present study contributes to the consolidation of the methodologies for pavement design and evaluation according to MeDiNa. It also contributes to increasing the database of pavement construction materials widely used in southern Brazil, such as the red latosols, present throughout Brazilian territory.

Acknowledgements

The authors are grateful to the ANP/PETROBRAS and Conselho Nacional de Desenvolvimento Científico e Tecnológico (CNPq) for their support and the reviewers for their valuable contributions.

Declaration of interest

The authors have no conflicts of interest to declare. All co-authors have observed and affirmed the contents of the paper and there is no financial interest to report.

Authors' contributions

Paula Taiane Pascoal: conceptualization, methodology and experimental procedures, formal analysis, writing – original draft, review and editing. Amanda Vielmo Sagrilo: validation, experimental procedures, writing – review e editing. Magnos Baroni: advisor, supervision, validation, writing – review e editing. Luciano Pivoto Specht: supervision, funding acquisition, project administration, writing – review. Deividi da Silva Pereira: funding acquisition, project administration, writing – review.

List of symbols

θ	Principal Stress
τ_{oct}	Octahedral Stress
k_1, k_2, k_3	Resilient Parameters Experimentally Determined
ρ_a	Atmospheric Pressure
σ_3	Confining Stress
σ_d	Deviator Stress

References

AASHTO NCHRP 1-37A. (2004). *Guide for mechanistic-empirical design of new and rehabilitated pavement structure*. American Association of State Highway and Transportation Officials, Washington, DC.

AASHTO MEPDG-1. (2008). *Mechanistic-empirical pavement design guide: a manual of practice*. American Association of State Highway and Transportation Officials, Washington, DC.

AASHTO T 307-99. (2012). *Determining the resilient modulus of soils and aggregate materials*. American Association of State Highway and Transportation Officials, Washington, DC.

Ackah, F.S., Zhuoochen, N., & Huaiping, F. (2020). Effect of wetting and drying on the resilient modulus and permanent strain of a sandy clay by RLTT. *International Journal of Pavement Research and Technology*, 336-377. http://dx.doi.org/10.1007/s42947-020-0067-3.

Balbo, J.T. (2007). *Pavimentação asfáltica: materiais, projetos e restauração*. Oficina de Textos.

Bayomy, F.M., & Al-Sanad, H.A. (1993). Deformation characteristics of subgrade soils in Kuwait. *Transportation Research Record: Journal of the Transportation Research Board*, (1406), 77-87. Retrieved in May 18, 2021, from http://worldcat.org/isbn/0309055539

Behak, L., & Núnez, W.P. (2017). Mechanistic behaviour under traffic load of a clayey silt modified with lime. *Road Materials and Pavement Design*, 1072-1088. http://dx.doi.org/10.1080/14680629.2017.1296884.

Bhuvaneshwari, S., Robinson, R.G., & Gandhi, S.R. (2018). Resilient modulus of lime treated expansive soil. *Geotechnical and Geological Engineering*, 305-315. http://dx.doi.org/10.1007/s10706-018-0610-z.

Biarez, J. (1962). *Contribution a l'étude des proprietes mecaniques des sols et des materiaux pulverents* [Unpublished Doctoral thesis, Grenoble]. Faculte des Sciences de Grenoble.

Buttanaporamakul, P., Rout, R.K., Puppala, A., & Pedarla, A. (2014). Resilient behaviors of compacted and unsaturated subgrade materials. In *Geo-Congress*. http://dx.doi.org/10.1061/9780784413272.136.

Camapum de Carvalho, J., Rezende, L.R., Cardoso, F.B.F., Lucena, L.C.F.L., Guimarães, R.C., & Valencia, Y.G. (2015). Tropical soils for highway construction: peculiarities and considerations. *Transportation Geotechnics*, 3-19. http://dx.doi.org/10.1016/j.trgeo.2015.10.004.

Ceratti, J.A., Gehling, W.Y.Y., & Núnez, W.P. (2004). Seasonal variations of a subgrade soil resilient modulus in Southern Brazil. *Transportation Research Record: Journal of the Transportation Research Board*, 165-173. http://dx.doi.org/10.3141/1874-18.

de Freitas, J.B., de Rezende, L.R., & Gitirana Junior, G.F.N. (2020). Prediction of the resilient modulus of two tropical subgrade soils considering unsaturated conditions. *Engineering Geology*, 270, 105580. http://dx.doi.org/10.1016/j.enggeo.2020.105580.

DNER CLA 259. (1996). *Classificação de solos tropicais para finalidades rodoviárias utilizando corpos-de-prova compactados em equipamento miniatura*. Departamento Nacional de Estradas de Rodagem, Vacaria, RS (in Portuguese).

DNIT 134. (2018a). *Pavimentação – Solos – Determinação do modulo de resiliência – Método do ensaio*. Departamento Nacional de Infraestrutura de Transportes, Rio de Janeiro (in Portuguese).

DNIT 179. (2018b). *Pavimentação – Solos – Determinação da deformação permanente – Instrução do ensaio*. Departamento Nacional de Infraestrutura de Transportes, Rio de Janeiro (in Portuguese).

El-Ashwah, A.S., Awed, A.M., El-Badawy, S.M., & Gabr, A.R. (2019). Prediction of the resilient modulus of two tropical subgrade soils considering unsaturated conditions. *Construction & Building Materials*, 372-385. http://dx.doi.org/10.1016/j.conbuildmat.2018.10.212.

Franco, F.A.C.P., & Motta, L.M.G. (2018). *MeDiNa - Método de Dimensionamento Nacional - Manual de Utilização, v. 1.0.0*. COPPE/UFRJ.

Franco, F.A.C.P., & Motta, L.M.G. (2020). *Execução de estudos e pesquisa para elaboração de método mecanístico-empírico de dimensionamento de pavimentos asfálticos. Manual de utilização do programa MeDiNa*. Convênio UFRJ-DNIT.

Guimarães, A.C.R. (2009). *Um método mecanístico - empírico para a previsão da deformação permanente em solos tropicais constituintes de pavimentos* [Doctoral thesis,

Federal University of Rio de Janeiro]. Federal University of Rio de Janeiro repository.
Guimarães, A.C.R., Motta, L.M.G., & Castro, C.D. (2018). Permanent deformation parameters of fine - grained tropical soils. *Road Materials and Pavement Design*, 1664-1681. http://dx.doi.org/10.1080/14680629.2018.1473283.
Guimarães, A.C.R., Motta, L.M.G., & Medina, J. (2001). Estudo de deformação permanente em solo típico de subleito de rodovia brasileira. In *Anais da 33ª Reunião Anual e Pavimentação* (pp. 336-354). Rio de Janeiro: ABPv.
Hicks, R.G., & Monismith, C.L. (1971). *Factors influencing the resilient properties of granular materials* (pp. 15-31). Transportation Research Board. Retrieved in May 18, 2021, from http://onlinepubs.trb.org/Onlinepubs/hrr/1971/345/345-002.pdf
Huang, H.Y. (1993). *Pavement analysis and design*. Prentice Hall.
Lambe, T.W., & Whitman, R.V. (1969). *Soil mechanics* (553 p.). Massachusetts Institute of Technology.
Li, D., & Selig, E. (1994). Resilient modulus for fine-grained subgrade soil. *Journal of Geotechnical Engineering*, 120, 939-957. http://dx.doi.org/10.1061/(ASCE)0733-9410(1994)120:6(939).
Lima, C.D.A., Motta, L.M.G., & Aragão, F.T.S. (2019). Effects of compaction moisture content on permanent deformation of soils subjected to repeated triaxial load tests. *Transportation Research Record: Journal of the Transportation Research Board*, 55, 1-11. http://dx.doi.org/10.1177/0361198118825124.
Lima, C.D.A., Motta, L.M.G., Aragão, F.T.S., & Guimarães, A.C.R. (2020). Mechanical characterization of fine-grained lateritic soils for mechanistic-empirical flexible pavement design. *Journal of Testing and Evaluation*, 48, 1-17. http://dx.doi.org/10.1520/JTE20180890.
Lima, C.D.A., Motta, L.M.G., Guimarães, A.C.R., & Aragão, F.T.S. (2018). Contribution to the study of Brazilian tropical soils as pavement materials. In *Proceedings of the 13th Conference on Asphalt Pavements – ISAP*. Fortaleza, Ceará, Brazil.
Medina, J. (1997). *Mecânica dos pavimentos* (380 p). Editora UFRJ.
Medina, J. (2006). Mecânica dos pavimentos: aspectos geotécnicos. *Solos e Rochas*, 29, 137-158.
Medina, J., & Motta, L.M.G. (2015). *Mecânica dos pavimentos* (638 p). Editora Interciência.
Medina, J., & Preussler, E.S. (1980). Características resilientes de solos em estudos de pavimentos. *Solos e Rochas*, 3, 3-26.
Medina, J., Motta, L.M.G., & Santos, J.D.G. (2006). Deformability characteristics of brazilian laterites. *Geotechnical and Geological Engineering*, 24, 949-971. http://dx.doi.org/10.1007/s10706-005-8507-z.
Nguyen, B.T., & Mohajerani, A. (2016). Possible simplified method for the determination of the resilient modulus of unbound granular materials. *Road Materials and Pavement Design*, 841-858. http://dx.doi.org/10.1080/14680629.2015.1130162.
Nogami, J.S., & Villibor, D.F. (1991). Use of lateritic fine-grained soils in road pavement base courses. *Geotechnical and Geological Engineering*, 9, 167-182. http://dx.doi.org/10.1007/BF00881739.
Nogami, J.S., & Villibor, D.F. (1995). *Pavimentação de baixo custo com solos lateríticos* (240 p.). Editora Villibor.
Pezo, R.F., Claros, G., Hudson, W.R., & Stokoe 2nd, K.H. (1992). *Development of reliable resilient modulus test for subgrade and non-granular subbase materials for use in routine pavement design. Final Report*. Retrieved in May 18, 2021, from https://trid.trb.org/view/369153
Rahman, M.M, & Gassman, S.L (2017). Effect of resilient modulus of undisturbed subgrade soils on pavement rutting. *International Journal of Geotechnical Engineering*, 152-161. http://dx.doi.org/10.1080/19386362.2017.1328773.
Razouki, S.S., & Ibrahim, A.N. (2017). Improving the resilient modulus of a gypsum sand roadbed soil by increased compaction. *The International Journal of Pavement Engineering*, 432-438. http://dx.doi.org/10.1080/10298436.2017.1309190.
Seed, H.B., Mitry, F.G., Monismith, C.L., & Chan, C.K. (1967). *Prediction of flexible pavement deflections from laboratory repeated load tests* (National Cooperative Highway Research Program: Report no. 35). Transportation Research Board. Retrieved in May 18, 2021, from http://worldcat.org/issn/00775614
Silva, M.F., Ribeiro, M.M.P., Furlan, A.P., & Fabbri, G.T.P. (2021). Effect of compaction water content and stress ratio on permanent deformation of a subgrade lateritic soil. *Transportation Geotechnics*, 26, http://dx.doi.org/10.1016/j.trgeo.2020.100443.
Souza Júnior, J.G., Motta, L.M.G., & Silva, R.C. (2019). Dimensionamento de pavimentos asfálticos pelo novo método normalizado no Brasil (MeDiNa). In *Anais do 9º Congresso Rodoviário Português* (Vol. 1). Brazil.
Svenson, M. (1980). *Ensaios triaxiais dinâmicos de solos argilosos* [Unpublished master's dissertation]. Federal University of Rio de Janeiro repository (in Portuguese).
Thadkamalla, G.B., & George, K.P. (1995). Characterization of subgrade soils at simulated field moisture. *Transportation Research Record: Journal of the Transportation Research Board*, 21-27. Retrieved in May 18, 2021, from http://worldcat.org/issn/03611981
Ubaldo, M.O., Motta, L.M.G., Fritzen, M.A., & Franco, F.A.C.P. (2019). Comparação entre avaliação de campo e o método de dimensionamento nacional em relação à deformação permanente. *Revista Estradas*, 23, 29-37. [in Portuguese]
Uzan, J. (1985). Characterization of granular materials. *Transportation Research Record: Journal of the Transportation Research Board*, (1022), 52-59. Retrieved in May 18, 2021, from http://worldcat.org/isbn/0309039118

Venkatesh, N., Heeralal, M., & Pillai, R. (2018). Resilient and permanent deformation behaviour of clayey subgrade soil subjected to repeated load triaxial tests. *European Journal of Environmental and Civil Engineering*, 1414-1429. http://dx.doi.org/10.1080/19648189.2018.1472041.

Zago, J.P., Pinheiro, R.J.B., Baroni, M., Specht, L.P., Delongui, L., & Sagrilo, A.V. (2021). Study of the permanent deformation of three soils employed in highway subgrades in the municipality of Santa Maria-RS, Brazil. *International Journal of Pavement Research and Technology*, 14, 729-739. http://dx.doi.org/10.1007/s42947-020-0129-6.

Zhang, J., Ding, L., Zheng, J., & Gu, F. (2020). Deterioration mechanism and rapid detection of performances of an existing subgrade in southern China. *Journal of Central South University*, 27, 2134-2147. http://dx.doi.org/10.1007/s11771-020-4436-5.

Soils and Rocks

An International Journal of Geotechnical and Geoenvironmental Engineering

www.soilsandrocks.com

ISSN 1980-9743
ISSN-e 2675-5475

CPTu-based approaches for cyclic liquefaction assessment of alluvial soil profiles

Catarina Ramos[1#], António Viana da Fonseca[1], Cristiana Ferreira[1]

Article

Keywords
Liquefaction
CPTu
Transition layers
Liquefaction Potential Index
Liquefaction Severity Number

Abstract

Over the years, methods to assess cyclic liquefaction potential based on piezocone penetration tests (CPTu) have been developed. This paper presents a comparative study between three CPTu-based methodologies, mainly in terms of the normalization procedures of overburden stresses, equivalent clean sand resistance, and magnitude scaling factor (*MSF*). Four CPTu profiles from a pilot site in southwest Portugal are thoroughly analysed with different methods, in terms of factor of safety against liquefaction, the Liquefaction Potential Index (*LPI*), and the Liquefaction Severity Number (*LSN*). The site presents very heterogeneous soil profiles, composed of alluvial deposits. Due to the presence of significant sand-silt–clay interbedded layers, the influence of transition zones and the use of different soil behaviour type index (I_c) cut-off values were also considered. From these analyses, a set of recommendations is presented for CPTu-based liquefaction assessment. Based on the extensive database of CPTu results in the pilot site area, a new classification relating *LPI* and *LSN* is proposed to assess liquefaction severity and damage.

1. Introduction

Over the last years, soil liquefaction has been one of the major topics discussed and studied in geotechnical earthquake engineering, since earthquake-induced liquefaction has caused significant damage in buildings and infrastructures (Cubrinovski et al., 2011; Aydan et al., 2012). The susceptibility of soils to liquefaction depends mainly on two aspects: the soil resistance to cyclic loading and the design seismic action (SA). While earthquakes are usually sudden and unexpected, the assessment of the seismic actions can be made using reference values, namely those provided in codes and standards, or by site-specific ground response analyses. However, the soil resistance to cyclic loading can be determined from laboratory or field-testing. Laboratory tests involve either the collection of high-quality samples, which requires expensive and very difficult procedures, or the preparation of reconstituted specimens, which may be less representative of the natural soil conditions. Therefore, the use of field tests is a simpler and more economical procedure.

The piezocone penetration test (CPTu) is a widely used field test, as it provides an almost nearly continuous soil profile information, based on the soil resistance and the pore pressure developed during penetration, and is more reliable and repeatable than the SPT (Robertson, 2012). Over the years, methods to evaluate liquefaction susceptibility based on different in situ tests have been developed (Robertson & Wride, 1998; Robertson, 2009; Moss et al., 2006; Idriss & Boulanger, 2008; Boulanger & Idriss, 2014). However, there is not much consensus concerning the best criteria for evaluating liquefaction resistance based on CPT results. According to each methodology, the correlations and normalization factors are obtained differently, since the expressions were derived from different earthquake databases that have been updated over the years.

Within the framework of the European H2020 LIQUEFACT project, an extensive database of CPTu was collected and complemented, to assess the earthquake-induced risk of soil liquefaction at the Lisbon region in Portugal. This work focuses on the detailed analysis of four soil profiles, in terms of factor of safety against liquefaction (FS_{liq}), Liquefaction Potential Index (*LPI*), and Liquefaction Severity Number (*LSN*), using Robertson (2009), Moss et al. (2006), and Boulanger & Idriss (2014) methodologies. These methods are compared and contrasted, highlighting the main differences in the normalization procedures, namely in terms of computation of overburden stresses, equivalent clean sand resistance, and magnitude scaling factor (MSF). Moreover, the impact of considering the transition layers correction and the influence of the soil behaviour type index (I_c) cut off value on LPI and LSN are discussed. In the end, a correlation between LPI and LSN is proposed and verified for 37 CPTu tests performed in the testing site area.

#Corresponding author. E-mail address: catarinacorreiaramos@gmail.com
[1]Faculdade de Engenharia da Universidade do Porto, Instituto de Investigação e Desenvolvimento de Estruturas e Construções, Porto, Portugal.

Submitted on May 3, 2021; Final Acceptance on August 11, 2021; Discussion open until February 28, 2022.
https://doi.org/10.28927/SR.2021.070121

2. Review of the methods for liquefaction assessment

2.1. Simplified stress-based approach

Seed & Idriss (1971) developed a simplified procedure to estimate the potential for cyclic liquefaction due to earthquake loading, introducing the factor of safety against the triggering of liquefaction (FS_{liq}). This factor of safety represents the ratio between the capacity of a soil to resist liquefaction (cyclic resistance ratio, *CRR*) and a measurement of the earthquake loading induced in the soil (cyclic stress ratio, *CSR*) (Equation 1). If the *CSR* is greater than the *CRR* (i.e. $FS_{liq} < 1$), cyclic liquefaction will likely occur.

$$FS_{liq} = \frac{CRR}{CSR} \tag{1}$$

To estimate *CSR*, a site-specific ground response analysis should be carried out. However, Seed & Idriss (1971) proposed a simplified method based on the peak ground acceleration (a_{max}), expressed in Equation 2, where g is the acceleration of gravity, σ_{vo} and σ'_{vo} are the initial total and effective vertical stresses, respectively, and r_d is a shear stress reduction coefficient. The r_d coefficient provides an approximated correction for flexibility of the soil profile as it is a function of the non-rigid response of the soil deposit. *MSF* and K_σ are adjustment factors to account for the earthquake magnitude and the overburden stress, respectively, and are discussed in section 2.2.

$$CSR = 0.65\left(\frac{a_{max}}{g}\right)\left(\frac{\sigma_{v0}}{\sigma'_{v0}}\right) r_d \frac{1}{MSF}\frac{1}{K_\sigma} \tag{2}$$

The *CRR* is a normalized value for an earthquake moment magnitude of 7.5 and effective vertical stress of 1 atm and can be obtained from correlations with field test results, namely the CPTu test. The *CRR* curve defines the boundary between liquefiable and non-liquefiable soils in the chart of *CSR versus* normalised cone resistance for clean sands.

The first "step" in the liquefaction assessment procedure based on CPT is to obtain the soil behaviour type index for each soil layer (Robertson, 1990). An iterative process relates the cone resistance (q_c), sleeve friction (f_s), and vertical stress (σ'_{vo}) normalization. The normalized cone resistance (Q_{tn}) and normalized friction ratio (F_r) are calculated using Equations 3 and 4 respectively, where σ'_{vo} is the initial effective vertical stress and σ_{vo} is the initial total vertical stress.

$$Q_{tn} = \left(\frac{q_c - \sigma_{v0}}{p_a}\right) \times \left(\frac{p_a}{\sigma'_{v0}}\right)^n \tag{3}$$

$$F_r = \left(\frac{f_s}{q_c - \sigma_{v0}}\right) \times 100\ \% \tag{4}$$

Over the years, the stress exponent (n) has been discussed and the most recent proposals (Robertson, 2009; Robertson, 2016), based on the critical-state soil mechanics framework, suggested that n varies with both I_c and effective overburden stress using Equation 5. The soil behaviour type index, which represents the normalised soil behaviour type (SBTn) zones in the $Q_{tn}-F_r$ chart, is defined by Equation 6 (Robertson & Wride, 1998).

$$n = 0.381 \times I_c + 0.05 \times \left(\frac{\sigma'_{v0}}{p_a}\right) - 0.15 \tag{5}$$

$$I_c = \left[\left(3.47 - \log Q_{tn}\right)^2 + \left(\log F_r + 1.22\right)^2\right]^{0.5} \tag{6}$$

According to the SBTn plot, $I_c < 1.31$ corresponds to gravel; $1.31 \leq I_c < 2.05$ is for sand; $2.05 \leq I_c < 2.60$ corresponds to silty sand to sandy silt; $2.60 \leq I_c < 2.95$ is for silty clay to clayey silt and $I_c \geq 2.95$ refers to clay.

As mentioned above, the *CRR* can be obtained using correlations with CPTu results. Youd et al. (2001) reported the recommendations from the NCEER/NSF workshops in 1996 and 1998 for liquefaction assessment based on CPT measurements. Since then, many researchers have provided improvements and alternatives considering more complete liquefaction case history databases and different assumptions. The present work explores three methodologies proposed by Robertson (2009), Moss et al. (2006), and Boulanger & Idriss (2014). To simplify the representation and discussion from hereon, the analysed methods are abbreviated to R2009, MEA2006, and B&I2014, respectively. The expressions used in each method are different as the quantity and quality of case histories has increased with recent earthquake events. The reinterpretation of the new and existing data allows for the evolution and update of these methodologies, from which new approaches to assess liquefaction have been devised.

The proposal from Robertson (2009) is an update from Robertson & Wride (1998), which is similar to the recommendations from Youd et al. (2001). The $CRR\text{-}Q_{tn,cs}$ curve was based on the proposal from Robertson & Campanella (1985), which in turn was derived from the CRR-SPT relationship from Seed et al. (1985), by applying the SPT blow count and equivalent CPT tip resistance relationships. Later, CPT data from liquefaction and no liquefaction case histories validated the curve. Robertson & Wride (1998) suggested a relationship between the normalized cone resistance for clean sands with the cyclic resistance ratio for an earthquake with 7.5 moment magnitude, depending on the resistance value, later updated by Robertson (2009). Equation 7 presents the expressions, based on the value of $Q_{tn,cs}$.

$$\begin{aligned} &if\ 50 \le Q_{tn,cs} \le 160 \qquad CRR_{7.5} = 93\left[\frac{Q_{tn,cs}}{1000}\right]^3 + 0.08 \\ &if\ Q_{tn,cs} < 50 \qquad CRR_{7.5} = 0.833\left[\frac{Q_{tn,cs}}{1000}\right]^3 + 0.05 \end{aligned} \quad (7)$$

The method from Moss et al. (2006) is strongly based on Cetin (2000) and Cetin et al. (2004). This method was developed directly from measured CPT data and included about 200 liquefaction and no liquefaction case histories. The proposed relationship is probabilistic, however, they suggested the consideration of P_L = 15% for deterministic purposes and comparison with other methods, where P_L is the probability of liquefaction occurrence. Moss et al. (2006) presented a correlation that employs a larger database of high-quality field case histories, using a Bayesian framework to account for all the uncertainties associated with seismic demand and liquefaction resistance. Equation 8 presents the expression used to calculate CRR, where $q_{c,1}$ is the normalized tip resistance (in MPa), R_f is the friction ratio (f_s/q_c, in percent), c is a normalization exponent, M_w is the moment magnitude, σ'_v is the effective vertical stress, and $\Phi^{-1}(P_L)$ is the inverse cumulative normal distribution function.

$$CRR = \exp\left\{\frac{\left[\begin{aligned} &q_{c,1}^{1.045} + q_{c,1}\left(0.110R_f\right) + \left(0.001R_f\right) + c\left(1 + 0.850R_f\right) \\ &-0.848\ln M_w - 0.002\ln\sigma'_v - 20.923 + 1.632\Phi^{-1}\left(P_L\right) \end{aligned}\right]}{7.177}\right\} \quad (8)$$

On the other hand, Boulanger & Idriss (2014) re-evaluated liquefaction triggering procedures and presented an update for the Idriss & Boulanger (2008) method, including data from recent earthquakes. The case history database was updated and the CRR curve changed slightly. This method, like MEA2006, was also derived directly from CPT case histories. The proposed correlation between $CRR_{7.5}$ and the normalized cone resistance for equivalent clean sand, q_{c1Ncs}, is presented in Equation 9.

$$CRR_{7.5} = \exp\left(\frac{q_{c1Ncs}}{113} + \left(\frac{q_{c1Ncs}}{1000}\right)^2 - \left(\frac{q_{c1Ncs}}{140}\right)^3 + \left(\frac{q_{c1Ncs}}{137}\right)^4 - 2.8\right) \quad (9)$$

A common feature of the three methods is the use of an equivalent clean sand cone resistance to determine *CRR*. However, the normalizations are based on different assumptions, as presented in Table 1.

Robertson (2009) and Moss et al. (2006) methods infer the effect of fines (fines content and plasticity) from the CPT tip and sleeve measurements, as well as from the soil behaviour type index. On the other hand, Boulanger & Idriss (2014) method developed the fines content (FC) adjustment with information from case history databases, with measurements of FC from soil samples.

Table 1 summarises and evidences the differences between the methods, namely in terms of the calculation of equivalent clean sand resistance. Robertson & Wride (1998) suggested a method to calculate the apparent fines content directly from CPT results, as I_c increases with increasing apparent fines content and soil plasticity. However, since the CPT penetration resistance is also influenced by other grain characteristics, such as mineralogy, plasticity, sensitivity, and stress history, they proposed the use of a correction factor, K_c, based on the I_c.

On the other hand, MEA2006 uses an additive factor as equivalent clean sand adjustment, despite computing *CRR* from q_{c1N} and not from the equivalent clean sand resistance. The CPT normalization for overburden stress is based on cavity expansion models, in conjunction with field and laboratory tests and corresponds to a function of cone tip resistance and friction ratio (Moss et al., 2006). Note that the normalization for overburden stress is performed similarly on R2009 and B&I2014, only changing the formulas of the stress exponents.

Boulanger & Idriss (2014) proposed an equivalent clean sand adjustment, empirically derived from liquefaction case history data, which was guided by the trends in q_c/N_{60} ratios versus FC (Idriss & Boulanger 2008). The proposal involves an iterative process with q_{c1Ncs} and the value of fines content, to take into account the increase of cyclic resistance with fines content.

2.2. Adjustment factors

As the basis of the simplified stress-based formulation from Seed & Idriss (1971) was intended for a reference earthquake magnitude of 7.5 (corresponding to an equivalent number of cycles of 15) and an effective stress of 1 atm, adjustment factors were proposed to account for sites with different conditions. These adjustment factors include the magnitude scaling factor, *MSF*, that reflects the duration of shaking and the associated number of loading cycles, and the overburden correction factor, K_σ, to account for the effect of the effective vertical stress, as well as the shear stress reduction coefficient, r_d. These normalization parameters are calculated differently, according to the method used, as presented in Table 2.

Robertson (2009) adjustment factors are based on the first considerations of Seed & Idriss (1971), when they proposed the simplified procedure. Following the proposal by Robertson & Wride (1998), the *MSF* is only dependent on the earthquake magnitude, and r_d is only influenced by depth. However, Robertson (2009) introduced an update regarding K_σ. The influence of the overburden stress is reflected in the general regression, in the form of the stress exponent *n*. As for MEA2006, this method derived the adjustment factors directly from the liquefaction case history database and included the magnitude in the regression to compute CRR (as shown in Table 1). Moss et al. (2006) reassessed the r_d expression from Cetin et al. (2004) using the ground response, being more representative of the induced cyclic shear stress. However, the majority of case history databases

Table 1. Calculation parameters for equivalent clean sand resistance according to the method.

	Robertson (2009)	Moss et al. (2006)	Boulanger & Idriss (2014)
Equivalent clean sand resistance	$Q_{tn,cs} = K_c Q_{tn}$	$q_{c,1,mod} = q_{c,1} + \Delta q_c$	$q_{c1Ncs} = q_{c1N} + \Delta q_{c1N}$
Factor to account for behaviour/fines content	$K_c = 1.0 \ if \ \ I_c \le 1.64$ $K_c = -0.403 I_c^{\,4} + 5.581 I_c^{\,3} - 21.63 I_c^{\,2}$ $+33.75 I_c - 17.88 \quad if \ I_c > 1.64$	$\Delta q_c = \left(0.38 R_f - 0.19\right) \ln CSR +$ $\left(1.46 R_f - 0.73\right)$	$\Delta q_{c1N} = \left(11.9 + \frac{q_{c1N}}{14.6}\right)$ $\exp\left(1.63 - \frac{9.7}{FC+2} - \left(\frac{15.7}{FC+2}\right)^2\right)$
Normalized cone resistance for overburden stress	$Q_{tn} = \left(\frac{q_t - \sigma_{vo}}{p_a}\right) \times \left(\frac{p_a}{\sigma'_{vo}}\right)^n$	$q_{c,1} = C_q q_c$ $C_q = \left(\frac{p_a}{\sigma'_v}\right)^c \le 1.7$	$q_{c1N} = C_N \frac{q_t}{p_a}$ $C_N = \left(\frac{p_a}{\sigma'_{vo}}\right)^m \le 1.7$
Stress exponent	$n = 0.381 \times I_c + 0.05 \times \left(\frac{\sigma'_{vo}}{p_a}\right) - 0.15$	$c = f_1 \left(\frac{R_f}{f_3}\right)^{f_2}$ $f_1 = 0.78 q_c^{-0.33}$ $f_2 = -\left(-0.32 q_c^{-0.35} + 0.49\right)$ $f_3 = \text{abs}\left[\log(10 + q_c)\right]^{1.21}$	$m = 1.338 - 0.249 \left(q_{c1Ncs}\right)^{0.264}$
Apparent fines content	$FC(\%) = 0 \ if \ I_c < 1.26$ $FC(\%) = 1.75 I_c^{3.25} - 3.7 \ \ if \ 1.26 \le I_c \le 3.5$ $FC(\%) = 100 \ \ if \ I_c > 3.5$	-	$FC(\%) = 80\left(I_c + C_{FC}\right) - 137$ C_{FC} considered 0

Table 2. Adjustment factors for each method.

	Robertson (2009)	Moss et al. (2006)	Boulanger & Idriss (2014)
Stress coefficient	$r_d = 1.0 - 0.00765 z$ $for \ z < 9.15 m$ $r_d = 1.174 - 0.0267 z$ $for \, 9.15 m < z < 23 m$	$r_d = \frac{\left[1 + \frac{-9.147 - 4.173 \cdot a_{max} + 0.652 \cdot M_w}{10.567 + 0.089 \cdot e^{0.089 \cdot (-d \cdot 3.28 - 7.760 \cdot a_{max} + 78.576)}}\right]}{\left[1 + \frac{-9.147 - 4.173 \cdot a_{max} + 0.652 \cdot M_w}{10.567 + 0.089 \cdot e^{0.089 \cdot (-7.760 \cdot a_{max} + 78.576)}}\right]}$	$r_d = \exp\left[\alpha(z) + \beta(z).M\right]$ $\alpha(z) = -1.012 - 1.126 \sin\left(\frac{z}{11.73} + 5.133\right)$ $\beta(z) = 0.106 + 0.118 \sin\left(\frac{z}{11.28} + 5.142\right)$
MSF	$MSF = \frac{10^{2.24}}{M_w^{\ 2.56}}$	$DWF_M = 17.84 \Delta M_w^{\ -1.43}$	$MSF = 1 + \left(MSF_{max} - 1\right)\left(8.64 \exp\left(\frac{-M}{4}\right) - 1.325\right)$
K_σ	1	1	$K_\sigma = 1 - C_\sigma \ln\left(\frac{\sigma'_v}{p_a}\right) \le 1.1$ $C_\sigma = \frac{1}{37.3 - 8.27 (q_{c1Ncs})^{0.263}} \le 0.3$

were limited to earthquake magnitudes between 6.9 and 7.6 (computing *MSF* close to 1) and effective stresses around 50 to 120 kPa. Outside these intervals, care should be taken, as the regressions may not be appropriate. On the other hand, Boulanger & Idriss (2014) considered the equivalent clean sand cone resistance in the calculations of *MSF* and K_σ and added the moment magnitude to the calculation of r_d, along with depth, making the parameters more dependent on soil type. B&I2014 applied a cap for small values of magnitude (M_w < 5.25). Moreover, the *MSF* is dependent on a soil type parameter, being related to the equivalent clean sand resistance.

In sum, each method presents its specific considerations, and should be applied consistently with its adjustment factors. In this work, the analyses were made by critically comparing the results without any direct or weighted averaging (such as in logic tree approaches), as the combination of methods can led to unrealistic solutions.

2.3. Liquefaction Severity Indices

The factor of safety provides information about whether liquefaction is likely to occur or not, but it does not give indications about the severity of the manifestation or its cumulative effect along the soil profile. Therefore, liquefaction severity indices were developed to study the damage potential and severity of surface manifestations of liquefaction. These qualitative methods have the advantage of providing a quantitative classification of the overall liquefaction response of the entire soil profile. However, by being computed as the sum of the behaviour of each data point individually, instead of the different macro layers, the values of these indices may be, in some cases, inaccurate or misleading, especially since these do not account for cross-interactions between different layers during the development of liquefaction and post-liquefaction, as discussed by Cubrinovski et al. (2019).

One of these frameworks is the liquefaction potential index (*LPI*), proposed by Iwasaki et al. (1978), which translates the liquefaction potential damage. The *LPI* is mainly dependent on the factor of safety and is defined as:

$$LPI = \int_{0}^{20\,m} F_1 w(z)\,dz \tag{10}$$

where $F_1 = 1 - FS_{liq}$ for $FS_{liq} \leq 1.0$ and $F_1 = 0$ for $FS_{liq} > 1$ and $w(z) = 10 - 0.5z$ for $0 \leq z \leq 20$ m and $w(z) = 0$ for $z > 20$ m, where FS_{liq} is the factor of safety and z is the depth above ground surface in meters. Iwasaki et al. (1978) defined the liquefaction severity as minor for $0 < LPI \leq 5$, moderate for $5 < LPI \leq 15$ and major for $LPI > 15$. Other authors suggested slightly different intervals (Toprak & Holzer, 2003; Lee et al., 2003; Sonmez, 2003).

To indicate the liquefaction-related vulnerability of residential dwellings, a parameter was developed by Tonkin & Taylor (Tonkin & Taylor, 2013; GeoLogismiki, 2017), named Liquefaction Severity Number (*LSN*). Equation 11 defines this parameter, which considers the volumetric densification strain within soil layers (ε_v) proposed by Zhang et al. (2002) and a power law for a depth weighting factor ($1/z$). The calculation of ε_v is a function of FS_{liq} and relative density, and describes the expected post-liquefaction volumetric deformations.

$$LSN = 1000 \int_{0}^{10\,m} \frac{\varepsilon_v}{z}\,dz \tag{11}$$

Based on this parameter, the liquefaction severity was defined as little to no expression for $LSN < 10$, minor for $10 < LSN < 20$, moderate for $20 < LSN < 30$, moderate to severe for $30 < LSN < 40$, major for $40 < LSN < 50$, and severe damage for $LSN > 50$. van Ballegooy et al. (2012) did not define a specific depth, while other researchers adopted *LSN* for the first 20 m of depth (Giannakogiorgos et al., 2015; Maurer et al., 2015). For clarity, a comparative analysis is presented in this work, emphasising the influence of considering the first 10 m (LSN_{10}) or 20 m (LSN_{20}) of the soil profile.

3. Experimental program

The experimental program was developed as part of the activities of European project LIQUEFACT for the microzonation for earthquake-induced risk of soil liquefaction at the Lisbon area in Portugal (Viana da Fonseca et al., 2019a). Several CPTu tests were performed in the municipalities of Benavente and Vila Franca de Xira, in Lisbon, Portugal, from which a selection is analysed and discussed in detail in this work. Historical records show that this zone is prone to liquefaction, as observed during historical earthquakes in the area (Jorge & Vieira, 1997). The geological, geomorphological, and seismic characteristics of the site emphasise this susceptibility due to the presence of recent alluvial sand deposits in a high seismicity zone (Ferreira et al., 2020). The pilot site is located in the Lower Tagus Valley and is composed of fluvial and marine sediments, from the Pliocene to Holocene, and presents stratification irregularities, with lenticular or bevelled layers, due to the sedimentation processes. Viana da Fonseca et al. (2019b) described the area in detail. In this work, four CPTu were analysed in detail, namely SI1, SI7, NB1, and NB2, and another 33 CPTu were used to verify the proposed *LPI*−*LSN* correlation, which locations are presented in Figure 1.

The CPTu were performed according to the procedures prescribed in the European standard (ISO, 2012), with recording measurements of cone tip resistance (q_c), sleeve friction (f_s), and pore pressure (u) every 1 cm depth, providing an almost continuous profile of the soils.

The four selected sites are constituted by alluvial sand deposits with clay-silt-sand interlayers, as is observed in Figure 2. SI1 presents many clay-sand interlayers. However, two sandy layers are identified at around 2 m to 3 m and from 5 m to 7 m, this last layer interbedded with two clay layers. SI7 is very heterogeneous with no clear sand layer, but many interlayers between 6 m to 14 m. NB1 presents a distinct sand layer at around 4 m to 7 m. In NB2, between 5 m and 13 m, the layers are mostly constituted of sand with some small-interbedded clays. These different profiles will help define the influence of the different layers in the liquefaction assessment of soil profiles.

4. Results

4.1. Factor of safety against liquefaction

As described above, each CPTu profile was analysed using the three methods. The seismic considerations followed

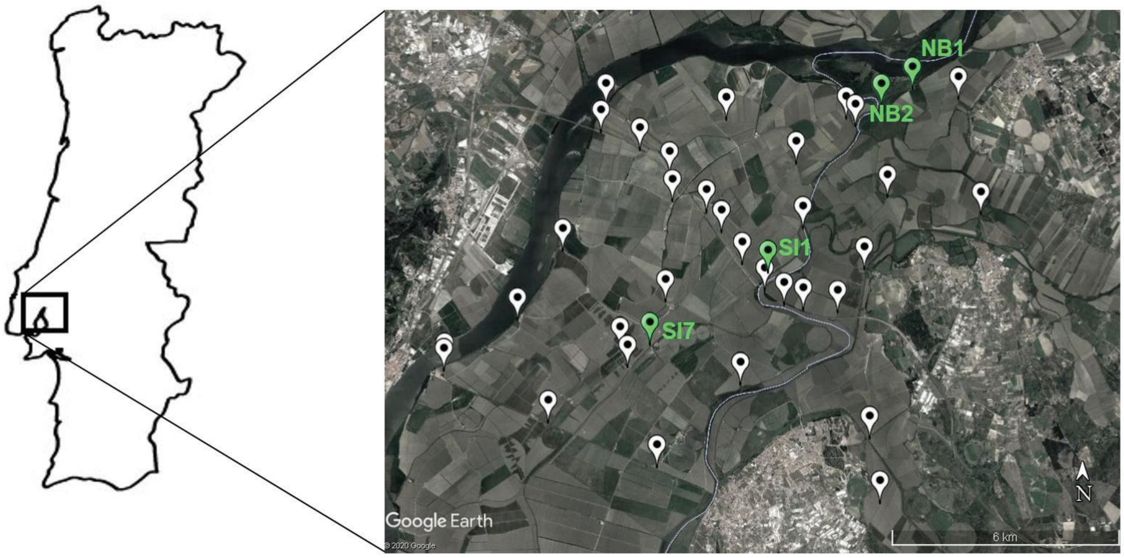

Figure 1. Location of the CPTu testing sites in the LIQUEFACT pilot site area.

the procedures included in the European Standard Eurocode 8 and the National Annex of Portugal (BSI, 2004, 2010). The seismic action was calculated for a return period of 475 years and ground type D, as the deposits were considered loose-to-medium cohesionless soil (Ferreira et al., 2020). The peak ground acceleration, a_{max}, considered at ground surface, was defined as 0.20g and 0.31g, for type 1 and 2 of seismic action (SA) respectively. As for the magnitude moment, EN 1998-5 (BSI, 2004) defines 7.5 and 5.2 for SA types 1 and 2, respectively, for the municipalities of Vila Franca de Xira and Benavente.

Figure 2 presents the profiles of cone resistance (q_c) and pore pressure (u), soil behaviour type index (I_c), and the factor of safety against liquefaction (FS_{liq}) for SA type 1, calculated according to Equation 1 for the three methods. Detailed SA type 2 results are available elsewhere (Ramos, 2021). Only FS_{liq} for layers with $I_c < 2.60$ are represented, as $I_c = 2.60$ corresponds to FC of approximately 35% in the Robertson (2009) method, and was defined in this work as the limit value for the occurrence of liquefaction. For SI1, a photograph of one of the SPT samples collected at around 4 m depth is also presented, where the interlayers are evident, with a clear distinction between thin layers of sand and clay.

SA type 1 is characterized by a lower a_{max} and higher M_w. In this case, the magnitude corresponds to the reference value of 7.5, so *MSF* is 1 and does not affect the results. In the more interlayered profiles, SI1 and SI7, the R2009 and MEA2006 methods compute more conservative results, showing lower FS_{liq} values. However, in the more homogeneous layers (for example between 4 m and 7 m in NB1 or between 5 m to 14 m in NB2), the B&I2014 is more conservative, generally resulting in lower values of FS_{liq}. Despite these differences, it is perceptible that all methods identify the same critical layers, being B&I2014 the most conservative in general, as it delivers lower values of FS_{liq}. These results also show that CPTu profile influences the prediction of liquefaction by the different methods, which is why consistency is important. The differences among the three methods are not easily distinguishable in the form of Figure 2. Therefore, in the following section, the analyses will be based only on *LPI* and *LSN*, which indirectly show the differences in FS_{liq}.

4.2. LPI and LSN

As mentioned above, the factor of safety against liquefaction is insufficient to provide indications about the severity of the manifestation or the cumulative effect throughout the soil profile. To better understand the influence of the different methods and assess the damages induced in the soil in case of liquefaction, the liquefaction potential index, *LPI* (Figure 3), and the liquefaction severity number, *LSN* (Figure 4), were analysed for the four profiles using the three methods.

For the *LPI*, the SA type plays an important role, as evidenced in the comparison of Figure 3a and 3b. The values from R2009 decrease significantly for SA type 2 (higher a_{max} and lower M_w) while B&I2014 values increase. The values of MEA2006 are nearly unaffected by SA type, despite a minor decrease for type 2. As expected, the soil profile highly influences the results. All soil profiles exhibit a high to very high risk of liquefaction, except for NB1 and NB2 for R2009 method with seismic action type 2. Once again, R2009 demonstrates higher dependency with *MSF*, since for the lower value of M_w ($M_w = 5.2$), the computed *MSF* value is very high, thus strongly decreasing *CSR* and delivering higher FS_{liq} values, hence lowering *LPI*.

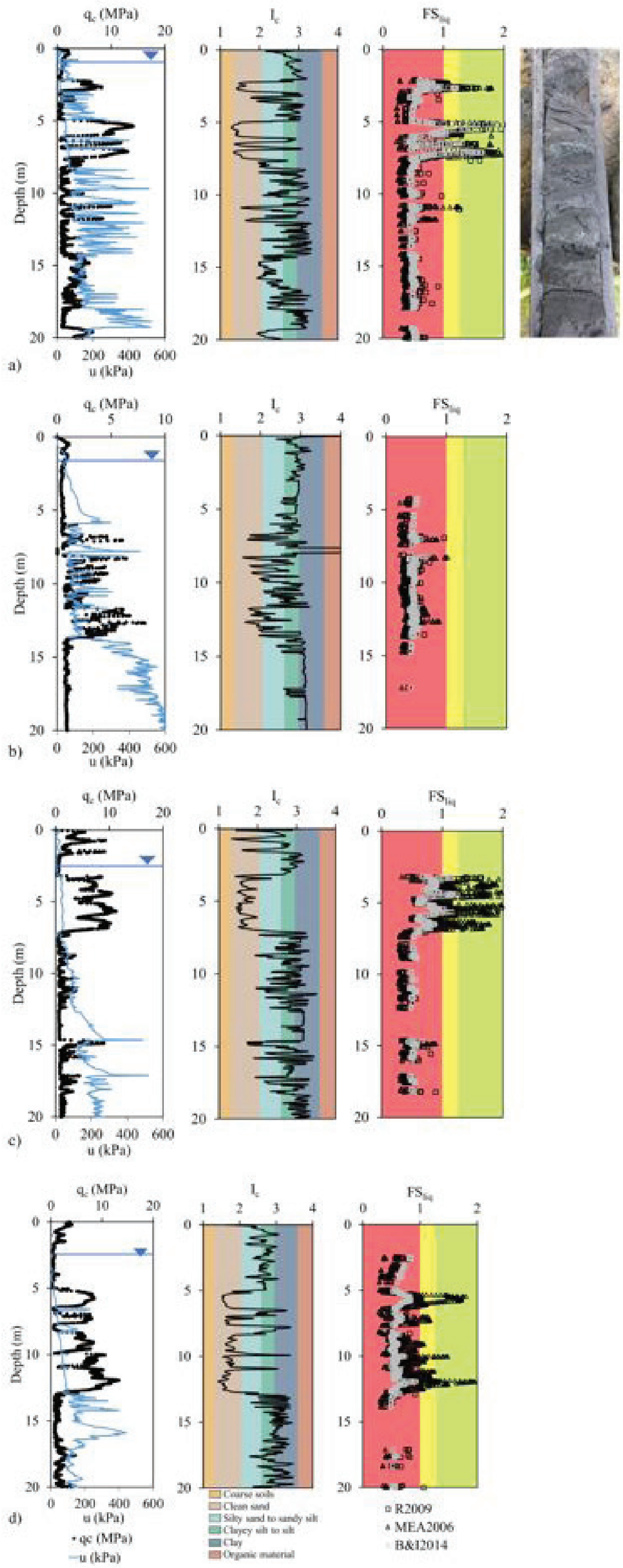

Figure 2. CPTu results in the experimental sites: (a) SI1 (including a photograph of the SPT sample collected at 4 m); (b) SI7 (c) NB1; (d) NB2.

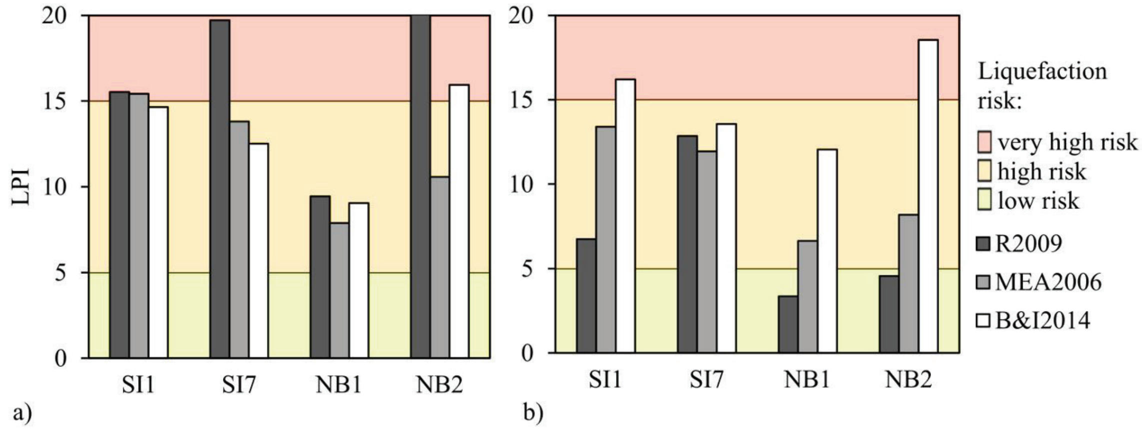

Figure 3. LPI results: (a) SA type 1, (b) SA type 2.

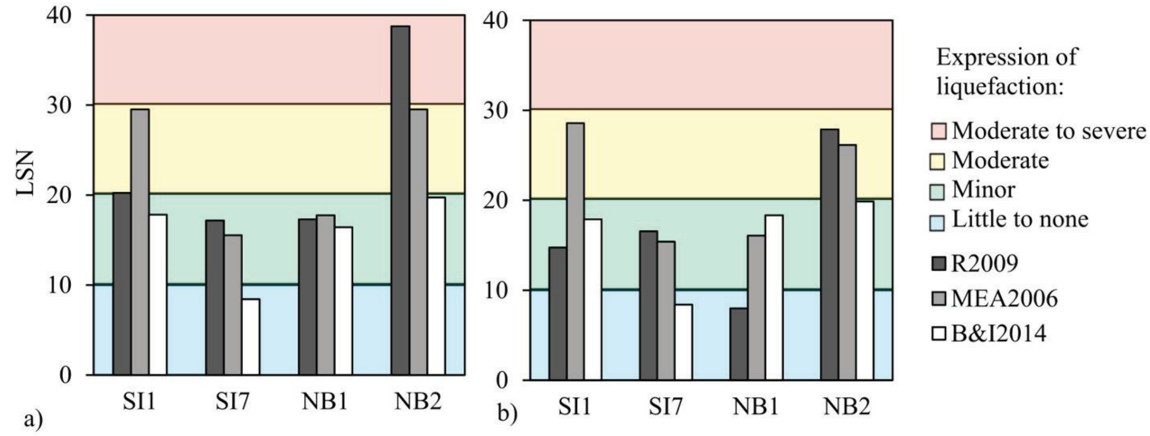

Figure 4. LSN_{10} results: (a) SA type 1, (b) SA type 2.

As for *LSN*, the differences are not so significant. Once more, the selection of the method influences the trends and the differences between the two SA types. R2009 method is the most affected by seismic action parameters, as *MSF* strongly varies according to the moment magnitude, producing higher values of FS_{liq} for SA type 2. In turn, MEA2006 and B&I2014 are less influenced by the SA type, since ε_v calculation depends on FS_{liq}. In effect, Zhang et al. (2002) calculation of ε_v considers a minimum FS_{liq} of 0.5, and since most FS_{liq} values for MEA2006 and B&I2014 are close to or lower than 0.5, the changes due to seismic action type are not visible. This also justifies the nearly identical results for SI7, even from R2009 method. The more interlayered profiles, SI1 and SI7, reveal minor to moderate expression of liquefaction. NB1 presents a minor expression of liquefaction, while NB2 is the most critical profile, presenting moderate to severe liquefaction expression. This is a consequence of the type of soils above 10 m, composed mainly of sands and silty sands with low FS_{liq}. Besides, it is interesting to note that the Zhang et al. (2002) method was proposed based on the $Q_{tn,cs}$ definition of Robertson & Wride (1998). However, in current practice, it can be assumed that the effect of the new definitions of the normalized cone tip resistance (according to Boulanger & Idriss, 2014) is expected to be negligible. Therefore, the use of Zhang et al. (2002) method with the safety factors computed according to B&I2014 is considered viable and reliable (as currently available in the CLiq software). Note that *LPI* is calculated for the layers where FS_{liq} is lower than 1.0, up to a depth of 20 m, while *LSN* is calculated for the first 10 m depth and with FS_{liq} lower than 2.0. For this reason, the two indices are not directly comparable. Nevertheless, it can be concluded that the tested area has a high to very high risk of liquefaction and minor to moderate expression of liquefaction damage. In an attempt to relate the results of *LPI* and *LSN*, *LSN* was calculated considering the first 20 m of depth (LSN_{20}). Figure 5 presents these results for SA types 1 and 2, showing that, as expected, the values are higher than those in Figure 4.

4.3. Consideration of other factors

As stated by Robertson & Wride (1998), the cone resistance is influenced by the soils ahead and behind the cone

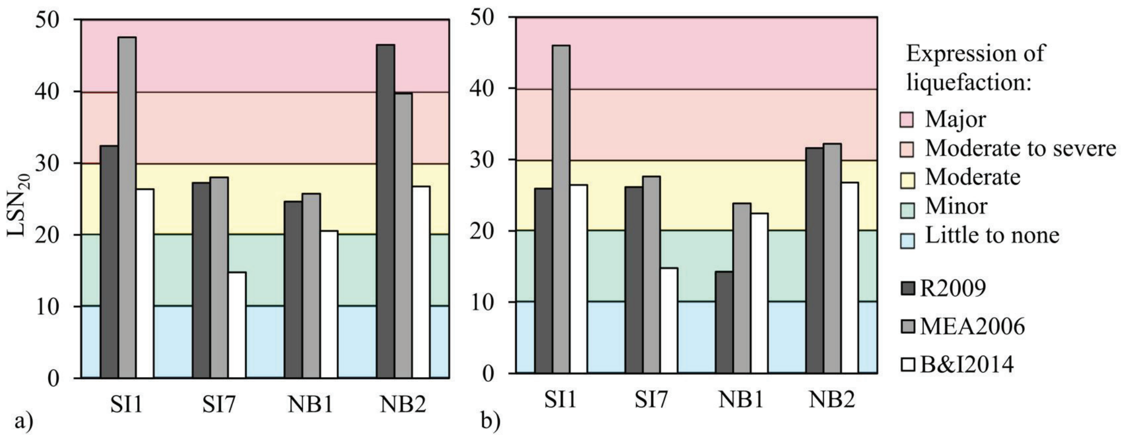

Figure 5. LSN_{20} results considering the first 20 m: (a) SA type 1, (b) SA type 2.

tip. Near the interface of two distinct soil layers, the changes in CPTu measurements are difficult to interpret and may be misleading. When the cone is moving from one soil type to another, especially if there is a significant difference in soil stiffness or strength (e.g. soft clay to sand), the CPT data within the transition zone is usually excessively conservative. This is particularly relevant when dealing with thinly interbedded soil. The analysed soil profiles are very heterogeneous, with sand-clay interlayers that affect the sensitivity of the CPTu measurements (see Figure 2). Considering the existence of such interlaying, a complementary analysis was performed excluding the transitional layers from the calculations, as a means to highlight and detect the differences between the consideration (or not) of those layers in the liquefaction assessment frameworks.

This procedure is already implemented in Cliq®, the software used to perform the CPTu calculations (version v.2.2.0.37, GeoLogismiki, 2017). The range of I_c where the transitional layers can be found was set to $1.80 < I_c < 3.00$ as these were the values considered to include silts and sandy silts. The transitional points are found when the I_c changes rapidly, defined as a rate of $\Delta I_c = 0.01$, where ΔI_c is the I_c change in a given thickness (Yi, 2018). The analysis presented below refers only to seismic action type 1, as the comparison between the two seismic actions was identical to the previous discussion.

Figure 6a presents the *LPI* and LSN_{20} values obtained with the correction of transitional layers, overlapping the results considering all layers. The values considering the correction of transitional layers are significantly lower, and consequently, the liquefaction hazard is lower than when considering all layers. It can be concluded that the initial analysis might be very conservative and the elimination of transitional layers increases the convergence of results of *LPI* and LSN_{20}. For the *LPI*, R2009 and B&I2014 are more conservative than MEA2006 and all methods are highly dependent on the soil type profile. For the LSN_{20}, the transition layer correction affects especially SI1 and SI7, which was expected, since these are the most interlayered profiles.

The $I_c = 2.60$ is normally considered as the cut-off between liquefiable and non-liquefiable soils (Robertson, 2009), corresponding to 35% of FC. However, R2009 and B&I2014 present very distinct relationships between FC and I_c. For $I_c = 2.6$, FC is around 70% in B&I2014 approach. These differences highlight the importance of the sensitivity study, using different I_c cut-off values, for the B&I2014 method, presented in Figure 6b. The values selected were $I_c = 2.80$ (a higher value to account for fine-grained soils with potentially low plasticity), $I_c = 2.60$ (the value suggested by R2009 and used throughout this work), $I_c = 2.15$ (I_c for FC = 35% in B&I2014) and $I_c = 2.35$ (an intermediate value suggested by Ferreira et al. 2020). The values of *LPI* and LSN_{20} decrease when considering lower I_c cut-off values, which is understandable as lower I_c values correspond to the consideration of fewer layers. The differences are considerable as the soil profiles are composed of many sandy silt and silty sand layers. It is important to note that I_c cut-off of 2.80 is only reasonable if the fines fraction has very low plasticity.

The selection of I_c cut-off value is a pertinent issue, since it expresses the typical behaviour of each soil layer, encompassing a variety of grain characteristics, not only the fines content. The choice of the I_c cut-off is, therefore, very conditioning, as it influences the layers considered in the calculations. Previous research (Boulanger & Idriss, 2014) stated that there is a lot of scattering when dealing with relationships between FC and I_c, likely due to the different plasticity of the fines. A soil with the same fines content can present low or high plasticity, which influences the soil to behave more like a sand (low plasticity) or a clay (high plasticity). This issue was also addressed by Facciorusso et al. (2019), when comparing the LPI obtained with various CPTu-based methods and considering different I_c cut-off values. They concluded that, if intermediate soils are considered, an increase of the cut-off from 2.6 to 2.7 can determine a significant increase in LPI. Therefore, if large differences in

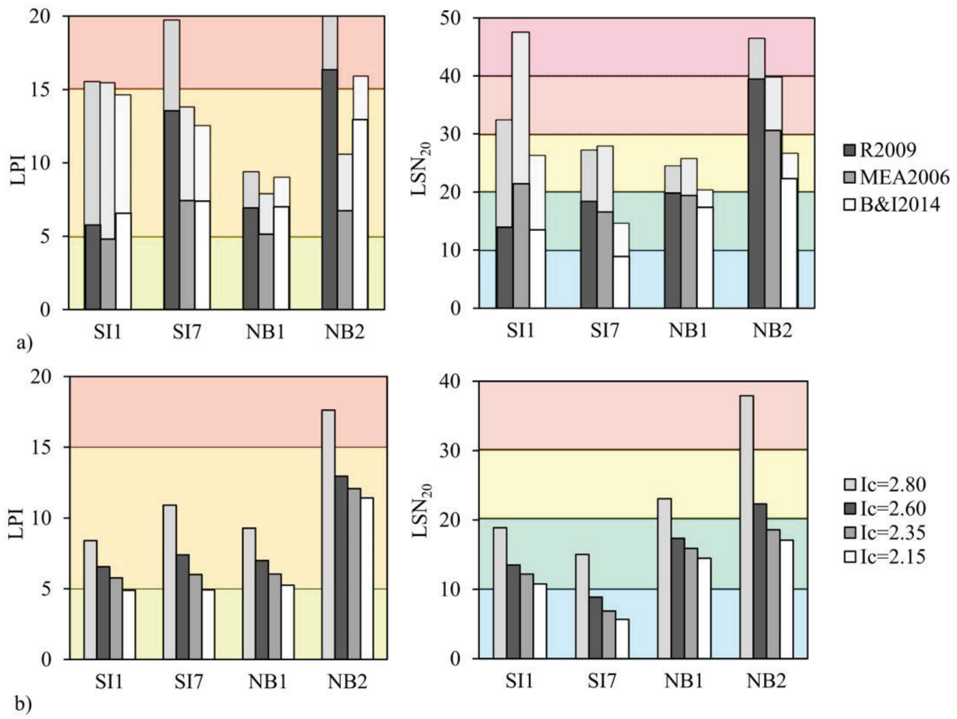

Figure 6. Impact of the consideration of different factors on the liquefaction hazard: (a) transitional layers, (b) I_c cut-off values.

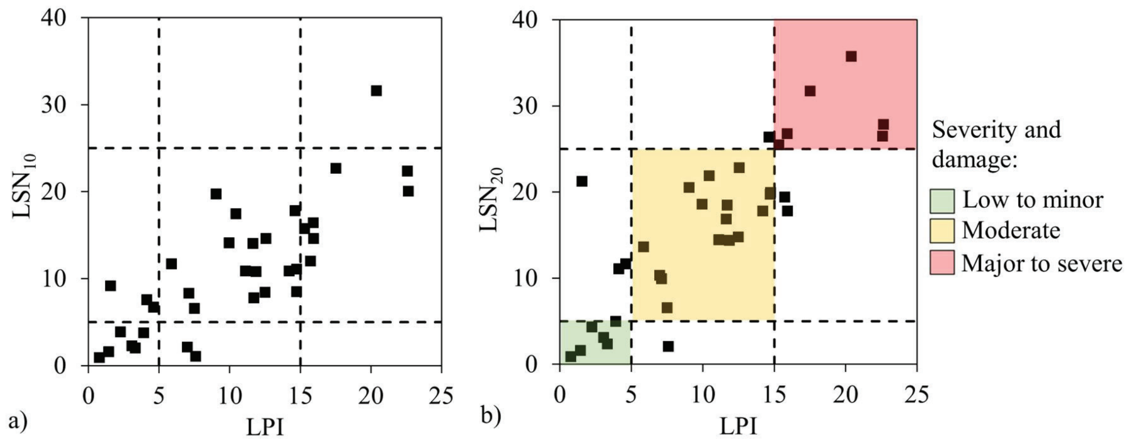

Figure 7. Severity and damage assessment using LPI and LSN results: (a) LSN_{10}, (b) LSN_{20}.

LPI are detected when adopting different I_c cut-off values, direct measurement of FC and plasticity index should be collected and integrated in the analyses. Estimates of the plasticity index (*PI*) from CPTu results are particularly difficult, due to the lack of substantial comparative results in the existing databases. Therefore, a sensitivity analysis should be performed to assess the effect of this parameter in the global liquefaction assessment.

5. Analysis and discussion

The comparison between *LPI* and *LSN* is not straightforward, as the original formulations state that *LPI* is calculated for the first 20 m and *LSN* for the first 10 m of the soil profile. However, to allow for a more direct comparison between the two indices, the *LSN* was also calculated for the first 20 m, and designated as LSN_{20}. This approach led to a convergence of the qualitative results of *LPI* and LSN_{20}, as the same critical layers were considered. Figure 7 presents the relationships between *LPI* and *LSN*, calculated for the first 10 m and 20 m, for the 4 analysed profiles together with other 33 CPTu tests, of the same pilot site (see Figure 1). The results were obtained using B&I2014 method for SA type 1. As expected, the consideration of LSN_{20} reduces the dispersion of the data points, thus increasing the compatibility of the expected liquefaction severity and damage. As a result, a classification based severity and damage assessment using both values of *LPI* and LSN_{20} is proposed in Figure 7b.

A critical analysis is recommended, as some points appear outside the selected limits but close to the boundaries, revealing the expected damage. The proposed severity and damage boundaries are: low to minor (LPI < 5 and LSN_{20} < 5), moderate (5 < LPI < 15 and 5 < LSN_{20} < 25) and major to severe (LPI > 15 and LSN_{20} > 25). It is important to state that this is a conceptual approach based on the current case study profiles, using *LPI* and *LSN* from CPTu results, not considering observed liquefaction damages. Some other works have suggested an *LPI-LSN* classification chart based on observed liquefaction manifestations after the Emilia-Romagna 2012 earthquake and the 2010–2011 Canterbury earthquake sequence (Giannakogiorgos et al., 2015; Papathanassiou et al., 2015). However, in this case, no data were available for that analysis.

6. Conclusions

A set of four CPTu tests was selected, from an extensive database of field tests performed at a pilot site in Vila Franca de Xira and Benavente, in Portugal, and thoroughly analysed to study the differences between various liquefaction assessment approaches, namely those proposed by Robertson (2009), Moss et al. (2006), and Boulanger & Idriss (2014). From the results, the following conclusions were drawn:

- The importance of consistency when using a CPTu-based liquefaction assessment method has been highlighted. Therefore, the implementation of averaging or logic tree approaches (Lai et al., 2020) is not recommended as it contradicts the coherence of the analyses discussed above;
- The authors propose the use of Boulanger & Idriss (2014) method, also recommended by Cubrinovski (2016). This method considers the effect of fines content, by directly introducing the fines content values in the calculations, which facilitates the use of laboratory grading data. Furthermore, the methodology was also developed for standard penetration tests (SPT) allowing to contrast and compare results from both tests. Besides, the B&I2014 is the most recent method, and is based on the largest dataset of liquefaction cases, including the 2010-2011 Canterbury earthquake sequence in New Zealand and the 2011 Tohoku earthquake in Japan, which were not available in the past. This methodology was also adopted for the analysis of an extensive database, developed under the LIQUEFACT project (Ferreira et al., 2020; Lai et al., 2020);
- The elimination of transitional layers, and the consideration of different I_c cut-off values when dealing with interbedded profiles is recommended. The I_c value expresses the typical behaviour of each soil layer, encompassing a variety of grain characteristics, not only the fines content. The plasticity of the fines is often responsible for the scatter when dealing with relationships between FC and I_c. As estimates of *PI* from CPTu results are particularly difficult, the sensitivity analysis considering different values of I_c cut-off allows for a more accurate global liquefaction assessment;
- A new classification chart relating LPI and LSN_{20} values was proposed to assess liquefaction severity and damage, based on an extensive database of CPTu results in the pilot site area;
- For larger projects, the CPTu results are fundamental to assess soil stratigraphy, resistance, and susceptibility to liquefaction, providing crucial information for additional field-testing and high-quality sampling.

Acknowledgements

The authors would like to acknowledge the Portuguese Foundation for Science and Technology (FCT) through the PTDC/ECM-GEO/1780/2014 (LIQ2PROEARTH) research project and the FCT Grant SFRH/BD/120035/2016, which supported this work at FEUP. This work was possible under the activities of the LIQUEFACT project ("Assessment and mitigation of liquefaction potential across Europe: a holistic approach to protect structures/infrastructures for improved resilience to earthquake-induced liquefaction disasters") funded by the European Union's Horizon 2020 research and innovation programme under grant agreement No. GAP-700748. This work was also financially supported by UIDB/04708/2020 and UIDP/04708/2020 of CONSTRUCT - Institute of R&D in Structures and Construction, funded by national funds through the FCT/MCTES (PIDDAC).

Declaration of interest

The authors declare there are no conflicting interests.

Authors' contributions

Catarina Ramos: conceptualization, data curation, formal analysis, funding acquisition, investigation, methodology, visualization, writing – original draft. António Viana da Fonseca: conceptualization, funding acquisition, methodology, project administration, supervision, validation, writing – review & editing. Cristiana Ferreira: conceptualization, investigation, methodology, visualization, validation, writing – review & editing.

List of symbols

ε_v	volumetric densification strain
σ_{vo}	initial vertical total stress
σ'_{vo}	initial vertical effective stress
σ'_v	vertical effective stress
$\Phi^{-1}(P_L)$	inverse cumulative normal distribution function

ΔI_c I_c	change in a given thickness
a_{max}	peak ground acceleration
B_q	pore pressure parameter ratio
C_{FC}	fines content fitting parameter
CPTu	piezocone penetration test
C_q, C_N	overburden correction factors
CRR	Cyclic resistance ratio
CSR	cyclic stress ratio
FC	fines content
FS_{liq}	Factor of safety against liquefaction
F_r	normalized friction ratio
f_s	sleeve friction stress
g	acceleration of gravity
I_c	soil behaviour type index
K_c	soil type correction factor
K_σ	overburden stress adjustment factor
LPI	Liquefaction Potential Index
LSN	Liquefaction Severity Number
LSN_{20}	Liquefaction Severity Number calculated for the first 20 m above ground surface
MSF	Magnitude Scaling Factor
M_w	moment magnitude
n, c, m	stress exponents
p_a	atmospheric pressure
PI	plasticity index
P_L	probability of liquefaction
q_c	cone resistance
q_{c1Ncs}	normalized cone resistance for clean sand (B&I2014 method)
Q_{tn}	normalized cone resistance (R2009 method)
$Q_{tn,cs}$	normalized cone resistance for clean sand(R2009 method)
r_d	shear stress reduction coefficient
R_f	friction ratio
SA	seismic action
SBTn	normalized soil behaviour type
SPT	Standard Penetration test
u	pore pressure
z	depth

References

Aydan, O., Ulusay, R., Hamada, M., & Beetham, D. (2012). Geotechnical aspects of the 2010 Darfield and 2011 Christchurch earthquakes, New Zealand, and geotechnical damage to structures and lifelines. *Bulletin of Engineering Geology and the Environment*, 71, 637-662. http://dx.doi.org/10.1007/s10064-012-0435-6.

Boulanger, R.W., & Idriss, I.M. (2014). *CPT and SPT based liquefaction triggering procedures - Report UCD/CGM-14/01*. Center for Geotechnical Modeling, Department of Civil and Environmental Engineering, University of California*,* Davis.

BSI EN 1998-5. (2004). *Eurocode 8: Design of structures for earthquake resistance – Part 5: Foundations, retaining structures and geotechnical aspects*. BSI, London. (in Portuguese).

BSI EN 1998-1. (2010). *Eurocode 8: Design of structures for earthquake resistance – Part 1: General Rules, seismic actions and rules for buildings*. BSI, London. (in Portuguese).

Cetin, K.O. (2000). *Reliability-based assessment of seismic soil liquefaction initiation hazard* [PhD dissertation, University of California at Berkeley]. University of California's repository. https://search.library.ucdavis.edu/permalink/01UCD_INST/9fle3i/alma991375175150653

Cetin, K.O., Seed, R.B., Der Kiureghian, A.K., Tokimatsu, K., Harder Junior, L.F., Kayen, R.E., & Moss, R.E.S. (2004). Standard penetration test-based probabilistic and deterministic assessment of seismic soil liquefaction potential. *Journal of Geotechnical and Geoenvironmental Engineering*, 130(12), 1314-1340. http://dx.doi.org/10.1061/(ASCE)1090-0241(2004)130:12(1314).

Cubrinovski, M., Bradley, B., Wotherspoon, L., Green, R., Bray, J., Wood, C., Pender, M., Allen, J., Bradshaw, A., Rix, G., Taylor, M., Robinson, K., Henderson, D., Giorgini, S., Ma, K., Winkley, A., Zupan, J., O'Rourke, T., DePascale, G., & Wells, D. (2011). Geotechnical aspects of the 22 February 2011 Christchurch Earthquake. *Bulletin of the New Zealand Society of Earthquake Engineering*, 44(4), 205-226. http://dx.doi.org/10.5459/bnzsee.44.4.205-226.

Cubrinovski, M., McMaunus, K., & Anderson, K. (2016). Earthquake geotechnical engineering practice. Module 3: Identification, assessment and mitigation of liquefaction hazards. *NZGS Guidelines*, 1-34.

Cubrinovski, M., Rhodes, A., Ntritsos, N., & Van Ballegooy, S. (2019). System response of liquefiable deposits. *Soil Dynamics and Earthquake Engineering*, 124, 212-229. http://dx.doi.org/10.1016/j.soildyn.2018.05.013.

Facciorusso, J., Madiai, C., Vannucchi, G., Gargini, E., & Baglione, M. (2019). Liquefaction potential evaluation of intermediate soils from mechanical and electrical CPT's. The case study of Barberino di Mugello (Italy). In *Proceedings of the 7th International Conference on Earthquake Geotechnical Engineering* (pp. 2299-2306, vol. 4). Boca Raton: CRC Press.

Ferreira, C., Viana da Fonseca, A., Ramos, C., Saldanha, A.S., Amoroso, S., & Rodrigues, C. (2020). Comparative analysis of liquefaction susceptibility assessment methods based on the investigation on a pilot site in the greater Lisbon area. *Bulletin of Earthquake Engineering*, 18(1), 109-138. http://dx.doi.org/10.1007/s10518-019-00721-1.

GeoLogismiki. (2017). *CLiq v.3.0 – CPT soil liquefaction software*. Retrieved in May 1, 2019, from https://geologismiki.gr/products/cliq/

Giannakogiorgos, A., Papathanassiou, G., & Vautherin, E. (2015). Quantitative assessment of liquefaction potential in selected areas in Christchurch, New Zealand. In *Proceedings of the 6th International Conference* *on Earthquake Geotechnical Engineering* (pp. 1-9). Christchurch.

Idriss, I.M., & Boulanger, R.W. (2008). Soil Liquefaction during Earthquake - EERI Publication, Monograph MNO-12. Earthquake Engineering Research Institute, Oakland, CA.

ISO 22476-1. (2012). *Geotechnical investigation and testing - Field testing - Part 1: Electrical cone and piezocone penetration test*. ISO - International Organization for Standardization, Geneva. https://www.iso.org/standard/57728.html

Iwasaki, T., Tatsuoka, F., Tokida, K., & Yasuda, S. (1978). A practical method for assessing soil liquefaction potential based on case studies at various sites in Japan. In *Proceedings of the 2nd International Conference on Microzonation for Safer Construction* (pp. 885-896). Alexandria, Virgínia: National Science Foundation.

Jorge, C., & Vieira, A.M. (1997). Liquefaction potential assessment – application to the Portuguese territory and to the town of Setúbal. In Pinto, P.S.S. (Ed.), *Seismic behaviour of ground and geotechnical structures* (pp. 33-43). Balkema. http://dx.doi.org/10.13140/RG.2.1.2231.5040.

Lai, C.G., Bozzoni, F., Conca, D., Famà, A., Özcebe, A.G., Zuccolo, E., Meisina, C., Bordoni, M., Cosentini, R.M., Martelli, L., Poggi, V., Viana da Fonseca, A., Ferreira, C., Rios, S., Cordeiro, D., Ramos, C., Molina-Gomez, F., Coelho, C., Logar, J., Macek, M., Oblak, A., Özçep, F., Bozbey, I., Oztoprak, S., Sargin, S., Aysal, N., Oser, C., & Kelesoglu, M.K. (2020). Technical guidelines for the assessment of earthquake induced liquefaction hazard at urban scale. *Bulletin of Earthquake Engineering*, 19, 4013-4057. http://dx.doi.org/10.1007/s10518-020-00951-8.

Lee, D.-H., Ku, C.-S., & Yuan, H. (2003). A study of liquefaction risk potential at Yuanlin, Taiwan. *Engineering Geology*, 71(1-2), 97-117. http://dx.doi.org/10.1016/S0013-7952(03)00128-5.

Maurer, B.W., Green, R.A., Cubrinovski, M., & Bradley, B.A. (2015). Calibrating the Liquefaction Severity Number (LSN) for varying misprediction economies: a case study in Christchurch, New Zealand. In *Proceedings of the 6th International Conference on Earthquake Geotechnical Engineering* (pp. 1-9). Christchurch.

Moss, R.E.S., Seed, R.B., Kayen, R.E., Stewart, J.P., Der Kiureghian, A., & Cetin, K.O. (2006). CPT-based probabilistic and deterministic assessment of in situ seismic soil liquefaction potential. *Journal of Geotechnical and Geoenvironmental Engineering*, 132(8), 1032-1051. http://dx.doi.org/10.1061/(ASCE)1090-0241(2006)132:8(1032).

Papathanassiou, G., Mantovani, A., Tarabusi, G., Rapti, D., & Caputo, R. (2015). Assessment of liquefaction potential for two liquefaction prone areas considering the May 20, 2012 Emilia (Italy) earthquake. *Engineering Geology*, 189, 1-16. http://dx.doi.org/10.1016/j.enggeo.2015.02.002.

Ramos, C. (2021). *Cyclic liquefaction susceptibility of soils from field and laboratory tests. Methodologies and critical analyses* [Doctoral thesis, Faculdade de Engenharia, Universidade do Porto]. Universidade do Porto's repository. https://hdl.handle.net/10216/136066

Robertson, P.K. (1990). Soil classification using cone penetration test. *Canadian Geotechnical Journal*, 27(1), 151-158. http://dx.doi.org/10.1139/t90-014.

Robertson, P.K. (2009). Interpretation of cone penetration tests: a unified approach. *Canadian Geotechnical Journal*, 46(11), 1337-1355. http://dx.doi.org/10.1139/T09-065.

Robertson, P.K. (2012). Mitchell Lecture: Interpretation of in-situ tests – some insight. In *Proceedings of the 4th International Conference on Geotechnical and Geophysical Site Characterization* (Vol. 1, pp. 3-24). Boca Raton: CRC Press.

Robertson, P.K. (2016). CPT-based soil behavior type (SBT) classification system – an update. *Canadian Geotechnical Journal*, 53(12), 1910-1927. http://dx.doi.org/10.1139/cgj-2016-0044.

Robertson, P.K., & Campanella, R.G. (1985). Liquefaction potential of sands using the cone penetration test. *Journal of Geotechnical Engineering*, 22(3), 298-307. http://dx.doi.org/10.1061/(ASCE)0733-9410(1985)111:3(384).

Robertson, P.K., & Wride, C.E. (1998). Evaluating cyclic liquefaction potential using the cone penetration test. *Canadian Geotechnical Journal*, 35(3), 442-459. http://dx.doi.org/10.1139/t98-017.

Seed, H.B., & Idriss, I.M. (1971). Simplified procedure for evaluating soil liquefaction potential. *Journal of the Geotechnical Engineering Division*, 97(9), 1249-1273.

Seed, H.B., Tokimatsu, K., Harder Junior, L.F., & Chung, R. (1985). Influence of SPT procedures in soil liquefaction resistance evaluations. *Journal of Geotechnical Engineering*, 111(12), 1425-1445. http://dx.doi.org/10.1061/(ASCE)0733-9410(1985)111:12(1425).

Sonmez, H. (2003). Modification to the liquefaction potential index and liquefaction susceptibility mapping for a liquefaction-prone area (Inegol-Turkey). *Environmental Geology*, 44(7), 862-871. http://dx.doi.org/10.1007/s00254-003-0831-0.

Tonkin & Taylor. (2013). *Liquefaction vulnerability study: Report to Earthquake Commission*. Tonkin & Taylor Ltd.

Toprak, S., & Holzer, T.L. (2003). Liquefaction potential index: field assessment. *Journal of Geotechnical and Geoenvironmental Engineering*, 129(4), 315-322. http://dx.doi.org/10.1061/(ASCE)1090-0241(2003)129:4(315).

van Ballegooy, S., Malan, P.J., Jacka, M.E., Lacrosse, V.I.M.F., Leeves, J.R., & Lyth, J.E. (2012). Methods for characterising effects of liquefaction in terms of damage severity. In *Proceedings of the 15th World Conference of Earthquake Engineering*, Lisbon (pp. 1-10). SPES.

Viana da Fonseca, A., Ferreira, C., Coelho, C., Quintero, J., Rios, S., Millen, M., & Cordeiro, D. (2019a). *Microzonation of the Lisbon Area in Portugal. Methodology for assessment of earthquake-induced risk of soil liquefaction at the four European testing sites (microzonation). Deliverable D2.7 of the European H2020 LIQUEFACT research project*

(Chap 3, pp. 51-126). Retrieved in July 15, 2019, from www.liquefact.eu

Viana da Fonseca, A., Ferreira, C., Ramos, C., & Molina-Gómez, F. (2019b). The geotechnical test site in the greater Lisbon area for liquefaction characterization and sample quality control of cohesionless soils. *AIMS Geosciences*, 5(2), 325-343. http://dx.doi.org/10.3934/geosci.2019.2.325.

Yi, F. (2018). Simulation of liquefaction and consequences of interbedded soil deposits using CPT data. In *Proceedings of the 4th International Symposium on Cone Penetration Testing (CPT'18)* (Vol. 1, pp. 723-729). Boca Raton: CRC Press.

Youd, T.L., Idriss, I.M., Andrus, R.D., Arango, I., Castro, G., Christian, J.T., Dobry, R., Liam Finn, W.D., Harder Junior, L.F., Hynes, M.E., Ishihara, K., Koester, J.P., Liao, S.S.C., Marcuson 3rd, W.F., Martin, G.R., Mitchell, J.K., Moriwaki, Y., Power, M.S., Robertson, P.K., Seed, R.B., & Stokoe 2nd, K.H. (2001). Liquefaction resistance of soils: summary report from the 1996 NCEER and 1998 NCEER/NSF Workshops on Evaluation of Liquefaction Resistance of Soils. *Journal of Geotechnical and Geoenvironmental Engineering*, 127(10), 817-833. http://dx.doi.org/10.1061/(ASCE)1090-0241(2001)127:10(817).

Zhang, G., Robertson, P.K., & Brachman, R.W.I. (2002). Estimating liquefaction-induced ground settlements from CPT for level ground. *Canadian Geotechnical Journal*, 39(5), 1168-1180. http://dx.doi.org/10.1139/t02-047.

Soils and Rocks

An International Journal of Geotechnical and Geoenvironmental Engineering

www.soilsandrocks.com

ISSN 1980-9743
ISSN-e 2675-5475

Experimental evaluation of the classical and alternative consolidation theories in predicting the volumetric change of contaminated and non-contaminated soil

Moisés Antônio da Costa Lemos[1], Lucas Martins Guimarães[2], André Luís Brasil Cavalcante[1#]

Article

Keywords
Consolidation
Collapsible soils
Collapse by contamination
Collapsibility index

Abstract

Several regions in Brazil and the world suffer from the presence of collapsible soils. The development of theories for understanding the phenomenon is significant because the increase of water content is associated with several reasons (e.g., precipitation, rupture of sewage, and water systems). Although some theories explain the behavior of various types of soils, they fail to explain collapsible and structured soils. In this research, an alternative interpretation of the consolidation theory is verified and calibrated for collapsible soil. The alternative model was applied to experimental data from a latosol from southeastern Brazil, and comparisons with the classical theory showed a difference in the saturated hydraulic conductivity of around 100 times. The observation showed promising results compared with the saturated hydraulic conductivity of the field (Guelph Permeameter). Furthermore, consolidation tests verified the collapse potential, the variation of consolidation coefficient and saturated hydraulic conductivity, and the total settlement prevision due to the presence of bleach and washing powder.

1. Introduction

One of the phenomena widely known in Geotechnical Engineering, especially in hot and humid regions, is collapse. The definition of collapse is vast and different interpretations associated with volume decrease due to increasing saturation exist. The fields of interpretation are related to changes in load or stress state, soil strength components reduction, and changes in physicochemical properties affecting soil cementation and interaction between particles, consequently influencing soil collapse.

Soil wetting is related to rising soil water levels, leaking sewage pipes, and fuel leaks. The impacts caused are especially important on constructions in collapsible soils. Building on collapsible soils requires designing structures that can withstand significant ground movement or treating the soils to make them less sensitive to water content variation (Abbeche et al., 2010). Natural clayey soils rarely meet the requirements of modern geotechnical engineering projects (Cheng et al., 2020).

Besides, there is a difference between truly collapsible soils and conditionally collapsible soils (Reginatto & Ferrero, 1975). The collapsible soils are those that undergo a reduction of volume only with increasing saturation. On the other hand, the conditionally collapsible soils reduce volume by increasing both saturation and external load. The increase in water content can be associated with contamination of the soil.

Understanding soil collapse is associated with increased water content because water or contaminants change the soil's physical-chemical properties. According to Hu et al. (2021), there is a deterioration mechanism regarding the microspores exposed to the contaminants. Also, the resultant macrospores' mechanical properties correlate with the deteriorated microspores' structural characteristics. Khodabandeh et al. (2020) showed that changes in soil collapse potential are much more significant in acidic conditions than alkaline conditions.

Geotechnical engineers face significant challenges due to the risk of building constructions on collapsible soils whose volumes tend to drop abruptly once moistened (Nokande et al., 2020). Research about collapsible and unsaturated soil due to the change in moisture has been an area of geotechnics with significant interest. These studies take into account physical indexes, field, and laboratory tests.

[#]Corresponding author. E-mail address: abrasil@unb.br
[1]Universidade de Brasília, Department of Civil and Environmental Engineering, Brasília, DF, Brasil.
[2]Universidade Federal de Viçosa, Department of Civil Engineering, Rio Paranaíba, MG, Brasil.

Submitted on August 3, 2021; Final Acceptance on November 2, 2021; Discussion open until February 28, 2022.
https://doi.org/10.28927/SR.2021.073721

The physical index methods consider the variation of the degree of saturation (Jennings & Knight, 1975), the volumetric moisture content, and the void ratio. The most widely used laboratory tests are the single and double consolidation tests (Jennings & Knight, 1975; Vargas, 1978) and the X-ray diffraction test for the information provided on the soil microstructure.

Thus, the studies to identify the collapse and its understanding made geotechnical engineers search for an approach to measuring volumetric change. Therefore, the one-dimensional consolidation theory of Terzaghi (1943), proposed for variable loading over time in saturated soils, had an essential contribution to developing new consolidation theories applied to unsaturated, structured, and collapsible soils.

Fredlund & Morgenstern (1976) proposed and verified the relationship between the volumetric change of unsaturated soils and the state variables experimentally. In later research, Fredlund & Hasan (1979) proposed a consolidation theory for unsaturated soils considering the dependence between state variables and vertical deformation. In this model, collapse behavior decreases resistance associated with reducing suction due to wetting (Fredlund & Gan, 1995).

The analysis of the deformation of unsaturated soils and collapse were later addressed by elastoplastic models (Lloret & Alonso, 1980; Alonso et al., 1990; Gens & Alonso, 1992). Such models show promising results to estimate the volumetric variation of soils. However, a large number of parameters taken from experimental tests are necessary. From the perspective of the collapse, it requires a smaller number of parameters. Nevertheless, other parameters are necessary for different types of soils and even soils with different natural conditions. Therefore, despite the good results, the use of the method becomes complex (Li et al., 2016).

This research discusses an alternative model of Terzaghi's theory since his theory underestimates the saturated hydraulic conductivity values observed in the field. The values for k_s from the in situ tests are usually higher than those from the lab tests (Reynolds & Zebchuk, 1996; Nam et al., 2021).

Thus, in the new approach, the coefficient of consolidation (c_v), obtained by graphical methods, and the saturated hydraulic conductivity, obtained from c_v, are unsuitable for use in unsaturated soils. In these soils, micro-collapses occur. Consequently, there are increases in pore pressure, not only a decrease, as proposed by Terzaghi. According to Ozelim et al. (2015), the increase in pore pressure is due to the momentary loss of support of the porous matrix due to the occurrence of collapse.

Experimental data is present in this research, justifying the applicability of the consolidation theory induced by micro-collapses (Ozelim et al., 2015). Furthermore, complementary odometer tests using contaminants show the importance of knowing the liquid of inundation in the collapse potential and the prevision of settlement. Because the inundation liquids used are present in the water supply system and residential sewage, which can break and cause soil collapsibility.

2. Problem overview

Among the various ways of identifying collapse, laboratory ones are very satisfactory. One can mention the simple and double consolidation tests. Simple consolidation tests are those that consist of applying successive loads to a sample with natural moisture content. In a given vertical stress, the inundation of the specimen occurs, and the test continues by the application of successive loading and, in the end, unloading. For the double consolidation test, two identical samples are prepared. One will be inundated entirely from the beginning of the test. The other will remain with the natural water content throughout the experiment.

Among the most relevant laboratory forms of verifying collapse from consolidation tests are the Jennings & Knight (1975), Vargas (1978), and Reginatto & Ferrero (1975) approaches

Jennings & Knight (1975) proposed a classification based on the severity of collapse and volumetric variation of collapsing soils through simple and double consolidation tests. For the simple consolidation test, it is possible to calculate and classify the collapse potential as:

$$CP = \frac{\Delta e}{1+e_0} \times 100 \tag{1}$$

where Δe = the void ratio difference before and after inundation (dimensionless); e_0 = the initial void ratio of the experimental test (dimensionless).

The collapse potential (CP) calculated by Equation 1 can be classified as none (0 to 1%), moderate (1 to 5%), problematic (5 to 10%), severe (10 to 20%), and very severe (up to 20%).

The wetting-induced collapse deformation can be calculated by (Hanna & Soliman, 2017):

$$CP = \frac{\Delta e}{1+e_i} \times 100 \tag{2}$$

where e_i = the void ratio before the inundation (dimensionless). Thus, in soils where $CP > 2\%$, this is considered collapsible (Vargas, 1978).

Reginatto & Ferrero (1975) described ways to identify the collapse from the double consolidation tests. For double consolidation tests, the collapsibility coefficient (C) is determined by:

$$C = \frac{\sigma'_{0,s} - \sigma_{v0}}{\sigma'_{0,n} - \sigma_{v0}} \tag{3}$$

where $\sigma'_{0,s}$ = preconsolidation stress of saturated soil (F L^{-2}); $\sigma'_{0,n}$ = preconsolidation stress in the natural condition (F L^{-2}); σ_{v_0} = vertical geostatic stress (F L^{-2}).

The collapsibility coefficient (C) value determines what type of collapse the soil will be subject to and even if the soil shows a collapsing behavior. The soil can be truly collapsible ($C < 0$), conditionally collapsible ($0 < C < 1$), not collapsible ($C = 1$) and collapsible and normally consolidated ($C \rightarrow -\infty$).

In addition to verifying the collapse, studies in the literature seek to understand the collapse with other inundation liquids besides distilled water (Rodrigues & Lollo, 2007). Then, it is possible to understand the behavior of soils contaminated by other residues such as washing powder, bleach, sanitary sewage, oil, and others. One of the reasons for the inundations, for example, is due to ruptures in plumbing in the sewage systems (surrounded by collapsing soils). Thus, Rodrigues & Lollo (2007) show the behavior of Brazilian soil, inundated with different liquids under specific concentrations, because of its presence in sanitary sewage.

The consolidation theory proposed by Terzaghi (soil-spring analogy) is of great value to explain most saturated soils' behavior. However, for soil that has experienced significant weathering processes, the behavior of a spring is not coherent because the soil's porous matrix is constantly collapsing. Terzaghi's theory does not take such behavior into account. So a new approach is still a challenge for Geotechnical Engineering.

3. Description of the new consolidation theory

Ozelim et al. (2015) presented a new model as an alternative way of interpreting the consolidation theory discussed by Terzaghi. Water pore pressure does not gradually decrease in the model, as is interpreted in the conventional consolidation theory. However, the soil undergoes micro-collapses allowing the pore pressure to increase in certain stages of the consolidation.

The proposed theory considers the soil as a collapsible telescopic structure associated with springs, unlike the Terzaghi model, which presents the saturated soil as just a spring. The idea of a telescopic structure is justified because it can represent a wide variety of soil behaviors, such as different cementations in soils and the effect of stress on the collapse of the structure.

In the Terzaghi approach, during consolidation, there is no increase in pore pressure. Therefore, the impression is that the saturated hydraulic conductivity is lower as water takes longer to percolate. Consequently, this is the only consideration that the new theory disagrees with Terzaghi's approach. Accordingly, the mathematical way of calculating the average degree of density does not change:

$$U_c(T_v) = 1 - \sum_{m=0}^{\infty} \frac{2}{M^2} \exp\left[-M^2 T_v\right] \tag{4}$$

and

$$M = \frac{\pi(2m+1)}{2} \tag{5}$$

However, the time factor (T_v) must undergo a time dilation, meaning that the collapse will decrease the average degree of consolidation. Thus, the need to reduce the time factor is justified (Ozelim et al., 2015).

Although the consideration is simple, knowing the exact moment of collapse in real applications is not viable due to the complex measurement. Instead of predicting the precise moment of the collapse, there is the consideration of a given collapse frequency f. Besides, the increase in pore pressure and the frequency at which collapses occur are related to a parameter called the collapsibility index, η, introduced by Ozelim et al. (2015).

The general equation for the average degree of consolidation for collapsible soils is given by:

$$U_c(T_v, \eta) = \frac{1 - \exp(-[5.9(1-\eta)T_v]^{2/3})}{1 + \exp(-[5.9(1-\eta)T_v]^{2/3})} \tag{6}$$

The authors pointed out that $0 \leq \eta \leq 1$, and the time factor is mathematically related according to the proposed by Terzaghi:

$$T_v = \frac{c_v t}{H_d^{\,2}} \tag{7}$$

where c_v = coefficient of consolidation (L^2 T^{-1}); t = time (T); H_d = drainage path length (L).

Also, the method shows that when η = 0, the collapse mechanism does not occur, so the conditions established by Terzaghi are valid. However, if η = 1, there is no pore pressure dissipation, so the consolidation has infinite duration.

Ozelim et al. (2015) show that a combination of consolidation and permeability experiments is necessary to determine the collapsibility index. Therefore, when the value of η is known from the consolidation test, it is possible to calculate the saturated hydraulic conductivity value. Once the value of η is found can be established regionally, with the possibility of being estimated.

Ozelim et al. (2015) point out that by relating the value of the coefficient of volumetric variation, m_v ($L^2 F^{-1}$), obtained from the consolidation test, with the value of the saturated hydraulic conductivity, k_s ($L T^{-1}$), obtained from the permeability test, the c_v can be estimated using the known equation:

$$c_v = \frac{k}{m_v \gamma_w} \tag{8}$$

where γ_w = specific weight of the water ($F L^{-2}$).

According to Ozelim et al. (2015), if the value of η is not known, it can be calculated as follows:

$$\eta = 1 - \frac{1000}{2086} \frac{|m|^{3/2} H_d{}^2 m_v \gamma_w}{\Delta h^{3/2} k} \tag{9}$$

where m = slope of the beginning of the curve of the graph h versus $t^{2/3}$ ($LT^{-2/3}$), h = height of the sample in the considered step of the consolidation test (L), Δh = height variation of the sample in the considered step of the consolidation test (L), therefore, η can be calculated for each step of the consolidation test.

Using Equation 9 and calculating η, the coefficient of consolidation can be adjusted as follows:

$$c_v = \frac{1000}{2086} \frac{|m|^{3/2} H_d{}^2}{\Delta h^{3/2} (1-\eta)} \tag{10}$$

To verify the method's suitability for these types of soils, comparing the field saturated hydraulic conductivity (k_s) with the obtained from the technique is necessary. Thus, there are ways to get k_s from field experiments (e.g., Guelph permeameter test). Therefore, the test consists of determining the k_s by the one or two-stage method. These consist of applying one or two successive heights of the water column in the Guelph permeameter. The main discussion is if the model prevision of the saturated hydraulic conductivity value is close to the field measure.

The settlement estimation and its change in time use edometric tests and the assumption of consolidation. When the incremental stress plus the initial stress is higher than the preconsolidation stress, the settlement (S_T) prevision is in the form:

$$S_T = \frac{C_s H}{1 + e_0} \log\left(\frac{\sigma'_c}{\sigma'_0}\right) + \frac{C_c H}{1 + e_0} \log\left(\frac{\sigma'_0 + \Delta\sigma'}{\sigma'_c}\right) \tag{11}$$

where C_s = swell index, H = length of the layer (L), C_c = compression index, σ'_c = preconsolidation stress ($F L^{-2}$), σ'_0 = in situ effective overburden pressure ($F L^{-2}$) and $\Delta\sigma'$ = incremental stress ($F L^{-2}$).

The time-dependent settlement (S_t) can be calculated considering the degree of consolidation of Equation 4 (Terzaghi, 1943) or Equation 6 (Ozelim et al., 2015):

$$S_t(t) = U_c(t) S_T \tag{12}$$

The ratio of the non-conventional and traditional degrees of consolidation (R_{DC}) is a helpful manner of understanding the differences between both methods:

$$R_{DC} = \frac{U_c(T_v, \eta)_{\text{Ozelim}}}{U_c(T_v)_{\text{Terzaghi}}} \tag{13}$$

4. Materials and methods

The experimental data comes from the city of Rio Paranaíba, located in the state of Minas Gerais (19º 12 '46 "S and 46º 13' 57" W). The location is 532 km from the capital of Brazil (Brasilia/DF) city already identified with collapse problems.

The experimental data are from a depth of 1.5 meters, aiming at depths where water supply pipes and sewage systems are commonly placed and subject to ruptures. Disturbed samples for the soil characterization tests and undisturbed samples for the consolidation tests were collected. The undisturbed specimens were removed, maintaining the natural characteristics, and stored with paraffin.

The grain size distribution was based on the sieve and hydrometer analysis (ASTM, 2007 and ASTM, 2017a). The natural moisture content was obtained using the drying method. The liquid and plastic limit tests are according to ASTM (2017b). The standard Proctor compaction test was according to ASTM (2012).

After soil characterization, the simple and double consolidation tests investigated the collapsible soil characteristics (ASTM, 2003). Besides, three different liquids were used for further verification: distilled water, distilled water with bleach (1: 120 by volume), and distilled water with washing powder (1: 120 by mass).

The consolidation test specimens were from the undisturbed sample in a confining ring with a diameter of 8 cm and a height of 1.99 cm. The simple consolidation test was initiated by applying the initial stress with the specimen in the natural water content until the stress of 156.1 kPa. The choice of this value (156.1 kPa) is because it is in the virgin consolidation curve and is close to values used in the literature to verify the collapse potential (Jennings & Knight, 1975). The test ended in the stress of 1249 kPa, ending with the unloading.

The double consolidation test consisted of two specimens with identical conditions, preserving the undisturbed samples collected. One of the tests started with natural moisture, and the other was inundated from the beginning. The latter allows to obtain all parameters of Equation 11 and calculate settlement of hypothetical layers.

For both consolidation tests, the inundation was performed with substances commonly found in domestic sewage and treated water pipes. Thus, this research also makes it possible to verify the collapse under the influence of the inundation liquid.

The consolidation theory induced by micro-collapse requires a set of consolidation and permeability tests for its verification. Thus, consolidation tests obtained all the required parameters and, therefore, the corrected coefficients. The considered value of η is an average of the values calculated per load since it is a soil property.

After obtaining the value of η, a consolidation test was carried out to correct the coefficient of consolidation (Equation 10). From the parameters taken from the test, the value of c_v is obtained per vertical stress. Thus, having both c_v and volumetric compressibility coefficient (m_v), the corrected saturated hydraulic conductivity value measured in the consolidation test is obtained (Equation 8).

Although the consistency of the method is comparing it with values obtained in the field, Ozelim et al. (2015) not executed it. Thus, in this research, the authors check the consistency of the method through the Guelph Permeameter. Furthermore, some comparisons of the alternative and classical theories were executed with contaminated and non-contaminated soil.

5. Results and discussion

Table 1 shows the main soil physical indexes. Figures 1 and 2 show the particle-size distribution and compaction curves, respectively, of the studied soil.

Table 1. Soil physical indexes.

Parameter	Value
Natural Specific Gravity (kg·m^{-3})	1410
Natural Void Index	1.33
Saturated Preconsolidation Stress (kPa)	150
Porosity (%)	57
Specific Gravity of Solids (kg·m^{-3})	2780
Maximum Dry Density (kg·m^{-3})	1390
Optimal Water Content (%)	32
Liquid Limit (%)	42
Plastic Limit (%)	32
Plasticity Index (%)	10
Clay (%)	47
Silt (%)	11
Sand (%)	42

Figure 3 shows the relationship between void ratio and vertical stress for the simple consolidation test. The potential collapse - Equation 1, according to Jennings & Knight (1975), for water, washing powder, and bleach are 7.56, 8.90, and 5.32. The potential collapse, according to Vargas (1978) – Equation 2, for water, washing powder, and bleach are 8.26, 9.92, and 6.52. Thus, according to Jennings & Knight (1975), the severity of the problem would be problematic for

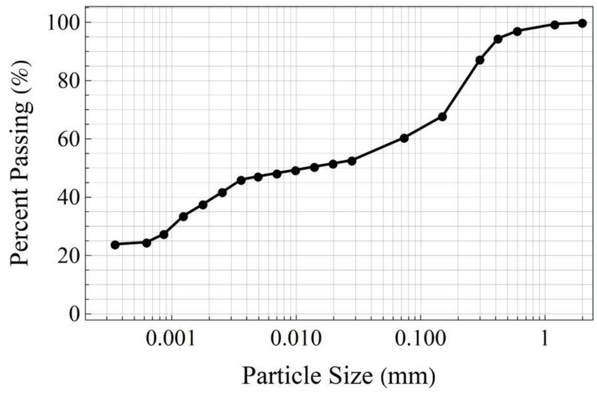

Figure 1. The particle-size distribution curve of the soil.

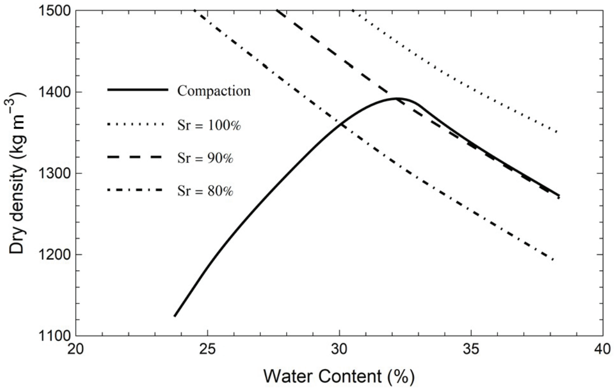

Figure 2. Compaction and saturation curves of the soil.

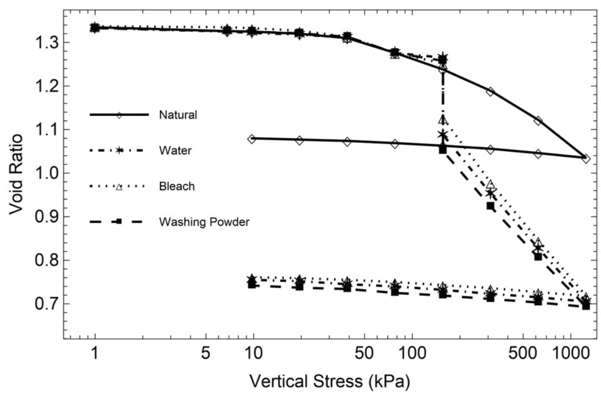

Figure 3. Relationship of void ratio and vertical stress for the simple consolidation test.

all inundation fluids. Moreover, according to Vargas (1978), for all inundation liquids, the soil has a collapsible behavior.

The type of collapse was verified in the double consolidation test, as proposed by Reginatto & Ferrero (1975). Figure 4 shows the relationship between void ratio and vertical stress for the double consolidation tests. The results of the collapsibility coefficient for water, washing powder, and bleach are 0.91, 0.25, and 0.58, respectively.

Thus, assuming the considerations of Reginatto & Ferrero (1975), the soil is conditionally collapsible. All results show the collapse potential of the soil and its characteristics of collapsing soil.

In Figure 5, there are the values obtained using the Terzaghi theory for the coefficient of consolidation (Figure 5a) and the hydraulic conductivity (Figure 5b) varying with the vertical stress. The coefficient of consolidation of the unsaturated condition (natural) was the highest one for all cases in higher stresses. Then, the consolidation process takes more time in the unsaturated condition.

5.1 Correction using the non-conventional consolidation theory

The input parameters proposed in Equation 9 are from the conventional consolidation test (I) (Figure 6) and its data. The preconsolidation stress calculated using the Casagrande method (Casagrande, 1936) is 150 kPa. Thus, the loading steps for validating the method are above this value.

Therefore, through the consolidation test, all the necessary parameters and the results obtained for the collapsibility index proposed by Ozelim et al. (2015) are found in Table 2.

Utilizing the η values obtained, it was then possible to correct the coefficients of consolidation of each step (Equation 10) and the hydraulic conductivity values (Equation 8). Figure 7 shows the relationship of void ratio and vertical stress for the other consolidation test (II) to correct the mentioned parameters.

The new values found for c_v e k_s according to the method is in Table 3.

After obtaining the new permeabilities adjusted by the proposed model, Equation 6 is helpful to compare the average degree of consolidation (U_c) for different values of η. Figure 8 shows the average degree of consolidation versus the

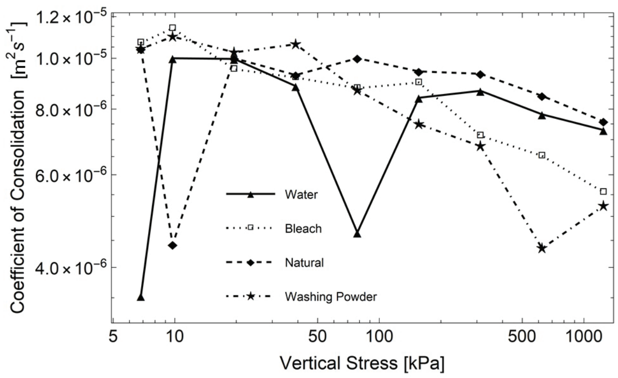

(a)

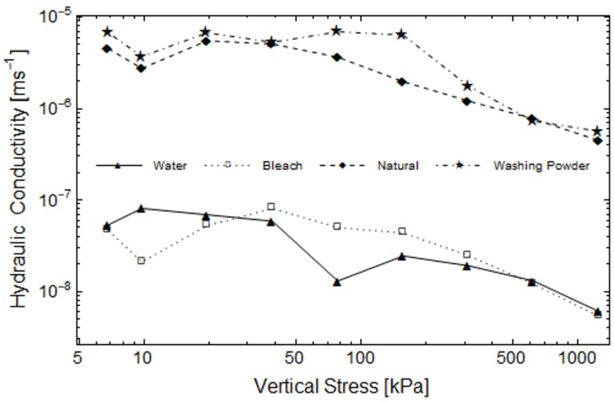

(b)

Figure 5. Vertical stress versus (a) coefficient of consolidation and (b) hydraulic conductivity (Terzaghi Theory)

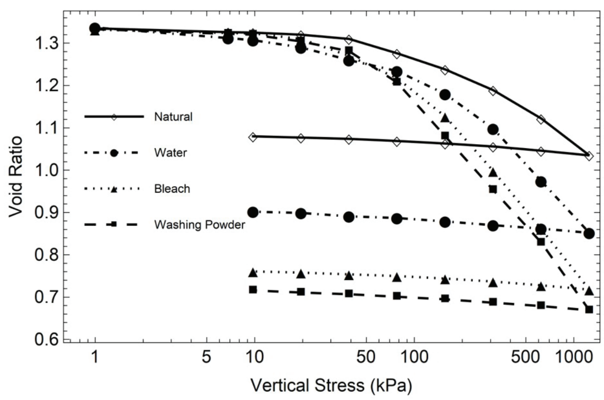

Figure 4. Relationship of void ratio and vertical stress for the double consolidation test.

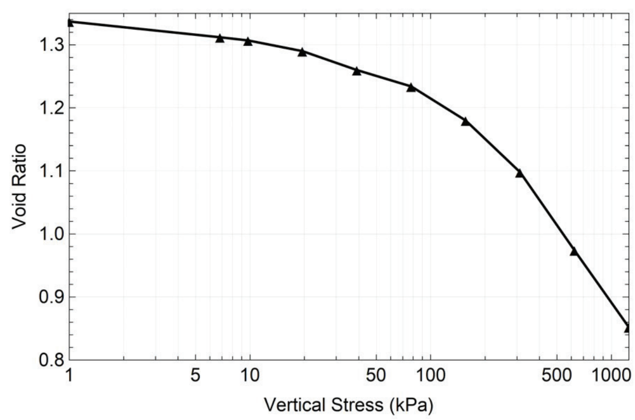

Figure 6. Relationship of void ratio and vertical stress (conventional consolidation test I).

Table 2. Collapsabilty index values (η) obtained from consolidation test I.

σ› (kPa)	m_v (kPa^{-1})	H_d (m)	c_v (m^2/s)	k_s (m/s)	η
156.1	2,95 x 10^{-4}	1,90 x 10^{-2}	8,41 x 10^{-6}	2.43x10^{-8}	0.867
312.2	2,25 x 10^{-4}	1,86 x 10^{-2}	8,90 x 10^{-6}	1.96x10^{-8}	0.872
624.5	1,68 x 10^{-4}	1,78 x 10^{-2}	7,82 x 10^{-6}	1.29x10^{-8}	0.839
1249	8,4 x 10^{-5}	1,68 x 10^{-2}	7,30 x 10^{-6}	6.03x10^{-9}	0.848
				η (mean)	0.856

Table 3. Values of c_v and k_s corrected using η = 0.856.

σ› (kPa)	m_v (kPa^{-1})	H_d (m)	c_v (m^2/s)	k_s (m/s)
156.1	4,94 × 10^{-4}	1,89 × 10^{-2}	4.00 × 10^{-6}	1.9 × 10^{-8}
312.2	3,53 × 10^{-4}	1,82 × 10^{-2}	6.23 × 10^{-6}	2.2 × 10^{-8}
624.5	1,88 × 10^{-4}	1,70 × 10^{-2}	4.38 × 10^{-4}	8.1 × 10^{-7}
1249	9,78 × 10^{-5}	1,59 × 10^{-2}	4.52 × 10^{-4}	4.34 × 10^{-7}

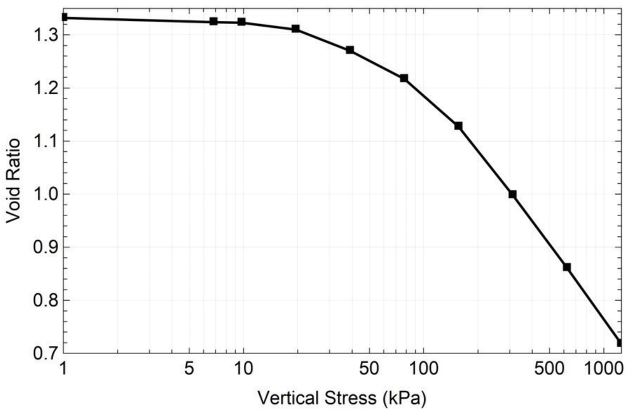

Figure 7. Relationship of void ratio and vertical stress (conventional consolidation test II).

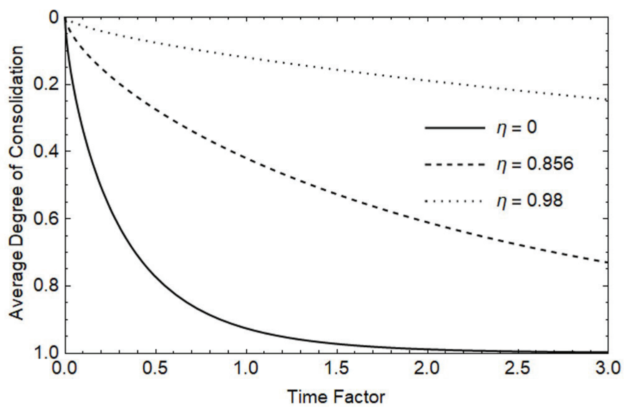

Figure 8. The average degree of consolidation (U_c) versus time factor (T_v), varying η.

time factor for different η. Figure 8 illustrates such behavior for the situation with no collapse (η = 0), the case of this research (η = 0.856), and the soil (η = 0.98) analyzed by Ozelim et al. (2015). As the consolidation coefficient proposed by Terzaghi, the collapsibility index is considered constant even varying with a load.

Analyzing Figure 8 can verify the importance of determining η for the correction of the average degree of consolidation and the effects of collapse causes in the degree of consolidation by considering the increase in pore pressure during micro-collapses.

5.2 Field saturated hydraulic conductivity of the soil (k_s)

The results of saturated hydraulic conductivity (k_s) obtained from the Guelph permeameter test were 7.6 × 10^{-7} m s^{-1} using a pressure head of 5 cm, 1.9 × 10^{-7} m.s^{-1} using a pressure head of 10 cm. Using the two-stage methodology (two pressure heads during the same test, H_1 = 5 cm e H_2 = 10 cm), the k_s was 7.3 × 10^{-8} m s^{-1}. The field saturated hydraulic conductivity (k_s) averages these values equal to 3.4 × 10^{-7} m s^{-1}.

The values obtained from the correction proposed by Ozelim et al. (2015), the field saturated hydraulic conductivity obtained by Guelph permeameter, and Terzaghi's theory are in Table 4. These results show that all saturated hydraulic conductivity was corrected. However, for the stress of 1249 kPa, the correction was up to 100 times. Moreover, the updated values had a better approximation of the actual value through the proposed theory, just the 156.1 kPa value that was similar.

Table 4. k_s comparison between the methodologies.

σ› (kPa)	$k_{s,cT}$ (m/s)	$k_{s,cO}$ (m/s)	$k_{s\ GP}$ (m/s)
156.1	2.43×10^{-8}	1.9×10^{-8}	3.4×10^{-7}
312.2	1.96×10^{-8}	2.2×10^{-8}	
624.5	1.29×10^{-8}	8.10×10^{-7}	
1249	6.03×10^{-9}	4.34×10^{-7}	

5.3 Settlement behavior

Using the results of the double consolidation tests (Figure 4), the swell index (C_s) for water, bleach, washing powder, and the soil in a natural condition are 0.024, 0.0159, 0.0188, and 0.0159, respectively. The compression index (C_c) for water, bleach, washing powder and the soil in a natural condition are 0.409, 0.4522, 0.4725, and 0.2571. The hypothetical saturated layer's thickness was considered 5 m and drained at both top and bottom. The considered incremental stress ($\Delta\sigma'$) was 1000 kPa. The value of the in situ effective overburden pressure was in the middle of the layer. The coefficient of consolidation of the traditional theory is in Figure 5a and the non-conventional in Table 3 for the vertical stress of 1249 kPa. All the remaining data is in Table 1.

In the analysis, the authors considered c_v fo the highest vertical stress (1249 kPa), although the collapsibility index was constant. The reason is that the higher the vertical stress, the higher is the adjustment of c_v.

According to Equations 11 and 12, the time-dependent settlement is present in Figure 9 for all inundation liquids. However, the application of the correction of the degree of consolidation of Ozelim et al. (2015) theory was just to the distilled water sample (Water-O). All other results in Figure 9 were calculated using the traditional Terzaghi theory for the degree of consolidation.

The highest value of the settlement (Figure 9) was the test with de powder, which had the highest collapse potential. The unsaturated sample presented the lowest settlement value mainly because of the strength increase due to suction compared with the saturated samples. Comparing the time-dependent settlement using the traditional (Water-T) and unconventional (Water-O) theories shows how collapse anticipates settlement.

The ratio of the non-conventional (Ozelim et al., 2015) and traditional (Terzaghi, 1943) degrees of consolidation (Equation 13) is helpful to understand how quickly the settlement occurs during the time. Figure 10 shows a result of varying thickness of drainage path length (H_d = 2.5, 5, and 10 m) in the degree of consolidation ratio. Because the coefficient of consolidation did not change in this situation, the maximum ratio was equal and approximately three times in all cases. However, the peak time differed, and the shorter the drainage path length, the faster the peak.

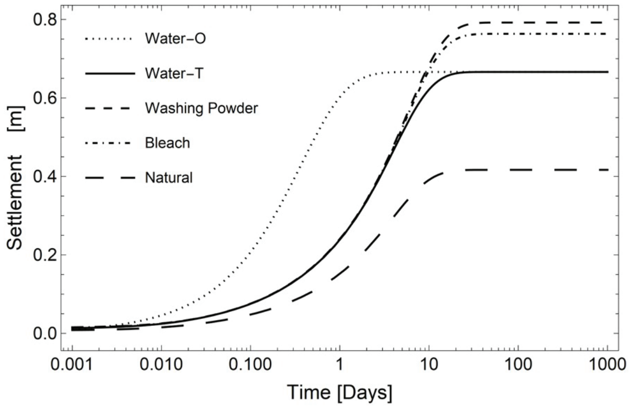

Figure 9. Time-settlement relation.

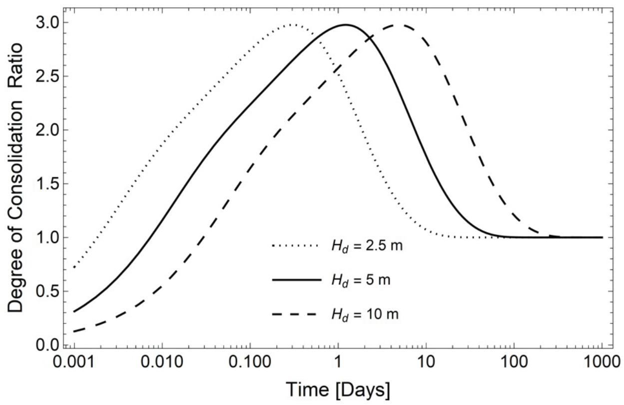

Figure 10. Predicted time history of degree of consolidation ratio.

6. Conclusion

Due to the soil characteristics in a region with a tropical and humid climate and a latosol that presents significant weathering, the soil shows collapsible features. The simple and double consolidation tests showed to be an essential measure to identify the potential of collapse. Therefore, it is recommended that more samples from other points at different depths are analyzed to understand the region's collapse spatially. One way to avoid doing many consolidation tests is to compare the soil characterization with other tests done in the area.

The alternative approach is relevant compared to the traditional one to estimate the consolidation and saturated hydraulic conductivity in consolidation tests. The results justify the new theory since the saturated hydraulic conductivity values by Terzaghi theory underestimates the saturated hydraulic conductivity values in collapsible and structured soils. The Guelph permeameter identified the hydraulic conductivity in the field. It was the tool utilized to compare the field with the laboratory parameters.

Although some of the corrected values show some discrepancy from the measured value in the field, it is essential to note that for all values, the hydraulic conductivity was updated. The method adjustment has come close to 100 times the value previously found by the conventional approach at specific stresses. Therefore, the method proposed is pertinent. Besides having a simple treatment, it was very relevant in places that have soils with collapsible characteristics.

Furthermore, if water content increases are associated with contamination instead of water, the collapse behavior changes significantly. This research shows that the presence of washing powder and bleach is associated with a higher collapse potential. In the settlement prevision, the contaminants had a higher total settlement compared with distilled water.

Acknowledgements

This study was financed in part by the Coordination for the Improvement of Higher Education Personnel – Brasil (CAPES) – Finance Code 001. The authors also acknowledge the support of the National Council for Scientific and Technological Development (CNPq Grants 304721/2017-4, 435962/2018-3, 140923/2020-9 and 305484/2020-6), the Foundation for Research Support of the Federal District (FAPDF Projects 0193.002014/2017-68 and 0193.001563/2017), and the University of Brasília.

Declaration of interest

The authors have no conflicts of interest to declare. All co-authors have observed and affirmed the paper's contents, and there is no financial interest to report.

Authors' contributions

Moisés Antônio da Costa Lemos: conceptualization, Data curation, Methodology, Visualization, Software, Writing – original draft. Lucas Martins Guimarães: conceptualization, Data curation, Investigation, Funding acquisition, Methodology, Resources, Supervision. André Luís Brasil Cavalcante: formal Analysis, Funding acquisition, Supervision, Methodology, Project administration, Resources, Validation, Writing – review & editing, Software.

List of symbols

CP	Collapse potential
C	Collapsibility coefficient
c_v	Coefficient of consolidation
e_0	Initial void ratio of the experimental test
e_i	Void ratio before the inundation
h	height of the sample in the considered step of the consolidation test
H	Length of the soil layer
H_d	Drainage path length
k_s	saturated hydraulic conductivity
m	Slope of the beginning of the curve of the graph h *versus* $t^{2/3}$
m_v	Coefficient of volumetric variation
R_{DC}	Ratio of the non-conventional and traditional degree of consolidation
S_T	Soil settlement
S_t	Time-dependent settlement
t	Time
T_v	Time factor
U_c	Average degree of consolidation
γ_w	Specific weight of the water
Δe	Void ratio difference before and after inundation
Δh	Height variation of the sample in the considered step of the consolidation test
$\Delta\sigma'$	Incremental stress
η	Collapsibility index
σ_c'	In situ effective overburden pressure
σ_0'	Preconsolidation stress
$\sigma_{0,s}'$	Preconsolidation stress of saturated soil
$\sigma_{0,n}'$	Preconsolidation stress in the natural condition
σ_{v_0}	Vertical geostatic stress

References

Abbeche, K., Bahloul, O., Ayadat, T., & Bahloul, A. (2010). Treatment of collapsible soils by salts using the double consolidation method. In *Proc. GeoShanghai International Conference* (pp. 69-78). Reston: ASCE. http://dx.doi.org/10.1061/41103(376)10.

Alonso, E.E., Gens, A., & Josa, A. (1990). A constitutive model for partially saturated soils. *Geotechnique*, 40(3), 405-430. http://dx.doi.org/10.1680/geot.1990.40.3.405.

American Society for Testing and Materials – ASTM. (2003). *ASTM D5333-03: standard test method for measurement of collapse potential of soils*. West Conshohocken: ASTM International. https://doi.org/10.1520/D5333-03.

American Society for Testing and Materials – ASTM. (2007). *ASTM D422-63: standard test method for particle-size analysis of soils*. West Conshohocken: ASTM International. https://doi.org/10.1520/D0422-63R07E02.

American Society for Testing and Materials – ASTM. (2012). *ASTM D698-12: standard test methods for laboratory compaction characteristics of soil using standard effort*. West Conshohocken: ASTM International. https://doi.org/10.1520/D0698-12.

American Society for Testing and Materials – ASTM. (2017a). *ASTM D7928-17: standard test method for particle-size distribution (gradation) of fine-grained soils using the sedimentation (hydrometer) analysis*. West Conshohocken: ASTM International. https://doi.org/10.1520/D7928-17.

American Society for Testing and Materials – ASTM. (2017b). *ASTM D4318-17: standard test methods for liquid limit, plastic limit, and plasticity index of soils*.

West Conshohocken: ASTM International. https://doi.org/10.1520/D4318-17E01.

Casagrande, A. (1936). Determination of the preconsolidation load and its practical significance. In *Proc. 1st International Conference on Soil Mechanics and Foundation Engineering* (Vol. 3, pp. 60-64). Cambridge: Harvard University.

Cheng, G., Zhu, H.-H., Wen, Y.-N., Shi, B., & Gao, L. (2020). Experimental investigation of consolidation properties of nano-bentonite mixed clayey soil. *Sustainability*, 12(2), 459. http://dx.doi.org/10.3390/su12020459.

Fredlund, D.G., & Gan, J.K.-M. (1995). The collapse mechanism of a soil subjected to one-dimensional loading and wetting. In E. Derbyshire, T. Dijkstra & I. J. Smalley (Eds.), *Genesis and properties of collapsible soils* (pp. 173-205). Dordrecht: Springer. http://dx.doi.org/10.1007/978-94-011-0097-7_9.

Fredlund, D.G., & Hasan, J.U. (1979). One-dimensional consolidation theory: unsaturated soils. *Canadian Geotechnical Journal*, 16(3), 521-531. http://dx.doi.org/10.1139/t79-058.

Fredlund, D.G., & Morgenstern, N.R. (1976). Constitutive relations for volume change in unsaturated soils. *Canadian Geotechnical Journal*, 13(3), 261-276. http://dx.doi.org/10.1139/t76-029.

Gens, A., & Alonso, E.E. (1992). A framework for the behavior of unsaturated expansive clays. *Canadian Geotechnical Journal*, 29(6), 1013-1032. http://dx.doi.org/10.1139/t92-120.

Hanna, A., & Soliman, S. (2017). Experimental investigation of foundation on collapsible soils. *Journal of Geotechnical and Geoenvironmental Engineering*, 143(11), 04017085. http://dx.doi.org/10.1061/(ASCE)GT.1943-5606.0001750.

Hu, W., Cheng, W.C., Wen, S., & Rahman, M.M. (2021). Effects of chemical contamination on microscale structural characteristics of intact loess and resultant macroscale mechanical properties. *Catena*, 203, 105361. http://dx.doi.org/10.1016/j.catena.2021.105361.

Jennings, J.E., & Knight, K. (1975). A guide to construction on or with materials exhibiting additional settlement due to collapse of grain structure. In *Proc. 6th Regional Conference for Africa on Soil Mechanics and Foundation Engineering* (Vol. 1, pp. 99-105). Durban: Balkema.

Khodabandeh, M.A., Nokande, S., Besharatinezhad, A., Sadeghi, B., & Hosseini, S.M. (2020). The effect of acidic and alkaline chemical solutions on the behavior of collapsible soils. *Periodica Polytechnica. Civil Engineering*, 64(3), 939-950. http://dx.doi.org/10.3311/PPci.15643.

Li, P., Vanapalli, S., & Li, T. (2016). Review of collapse triggering mechanism of collapsible soils due to wetting. *Journal of Rock Mechanics and Geotechnical Engineering*, 8(2), 256-274. http://dx.doi.org/10.1016/j.jrmge.2015.12.002.

Lloret, A., & Alonso, E.E. (1980). Consolidation of unsaturated soils including swelling and collapse behaviour. *Geotechnique*, 30(4), 449-477. http://dx.doi.org/10.1680/geot.1980.30.4.449.

Nam, S., Gutierrez, M., Diplas, P., & Petrie, J. (2021). Laboratory and in situ determination of hydraulic conductivity and their validity in transient seepage analysis. *Water*, 13(8), 1131. http://dx.doi.org/10.3390/w13081131.

Nokande, S., Khodabandeh, M.A., Hosseini, S.S., & Hosseini, S.M. (2020). Collapse Potential of oil-contaminated Loessial Soil (Case Study: Golestan, Iran). *Geotechnical and Geological Engineering*, 38(1), 255-264. http://dx.doi.org/10.1007/s10706-019-01014-9.

Ozelim, L.C.S.M., Carvalho, J.C., Cavalcante, A.L.B., Silva, J.P., & Muñeton, C.M.G. (2015). Novel approach to consolidation theory of structured and collapsible soils. *International Journal of Geomechanics*, 15(4), 04014064. http://dx.doi.org/10.1061/(ASCE)GM.1943-5622.0000409.

Reginatto, A.R., & Ferrero, J.C. (1975). Collapse potential of soils and soil-water chemistry. *International Journal of Rock Mechanics and Mining Sciences & Geomechanics Abstracts*, 12(4), 59. http://dx.doi.org/10.1016/0148-9062(75)90062-5.

Reynolds, W.D., & Zebchuk, W.D. (1996). Hydraulic conductivity in a clay soil: two measurement techniques and spatial characterization. *Soil Science Society of America Journal*, 60(6), 1679-1685. http://dx.doi.org/10.2136/sssaj1996.03615995006000060011x.

Rodrigues, R.A., & Lollo, J.A. (2007). Influence of domestic sewage leakage on the collapse of tropical soils. *Bulletin of Engineering Geology and the Environment*, 66(2), 215-223. http://dx.doi.org/10.1007/s10064-006-0065-y.

Terzaghi, K. (1943). *Theoretical soil mechanics*. New York: Wiley. http://dx.doi.org/10.1002/9780470172766.

Vargas, M. (1978). *Introdução à mecânica dos solos* (2. ed.). São Paulo: McGraw-Hill do Brasil.

Soils and Rocks
An International Journal of Geotechnical and Geoenvironmental Engineering
www.soilsandrocks.com
ISSN 1980-9743
ISSN-e 2675-5475

Compressibility and consolidation properties of Santos soft clay near Barnabé Island

Vitor Nascimento Aguiar[1#], Maurício do Espírito Santo Andrade[2], Ian Schumann Marques Martins[3], Jean Pierre Paul Rémy[4], Paulo Eduardo Lima de Santa Maria[5]

Article

Keywords
Santos soft clay
Geotechnical characterization
One-dimensional consolidation test
Sample quality
Remolding effects
Strain-rate effects

Abstract

A geotechnical study based on characterization tests and seventy incremental loading one-dimensional consolidation tests was carried out on high-quality undisturbed samples taken from Santos Harbor Channel subsoil near to Barnabé Island, where a pilot embankment was built. The characterization profiles revealed a stratigraphy following the pattern described by Massad (2009), with a 9 m-thick fluvial-lagoon-bay sediments (SFL) clay layer. The consolidation tests were performed following two loading criteria. In criterion A (series one tests), a new loading was applied whenever the strain rate ($\dot{\varepsilon}$) reached 10^{-6} s^{-1}, the highest integer power of 10 after the "end of primary" consolidation for double drained 2 cm-thick specimens. In criterion B (series two tests), the standard procedure of 24 hour-long stages was adopted. Criterion A reduced the total duration of the consolidation tests from ten to about three days. The preconsolidation (yield) stress (σ'_p) and the compressibility parameters C_c and C_r obtained from "e versus σ'_v (log)" compression curves of all tests are provided. Series two tests showed that the 24-hour "e versus σ'_v (log)" compression curves are translated to the left of the $\dot{\varepsilon} = 10^{-6}$ s^{-1} "e versus σ'_v (log)" compression curves, keeping C_r and C_c average values unchanged, but decreasing σ'_p by about 8%. The SFL clay $C_c/(1+e_0)$ values obtained herein are higher than those presented by Massad (2009) due to the higher-quality samples tested in this study. It is shown that it is feasible to carry out a high-quality laboratory test program for design purposes following current standards.

1. Introduction

The city of Santos is in the coast of São Paulo State, 80 km far from the city of São Paulo. The Santos lowlands consist of thick layers of soft clayey soils, which imply important civil engineering problems due to their high compressibility and low shear strength. In the last few decades, several geotechnical studies have been carried out on the Santos soft clays (Massad, 2009).

According to Suguio & Martin (1994), the fluctuations in sea level during the Quaternary was the main mechanism that formed the marine sediments of the São Paulo State coastal plains. Two transgressive episodes would have been responsible for different types of sediments. The first, called Cananeia Transgression, occurred in the Pleistocene between 100,000 and 120,000 years ago, when the sea level was probably 8 ± 2 m above the present sea level. The second episode, called Santos Transgression, occurred in the Holocene (last 11,000 years), when the sea level reached its maximum between 2.3 m and 5.0 m above the present level 5100 years ago.

Massad (1985) proposed a genetic classification for the Santos lowlands clays, grouping them into three main units: Mangrove clays, SFL clays and Transitional clays. Massad (2009, Table 5.1) described the Mangrove clays as "modern" deposits that show preconsolidation (yield) stress (σ'_p) ≤ 30 kPa, void ratio (e) > 4 and SPT blow count (N) = 0. SFL clays (fluvial-lagoon-bay sediments) were deposited during the Santos Transgression about 5000-7000 years

[#]Corresponding author. E-mail address: vitornaguiar@hotmail.com
[1]Pontifícia Universidade Católica do Rio de Janeiro, Department of Civil and Environmental Engineering, Rio de Janeiro, RJ, Brasil.
[2]Universidade Tecnológica Federal do Paraná, Department of Civil Engineering, Toledo, PR, Brasil.
[3]Universidade Federal do Rio de Janeiro, Graduate School and Research in Engineering, Department of Civil Engineering, Rio de Janeiro, RJ, Brasil.
[4]Mecasolo Engenharia e Consultoria Eireli, Nova Friburgo, RJ, Brasil.
[5]SM Engenheiros Consultores Ltda, Rio de Janeiro, RJ, Brasil.

Submitted on September 5, 2021; Final Acceptance on November 10, 2021; Discussion open until February 28, 2022.

https://doi.org/10.28927/SR.2021.074821

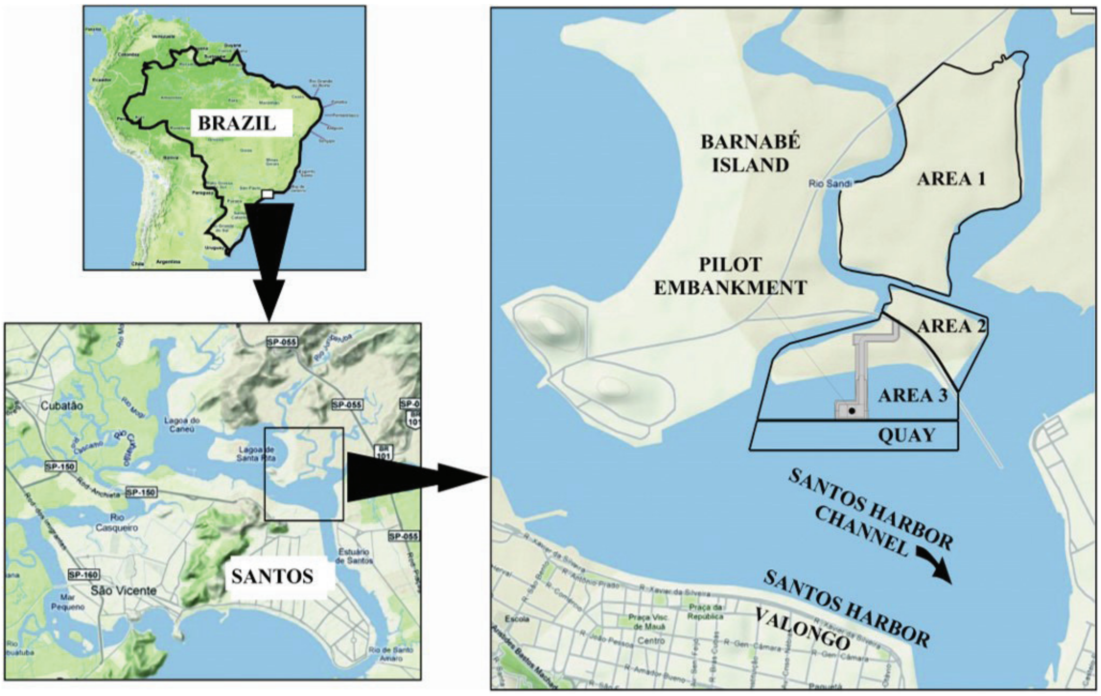

Figure 1. Pilot embankment site (adapted from Rémy et al., 2011).

ago, with 30 kPa $\leq \sigma'_p \leq$ 200 kPa, 2 $\leq e \leq$ 4 and 0 $\leq$ N $\leq$ 4. Transitional clays, deposited in a mixed continental-marine environment during the Cananeia Transgression, have 200 kPa $\leq \sigma'_p \leq$ 700 kPa, $e <$ 2 and 5 $\leq$ N $\leq$ 25. Massad (2009) provided a complete characterization, physical indexes and compressibility, consolidation and shear strength parameters of the three genetic units.

The Santos harbor is the largest and most important port complex in Latin America. There are currently several expansion projects alongside the Santos harbor channel. A multipurpose terminal covering an area of 800,000 m^2 was built on Barnabé Island, on the left bank of the Santos harbor channel (Figure 1). An instrumented pilot embankment was built in 2007 to provide field compressibility, consolidation and shear strength data of the soft clay foundation deposit (Rémy et al. 2011). A comprehensive laboratory test program on high-quality samples as well as *in situ* geotechnical investigation were also carried out.

The purpose of this paper is to present the characterization test results and the compressibility and consolidation parameters obtained from one-dimensional consolidation tests of the subsoil samples taken in the pilot embankment area before its construction.

2. Materials and methods

2.1 Sampling, transportation and storage

Figure 2 shows the boreholes location for standard penetration tests (SPM) and for taking undisturbed samples (SRA) in the pilot embankment area. The undisturbed samples

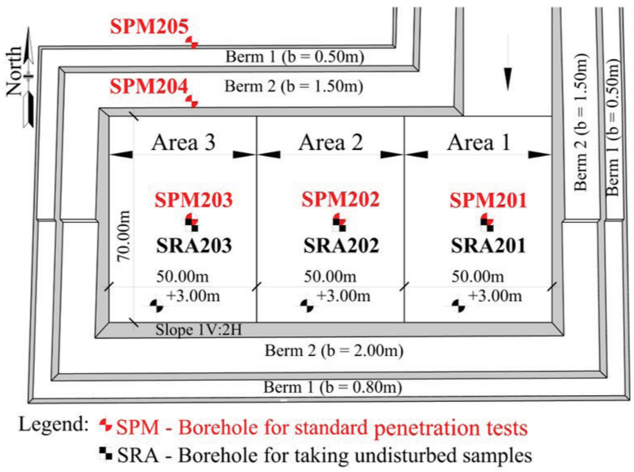

Figure 2. Boreholes location in the pilot embankment area (adapted from Rémy et al., 2011).

taken from borehole SRA203 were sent to the Soil Rheology Laboratory of the Federal University of Rio de Janeiro, where they were tested. The samples taken from boreholes SRA201 and SRA202 were tested in another laboratory and are not presented herein.

To take good-quality samples, ABNT (1997) and "*Technical specification for taking undisturbed samples*" (Aguiar, 2008) were followed. 10 cm-inner diameter and 70 cm-long thin-wall fixed piston samplers were used. The samples were taken by a team trained by two of the authors when taking the first samples. Figure 3 shows the position of the twelve undisturbed samples taken from borehole SRA203 along the borehole SPM203 profile.

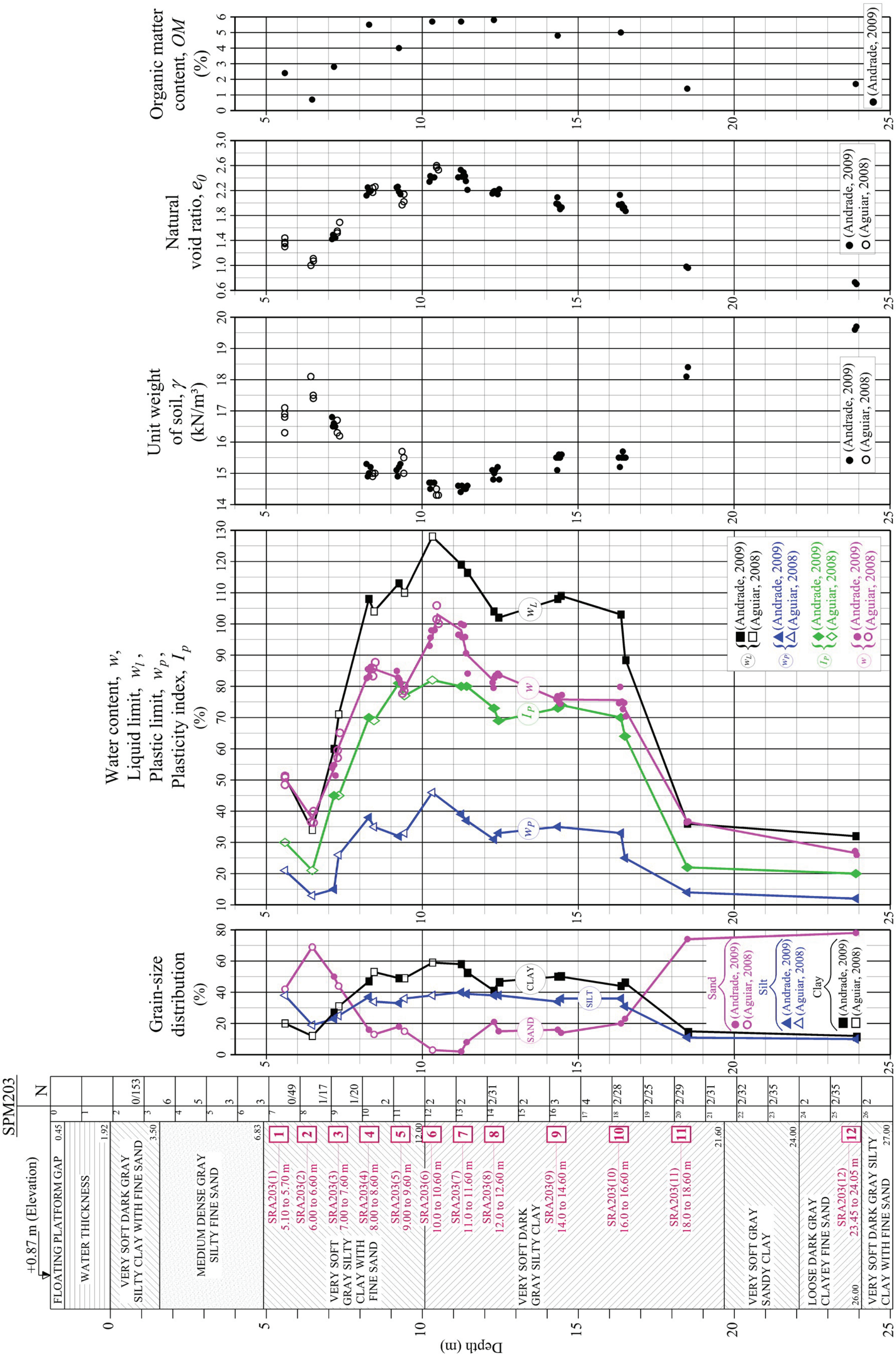

Figure 3. Subsoil profile based on borehole SPM203 and characterization test results carried out on SRA203 samples.

The borehole SPM203 showed a first layer of very soft clay 1.60 m thick with N = 0. According to the Massad (2009) genetic classification, this layer is a Mangrove clay. It must be recognized that N = 0 terminology comprises a wide range of soft clay consistencies, that goes from P/30, meaning a 30 cm penetration of the SPT sampler under the hammer's weight, to 0/XXX, where XXX means the penetration in centimeters of the SPT sampler under the rod set weight only. For instance, in Figure 3, at 1.0 m depth the symbol 0/153 means that the SPT sampler penetrated 153 cm under the rod set weight. Such consistency range is usually found in Santos Mangrove clay layers. Underlying this clay layer, there is a 3.30 m-thick sand layer with N between 3 and 6. The first undisturbed sample was taken 10 cm below the bottom of this sand layer (Figure 3).

The sample ends were covered with PVC film and aluminum foil and sealed with paraffin wax. The sampler tip was protected against bumps with a 10 cm-high PVC rigid ring. The samples were shipped in vertical position into wood containers with the tip downwards (ASTM, 2007). After sampling, the samplers were placed into the wood containers, stored in a room protected from the sun, where people circulation was not allowed. After taking the last sample, the containers were sent to the laboratory and stored in a humid room.

2.2 Geotechnical characterization

Table 1 shows grain-size distribution (ABNT, 1995), liquid limit (w_L), plastic limit (w_P), plasticity index (I_P), specific gravity (G_s) and organic matter content (OM) obtained for the indicated segments of each SRA203 sample (second column of Table 1). Water content (w), unit weight of soil (γ), natural void ratio (e_0) and degree of saturation (S_r) are the average values obtained from the undisturbed consolidation test specimens belonging to each sample segment.

Figure 3 shows the subsoil profile according to tactile-visual examination of the SPT samples from borehole SPM203 only. Figure 3 also shows the laboratory characterization test results carried out on SRA203 samples and w, γ and e_0 values are plotted for all undisturbed consolidation test specimens.

Table 1. Characterization test results of samples SRA203(1) to SRA203(12).

Sample	Depth[(a)] (m)	w (%)	G_s	S_r (%)	e_0	γ (kN/m³)	Atterberg Limits (%)			Grain-size distribution (%)			OM (%)
							w_L	w_P	I_P	sand	silt	clay	
SRA203(1)	5.55 - 5.65	50.5	2.64	98	1.37	16.8	51	21	30	42	38	20	2.4
SRA203(2)	6.40 - 6.55	37.6	2.65	94	1.06	17.7	34	13	21	69	19	12	0.7
SRA203(3)	7.10 - 7.25	53.7	2.63	98	1.46	16.6	60	15	45	50	23	27	2.8
	7.25 - 7.40	60.6	2.64	99	1.59	16.4	71	26	45	44	25	31	-
SRA203(4)	8.20 - 8.38	84.4	2.60	100	2.18	15.1	108	38	70	16	37	47	5.5
	8.38 - 8.53	85.6	2.60	100	2.22	15.0	104	35	69	13	34	53	-
SRA203(5)	9.17 - 9.34	82.7	2.65	99	2.21	15.1	113	32	81	18	33	49	4.0
	9.34 - 9.45	78.8	2.62	99	2.04	15.4	110	33	77	15	36	49	-
SRA203(6)	10.22 - 10.43	96.1	-	100	2.40	14.7	-	-	-	-	-	-	5.7
	10.43 - 10.55	103	2.53	100	2.57	14.4	128	46	82	3	38	59	-
SRA203(7)	11.14 - 11.36	98.0	-	100	2.46	14.6	119	39	80	2	40	58	5.7
	11.36 - 11.49	90.2	2.55	98	2.33	14.5	117	37	80	8	39	53	-
SRA203(8)	12.24 - 12.36	81.7	2.59	99	2.18	15.0	104	31	73	21	38	41	5.8
	12.40 - 12.50	83.8	2.62	99	2.18	15.0	102	33	69	15	38	47	-
SRA203(9)	14.29 - 14.40	75.8	2.63	99	2.01	15.4	108	35	73	16	34	50	4.8
	14.40 - 14.50	75.8	2.58	100	1.92	15.6	109	35	74	14	36	50	-
SRA203(10)	16.29 - 16.45	75.6	2.64	100	2.00	15.5	103	33	70	20	36	44	5.0
	16.45 - 16.55	72.6	2.60	99	1.90	15.5	89	25	64	23	31	46	-
SRA203(11)	18.45 - 18.55	36.6	2.63	99	0.97	18.3	36	14	22	74	11	15	1.4
SRA203(12)	23.85 - 23.95	26.6	2.66	99	0.72	19.7	32	12	20	78	10	12	1.7

[(a)]The depths indicated are not the depths at the top and bottom of the undisturbed samples as shown in Figure 3, but rather the depths of segments of the samples where the undisturbed consolidation test specimens were trimmed.

Samples SRA203(1), SRA203(2) and SRA203(3) test results revealed that the subsoil profile corresponding to their depths should be better described as "silty clayey sand". According to sample SRA203(11) test results, the subsoil profile at its depth should be better described as "clayey sand".

2.3 One-dimensional consolidation test procedure

Incremental loading one-dimensional consolidation tests were carried out on the twelve samples from borehole SRA203.

Long-term loading stages were run in selected tests to investigate secondary consolidation and stress relaxation. However, these results are outside the scope of this paper.

2 cm-high and 7 cm-diameter specimens were trimmed following Ladd and DeGroot (2003) recommendations and additional cares described by Aguiar (2008) and Andrade (2009).

Specimens are identified by the acronym CPMX, where CP means specimen, M is the sample number and X the letter that denotes the order position of the specimen in sample M, for instance: CP6E is the fifth (letter E) specimen trimmed in sample SRA203(6). Tables A1 and A2 (see Appendix) indicate the depth interval from which each specimen was trimmed.

All tests were carried out on Bishop-type consolidation frames, with settlements being measured by 0.01 mm/division dial gages, under temperature of 20 ± 1 ºC. Temperature variations were daily monitored by a *maximum* and *minimum* thermometer.

Each consolidation test was performed using one out of two loading criteria: criterion A, based on the specimen vertical strain rate ($\dot{\varepsilon}$), and criterion B, based on stage duration.

In criterion A, a new loading stage was applied whenever the vertical strain rate ($\dot{\varepsilon}$) reached 10^{-6} s^{-1}, calculated as:

$$\dot{\varepsilon} = \frac{1}{\Delta t}\left(\frac{\Delta H}{H}\right) \tag{1}$$

where:
H: specimen height corresponding to reading of order i;
ΔH: settlement difference $\left(H_i - H_{i+1}\right)$;
Δt: time elapsed between readings of orders i and i + 1.

For samples SRA203(4) to SRA203(10), it was observed that $\dot{\varepsilon}$ =10^{-6} s^{-1} corresponded to the higher integer power of 10 after the "end of primary" consolidation, calculated by both Taylor (1942) ($\sqrt{t}$) and Casagrande (*log(t)*) methods of coefficient of consolidation (c_v) determination for specimens whose drainage path is about 1 cm.

A first series of consolidation tests ("series one") was performed on all twelve samples using criterion A. The following specimens were tested:

- four undisturbed specimens from sample SRA203(1),
- three undisturbed specimens and one remolded specimen from each out of samples SRA203(2) to SRA203(7),
- two undisturbed specimens from each out of samples SRA203(8) to SRA203(12), totalizing thirty eight tests, being thirty two on undisturbed specimens and six on remolded specimens.

Remolding was done prior to specimen trimming, by smashing an amount of sample inside a plastic bag. Consolidation tests on remolded specimens were carried out to check the quality of the undisturbed specimens by comparing their results.

All tests in series one underwent the following loading sequence up to 100 kPa: 3.13, 6.25, 12.5, 25, 50 and 100 kPa. From 100 kPa on, the loading and unloading sequences followed different patterns, as shown in Table 2. In some tests, a loading stage was selected to monitor secondary consolidation under a chosen overconsolidation ratio (*OCR*). In other tests, stress relaxation was observed by preventing specimen settlements. These stages were analyzed by Aguiar (2008) and Andrade (2009).

In tests with specimens CP7A, CP7B, CP7C and CP7D, influence of temperature was investigated in loading stages beyond 300 kPa. As σ'_p values of these specimens are not greater than 160 kPa and the compression index (C_c) values were determined in the virgin compression curves immediately after σ'_p , the C_c values obtained were not affected by the loading stages in which temperature effects were investigated.

A second series of consolidation tests ("series two") was carried out using criterion B, in which four undisturbed specimens were tested from each out of samples SRA203(3) to SRA203(10), totalizing thirty two tests.

In criterion B, the loading stages lasted 24 hours and the loading sequence was 3.13, 6.25, 12.5, 25, 50, 100, 150, 200, 300, 500 and 800 kPa, followed by unloading to 400 and 200 kPa, except for specimens CP8C, CP8D, CP8E and CP8F, which were unloaded to different stresses in order to investigate secondary consolidation under different *OCR* values, as shown in Table 3. These unloading stages were analyzed by Andrade (2009).

Stress increment ratio ($\Delta\sigma/\sigma$) < 1 in the loading sequence of series two was intended to determine σ'_p with more accuracy and to define more clearly the compression curve.

Hence, seventy consolidation tests were run in the two test series, being sixty four on undisturbed specimens and six on remolded ones.

3. Test results

Vertical strain (ε) versus vertical effective stress (σ'_v) (log) and void ratio (e) versus σ'_v (log) compression curves of series one specimens were plotted with ε and e of each loading stage corresponding to:

a) "end of primary" consolidation calculated by Taylor's (1942) method and
b) vertical strain rate ($\dot{\varepsilon}$) of 10^{-6} s^{-1}.

ε versus σ'_v (log) and e versus σ'_v (log) compression curves of series two specimens were plotted with ε and e of each loading stage corresponding to:

a) "end of primary" consolidation calculated by Taylor's (1942) method,

Table 2. Loading and unloading sequences from 100 kPa on of series one specimens.

Specimen	Loading and unloading sequences (kPa)
CP1A	100/200 (sec. cons. for 42 days, *OCR*=1.00)/400/350/200/100
CP1B	100 - 200 (stress relax. for 42 days) - 400 - 350 - 200 -100
CP1C	100 - 250 - 200 (sec. cons. for 42 days, *OCR*=1.25) - 250 - 400 - 350 - 200 - 100
CP1D	100 - 300 - 200 (sec. cons. for 42 days, *OCR*=1.50) - 300 - 400 - 350 - 200 - 100
CP2A	100 - 200 (sec. cons. for 19 days, *OCR*=1.00) - 400 - 800 - 400 - 200
CP2B	100 - 200 (stress relax. for 19 days) - 400 - 800 - 400 - 200
CP2C	100 - 250 - 200 (sec. cons. for 19 days, *OCR*=1.25) - 250 - 400 - 800 - 400 - 200
CP2D[(a)]	100 - 200 - 50 (sec. cons. for 19 days, *OCR*=4.00) - 100 - 200 - 400 - 800 - 400 - 200
CP3A	100 - 200 (sec. cons. for 17 days, *OCR*=1.00) - 400 - 800 - 400 - 200
CP3B	100 - 200 (stress relax. for 17 days) - 400 - 800 - 400 - 200
CP3C	100 - 250 - 200 (sec. cons. for 17 days, *OCR*=1.25) - 250 - 400 - 800 - 400 - 200
CP3D[(a)]	100 - 200 - 50 (sec. cons. for 17 days, *OCR*=4.00) - 100 - 200 - 400 - 800 - 400 - 200
CP4A	100 - 200 (sec. cons. for 19 days, *OCR*=1.00) - 400 - 800 - 400 - 200
CP4B	100 - 200 (stress relax. for 19 days) - 400 - 800 - 400 - 200
CP4C	100 - 300 - 200 (sec. cons. for 19 days, *OCR*=1.50) - 300 - 400 - 800 - 400 - 200
CP4D[(a)]	100 - 200 -100 - 50 (sec. cons. for 19 days, *OCR*=4.00) - 100 - 200 - 400 - 800 - 400 - 200
CP5A	100 - 150 - 200 (sec. cons. for 47 days, *OCR*=1.00) - 300 - 400 - 800 - 400 - 200
CP5B	100 - 150 - 200 - 300 (stress relax. for 47 days) - 400 - 800 - 400 - 200
CP5C	100 - 150 - 200 - 300 - 200 (sec. cons. for 47 days, *OCR*=1.50) - 300 - 400 - 800 - 400 - 200
CP5D[(a)]	100 - 200 -100 - 50 (sec. cons. for 47 days, *OCR*=4.00) - 100 - 200 - 400 - 800 - 400 - 200
CP6A	100 - 150 - 200 - 400 (sec. cons. for 42 days, *OCR*=1.00) - 800 - 400 - 200
CP6B	100 - 150 - 200 - 400 - 720 - 400 (sec. cons. for 42 days, *OCR*=1.80) - 720 - 800 - 400 - 200
CP6C	100 - 150 - 200 - 400 - 640 - 400 (sec. cons. for 42 days, *OCR*=1.60) - 640 - 800 - 400 - 200
CP6D[(a)]	100 - 200 -100 - 50 (sec. cons. for 42 days, *OCR*=4.00) - 100 - 200 - 400 - 800 - 400 - 200
CP7A	100 - 150 - 200 - 400 - 300 (sec. cons. for 60 days, *OCR*=1.33, 20°C → 35°C) - 400 (sec. cons. for 66 days, *OCR*=1.00, 35°C) - 650 (35°C → 20°C) - 1000 - 500 (sec. cons. for 59 days, *OCR*=2.00) - 250
CP7B	100 - 150 - 200 - 450 (stress relax. for 60 days, 20°C → 35°C; sec. cons. for 23 days, *OCR* = 1,00, 35°C; stress relax. for 44 days, 35°C) - 650 (35°C → 20°C) - 1000 - 500 (sec. cons. for 59 days, *OCR*=2.00) - 250
CP7C	100 - 150 - 200 - 500 - 300 (sec. cons. for 60 days, 20°C → 35°C) - 400 (sec. cons. for 66 days, 35°C) - 650 (35°C → 20°C) - 1000 - 500 - 250 (sec. cons. for 57 days, *OCR*=4.00)
CP7D[(a)]	100 - 200 - 400 - 800 - 400 - 200 (sec. cons. for 186 days, *OCR*=4.00, 20°C → 35°C → 20°C)
CP8A	100 - 150 - 200 - 400 - 800 - 400 - 200
CP8B	100 - 150 - 200 - 400 - 800 - 400 - 200
CP9A	100 - 150 - 200 - 300 - 500 - 800 - 400 - 200
CP9B	100 - 150 - 200 - 300 - 500 - 800 - 400 - 200
CP10A	100 - 200 - 300 - 500 - 800 - 400 - 200
CP10B	100 - 200 - 300 - 500 - 800 - 400 - 200
CP11A	100 - 200 - 300 - 500 - 800 - 400 - 200
CP11B	100 - 200 - 300 - 500 - 800 - 400 - 200
CP12A	100 - 200 - 300 - 400 - 600 - 800 - 400 - 200
CP12B	100 - 200 - 300 - 400 - 600 - 800 - 400 - 200

[(a)]specimen remolded in the laboratory; sec.cons.: secondary consolidation; stress relax.: stress relaxation (settlement prevented).

Table 3. Unloading sequence from 800 kPa of series two SRA203(8) specimens.

Specimen	Unloading sequence (kPa)
CP8C	800 - 350 (secondary consolidation for 20 days, *OCR*=2.29) - 200
CP8D	800 - 400 (secondary consolidation for 20 days, *OCR*=2.00) - 200
CP8E	800 - 300 (secondary consolidation. for 20 days, *OCR*=2.67) - 200
CP8F	800 - 500 (secondary consolidation for 20 days, *OCR*=1.60) - 200

b) vertical strain rate ($\dot{\varepsilon}$) of 10^{-6} s^{-1} and
c) end of 24 hours.

Compression curves plotted in terms of void ratio (*e*) according to the criteria mentioned above were compared. Figure 4 shows an example of such comparison for specimen CP5E, from series two. The comparisons of all the other specimens were presented by Aguiar (2008) and Andrade (2009). As observed in all tests, the 24-hour compression curve lies below the $\dot{\varepsilon} = 10^{-6}$ s^{-1} compression curve, which, in its turn, lies below the "end of primary" compression curve.

From 12.5 kPa on, c_v values were determined by Taylor's (1942) method and plotted against the average σ'_v values of the respective loading stages. ε versus σ'_v(log) and *e* versus σ'_v(log) compression curves corresponding to "end of primary", $\dot{\varepsilon} = 10^{-6}$ s^{-1} and 24 hours, together with the c_v(log) versus average σ'_v(log) curves, of all seventy specimens were presented by Aguiar (2008) and Andrade (2009). Figure 5 shows the ε versus σ'_v(log) curves corresponding to $\dot{\varepsilon} = 10^{-6}$ s^{-1} and the c_v(log) versus average σ'_v(log) curves of all SRA203(6) specimens. Specimen CP6D was remolded. Figure 6 shows the ε versus σ'_v(log) curves corresponding to 24 hours and the c_v(log) versus average σ'_v(log) curves of series two SRA203(8) specimens. The excellent repeatability of the results obtained for the SRA203(6) and SRA203(8) specimens (Figures 5 and 6) was also observed in all SRA203(4) to SRA203(10) specimens, which belong to the SFL clay layer, as discussed further.

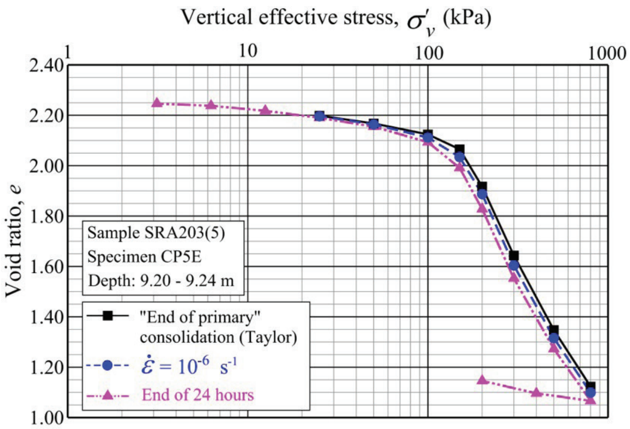

Figure 4. *e* versus σ'_v(log) curves of specimen CP5E.

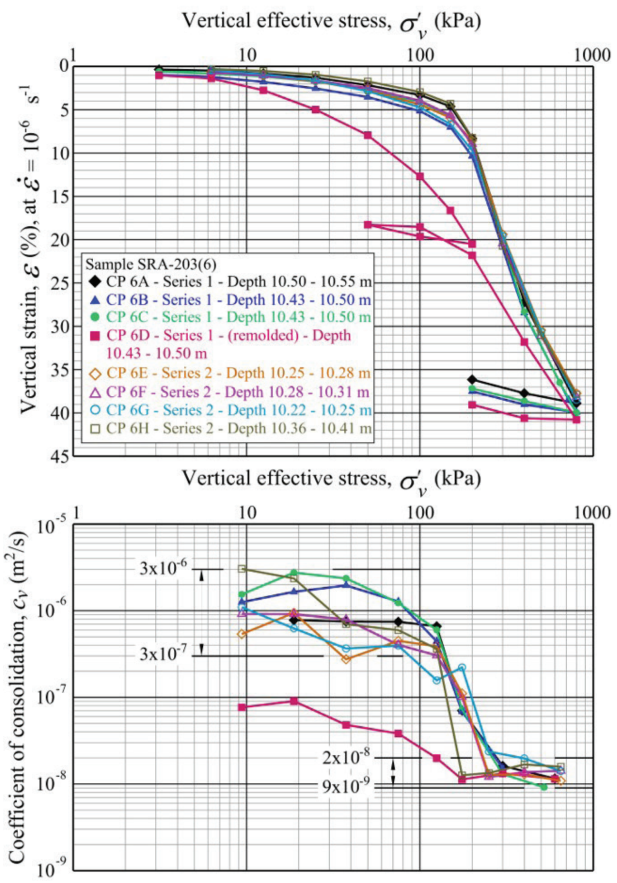

Figure 5. ε versus σ'_v(log) curves corresponding to $\dot{\varepsilon} = 10^{-6}$ s^{-1} and c_v(log) versus average σ'_v(log) curves of all SRA203(6) specimens (adapted from Rémy et al., 2011).

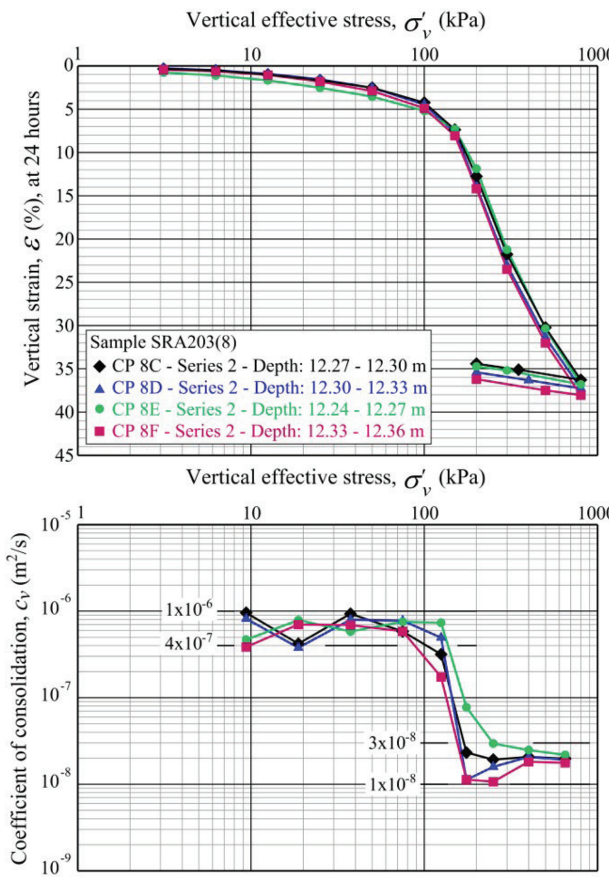

Figure 6. ε versus σ'_v(log) curves corresponding to 24 hours and c_v(log) versus average σ'_v(log) curves of series two SRA203(8) specimens.

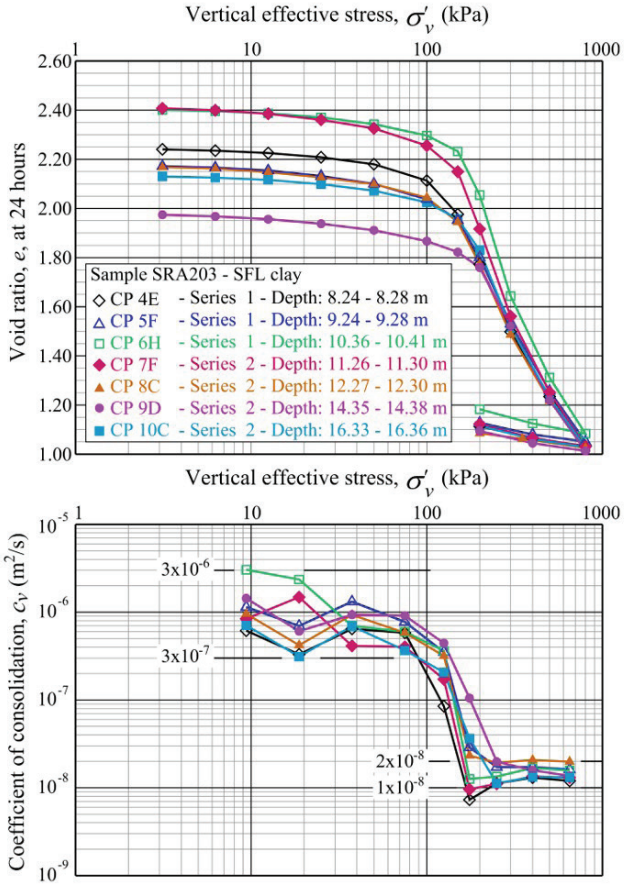

Figure 7. *e* versus σ'_v(log) typical curves corresponding to 24 hours and their respective c_v(log) versus average σ'_v(log) curves from samples SRA203(4) to SRA203(10).

Figure 7 gathers typical *e* versus σ'_v(log) curves corresponding to 24 hours and their respective c_v(log) versus average σ'_v(log) curves from one undisturbed specimen of each sample from SRA203(4) to SRA203(10). Compression curves for samples SRA203(1), SRA203(2), SRA203(3), SRA203(11) and SRA203(12) are not included since they are sand. Figure 7 shows that, for practical purposes, samples SRA203(4) to SRA203(10) can be assumed to belong to a single "homogeneous" clay layer.

The preconsolidation (yield) stress (σ'_p), compression index (C_c) and recompression index (C_r) were obtained for all specimens (series one and two) from *e* versus σ'_v(log) curves corresponding to $\dot{\varepsilon} = 10^{-6}$ s^{-1} as shown in Table A1 (see Appendix A), which also shows $C_c/(1+e_0)$ and C_r/C_c values. The same parameters, including the swelling index (C_s), were also obtained for series two specimens from *e* versus σ'_v(log) curves corresponding to 24 hours as shown in Table A2 (see Appendix A), which also shows $C_c/(1+e_0)$ and C_r/C_c values. All C_s values correspond to an $OCR = 4$. The σ'_p values were obtained according to Silva (1970) method. The C_r, C_c and C_s values were determined as shown in Figure 8. σ'_{v0} is the effective overburden stress.

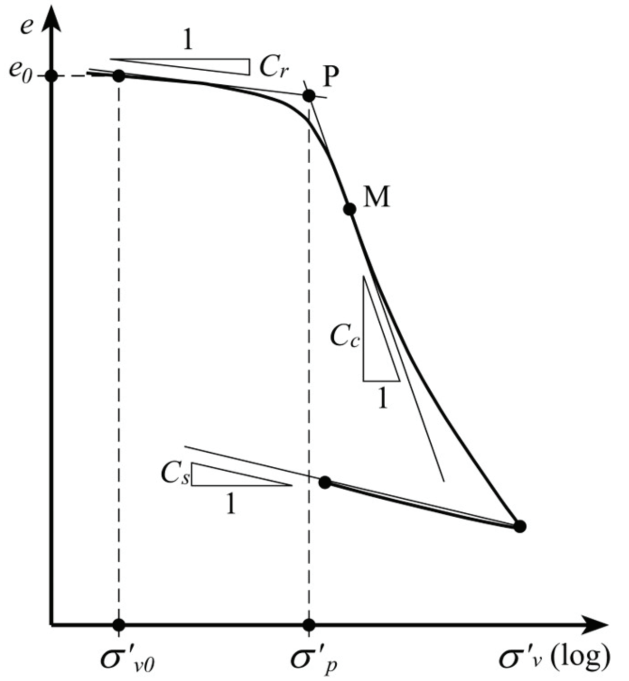

Figure 8. Procedure for determining C_r, C_c e C_s values.

Figure 9 shows the profiles of σ'_p, $C_c/(1+e_0)$ and C_r/C_c obtained from *e* versus σ'_v(log) curves corresponding to $\dot{\varepsilon} = 10^{-6}$ s^{-1} of all specimens (series one and two - Table A1), and from *e* versus σ'_v(log) curves corresponding to 24 hours of all series two specimens (Table A2).

4. Discussion

4.1 Stratigraphy and characterization

Figure 10 shows the stratigraphy of the subsoil based on borehole SPM203 SPT samples, characterization tests and physical indexes of the undisturbed samples as well as on tactile-visual examination when trimming the consolidation test specimens.

Since no undisturbed samples were obtained from the mangrove clay layer, a unit weight of 13.0 kN/m³ was assigned to it based on Massad (2009, pp. 106). The existence of this layer was confirmed *in situ* via SPT samples examination. As no undisturbed samples were obtained from the top sand layer, a unit weight of 20.0 kN/m³ was assigned to it since this layer is sandier than SRA203(12) sample, which unit weight is 19.7 kN/m³ (Table 1).

Between the top sand layer and the SFL clay layer, there is a transition layer composed by three sandy sublayers identified based on samples SRA203(1), SRA203(2) and SRA203(3) characterization tests and physical indexes.

Samples SRA203(4) to SRA203(10) characterization tests and physical indexes revealed that they belong to a single SFL clay layer according to the Massad (2009) genetic

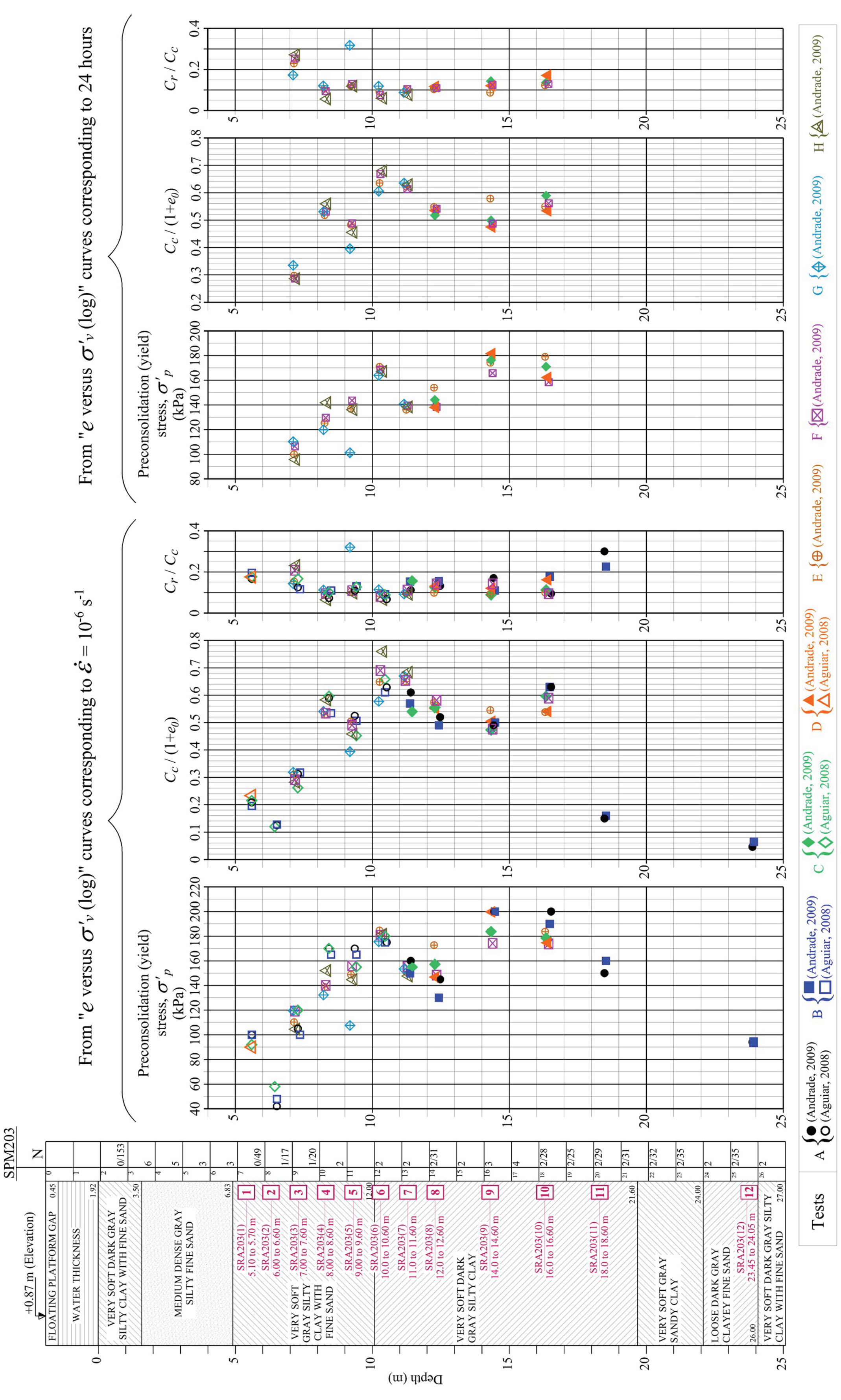

Figure 9. Profiles of σ'_p, $C_c/(1+e_0)$ and C_r/C_c from "e versus σ'_v(log)" curves corresponding to $\dot{\varepsilon} = 10^{-6}\ s^{-1}$ and to 24 hours.

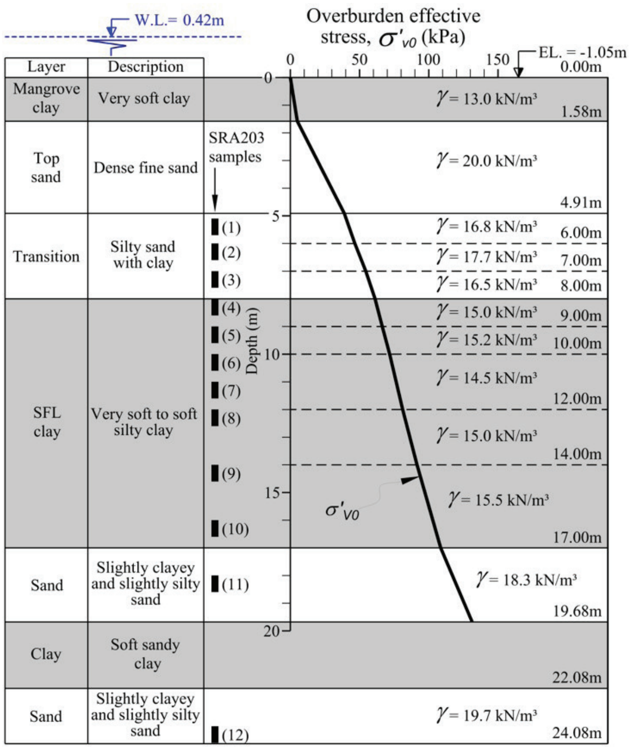

Figure 10. Geotechnical profile of the subsoil.

classification. It is worth noting the increase of water content and plasticity from sample SRA203(3) to SRA203(4), as well as the decrease of water content and plasticity from sample SRA203(10) to SRA203(11). Samples SRA203(6) and SRA203(7) have water content, void ratio, liquid limit and clay content higher than the others. Presence of kaolinite, smectite and illite was identified along the SFL clay layer by X-ray diffraction.

Samples SRA203(11) and SRA203(12) characterization tests and physical indexes showed that they belong to sand layers below the SFL clay layer.

The unit weights shown in Figure 10 are the average values from undisturbed consolidation test specimens of each sample and the effective overburden stress (σ'_{v0}) profile was estimated with these unit weights.

4.2 Sample quality and remolding effects on one-dimensional compression curves

The comparisons between compression curves of remolded and undisturbed specimens (Figure 5) highlighted the following remolding effects (Ladd, 1973):

1) Decreases the void ratio (or increases the strain) at any given σ'_v value;
2) Makes it difficult to define the point of minimum radius, thus obscuring σ'_p;
3) Lowers the estimated value of σ'_p;
4) Increases the compressibility in the recompression region;
5) Decreases the compressibility in the virgin compression region.

Coutinho (1976) and Martins (1983) have also observed that remolding turns the concave shape of the virgin compression curve into a straight line. As σ'_v increases, structure of undisturbed specimens is destroyed, making their behavior approach to that of the remolded specimen. Thus, as σ'_v increases, the compression curves of all specimens tend to merge into a single curve (Figure 5).

Another remarkable feature of high-quality specimens is the abrupt fall of the c_v versus σ'_v(log) curves when σ'_v straddles σ'_p. Such fall may be of two orders of magnitude (Figures 5, 6 and 7). This is not observed in the c_v versus σ'_v(log) curve of the remolded specimen (Figure 5). The smaller c_v values in the recompression region of the remolded specimen are due to the compressibility increase in the recompression region caused by remolding.

Although not shown herein, no difference at all was observed between the compression curve of the remolded specimen and those of the "undisturbed" specimens trimmed on sample SRA203(2), which is 69% sand (Aguiar, 2008).

Regarding footnote (b) in Table A1, C_r values could not be obtained according to Figure 8 since remolding pushed σ'_p to a value lower than σ'_{v0}.

Table 4 shows the quality classification of series two specimens according to Lunne et al. (1997), Coutinho (2007) and Coutinho (2007) modified by Andrade (2009) criteria. Based on his experience with highly plastic soft clays, Coutinho (2007) proposed a modification of Lunne et al. (1997) criterion. Andrade (2009) observed the following shortcoming in both criteria: the quality assigned to the upper bound of a class does not coincide with the quality assigned to the lower bound of the immediately above class. Andrade (2009) was able to solve this shortcoming by subdividing the classes in such a way that on the borderline of two subsequent classes, the quality to be assigned is the common term of both classes (Table 5). For instance: for $\Delta e/e_0 = 0.080$ the quality to be assigned is "fair".

Only three specimens (CP5G, CP10D and CP10F) out of thirty two were classified below "Good to Fair" according to the Coutinho (2007) modified criterion (Table 4).

4.3 Compressibility

4.3.1 Comparison between compressibility parameters obtained from $\dot{\varepsilon} = 10^{-6}$ s^{-1} and 24-hour compression curves

Table 6 compares σ'_p, C_r and C_c values obtained from $= 10^{-6}$ s^{-1} and 24-hour "e versus σ'_v (log)" curves of series two specimens from the SFL clay layer.

The ratio between σ'_p from the $\dot{\varepsilon} = 10^{-6}$ s^{-1} compression curve, denoted by σ'_p (10^{-6} s^{-1}), and σ'_p from the 24-hour

Table 4. Quality classification of series two specimens.

Specimen	σ'_{v0} (kPa)	σ'_p (kPa)	*OCR*	e_0	e (σ'_{v0})	$\Delta e/e_0$	Lunne et al. (1997)	Coutinho (2007)	Coutinho (2007) modified
CP3E	53.9	100	1.9	1.49	1.39	0.067	Good to fair	Good to fair	Good to fair
CP3F	54.1	106	2.0	1.47	1.39	0.054	Good to fair	Good to fair	Very good to good
CP3G	53.7	110	2.0	1.42	1.33	0.063	Poor	Good to fair	Very good to good
CP3H	54.4	96.0	1.8	1.44	1.34	0.069	Good to fair	Good to fair	Good to fair
CP4E	60.8	125	2.1	2.25	2.17	0.036	Good to fair	Excellent to very good	Excellent to very good
CP4F	61.0	130	2.1	2.17	2.07	0.046	Good to fair	Excellent to very good	Excellent to very good
CP4G	60.6	120	2.0	2.12	2.01	0.052	Good to fair	Good to fair	Very good to good
CP4H	61.3	142	2.3	2.19	2.11	0.037	Good to fair	Excellent to very good	Excellent to very good
CP5E	65.6	137	2.1	2.26	2.14	0.053	Poor	Good to fair	Very good to good
CP5F	65.9	144	2.2	2.18	2.08	0.046	Good to fair	Excellent to very good	Excellent to very good
CP5G	65.5	101	1.5	2.25	2.05	0.089	Poor	Poor	Fair to poor
CP5H	66.1	136	2.1	2.14	2.03	0.051	Poor	Good to fair	Very good to good
CP6E	70.9	171	2.4	2.43	2.29	0.058	Poor	Good to fair	Very good to good
CP6F	71.0	169	2.4	2.40	2.29	0.046	Good to fair	Excellent to very good	Excellent to very good
CP6G	70.8	164	2.3	2.34	2.20	0.060	Poor	Good to fair	Very good to good
CP6H	71.5	167	2.3	2.41	2.32	0.037	Good to fair	Excellent to very good	Excellent to very good
CP7E	75.3	136	1.8	2.53	2.38	0.059	Good to fair	Good to fair	Very good to good
CP7F	75.5	140	1.9	2.42	2.29	0.054	Good to fair	Good to fair	Very good to good
CP7G	74.9	141	1.9	2.41	2.28	0.054	Good to fair	Good to fair	Very good to good
CP7H	75.7	138	1.8	2.49	2.35	0.056	Good to fair	Good to fair	Very good to good
CP8C	80.1	144	1.8	2.18	2.07	0.050	Good to fair	Good to fair	Very good
CP8D	80.3	138	1.7	2.19	2.07	0.055	Good to fair	Good to fair	Very good to good
CP8E	80.0	154	1.9	2.15	2.00	0.070	AMBIGUOUS	Good to fair	Good to fair
CP8F	80.4	138	1.7	2.19	2.06	0.059	Good to fair	Good to fair	Very good to good
CP9C	90.8	176	1.9	2.09	1.96	0.062	Good to fair	Good to fair	Very good to good
CP9D	91.0	182	2.0	1.98	1.87	0.056	AMBIGUOUS	Good to fair	Very good to good
CP9E	90.7	174	1.9	1.99	1.87	0.060	Good to fair	Good to fair	Very good to good
CP9F	91.1	166	1.8	1.96	1.86	0.051	Good to fair	Good to fair	Very good to good
CP10C	102	171	1.7	2.13	2.02	0.052	Good to fair	Good to fair	Very good to good
CP10D	102	162	1.6	1.98	1.82	0.081	Poor	Poor	Fair to poor
CP10E	102	179	1.8	1.97	1.84	0.066	Good to fair	Good to fair	Good to fair
CP10F	102	158	1.5	1.91	1.72	0.099	Poor	Poor	Fair to poor

Table 5. Coutinho (2007) modified by Andrade (2009) criterion for specimen quality classification.

OCR	$\Delta e/e_0$					
	Excellent to Very good	Very good to Good	Good to Fair	Fair to Poor	Poor to Very poor	Very poor
1→2.5	< 0.050	0.050 to 0.065	0.065 to 0.080	0.080 to 0.110	0.110 to 0.140	> 0.140

compression curve, denoted by σ'_p (24 h), is within 1.03 and 1.12, with an average of 1.08, which is among the rate effects described by Graham et al. (1983), Leroueil et al. (1985) and Crawford (1986). For the Santos soft clay studied herein, σ'_p (10^{-6} s^{-1}) is 8% higher, on average, than σ'_p (24 h). As shown by Leroueil et al. (1985), σ'_p depends on the strain rate adopted to plot the one-dimensional compression curve "e versus σ'_v (log)", σ'_p being higher, the higher the strain rate. This phenomenon is associated with the squeezing out of the viscous adsorbed water layers surrounding clay particles (Terzaghi, 1941; Taylor 1942; Lambe & Whitman 1979, pp. 299). The higher the plasticity index, the greater the thickness of the adsorbed water layer, in the sense explained by Bjerrum (1972; 1973), magnifying secondary compression. Being so, the higher the plasticity index, the wider the spacing expected between $\dot{\varepsilon}$ = constant normally consolidated one-dimensional compression lines (isotaches) in the e versus σ'_v (log) plot. Therefore, the dependence of σ'_p on the strain rate is expected to be higher, the higher the clay plasticity. This also suggests that there is a viscous

Table 6. Ratio between σ'_p and compressibility parameters from $\dot{\varepsilon}$ = 10^{-6} s^{-1} and 24-hour compression curves of series two specimens from the SFL clay layer.

Specimen	$\dfrac{\sigma'_p\left(10^{-6}s^{-1}\right)}{\sigma'_p\left(24\,h\right)}$	$\dfrac{C_c\left(10^{-6}s^{-1}\right)}{C_c\left(24\,h\right)}$	$\dfrac{C_r\left(10^{-6}s^{-1}\right)}{C_r\left(24\,h\right)}$
CP4E	1.11	1.02	0.89
CP4F	1.08	1.01	1.00
CP4G	1.10	1.02	0.95
CP4H	1.07	1.04	1.20
CP5E	1.09	1.04	0.89
CP5F	1.08	1.01	0.85
CP5G	1.07	0.99	1.00
CP5H	1.07	1.01	0.82
CP6E	1.08	1.02	1.05
CP6F	1.07	1.04	1.12
CP6G	1.07	0.96	0.92
CP6H	1.09	1.05	1.14
CP7E	1.11	1.04	1.00
CP7F	1.11	1.07	1.14
CP7G	1.09	1.05	1.11
CP7H	1.07	1.08	1.29
CP8C	1.09	1.07	1.22
CP8D	1.07	1.03	1.15
CP8E	1.12	1.05	1.00
CP8F	1.07	1.07	1.26
CP9C	1.05	0.95	0.59
CP9D	1.10	1.06	1.06
CP9E	1.06	0.94	1.00
CP9F	1.05	0.98	1.11
CP10C	1.05	1.02	0.84
CP10D	1.07	1.02	0.96
CP10E	1.03	0.98	0.80
CP10F	1.10	1.04	0.76

component in σ'_v, as stated by Terzaghi (1941), Taylor (1942) and Taylor (1948, pp. 245) (see also Lima, 1993; Garcia, 1996; Santa Maria, 2002; Aguiar, 2008; Andrade, 2009). Nevertheless, a detailed discussion on this subject is out of scope of this article and will be presented in another article where the long-term loading stages run to investigate secondary consolidation and stress relaxation will be shown.

The ratio between C_c from the $\dot{\varepsilon}$ = 10^{-6} s^{-1} compression curve, denoted by C_c (10^{-6} s^{-1}), and C_c from the 24-hour compression curve, denoted by C_c (24 h), is within 0.94 and 1.08, with an average of 1.02. The ratio between C_r from the $\dot{\varepsilon}$ = 10^{-6} s^{-1} compression curve, denoted by C_r (10^{-6} s^{-1}), and C_r from the 24-hour compression curve, denoted by C_r (24 h), is within 0.76 to 1.29, with an average of 1.02 (value of 0.59 not included). A practical conclusion is that it is possible to reduce the total duration of a consolidation test from ten to about three days by using the $\dot{\varepsilon}$ = 10^{-6} s^{-1} loading criterion without changes in C_c and C_r values.

Table 7. Comparison between SFL clay compressibility parameters obtained in this study and those presented by Massad (2009).

Parameter	Massad (2009)	present study
σ'_p (kPa)	30-200	120-182
OCR	1.5-2.5	1.7-2.4
C_r/C_c	0.05-0.14 (average: 0.08)	0.06-0.14 (average: 0.11)
$C_c/(1+e_0)$	0.33-0.51 (average: 0.43)	0.46-0.68 (average: 0.56)

4.3.2 Comparison between the SFL clay layer compressibility parameters obtained in this study and by Massad (2009)

Since the Massad (2009) compressibility parameters are interpreted as having been obtained from 24-hour compression curves, only the compressibility parameters obtained in the same way are considered for comparison purposes.

Table 7 shows the ranges of SFL clay compressibility parameters presented by Massad (2009, Tables 5.1 and 5.2) and those obtained from series two specimens from samples SRA203(4) to SRA203(10), disregarding specimens CP5G, CP10D and CP10F, classified as "fair to poor" according to Coutinho (2007) modified criterion.

The σ'_p, *OCR* and C_r/C_c obtained in this study are within the ranges presented by Massad (2009). However, the lower and upper bounds of the $C_c/(1+e_0)$ range in this study are higher than those presented by Massad (2009), with the average in this study being higher than the upper bound of the Massad (2009) range.

The series two specimens of samples SRA203(6) and SRA203(7) showed $C_c/(1+e_0)$ within 0.60 and 0.68, whereas all the other series two specimens from samples SRA203(4) to SRA203(10) showed $C_c/(1+e_0)$ within 0.46 and 0.59 (average of 0.52). Nevertheless, even excluding samples SRA203(6) and SRA203(7), the $C_c/(1+e_0)$ values are still higher than the Massad (2009) values. Since disturbance decreases the compressibility in the virgin compression domain, Massad (2009) specimens seem to be of poorer quality than the ones studied herein, which is corroborated by the straight shape of the virgin compression lines shown by Massad (2009, Figures 5.43, 5.45 and 5.46), a disturbance effect also discussed in section 4.2.

It must be pointed out that Santos soft clay compressibility data available in the literature were mainly obtained before the nineties, when sampling standards and testing procedures were different from the current ones.

Unfortunately, in civil engineering practice, even today, sampling and testing procedures do not usually receive due care recommended by current standards. The authors' intention is to highlight the importance of following rigorously the current standards as well as special technical specifications (see Ladd & DeGroot, 2003) in order to obtain better-quality results.

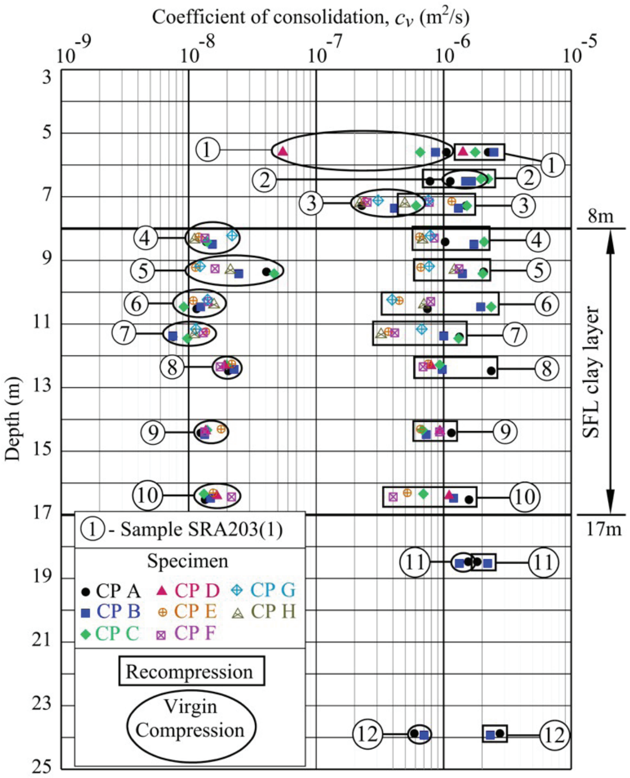

Figure 11. Coefficient of consolidation (c_v) average values profile.

4.4 Coefficient of consolidation

Figure 11 shows the c_v average values profile in the recompression (between σ'_{v0} and σ'_p) and virgin compression domain of all undisturbed specimens. Except for sample SRA203(2), which is sand, for all specimens, c_v values in the recompression domain are higher than those in the virgin compression domain. The sandy specimens, which do not belong to the SFL clay layer, showed smaller differences between c_v values from the two domains than the SFL clay specimens.

The SFL clay specimens showed c_v values in the recompression domain within 3.0 x 10^{-7} m²/s and 2.5 x 10^{-6} m²/s. In the virgin compression domain, c_v values are within 7.0 x 10^{-9} m²/s and 5.0 x 10^{-8} m²/s, the values between 1.0 x 10^{-8} m²/s and 2.5 x 10^{-8} m²/s being more frequent.

5. Conclusions

1) The stratigraphy of the Santos soft clay deposit near Barnabé Island follows the genetic pattern described by Massad (2009).
2) Following ABNT (1997) and additional cares in sampling, transportation, storage and specimen trimming (Aguiar, 2008; Andrade, 2009), high-quality one-dimensional consolidation test specimens were obtained.
3) Comparison between undisturbed and remolded specimen compression curves evidenced all the remolding effects described by Ladd (1973), Coutinho (1976) and Martins (1983).
4) In the authors' experience with highly plastic clays, incremental loading one-dimensional consolidation tests, which usually last ten days adopting 24-hour loading stages on double drained 20 mm-high specimens, are reduced to three days by starting a new loading stage whenever $\dot{\varepsilon}$ =10^{-6} s^{-1}.
5) Series two tests showed 24-hour "*e* versus σ'_v (log)" curves displaced to the left of the $\dot{\varepsilon}$ = 10^{-6} s^{-1} "*e* versus σ'_v (log)" curves, keeping C_r and C_c average values unchanged.
6) For the Santos soft clay studied herein, σ'_p from 24-hour compression curve is about 8% lower than σ'_p from $\dot{\varepsilon}$ = 10^{-6} s^{-1} compression curve, confirming that σ'_p depends on strain rate.
7) SFL clay $C_c/(1+e_0)$ values of this study are higher than those presented by Massad (2009). Since disturbance decreases the compressibility in the virgin compression region, Massad (2009) specimens seem to be of poorer quality than the ones studied herein.
8) It is feasible to carry out a high-quality laboratory test program for design purposes following current standards rigorously.

Acknowledgements

The authors thank EMBRAPORT on behalf of engineer Juvencio Pires Terra for having taken the samples and transported them to the *Soils Rheology Laboratory* (UFRJ) and engineer Silvia Suzuki for having supervised the sampling operations. The authors are indebted to Luis Carlos de Oliveira, from COPPE/UFRJ, who diligently performed the characterization tests. The authors are also very grateful to Alexandre Oliveira da Silva, from *Mecasolo Engenharia e Consultoria Eireli*, for having prepared the figures. Finally, the authors thank to *Conselho Nacional de Desenvolvimento Científico e Tecnológico* (CNPQ) for having provided financial support for the Master's in Science researches of the two first authors.

Declaration of interest

The authors have no conflicts of interest to declare. All co-authors have observed and affirmed the contents of the paper and there is no financial interest to report.

Authors' contributions

Vitor Nascimento Aguiar: conceptualization, Data curation, Formal Analysis, Funding acquisition, Investigation, Visualization, Writing - original draft, Writing

- review & editing. Maurício do Espírito Santo Andrade: conceptualization, Data curation, Formal Analysis, Funding acquisition, Investigation, Visualization, Writing - original draft, Writing - review & editing. Ian Schumann Marques Martins: conceptualization, Investigation, Methodology, Project administration, Resources, Supervision, Visualization, Writing - review & editing. Jean Pierre Paul Rémy: conceptualization, Resources, Supervision, Validation, Writing - review & editing. Paulo Eduardo Lima de Santa Maria: conceptualization, Resources, Supervision, Validation, Writing - review & editing.

List of symbols

c_v	Coefficient of consolidation
C_c	Compression index
C_r	Recompression index
C_s	Swelling index
CP	Specimen
e	Void ratio
e_0	Natural void ratio
G_s	Specific gravity
H	Specimen height
i	Order of dial reading
I_P	Plasticity index
N	SPT blow count
OCR	Overconsolidation ratio
OM	Organic matter content
S_r	Degree of saturation
SFL	Fluvial-lagoon-bay sediments
SPM	Borehole for standard penetration tests
SPT	Standard penetration test
SRA	Borehole for taking undisturbed samples
t	Time
w	Water content
w_L	Liquid limit
W.L.	Water level
w_P	Plastic limit
ΔH	Specimen settlement
$\Delta\sigma / \sigma$	Stress ratio increment
Δt	Time elapsed between dial readings of order i and i +1
ε	Specimen vertical strain
$\dot{\varepsilon}$	Specimen vertical strain rate
γ	Unit weight of soil
σ'_p	Preconsolidation (yield) stress
σ'_v	Vertical effective stress
σ'_{v0}	Effective overburden stress

References

Aguiar, V.N. (2008). *Consolidation characteristics of the Santos harbor channel clay near Barnabé Island* [Master's dissertation, Federal University of Rio de Janeiro]. Federal University of Rio de Janeiro's repository (in Portuguese).

American Society for Testing and Materials – ASTM. (2007). *ASTM D4220-95: standard practices for preserving and transporting soil samples*. West Conshohocken: ASTM International. https://doi.org./10.1520/D4220.95R07.

Andrade, M.E.A. (2009). *Contribution to the study of soft clays from the city of Santos* [Master's dissertation, Federal University of Rio de Janeiro]. Federal University of Rio de Janeiro's repository (in Portuguese).

Associação Brasileira de Normas Técnicas – ABNT. (1995). *ABNT NBR 6502: rocks and soils: terminology.* Rio de Janeiro: ABNT (in Portuguese).

Associação Brasileira de Normas Técnicas – ABNT. (1997). *ABNT NBR 9820: assessment of undisturbed low consistency soil samples from boreholes.* Rio de Janeiro: ABNT (in Portuguese).

Bjerrum, L. (1972). Embankments on soft ground: state-of-the-art Report. In *Proceedings of the ASCE Specialty Conference on Performance of Earth and Earth Supported Structures* (Vol. 2, pp. 1-54). Lafayette: Purdue University.

Bjerrum, L. (1973). Problems of soil mechanics and construction on soft clays and structurally unstable soils (collapsible, expansive and others). In *Proceedings of the 8th International Conference on Soil Mechanics and Foundation Engineering* (Vol. 3, pp. 111-159), Moscow.

Coutinho, R.Q. (1976). *Características de adensamento com drenagem radial de uma argila mole da Baixada Fluminense* [Master's dissertation, Federal University of Rio de Janeiro]. Federal University of Rio de Janeiro's repository (in Portuguese).

Coutinho, R.Q. (2007). Characterization and engineering properties of Recife soft clays - Brazil. In *Proceedings of the Second International Workshop on Characterisation and Engineering Properties of Natural Soils* (Vol. 3, pp. 2049-2100). Singapore: Balkema.

Crawford, C.B. (1986). State of the art: evaluation and interpretation of soil consolidation tests. In *Proceedings of the Symposium Sponsored by ASTM Committee D-18 on Soil and Rock* (ASTM Special Technical Publication, No. 892, pp. 71-103). West Conshohocken: ASTM.

Garcia, S.G.F. (1996). *Relationship between secondary consolidation and stress relaxation of a soft clay in oedometric compression* [Master's dissertation, Federal University of Rio de Janeiro]. Federal University of Rio de Janeiro's repository (in Portuguese).

Graham, J., Crooks, J.H.A., & Bell, A.L. (1983). Time effects on the stress-strain behavior of natural soft clays. *Geotechnique*, 33(3), 327-340. http://dx.doi.org/10.1680/geot.1983.33.3.327.

Ladd, C.C. (1973). *Estimating settlements of structures supported on cohesive soils* (MIT 1971 Special Summer Program 1.34s). Cambridge: MIT.

Ladd, C.C., & DeGroot, D. (2003). Recommended practice for soft ground site characterization: Arthur Casagrande Lecture. In *Proceedings of the 12th Pan-American Conference on Soil Mechanics and Geotechnical Engineering* (Vol. 1, 3-57), Boston.

Lambe, T.W., & Whitman, R.V. (1979). *Soil mechanics* (SI version). New York: John Wiley & Sons.

Leroueil, S., Kabbaj, M., Tavenas, F., & Bouchard, R. (1985). Stress-strain-strain rate relation for the compressibility of sensitive natural clays. *Geotechnique*, 35(2), 159-180. http://dx.doi.org/10.1680/geot.1985.35.2.159.

Lima, G.P. (1993). *A non-linear theory of consolidation* [Master's dissertation, Federal University of Rio de Janeiro]. Federal University of Rio de Janeiro's repository (in Portuguese).

Lunne, T., Berre, T., & Strandvik, S. (1997). Sample disturbance effects in soft low plastic Norwegian clay. In *Proceedings of the Symposium on Recent Developments in Soil and Pavement Mechanics* (pp. 81-102), Rio de Janeiro.

Martins, I.S.M. (1983). *Sobre uma nova relação índice de vazios tensão em solos* [Master's dissertation, Federal University of Rio de Janeiro]. Federal University of Rio de Janeiro's repository (in Portuguese).

Massad, F. (1985). *Argilas quaternárias da Baixada Santista: características e propriedades geotécnicas* [Habilitation thesis, University of São Paulo]. University of São Paulo's repository (in Portuguese).

Massad, F. (2009). *Solos marinhos da Baixada Santista: características e propriedades geotécnicas*. São Paulo: Oficina de Textos (in Portuguese).

Rémy, J.P.P., Martins, I.S.M., Santa Maria, P.E.L., Aguiar, V.N., & Andrade, M.E.S. (2011). Working hypothesis, special laboratory tests, working tools, analysis of the monitoring of a pilot embankment built on soft clay in Santos with wick drains and its application to the final design. *Soil and Rocks*, 34(4), 277-316.

Santa Maria, F.C.M. (2002). *Rheological experimental study of the coefficient of earth pressure at rest, K0* [Doctoral thesis, Federal University of Rio de Janeiro]. Federal University of Rio de Janeiro's repository (in Portuguese).

Silva, F.P. (1970). Uma nova construção gráfica para determinação da pressão de pré-adensamento de uma amostra de solo. In *Anais do 4º Congresso Brasileiro de Mecânica dos Solos e Engenharia de Fundações* (Vol. 2, No. 1, pp. 219-223). Rio de Janeiro: ABMS.

Suguio, K., & Martin, L. (1994). Geologia do quaternário. In F.F. Falconi & A. Nigro Junior (Eds.), *Solos do litoral de São Paulo* (pp. 235-264). São Paulo: ABMS-NRSP.

Taylor, D.W. (1942). *Research on consolidation of clays* (Serial, No. 82). Massachusetts: Department of Civil and Sanitary Engineering, Massachusetts Institute of Technology.

Taylor, D.W. (1948). F*undamentals of soil mechanics*. London: John Wiley & Sons.

Terzaghi, K. (1941). Undisturbed clay samples and undisturbed clays. *Journal of the Boston Society of Civil Engineers*, 28(3), 45-65.

Appendix A. σ'_p and compressibility parameters.

Table A1. σ'_p and compressibility parameters of all specimens (series one and two) obtained from e versus σ'_v(log) curves corresponding to $\dot{\varepsilon} = 10^{-6}$ s^{-1}.

Specimen	Depth (m)	Test series	e_0	σ'_p (kPa)	C_c	$C_c/(1+e_0)$	C_r	C_r/C_c
CP1A	5.55 - 5.65	1	1.30	100	0.48	0.21	0.08	0.17
CP1B	5.55 - 5.65	1	1.35	100	0.46	0.20	0.09	0.20
CP1C	5.55 - 5.65	1	1.37	92	0.51	0.22	0.09	0.18
CP1D	5.55 - 5.65	1	1.44	90	0.57	0.23	0.10	0.18
CP2A	6.48 - 6.55	1	1.07	42	0.26	0.13	[b]	[b]
CP2B	6.48 - 6.55	1	1.11	48	0.27	0.13	[b]	[b]
CP2C	6.40 - 6.48	1	1.00	58	0.24	0.12	[b]	[b]
CP2D[a]	6.40 - 6.48	1	1.11	23	0.22	0.10	[b]	[b]
CP3A	7.25 - 7.32	1	1.55	105	0.80	0.31	0.10	0.13
CP3B	7.32 - 7.40	1	1.69	100	0.86	0.32	0.10	0.12
CP3C	7.25 - 7.32	1	1.52	120	0.66	0.26	0.11	0.17
CP3D[a]	7.32 - 7.40	1	1.83	35	0.67	0.23	[b]	[b]
CP3E	7.13 - 7.16	2	1.49	110	0.78	0.31	0.12	0.15
CP3F	7.16 - 7.19	2	1.47	119	0.72	0.29	0.15	0.21
CP3G	7.10 - 7.13	2	1.42	120	0.77	0.32	0.11	0.14
CP3H	7.19 -7.25	2	1.44	105	0.69	0.28	0.16	0.23
CP4A	8.38 - 8.46	1	2.24	170	1.91	0.59	0.14	0.07
CP4B	8.46 - 8.53	1	2.26	165	1.73	0.53	0.19	0.11
CP4C	8.38 - 8.46	1	2.17	170	1.89	0.60	0.19	0.10
CP4D[a]	8.46 - 8.53	1	2.31	70	0.90	0.27	0.47	0.52
CP4E	8.24 - 8.28	2	2.25	139	1.72	0.53	0.16	0.09
CP4F	8.28 - 8.32	2	2.17	140	1.69	0.53	0.16	0.09
CP4G	8.20 - 8.24	2	2.12	132	1.69	0.54	0.19	0.11
CP4H	8.32 - 8.38	2	2.19	152	1.86	0.58	0.12	0.06
CP5A	9.34 - 9.39	1	1.97	170	1.56	0.53	0.17	0.11
CP5B	9.39 - 9.45	1	2.02	165	1.53	0.51	0.20	0.13
CP5C	9.39 - 9.45	1	2.14	155	1.42	0.45	0.18	0.13
CP5D[a]	9.45 - 9.53	1	2.13	65	0.66	0.21	0.50	0.76
CP5E	9.20 - 9.24	2	2.26	149	1.64	0.50	0.17	0.10
CP5F	9.24 - 9.28	2	2.18	156	1.56	0.49	0.17	0.11
CP5G	9.17 - 9.20	2	2.25	108	1.28	0.39	0.41	0.32
CP5H	9.28 - 9.34	2	2.14	145	1.44	0.46	0.14	0.10
CP6A	10.50 - 10.55	1	2.53	175	2.22	0.63	0.15	0.07
CP6B	10.43 - 10.50	1	2.57	175	2.18	0.61	0.20	0.09
CP6C	10.43 - 10.50	1	2.60	180	2.37	0.66	0.21	0.09
CP6D[a]	10.43 - 10.50	1	2.58	80	1.17	0.33	[b]	[b]
CP6E	10.25 - 10.28	2	2.43	185	2.23	0.65	0.21	0.09
CP6F	10.28 - 10.31	2	2.40	181	2.35	0.69	0.19	0.08
CP6G	10.22 - 10.25	2	2.34	176	1.93	0.58	0.22	0.11
CP6H	10.36 - 10.41	2	2.41	182	2.44	0.72	0.16	0.07
CP7A	11.39 - 11.42	1	2.35	160	2.06	0.61	0.23	0.11
CP7B	11.36 - 11.39	1	2.43	150	1.96	0.57	0.30	0.15
CP7C	11.42 - 11.49	1	2.21	155	1.73	0.54	0.27	0.16
CP7D[a]	11.42 - 11.49	1	2.18	55	0.95	0.30	0.45	0.47
CP7E	11.22 - 11.26	2	2.53	151	2.29	0.65	0.22	0.10
CP7F	11.26 - 11.30	2	2.42	155	2.24	0.65	0.25	0.11
CP7G	11.14 - 11.18	2	2.41	153	2.27	0.67	0.21	0.09
CP7H	11.30 - 11.36	2	2.49	148	2.39	0.68	0.22	0.09

[a]specimen remolded in the laboratory; [b]see discussion in section 4.2.

Table A1. Continued...

Specimen	Depth (m)	Test series	e_0	σ'_p (kPa)	C_c	$C_c/(1+e_0)$	C_r	C_r/C_c
CP8A	12.45 - 12.50	1	2.22	145	1.67	0.52	0.22	0.13
CP8B	12.40 - 12.45	1	2.14	130	1.54	0.49	0.24	0.16
CP8C	12.27 - 12.30	2	2.18	157	1.76	0.55	0.22	0.13
CP8D	12.30 - 12.33	2	2.19	147	1.76	0.55	0.23	0.13
CP8E	12.24 - 12.27	2	2.15	173	1.82	0.58	0.18	0.10
CP8F	12.33 - 12.36	2	2.19	148	1.85	0.58	0.24	0.13
CP9A	14.40 - 14.45	1	1.90	200	1.41	0.49	0.24	0.17
CP9B	14.45 - 14.50	1	1.93	200	1.46	0.50	0.16	0.11
CP9C	14.32 - 14.35	2	2.09	184	1.46	0.47	0.13	0.09
CP9D	14.35 - 14.38	2	1.98	200	1.50	0.50	0.18	0.12
CP9E	14.29 - 14.32	2	1.99	184	1.63	0.55	0.15	0.09
CP9F	14.38 - 14.40	2	1.96	174	1.41	0.48	0.20	0.14
CP10A	16.50 - 16.55	1	1.87	200	1.80	0.63	0.17	0.09
CP10B	16.45 - 16.50	1	1.93	190	1.86	0.63	0.33	0.18
CP10C	16.33 - 16.36	2	2.13	179	1.87	0.60	0.21	0.11
CP10D	16.39 - 16.42	2	1.98	174	1.61	0.54	0.26	0.16
CP10E	16.29 - 16.33	2	1.97	184	1.60	0.54	0.16	0.10
CP10F	16.42 - 16.45	2	1.91	174	1.70	0.58	0.16	0.09
CP11A	18.45 - 18.50	1	0.98	150	0.30	0.15	0.09	0.30
CP11B	18.50 - 18.55	1	0.96	160	0.31	0.16	0.07	0.23
CP12A	23.85 - 23.90	1	0.73	94	0.08	0.05	[b]	[b]
CP12B	23.90 - 23.95	1	0.70	94	0.11	0.06	[b]	[b]

[a]specimen remolded in the laboratory; [b]see discussion in section 4.2.

Table A2. σ'_p and compressibility parameters of series two specimens obtained from e versus σ'_v(log) curves corresponding to 24 hours.

Specimen	Depth (m)	e_0	σ'_p (kPa)	C_c	$C_c/(1+e_0)$	C_r	C_r/C_c	C_s
CP3E	7.13 - 7.16	1.49	100	0.74	0.30	0.17	0.23	0.05
CP3F	7.16 - 7.19	1.47	106	0.71	0.29	0.18	0.25	0.05
CP3G	7.10 - 7.13	1.42	110	0.81	0.33	0.14	0.17	0.05
CP3H	7.19 - 7.25	1.44	96	0.70	0.29	0.19	0.27	0.05
CP4E	8.24 - 8.28	2.25	125	1.69	0.52	0.18	0.11	0.13
CP4F	8.28 - 8.32	2.17	130	1.68	0.53	0.16	0.10	0.13
CP4G	8.20 - 8.24	2.12	120	1.66	0.53	0.20	0.12	0.12
CP4H	8.32 - 8.38	2.19	142	1.78	0.56	0.10	0.06	0.14
CP5E	9.20 - 9.24	2.26	137	1.57	0.48	0.19	0.12	0.13
CP5F	9.24 - 9.28	2.18	144	1.55	0.49	0.20	0.13	0.13
CP5G	9.17 - 9.20	2.25	101	1.29	0.40	0.41	0.32	0.14
CP5H	9.28 - 9.34	2.14	136	1.43	0.46	0.17	0.12	0.11
CP6E	10.25 - 10.28	2.43	171	2.18	0.64	0.20	0.09	0.18
CP6F	10.28 - 10.31	2.40	169	2.27	0.67	0.17	0.07	0.18
CP6G	10.22 - 10.25	2.34	164	2.02	0.60	0.24	0.12	0.18
CP6H	10.36 - 10.41	2.41	167	2.33	0.68	0.14	0.06	0.16
CP7E	11.22 - 11.26	2.53	136	2.20	0.62	0.22	0.10	0.15
CP7F	11.26 - 11.30	2.42	140	2.10	0.61	0.22	0.10	0.15
CP7G	11.14 - 11.18	2.41	141	2.17	0.64	0.19	0.09	0.16
CP7H	11.30 - 11.36	2.49	138	2.21	0.63	0.17	0.08	0.16
CP8C	12.27 - 12.30	2.18	144	1.64	0.52	0.18	0.11	0.10
CP8D	12.30 - 12.33	2.19	138	1.71	0.54	0.20	0.12	0.10
CP8E	12.24 - 12.27	2.15	154	1.73	0.55	0.18	0.10	0.11
CP8F	12.33 - 12.36	2.19	138	1.73	0.54	0.19	0.11	0.10
CP9C	14.32 - 14.35	2.09	176	1.54	0.50	0.22	0.14	0.13

Table A2. Continued...

Specimen	Depth (m)	e_0	σ'_p (kPa)	C_c	$C_c/(1+e_0)$	C_r	C_r/C_c	C_s
CP9D	14.35 - 14.38	1.98	182	1.41	0.47	0.17	0.12	0.13
CP9E	14.29 - 14.32	1.99	174	1.73	0.58	0.15	0.09	0.13
CP9F	14.38 - 14.40	1.96	166	1.44	0.49	0.18	0.13	0.12
CP10C	16.33 - 16.36	2.13	171	1.84	0.59	0.25	0.14	0.15
CP10D	16.39 - 16.42	1.98	162	1.58	0.53	0.27	0.17	0.12
CP10E	16.29 - 16.33	1.97	179	1.63	0.55	0.20	0.12	0.13
CP10F	16.42 - 16.45	1.91	158	1.63	0.56	0.21	0.13	0.11

TECHNICAL NOTES

Soils and Rocks
An International Journal of Geotechnical and Geoenvironmental Engineering
www.soilsandrocks.com
ISSN 1980-9743
ISSN-e 2675-5475

Assessing the undrained strength of very soft clays in the SPT

Francisco R. Lopes[1#], Osvangivaldo C. Oliveira[2], Marcio S. S. Almeida[1]

Technical Note

Keywords
Site investigation
Standard Penetration Test
In-situ tests
Undrained shear strength of soft clays

Abstract

The log of a SPT in very soft clay may simply indicate a zero blow-count, or present information on the penetration – under self-weight – of the composition (sampler, rods and hammer) as recommended by some standards. The second type of information is often disregarded by design engineers due to the lack of a standard procedure for measuring these penetrations or because the test is regarded as not sensitive enough to give an indication on the undrained shear strength of soft clays. The penetration under the composition's self-weight, however, can indicate the magnitude of S_u, which, along with other more specific and sensitive tests, can help in assessing the spatial distribution of clay consistency in a large deposit. A proposed test procedure and interpretation had been given in an earlier technical note. This note presents an extended formulation and an evaluation of S_u via the SPT at a construction site in Rio de Janeiro, including comparisons with results of piezocone and vane tests. The values of S_u obtained with the SPT lie between the profiles given by vane tests, corrected by Plasticity Index, and the Critical State Theory, the latter representing a lower bound to the clay strength.

1. Introduction

The Standard Penetration Test (SPT) is part of any site investigation campaign, being the first test performed, with the aim of defining the stratigraphy. During the test, when a layer of very soft clay is encountered, the sampler does not need to be driven by hammer blows, and penetrates under self-weight. Some SPT standards prescribe the recording of the penetration of the sampler plus rods with or without the hammer (the Brazilian standard, with the hammer resting on top of the rods; ABNT, 2020). In this case, the log presents, at the depth of starting the test, the information *W/L*, where *W* indicates "self-weight" and *L* is the recorded penetration of the composition. Other standards just require that, if the sampler penetrates 45 cm under self-weigh, the operator records *N=0* and removes the sampler so that boring proceeds to the next test depth (usually 1.0 m ahead). Due to the lack of a standard test procedure and an interpretation guidance, or to the concept that SPT is not sensitive to provide any data for very soft clays, most design engineers disregard the information on self-weight penetration.

The undrained shear strength of clays, S_u, is usually determined by in-situ and laboratory tests (e.g., Almeida & Marques, 2013). For a number of reasons, in-situ tests are generally preferred for defining S_u, and this topic was covered in detail by Wroth (1984). Both in-situ and laboratory tests are scheduled after an initial site investigation, based on SPTs, to define the stratigraphy of the site. Therefore, it would be interesting if an assessment of the undrained shear strength of the clays is made in this first campaign, which is the objective of this note.

In a previous note (Lopes, 1995), a standard procedure for the case of self-weight penetration and a formulation for data interpretation was put forward. The interpretation is analogous to that of a pile at failure in a static load test.

This note suggests a procedure for evaluating a lower bound value for S_u from the SPT and presents results of tests carried out at a site in Rio de Janeiro, Brazil, where a very soft clay layer was investigated by other methods (CPTu and vane). SPT tests in soft clays have also been useful for providing a water content profile, with data obtained from the clay at the sampler tip; the water content is then related to S_u by other tests, such as vane and UU triaxial tests (e.g., Almeida & Marques, 2013). An evaluation of S_u of clays is also possible via the torque applied to the sampler, in the so-called SPT-T (Décourt, 2002).

2. Proposed test interpretation

The problem of penetration, followed by stabilization, of a sampler under the static action of self-weight and hammer can be considered as being equivalent to that of the

[#] Corresponding author. E-mail address: flopes@coc.ufrj.br
[1] Universidade Federal do Rio de Janeiro, Rio de Janeiro, RJ, Brasil.
[2] Engenheiro independente, Salvador, BA, Brasil.

Submitted on November 25, 2020; Final Acceptance on June 29, 2021; Discussion open until February 28, 2022.
https://doi.org/10.28927/SR.2021.060520

failure of a pile in a static load test. When the penetration of the sampler stabilizes, the configuration is that of a cylindrical element in which the weight of the sampler plus rods and hammer reaches equilibrium with the soil resistance developed along its external lateral surface and its base or tip area (Figure 1).

A very similar condition occurs when a pile develops its full bearing capacity in clay. In this condition, the ultimate bearing capacity of the pile – in a homogeneous, undisturbed clay – can be obtained with:

$$Q_{ult} = q_{ult}\, A + U\, \Sigma\, f_s\, \Delta l = \left(S_u N_c + \sigma_{vo}\right) A + U\, L\, S_u \quad (1a)$$

As for the sampler, if its penetration, L, is less than its length (approximately 800 mm), the bearing capacity equation above can be modified to (Figure 1a):

$$Q_{ult} = \left(S_u N_c + \sigma_{vo}\right) A + U\, L\, \eta_1\, S_u \quad (1b)$$

where η_1 is a disturbance factor for the clay along the sampler shaft. After a 45 cm penetration, the sampler is filled with soil and functions as a close-ended pile.

Equation 1b can be rewritten with the ultimate load replaced by the sum of the weights of the sampler, rods and hammer:

$$W_s + W_r + W_h = \left(S_u N_c + \sigma_{vo}\right)\frac{\pi D^2}{4} + \pi\, D\, L\, \eta_1\, S_u \quad (2)$$

If the sampler penetrates more than its length (approx. 800 mm), the clay will then act on the rods and will be strongly remolded (Figure 1b). In this case, a given length of the rod, L_r, penetrates the clay, and a slightly more complex expression is necessary (Figure 1b):

$$W_s + W_r + W_h = \left(S_u N_c + \sigma_{vo}\right)\frac{\pi D^2}{4} + \pi\left(D\, L_s\, \eta_1\, S_u + d\, L_r\, \eta_2\, S_u\right) \quad (3)$$

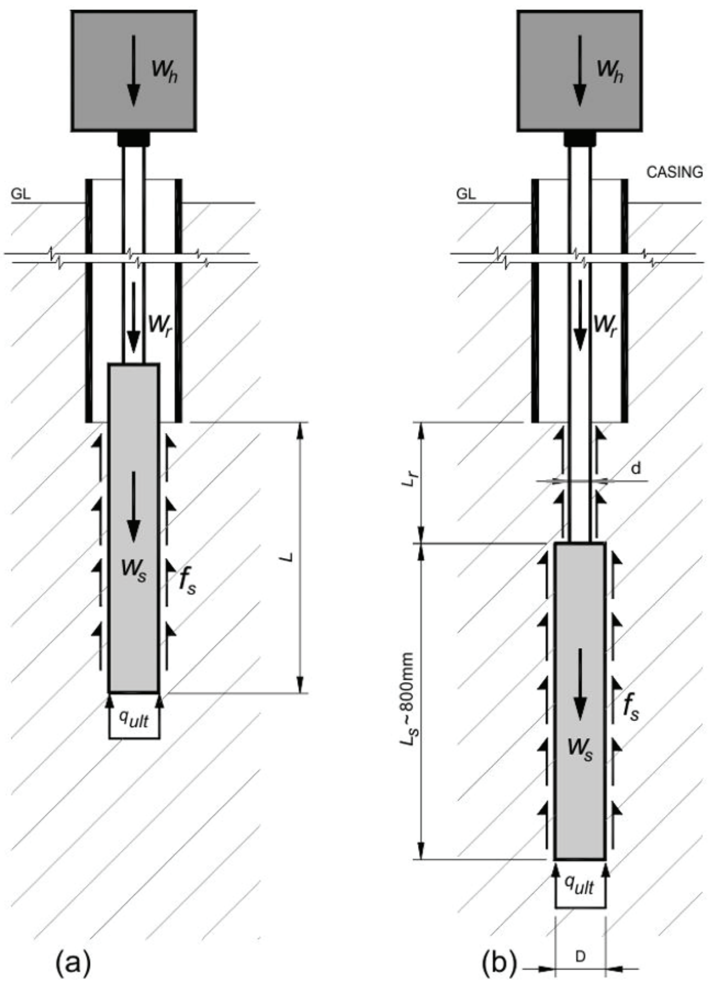

Figure 1. Test scheme, with sampler penetration (a) less than and (b) greater than the sampler length (L_s = sampler length, L_r = rod penetration).

where η_2 is a second clay disturbance factor. If the weight of the composition and its penetration are known, and the disturbance factors are estimated, the above expression leaves S_u as the sole unknown.

For tip unit resistance of both the pile and the sampler, the classical factor $N_c = 9.0$, suggested by Skempton (1951), can be used.

The disturbance factors are the ratio of the mobilized shear strength of the clay on the side of the sampler/rod to its undisturbed strength, S_u. They can be evaluated for each clay or investigation site, but some typical values can be derived from the experience with the relation between S_u and side friction f_s in CPTu. In clays of low to moderate sensitive, such as in Rio de Janeiro, where $S_t \leq 5$, the (local) sleeve friction is typically half of S_u, i.e., $f_s/S_u \sim 0.5$ (e.g., Jannuzzi et al., 2015). This would be an upper bound to the disturbance factor as the sleeve displacement in the CPTu does not cause full disturbance of the clay. For a large relative displacement, as expected for the SPT sampler in very soft clays, full disturbance is likely to occur, and it can be hypothesized that η_1 could ultimately be as low as the inverse of clay sensitivity (i.e., $\eta_1 = 1/S_t$). Considering $S_t = 5$, η_1 would be in the range of:

$$0.2 \leq \eta_1 \leq 0.5 \tag{4}$$

For η_2, as the clay around the rod is fully remolded mainly due to the reduction in diameter, it can be assumed that η_2 is the inverse of the clay sensitivity, as described in Equation 5.

$$\eta_2 \sim \frac{1}{S_t} \tag{5}$$

3. Proposed test procedure

The following test procedure is suggested:

(a) At the test depth, the sampler and necessary rods are carefully lowered in the borehole. The penetration should be slow, controlled with the help of a rod holding (or "U") key (Figure 2a). The rod length must exceed the casing by at least 1.0 m.

(b) The penetration under the action of the weight of the sampler and rods is recorded for a first calculation of S_u (Figure 2b) making use of Equation 2 without the hammer weight.

(c) The hammer is then put on the top of the rods while the rods are held with the U key (Figure 2c). The key is than loosened slowly to ensure a quasi-static penetration. In a very soft clay one (or more) rod segments can be necessary as the hammer comes close to seat on the top of the casing. The hammer can be lifted to allow the addition of a new rod segment, and is then put on the top of the rods as before.

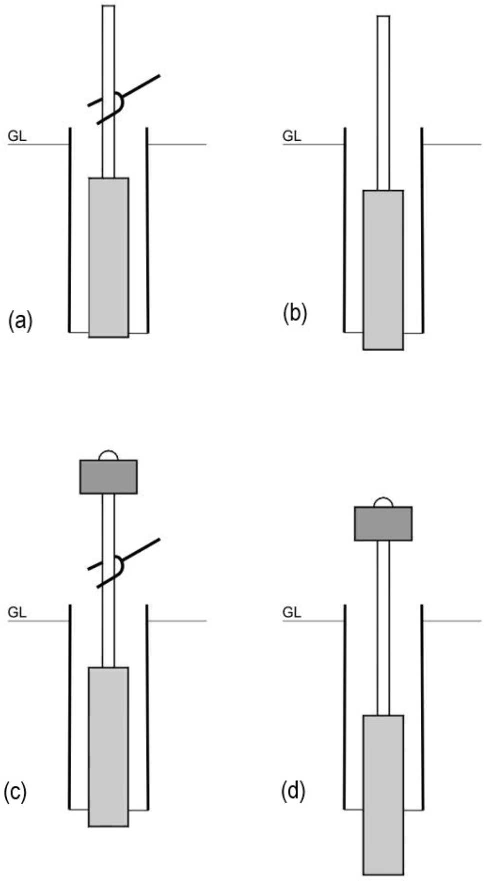

Figure 2. Suggested procedure: (a) the sampler and rods lowered in borehole, (b) the composition slowly released until penetration stops, (c) hammer rests on the top of the (held) rods and (c) the composition slowly released until penetration stops.

(d) The final penetration is then recorded (Figure 2d) and Equation 2 is used.

It should be noted that the proposed calculations are applicable only if the thickness of the remaining clay layer is greater than the penetration observed in the test.

On the shear strength profile, the calculated strength should be indicated at the mid-point of the penetration. As there is usually an increase in strength with depth, the calculated shear strength corresponds to the average along the penetrated length.

4. Application at a construction site

The proposed test procedure and interpretation were applied during the investigation of a construction site in Jacarepagua neighborhood, Rio de Janeiro, Brazil. The site presents a soft clay deposit, 11-12 m thick, with the water level almost at ground level. Vane tests, piezocone tests, laboratory vane and UU triaxial tests were also performed (Figure 3). A comprehensive description of the site investigation campaign can be seen in Almeida (1998) and Almeida et al.

Table 1. S-14 SPT data and interpretation.

Depth at start of test (m)	Pene-tration, L (m)	Rods		Hammer ?	Com-position weight (kN)	σvo at tip (kN/m^2)	η_1	S_u (kN/m^2)
		Length (m)	Weight (kN)					
4.9	0.3	6	0.18	No	0.28	68	0.4	5.1
4.9	2.2	6	0.18	Yes	0.93	92	0.2	8.7
7.4	1.6	8	0.24	Yes	0.99	117	0.2	9.1
9.0	1.9	12	0.36	Yes	1.11	142	0.2	10.1

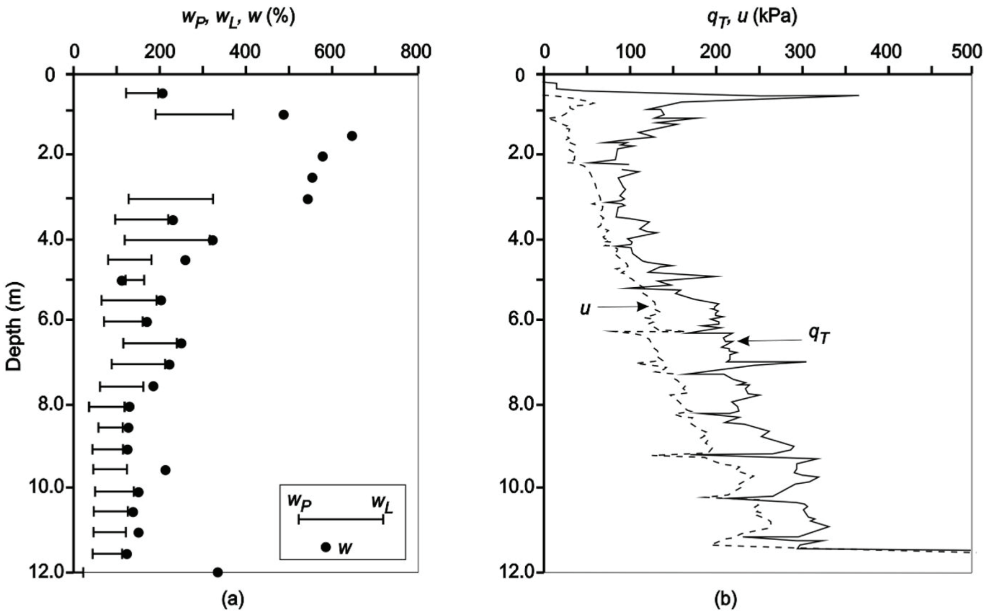

Figure 3. Profiles of (a) water content and (b) typical pore-pressure and tip resistance from CPTu (Almeida, 1998).

(2000). Further data on the clay can be seen in Baroni & Almeida (2012) and Riccio et al. (2013).

Water content and piezocone profiles presented in Figure 3 indicate that three layers can be distinguished: (i) an upper organic clay crust, 3 m thick, with a water content as high as 600%, (ii) a second clay layer, 4 m thick, with a water content typically of 200%, and (iii) a third layer, 4 m thick, with a water content typically of 100%. Laboratory tests also indicated an *OCR* of 2.2 near the ground surface (typical of water table fluctuations), reducing to 1.5 (typical of aging) at 4 m depth and then remaining constant.

Undrained shear strength profiles from vane tests, as measured and corrected, are shown in Figure 4. The corrected S_u profile shown in Figure 4 was obtained with Bjerrum's correction by the *PI* values (Bjerrum, 1973). The correction factor μ used in the present case was 0.6 as the clay's *PI* value is around 100%, which is consistent with the Brazilian experience (Sandroni, 1993). It can be observed that corrected S_u values varied from 5 to 15 kPa.

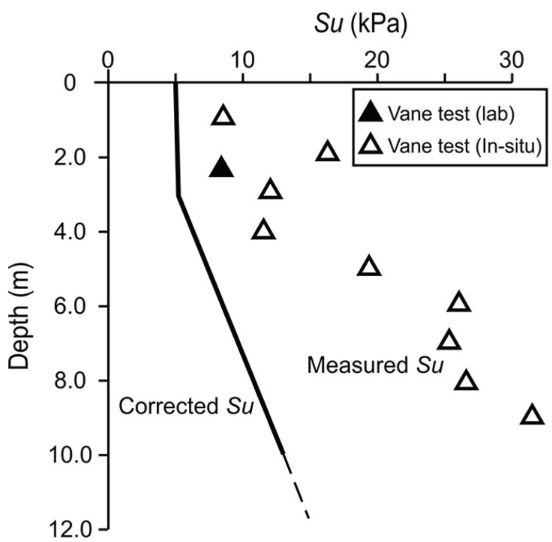

Figure 4. S_u profile as determined by vane tests.

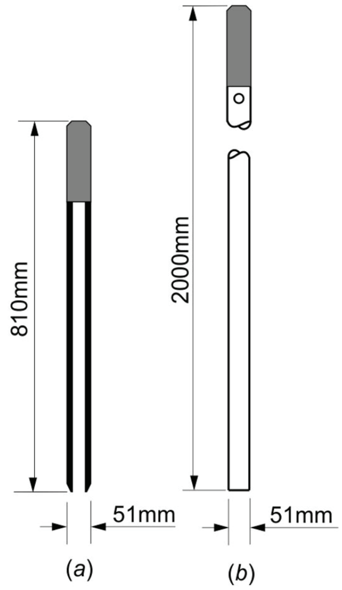

Figure 5. (a) Standard SPT sampler and (b) 2.0 m false sampler.

The proposed procedure for the SPT was applied at a few borings, using a longer, false sampler to avoid the question of a change in diameter between the sampler and the rods. The false sampler was a 2 m long aluminum tube, close-ended, with a rough external surface to ensure full adherence to the clay (Figure 5b).

Penetrations without the hammer weight did not exceed 0.3 m, but reached 2.00 m with the hammer. A typical record of the SPT field data and subsequent interpretation is presented in Table 1. In the computations shown in this table, η_1 = 0.2 – 0.4, η_2 = 0.2 and γ_{sat} = 13 kN/m^3 (assumed to calculate σ_{vo}). The weight of the composition considered the false sampler, with 70 N, the rods, with 30 N/m, and an anvil with 35 N.

S_u values obtained with the proposed SPT procedure and the corrected vane test profile are shown in Figure 6, with values marked at the center of the penetration length. S_u values obtained with the SPT were close to the corrected vane test profile but did not exhibit the same increase with depth. Another profile was added to this figure, based on the soil stress history (Ladd et al., 1977) and anchored on the Critical State Theory (Almeida, 1982; Wroth, 1984). S_u values were obtained with:

$$\frac{S_u}{\sigma'_{vo}} = K.OCR^m \quad (6)$$

where K and m for Rio de Janeiro clays have typical values of 0.3 and 0.8, respectively (Almeida, 1982).
Considering OCR = 1.5 and γ' = 3 kN/m^3, for z = 3 m, S_u = 3.7 kN/m^2; for z = 12 m, S_u = 14.9 kN/m^2, as indicated by the dashed line in Figure 6.

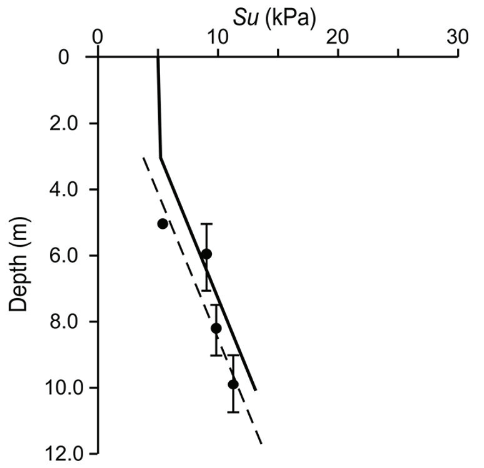

Figure 6. S_u values determined in S-14 (penetration lengths indicated) and profiles of corrected vane tests (solid line) and based on stress-history/critical-state (dashed line).

5. Concluding remarks

A procedure that can aggregate information to the SPT in very soft clay has been proposed. The proposal does not intend to replace more precise and well-established in-situ tests for these soils, such as the vane test and CPTu. It has been proposed that an information that is usually obtained without standardization − and usually disregarded − should be improved in order to be useful, combined with other tests, to present a spatial distribution of consistency in a large soft clay deposit.

The test and interpretation procedures were applied in a site investigation campaign in Rio de Janeiro, Brazil, and produced S_u values close to profiles given by corrected vane tests and the Critical State Theory, the latter representing a lower bound to the clay strength. These results are believed to encourage further investigation of the procedure, and – combined with other test results – appear to be suitable for use in preliminary stability analysis of embankments on soft clays.

Acknowledgements

The second author received a MSc scholarship from CNPq - Brazilian Research Council. This study was partly financed by CAPES - Coordenação de Aperfeiçoamento de Pessoal de Nivel Superior, Brazil, under Finance Code 001.

Declaration of interest

There is no conflict of interests in the material presented.

Authors' contributions

Francisco Lopes: conceptualization, methodology, original draft preparation. Osvangivaldo Oliveira: investigation, tests.

Marcio Almeida: conceptualization, discussion of results, review and approval of the final version of the manuscript.

List of symbols

A	sampler base or tip area
D	sampler diameter (51 mm or 2")
d	rod diameter (usually 25 mm or 1")
f_s	unit shaft resistance
K	parameter in normalized undrained strength equation
L	penetration length (general)
L_s	sampler length
L_r	rod penetration length
m	power in normalized undrained strength equation
N_c	pile bearing capacity factor due to cohesion
OCR	overconsolidation ratio
PI	Plasticity Index
Q_{ult}	bearing capacity of a pile (also of the sampler)
q_{ult}	unit base or tip resistance
S_t	clay sensitivity
S_u	undrained shear strength
U	perimeter
W	weight of the composition sampler + rods + hammer
W_h	weight of hammer
W_r	weight of rods
W_s	weight of sampler
w	water content
w_L	Liquid Limit
w_P	Plasticity Limit
η	disturbance factor
μ	Bjerrum's correction factor
σ_{vo}	total vertical geostatic stress at the tip level
σ'_{vo}	effective vertical geostatic stress

References

ABNT NBR 6484. (2020). *Soil - Simple investigation with SPT - Test method*. ABNT – Associação Brasileira de Normas Técnicas, Rio de Janeiro, RJ. [Portuguese].

Almeida, M.S.S. (1982). The undrained behaviour of the Rio de Janeiro Clay in the light of Critical State theories. *Solos e Rochas*, 5(2), 3-24.

Almeida, M.S.S. (1998). *Site characterization of a lacustrine very soft Rio de Janeiro organic clay. Proc. Geotechnical Site Characterization ISC'98* (pp. 961-966). Balkema.

Almeida, M.S.S., & Marques, M.E.S. (2013). *Design and performance of embankments on very soft soils.* CRC Press.

Almeida, M.S.S., Santa Maria, P.E.L., Martins, I.S.M., Spotti, A.P., & Coelho, L.B.M. (2000). Consolidation of a very soft clay with vertical drains. *Geotechnique*, 50(6), 633-643. http://dx.doi.org/10.1680/geot.2000.50.6.633.

Baroni, M., & Almeida, M.S.S. (2012). In situ and laboratory parameters of extremely soft organic clay deposits. In International Society for Soil Mechanics and Geotechnical Engineering (Ed.), *Proc. 4th International Conference on Geotechnical and Geophysical Site Characterization ISC-4* (pp. 1611-1620). Porto de Galinhas: CRC Press.

Bjerrum, L. (1973). Problems of soil mechanics and construction on soft clays and structurally unstable soils. In N. A. Tsytovich & N. S. Chetyrkin (Eds.), *Proc. 8th International Conference on Soil Mechanics and Foundation Engineering* (pp. 111-159). Moscow: Springer.

Décourt, L. (2002). *SPT, SPT-T: a prática brasileira; vantagens, limitações e críticas*. ABMS - Associação Brasileira de Mecânica dos Solos.

Jannuzzi, G.M.F., Danziger, F.A.B., & Martins, I.S.M. (2015). Geological-geotechnical characterisation of Sarapuí II clay. *Engineering Geology*, 190, 77-86.

Ladd, C.C., Foot, R., Ishihara, K., Schlosser, F., & Poulos, H.G. (1977). Stress-deformation and strength characteristics. In Japanese Society of Soil Mech & Foundation Engrs (Ed.), *Proc. 9th International Conference on Soil Mechanics and Foundation Engineering* (pp. 421-494). Tokyo: Japanese Society of Soil Mechanics and Foundation Engineering.

Lopes, F.R. (1995). A proposal for evaluating the shear strength of soft clays within the SPT. *Solos e Rochas*, 18(3), 169-172. [Portuguese]

Riccio, M.V., Baroni, M., & Almeida, M.S.S. (2013). Ground improvement in soft soils in Rio de Janeiro: the case of the Athletes' Park. *Proceedings of the Institution of Civil Engineers. Civil Engineering*, 166, 36-43. http://dx.doi.org/10.1680/cien.13.00008.

Sandroni, S.S. (1993). On the use of vane tests for embankments on soft clays. *Solos e Rochas*, 16(3), 207-213. [Portuguese]

Skempton, A.W. (1951). The bearing capacity of clays. In A. W. Skempton (Ed.), *Proc. Building Research Congress* (pp. 180-189). London: Building Research Congress.

Wroth, C.P. (1984). The interpretation of in situ soil tests. *Geotechnique*, 34(4), 449-489. http://dx.doi.org/10.1680/geot.1984.34.4.449.

CASE STUDY

Soils and Rocks
An International Journal of Geotechnical and Geoenvironmental Engineering
www.soilsandrocks.com
ISSN 1980-9743
ISSN-e 2675-5475

Geological-geotechnical risk mapping of gravitational mass movements in an urban area in Colombo, Brazil

Carla Vieira Pontes[1#], Roberta Bomfim Boszczowski[2], Leonardo Ercolin Filho[3]

Case Study

Keywords
Susceptibility to landslides
Geoprocessing
Risk mapping

Abstract

This work presents a geological-geotechnical risk map of gravitational mass movements and a susceptibility map to shallow translational slides to Vila Nova community, located in the municipality of Colombo, Brazil. The first map was created through a qualitative mapping methodology and the second one was elaborated using a deterministic method of slope stability. An aerial photogrammetric survey with UAV technology was performed, as well as field reconnaissance, laboratory testing, and geoprocessing techniques. Seven slope failures were identified as well as a range of other evidences of instability associated with the predisposition of the terrain to erosive and gravitational movements linked to human intervention without urban planning and engineering techniques. Moreover, the qualitative and quantitative analyses pointed out that 13% to 9% of the study area, respectively, are in a very high-risk condition for landslides. Thus, the resulting cartographic products are presented as an important technical contribution for landslide risk management as well as land use planning for reducing the geotechnical problems faced on site.

1. Introduction

Among the natural disasters that most affect the Brazilian population, in the number of people, gravitational mass movements stand out. They are natural geological phenomena which can occur in any area of high slope on the occasion of, above all, intense and prolonged rains (Brasil, 2004). However, human intervention, especially those that do not consider the hydromechanical limitations of the physical environment, can also unbalance the system of forces existing inside the mass of soil, rock or debris, which keeps it in static equilibrium. This is due to the reduction of the shear resistance of the material or due to the increase in the shear stresses of a given potential failure surface, caused by internal (predisposing) or external (triggering) factors (Duncan et al., 2014).

Urban unregulated settlement in areas susceptible to landslides and without drainage infrastructure represent 39.5% and 35.5% of landslide records in Brazilian municipalities between 2013 and 2017, respectively (IBGE, 2017). The anthropic intervention that the most interfere in the triggering of slope ruptures are the execution of cuts and landfills with inadequate geometry and degree of compaction, the deficiency of rainwater drainage systems and wastewater collections, the disposal of urban solid waste, and the removal of vegetation cover (Gerscovich, 2016).

Despite being complex and recurrent phenomena in nature, they can be minimized through preventive actions such as mapping, territorial planning, and monitoring in order to protect populations in risk areas.

The Federal Law 12,608 of 2012 (Brasil, 2012a) instituted the National Policy for Protection and Civil Defense (PNPDEC) in Brazil that covers prevention, mitigation, preparedness, response, and recovery actions aimed at protection and civil defense in terms of natural disasters. It delegated to the municipalities the task of promoting the identification and evaluation of susceptibilities, hazards, and vulnerabilities to disasters, in order to avoid or reduce their occurrences, resulting in the elaboration of cartographic products as a result/consequence.

The land geotechnical susceptibility map is the basic and essential technical product of the action plan required by PNPDEC for the cities. According to Prandini et al. (1995), geotechnical maps are a practical expression of geological knowledge applied to confront the problems posed by land use of slopes, seeking to understand the interaction between

[#]Corresponding author. E-mail address: carlavieirap97@gmail.com
[1]Universidade Federal do Paraná, Curitiba, PR, Brasil.
[2]Universidade Federal do Paraná, Departamento de Construção Civil, Curitiba, PR, Brasil.
[3]Univesidade Federal do Paraná, Departamento de Geomática, Curitiba, PR, Brasil.

Submitted on May 7, 2021; Final Acceptance on September 28, 2021; Discussion open until February 28, 2022.
https://doi.org/10.28927/SR.2021.070721

settlements and the physical environment as well as guiding preventive, corrective, or emergency measures when necessary. Geotechnical and hazard reconnaissance and the field and laboratory testing are applied in a qualitative criterion and/or mathematical modeling to correlate data and interpret physical phenomena resulting in digital geoprocessing works (Soeters & van Westen, 1996).

Analytical or numerical models of slope stability, based on deterministic methods, are the most widely way used to verify the safety of a slope in engineering approaches (Soeters & van Westen, 1996). They are especially employed in slope stabilization designs, for example.

However, to overcome the limitations imposed by the heterogeneity and anisotropy of soils and rocks involved in extensive mountainous areas, in addition to the limitations of deadlines and budgets, the analysis of slope stability based on qualitative methodologies, semi-empirical methods associated with geoprocessing techniques, has gained prominence in recent decades (Soeters & van Westen, 1996). These analyses, in general, lead to the identification and classification of weights of danger events in the field, deriving out of the study of the natural condition of the physical environment and the possible mechanisms that can generate instabilities (Ahrendt, 2005).

In this context, this work sought to identify the predisposing factors and signs of instability in terrain, translated into its susceptibility, as well as the pattern of the settlement and its vulnerability, to analyze the risk of soil landslides in the Vila Nova community, in the municipality of Colombo, Brazil. Through this analysis, a geological-geotechnical risk map of gravitational mass movements was elaborated through a qualitative mapping methodology. Also, it aimed to understand the phenomenon of more recurrent instability in the study area and the geomechanical properties of the involved materials to elaborate a susceptibility map to shallow landslides through a deterministic method of slope stability analysis.

Such cartographic products can be used as technical tools to landslide risk management and land use planning in coping with the geotechnical problems faced on site.

2. Materials and methods

2.1. Characteristics of the study area

The community of Vila Nova is in the Roça Grande neighborhood, in Colombo County, Metropolitan Region of Curitiba, state of Paraná, and covers 48,500 m^2 in a densely occupied valley with approximately 300 houses. It is bordered by the streets Rio Araguaia, Rio Iguaçu, Rio Guaporé, Rio Grande do Norte, and Santa Bárbara (Figure 1).

It is based on the sub-unit morphosculpture of Curitiba Plateau and in the region where the rocks are surfaced

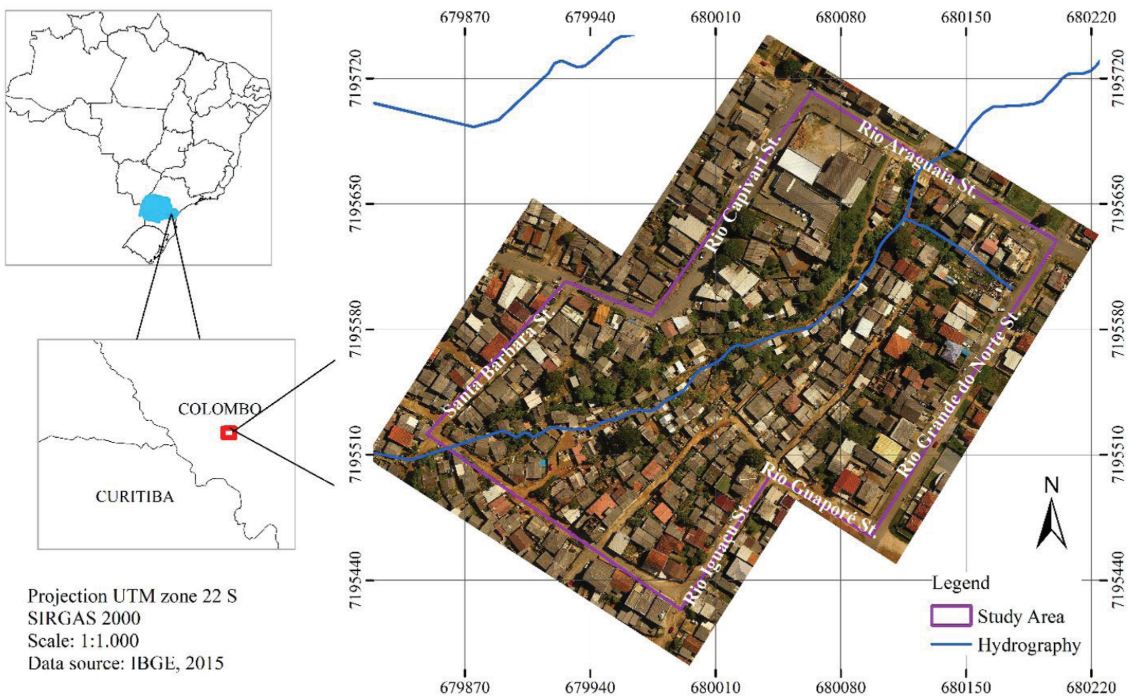

Figure 1. Location map of Vila Nova community, in Colombo, State of Paraná, Brazil.

and the residual soils of the crystalline basement of the Curitiba Sedimentary Basin, the Atuba Complex, are formed (IAT, 2000, 2005). There are mainly gneiss and migmatite, but also paragneiss, quartzite, quartz schist, mica schist, amphibolite and gneiss granite (Salamuni, 1998).

The studied area is located on one of the possible geological faults mapped by Salamuni (1998), geomorphological failures that occur, in general, towards NE-SW and NW-SE.

At the bottom of the valley, it permeates a stream of low flow water in times of drought and high flow in times of floods. It belongs to the Manjolo Cabeceira hydrographic sub-basin, which is part of the Atuba River basin, from Alto Iguaçu (IAT, 2000).

2.2. Topographic survey of the study area

The technique of aerial photogrammetry with Unmanned Aerial Vehicle (UAV) technology was used to perform the topographic survey of the study area. Through this technique, it was possible to obtain the terrain coordinates to generate the 3D terrain model with a density of 350 points/m^2, as well as a high-resolution orthoimage with a 4 cm spatial resolution. The UAV equipment used was the Phantom 4 model developed and manufactured by the Chinese company SZ DJI Technology Co., Ltd. The flight was carried out under favorable weather conditions at an approximate height of 70 m AGL (Above Ground Level) and in VLOS (Visual Line Of Sight) mode (Figure 2).

To generate the cartographic products, a GNSS (Global Navigation Satellite System) receiver was used to collect ground control and check points. Then, the SfM (Structure from Motion) technique was used to perform the bundle block adjustment to the image georeferencing, as well the dense cloud, digital surface model (DSM) and orthoimage generation. This whole process ensured the generation of cartographic products according to the Brazilian Accuracy Standards (PEC-A) for cadastral mapping. Also, in order

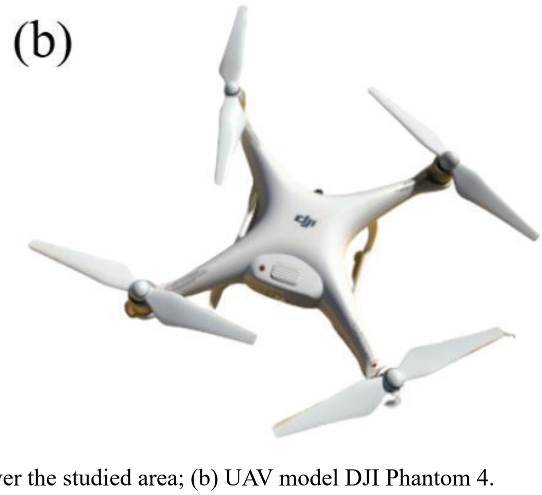

Figure 2. (a) crosshatch flight plan over the studied area; (b) UAV model DJI Phantom 4.

to generate precisely the Digital Terrain Model (DTM), the contour lines were extracted using 3D stereo compilation, due to the obstruction of the soil surface caused by the buildings and vegetation. The map projection adopted was the Universal Transverse Mercator (UTM), Zone 22 South, and horizontal datum SIRGAS2000. The altitudes were referenced to the ellipsoid of SIRGAS2000. All cartographic information was obtained by CEPAG (Geoinformation Applied Research Center of UFPR).

2.3. Qualitative landslide risk

The following methodology is based on the geological, geotechnical, and hydrological mapping and risk analysis manuals developed by the Brazilian Ministry of Cities (Brasil, 2018) and the Geological Service of Brazil (CPRM, 2018). Instructions from Soeters & van Westen (1996) are also used for the practice of landslides zoning.

2.3.1. Assessment of susceptibility, vulnerability, and risk

In the field zoning phase, a landslide inventory was made and the evaluation and classification of terrain susceptibility to the occurrence of landslides, followed criteria of the severity of evidence representing current or potential mass movements, as shown in Table 1. Through the steepness of the slopes, the danger mapping also followed topographical criteria. Based on the Law 6,766 of 1979 (Brasil, 1979) of land use urban zoning, areas whose inclination are greater than 30% (17°) cannot be urbanized, as this being the first topographical criterion. Ahrendt (2005) also identified that the landslides that took place in the residual soils of gneiss-migmatite and landfill in densely populated areas in the municipality of Campos do Jordão occurred more frequently in slopes steeper than 25°, once those of greater magnitude are among the slopes of 30° to 40°. Thus, it was defined that those areas with angles greater than 25° are more critical to the occurrence of landslides, which is the second topographic criterion, following the classification presented in Table 1. These danger evidence and inclinations were then classified as low susceptibility (S1) to very high susceptibility (S4).

Regarding the diagnosis of the pattern of land use it was sought to define a classification criterion of how vulnerable to an extreme landslides event the constructions of Vila Nova are, as shown in Table 1. Also, the presence of vegetation, drainage system and anthropic interventions in the physical environment was observed. The analyzed areas were classified as low vulnerability (V1) to very high vulnerability (V4).

The consolidated and unconsolidated materials were recognized seeking to observe general geological-geotechnical aspects such as lithology, genesis (residual soil, landfill soil, etc.), and geomorphological features of the relief (Table 1).

At all the points analyzed in the field, its georeferenced position was plotted in the mosaic obtained by aerial photogrammetry.

The relationship between the landslide potential along the area (susceptibility) and the expected losses to life and property (vulnerability) by a landslide occur is expressed by the risk. Thus, empirical multiplications were performed between the degrees of susceptibility and vulnerability identified in each area, or pixel in the GIS environment, to determine its risk. This one was established to be higher than the highest degree of danger or consequence associated, a decision made on behalf of security, as also adopted in the work of the CPRM (2018). Hence, the four risk classes ranging from low (R1) to very high (R4) are the result of interactions between the degrees of susceptibility (S1 to S4) and vulnerability (V1 to V4). Table 2 shows the description of the risk classes employed.

2.4. Quantitative landslides susceptibility

The quantitative analysis of the susceptibility of the lands of Vila Nova to landslides were conducted deterministically using the Infinite Slope model, based on the Limit Equilibrium Method, coupled to the GIS environment, to calculate the safety factors of each pixel of the elaborated map. Conceptually,

Table 1. Aspects for risk classification of current and potential gravitational mass movements.

Geological/geomorphological diagnosis	Diagnosis of land use (vulnerability)	Diagnosis of evidence of mass movements (susceptibility)
Local geology (main lithology of rocks and genesis of unconsolidated materials, presence of geological structures, waste, etc.)	The material used (masonry, generally representing low and medium vulnerability, or wood, representing, in general, high and very high vulnerability)	Steps, subsidence, and fissures in the ground, retaining walls cracked or bowed, soil moistening by sewage/ leaks deposition, trees tilted downhill (representing high susceptibility)
Local geomorphology (presence of steep slopes and/or poorly executed cuts and fills)	Constructive pattern and presence of visible structural damage	Presence of scars of movements (representing very high susceptibility)
	Local vegetation (presence and type)	Terrain slope greater than 17° (representing medium susceptibility)
	Inefficient/non-existent drainage or sewage system	Terrain slope greater than 25° (representing high susceptibility)

Table 2. Risk hierarchy criterion.

Risk intensity	Description
Low risk (R1)	Absence of unfavorable topography to stability and indications of gravitational mass movements. High level of building resistance. Maintaining the conditions of the land use, the possibility of destruction of buildings by landslides is low.
Medium risk (R2)	Meets the first topographic criterion (slope greater than 17°), but the terrain shows no indications or records of gravitational mass movements. High to the moderate level of resistance of the buildings. Maintaining the moderate conditions of the land use, the possibility of destruction of buildings by landslides is moderated.
High-risk (R3)	It meets all topographic criteria unfavorable to stability and presents indications of gravitational mass movements, although not intensely. High to the low level of resistance of buildings. Maintaining the moderate conditions of land use, the possibility of destruction of buildings by landslides of land is high.
Very high-risk (R4)	It meets all topographic criteria unfavorable to stability and the terrain presents intense indications or records of gravitational mass movements. High to the very low level of resistance of buildings. Maintaining the conditions of the land use, the possibility of destruction of buildings by landslides of land is very high.

the safety factor is defined as the relationship between the mobilized shear strength of the soil (τ_m) and the shear stress (τ) on a potential failure surface (Lambe & Whitman, 1969). In the Infinite Slope model, the failure surface is rectilinear and parallel to the surface of the ground, resembling shallow translational slides. Because it is a simple model of Limit Equilibrium, the implementation of Infinite Slope in a georeferenced computational environment is relatively simple, demanding few topographical and geotechnical parameters and facilitating the quantification of safety factors of extensive areas. In Equation 1 the mathematical formulation for calculating safety factors (SF) is presented using the Infinite Slope model.

$$SF = \frac{\tau_m}{\tau} = \frac{c' + \left(\gamma h \cos^2\beta - \gamma_w h_w\right) tan\,\phi'}{\gamma h \cos\beta \sin\beta} \quad (1)$$

Being c' the effective cohesive intercept of the soil, in kPa; γ the unit soil weight, in kN/m^3; h the depth of the failure surface, in meters; β slope of the ground as well as of the failure surface, in degree; γ_w unit water weight, in kN/m^3; h_w the depth of the groundwater table, in meters; and ϕ' the effective internal friction angle of the ground, in degree.

2.4.1. Laboratory tests

The soil modeled in the calculation of safety factors is a landfill soil, quite recurrent on-site due to cut and landfill activities for laying the residences and opening accesses. To determine the residual resistance parameters of these soil, Direct Shear Tests were conducted using the reversal technique at vertical stresses of 25 kPa, 50 kPa, 100 kPa e 200 kPa in a residual soil collected on-site, since the collection in a landfill soil was hindered. It was sought to identify soil resistance under the condition of large deformations because it is possibly to be soils with pre-existing failures or progressive internal failures, resulting in a minimum of shear resistance.

2.4.2. Map algebra in GIS environment

The elaboration of the geotechnical maps was conducted in ArcGIS 10.8 ESRI software. For calculation of safety factors, the map algebra presented below was carried out using the georeferenced terrain coordinates data obtained by aerial photogrammetry. For elaboration of the qualitative map, thematic maps as slope of the terrain were also necessary.

- Digital Elevation Model (DEM): terrain elevation raster surface with a spatial resolution of 0.5 m created through ArcToolbox's Topo to Raster interpolation using contour lines as input;
- Slope: slope raster surface created through the ArcToolbox's Slope tool using DEM as input;
- Safety factor variables: raster surfaces for each one of the input parameters involved in the formulation of safety factors (Equation 1) obtained through the ArcToolbox's Raster Calculator tool;
- Safety factor map: raster surface with the safety factor values for each cell of the geotechnical map using the ArcToolbox's Raster Calculator tool.

It has to be emphasized that the values of unit weight, cohesive intercept, friction angle, and depth of the rupture surface were kept constant; then, the inclination is the only spatially variable attribute.

3. Results

3.1. Geology and laboratory tests

During the field reconnaissance, it could be observed that the studied area is characterized by an intense heterogeneity of surface soils ranging from the residual soils of gneiss-migmatite in different degrees of weathering to the alluvial soils in the stream bed that permeates the Vila Nova valley, through landfills with high presence of domestic solid waste and civil construction, coluvionar materials, and rocky outcrops. Along the slopes was verified the predominant occurrence of residual soils and landfill soils, as well as the second one was the most critical for stability and, then, used in the analysis of safety factors. Through the characterization tests conducted in the laboratory, the landfill soil was classified as a silty sandy clay, with natural moisture of 31.93% and a unit mass of grains of 2.52 g/cm^3.

The sample of young residual soil tested using the reversal technique in the Direct Shear press has a unit natural weight around 17.5 kN/m^3 and a degree of saturation around 95%. The tests were operated according to the requirements of BS 1377-7 (BSI, 1990). The sample was submerged in water before consolidation and the shearing speed was defined from parameters of consolidation as proposed by Gibson & Henkel (1954), allowing to perform the test in drained conditions. Was adopted a great displacement for the determination of the parameters of residual resistance, applying a deformation of 8% (4.8 mm) per shear cycle, to reach the stability of the curve without more variations of the shearing strength (Tchalenko, 1970; Advincula, 2016; Trevizolli, 2018).

The Mohr-Coulomb shear resistance envelope was obtained for the data from the tenth shear cycle performed in the test and is shown in Figure 3. Through it, were obtained the effective cohesive intercept of 12.7 kPa and the effective internal friction angle of 23° for the residual soil. In the analysis of safety factors, simulating a landfill soil, it was adopted a unit weight of 17 kN/m^3, a cohesive intercept of 1.5 kPa and a friction angle of 22°. Those parameters were adopted based on interpretation of the results of the tests attended by the residual soil, on results of tests in landfill soils carried out in Campos do Jordão (Brazil) in the study

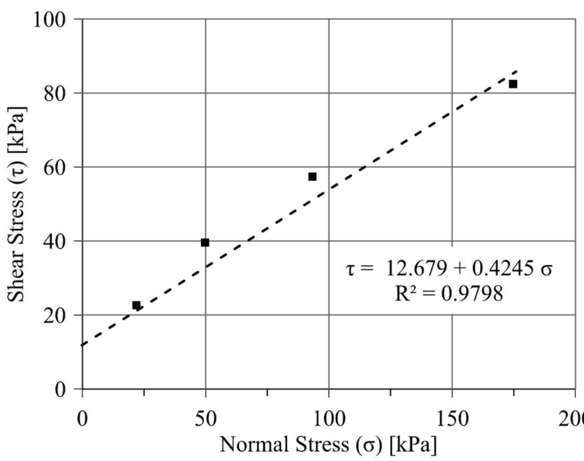

Figure 3. Mohr-Coulomb envelope for the tested residual soil under the condition of shear cycles and reversals.

of Ahrendt (2005), and on review of several references for different types of Brazilian tropical soils presented by Bressani et al. (2001). The input variables in the calculation of safety factors are presented in Table 3.

As verified in the field, the most recurrent depth of the landslides on-site is around 1 m depth in landfill soils on a predominantly plane rupture surface. Thus, it was adopted for the deterministic analysis, being model of Infinite Slope adequate for these failure conditions. The presence of a water table up to 1 m depth was not considered, as it was not found in outcrops on the slopes on-site inspections and, mainly, because the hydrogeological conditions of the substrate are not known through field tests. Nevertheless, soil resistance parameters were considered when it is close to saturation, a condition that can be achieved during the occurrence of rainfall events and/or by dumping/leaks of water and sewage pipes.

3.2. Landslides risk map – Qualitative analysis

During the field reconnaissance, held between October 2018 and December 2019, there was identified the presence of seven previous shallow landslides, which locality were classified as very high susceptibility (S4), and a range of other indications of instabilities, such as steps, subsidence, and fissures in the ground, retaining walls cracked or bowed, trees tilted downhill, disposal or leakage of water and sewage, localities classified as high susceptibility (S3), totaling 18 points analyzed.

The seven scars of shallow translational landslide were delimited to approximately 1 m depth, with mostly rectilinear shear surfaces parallel to the slope as well as with a considerably deformed and heterogeneous displaced mass. All of them were recorded in landfill soils, which denotes their high susceptibility to extreme events of slope instability, and in regions whose slope of the land is between 25° and 40°, corroborating the choice of classification of high danger areas (S3) to those steeper than 25°. It has to be emphasized that the recording of some of the movements was closely linked to a previous rainfall event.

It was observed that all the constructions in the discretized points are mostly built with wood, some in masonry, with precarious construction techniques, both infrastructure (foundation) and superstructure, some presenting structural damage. Thus, all were classified as very high vulnerability to landslide events. Figure 4 shows photographic records of two of the identified shallow translational slides and four records of indications of mass movements, as well as their

Table 3. Geotechnical parameters for stability analysis using the Infinite Slope method.

Depth of failure ( )	Unit natural weight (γ)	Cohesive intercept (c')	Friction angle (ϕ')
(m)	(kN/m^3)	(kPa)	(°)
1.0	17.0	1.5	22

Figure 4. (a) very high susceptibility (S4): translational landslide scar of approximately 1 m depth in landfill soil; (b) very high susceptibility (S4): translational landslide scar approximately 1 m depth in landfill soil; (c) high susceptibility (S3): steps on the ground; (d) high susceptibility (S3): retaining wall cracked and bowed; (e) high susceptibility (S3): subsidence and damping by sewage deposition; (f) high susceptibility (S3): tree tilted downhill.

susceptibility terrain classifications. Other pictures can be verified in Pontes (2019).

From the analysis of the interaction between the susceptibility of the terrain and the degrees of vulnerability to a sliding process, the risk levels to translational landslides of the study site in a GIS environment on a scale of 1:1000 were qualified. As a result, 13% of the community area of Vila Nova, that is, 6,086 m^2, is in a very high-risk area to occurrence and damages from a landslide event. In higher percentages, 19% is in a medium risk area and 68% in a site of low risk of occurrences and consequences of translational mass movements, as shown in Figure 5.

3.3. Landslide susceptibility map (safety factor map) – Quantitative analysis

The determination of quantitative susceptibility to shallow translational landslides in landfill soils in the analyzed stretch of Vila Nova was based on the map of safety factors determined for this unconsolidated material with the resistance parameters and failure surfaces stipulated and presented in Table 3. It is important highlight that was assumed geological occurrence of the landfill soil throughout the length of the studied area.

The analysis resulted in a conjuncture in which 9% of the area, that is, 4,451 m^2, is in a scenario of very high susceptibility to shallow translational landslide (FS $\leq$ 1), 17% in a scenario of high susceptibility, 16% in a context of medium susceptibility and 56% in an area of low susceptibility to the occurrence of movements, as shown in Figure 6.

It is noteworthy that the considerable percentage of areas whose safety factors are less than 1.0 can be attributed to the simplifications of the Infinite Slope method adopted, which does not consider, for example, unsaturated soil scenarios with suction (negative pore pressure) as a contributor in their shear resistance.

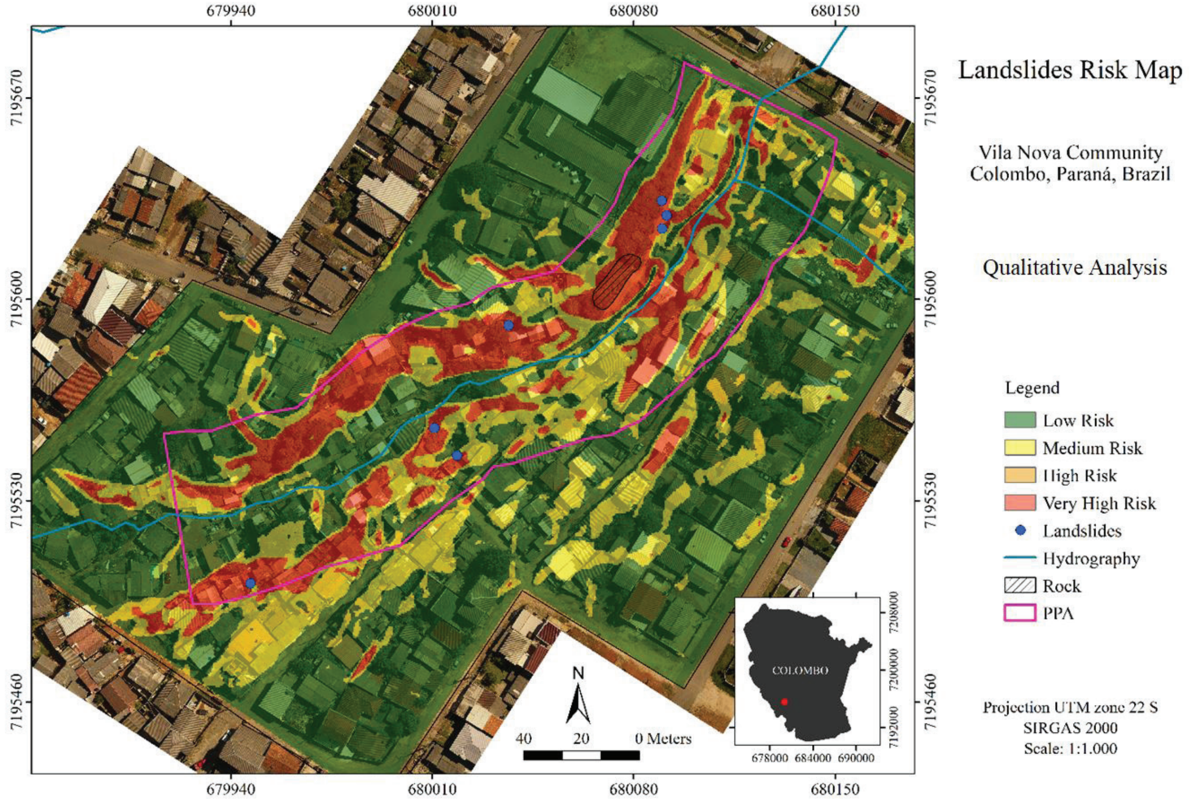

Figure 5. Landslides risk map of Vila Nova community – Qualitative analysis.

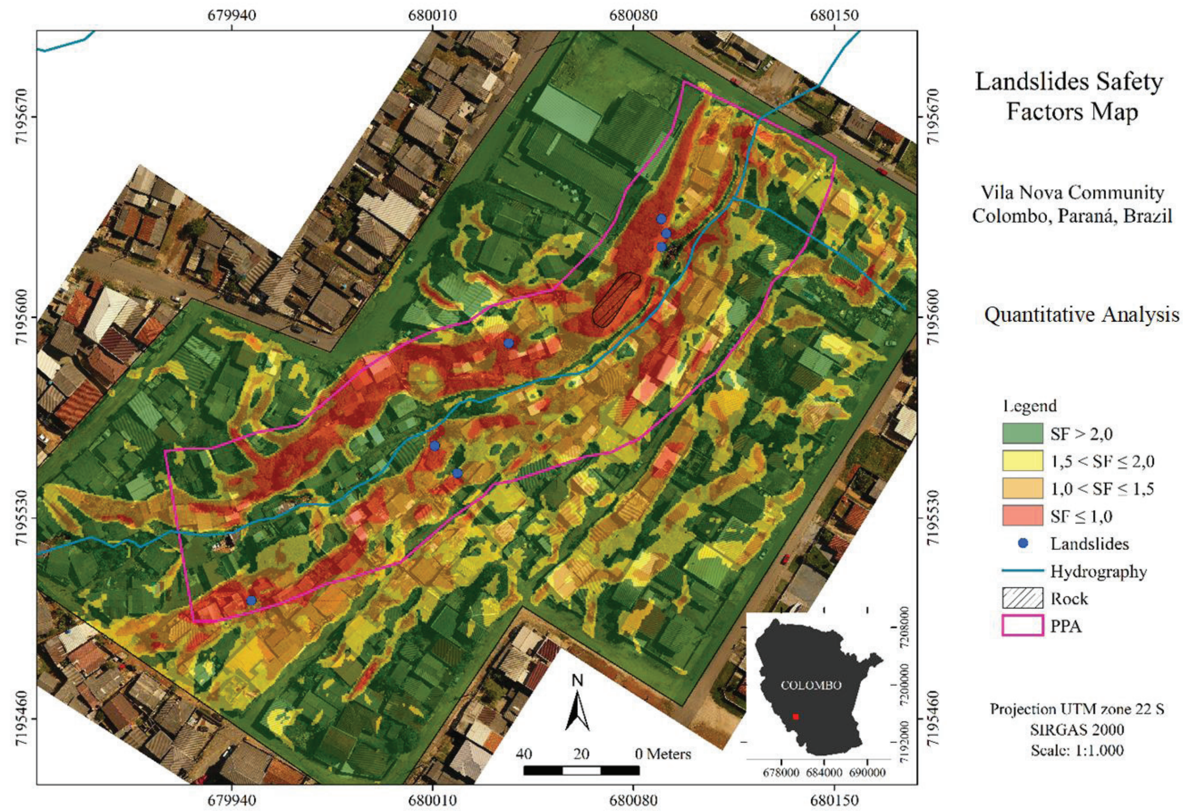

Figure 6. Landslide susceptibility (safety factors) map of Vila Nova community – Quantitative analysis.

4. Conclusions

The present work aimed to evaluate a section of the community of Vila Nova, in Colombo, Brazil, regarding its susceptibility and vulnerability to landslides, in order to identify regions and dwellings with higher risks of gravitational mass movements. The research culminated in the elaboration of a geological-geotechnical risk map, as well as a susceptibility map to shallow translational landslides.

Based on the two methodologies applied - qualitative and quantitative - about 11% of the study area covering approximately 50 residences is indicative of very high geotechnical risk of shallow translational landslides.

It was possible to observe that the high-risk areas in Vila Nova are associated with anthropic interventions without either urban planning or engineering techniques in steep slopes, since the records of landslides occurred in areas whose average slope is greater than 27° and in poorly executed cut and landfill soils. In addition to the landslide inventory, it was also pointed out the precariousness of the construction techniques of the residences, the intense clearing of the local vegetation, disposal of domestic solid waste along the slopes and the stream bed, the recurrent floods, the existence of irregular and damaged networks of water and sewage that can lead the soil to saturation and contribute to weakening the land as to the triggering of landslides.

It can be inferred that for the case analyzed, the application of a qualitative method was an efficient alternative for geological-geotechnical risk zoning due to the similarities found between the maps produced from the two methodologies. A qualitative method demands lower financial, time and computational resources, but can be well applied in conditions of urban and geotechnical precariousness exposed to naked eye in field reconnaissance. Nevertheless, it is important to highlight the relevance of quantitative analyses of landslides to perform a more accurate slope stability analysis, especially for time and spatial evaluations.

Regarding the topographic survey performed by aerial photogrammetry with UAV technology, it was possible to notice that this technique has advantages over conventional topography in conditions of time, financial and access limitations. Even though this technology allows a practical and fast survey, it is an indirect technique of obtaining the three-dimensional coordinates of the terrain. Therefore, all theoretical and practical aspects of photogrammetry must be followed for the production of cartographic products with accuracy compatible with the characteristics of the project.

Based on the geological-geotechnical analyses, hydraulically oriented studies about the stream channel, and socioeconomic exams, the residences in the most vulnerable locations should be reallocated to a safer place, and intervention works should be done on the land suitable for urbanization. Thus, the vulnerability would be eliminated and the hazard reduced. In addition, the Permanent Preservation Area (PPA), meeting the Brazilian Forest Code - Law No. 12,651 (Brasil, 2012b), would be restored to preserve the natural ecosystem within the 30 m-length lane from the stream at the bottom of the Vila Nova valley – the very same most hazardous area based on the present study.

Acknowledgements

The authors thank the Federal University of Paraná, on behalf of the Geotechnics Study Group and the Geoinformation Applied Research Center for their support in carrying out this research and the Pro-Rectory of Extension and Culture for their financial support.

Declaration of interest

The authors declare that there are no conflicting interests associated with this publication among them or other parties (people, support financial agencies, etc.). They confirm that the manuscript has been read and approved by all named authors and that there are no other people who satisfied the criteria for authorship but are not listed. There is no financial interest to report.

Authors' contributions

Carla Vieira Pontes: conceptualization, data curation, formal analysis, investigation, methodology, software, validation, visualization, writing – original draft. Roberta Bomfim Boszczowski: conceptualization, funding acquisition, supervision, writing – review & editing. Leonardo Ercolin Filho: data curation, writing – review & editing.

List of symbols and abbreviations

c'	Effective intercept cohesion
h	Vertical depth of rupture surface
h_w	Vertical depth of groundwater table
SF	Safety factor
β	Slope of the terrain as well as of the failure surface
γ	Unit soil weight
γ_w	Unit water weight
τ_m	Mobilized shear strength
τ	Shear stress
$\varnothing'$	Effective internal friction angle
CEPAG	Geoinformation Applied Research Center of UFPR
GEGEO	Geotechnical Study Group of UFPR
PNPDEC	National Policy for Protection and Civil Defense (Brazil)
PPA	Permanent Prevention Area
UAV	Unmanned Aerial Vehicle
UFPR	Federal University of Paraná

References

Advincula, M.R.E. (2016). *Avaliação do efeito de aumento de poropressão nas características de resistência de três solos tropicais* [Doctoral thesis, Pontifical Catholic University of Rio de Janeiro]. Pontifical Catholic University of Rio de Janeiro's repository. https://doi.org/10.17771/PUCRio.acad.30293.

Ahrendt, A. (2005). *Movimentos de massa gravitacionais – proposta de um sistema de previsão: aplicação na área urbana de Campos do Jordão – SP* [Doctoral thesis, University of São Paulo]. University of São Paulo's repository. http://www.doi.org/10.11606/T.18.2005.tde-06102006-090547.

Brasil. (1979). Lei no 6.766, de 19 de Dezembro de 1979. Dispõe sobre o Parcelamento do Solo Urbano e dá outras Providências. *Diário Oficial [da] República Federativa do Brasil.* Retrieved in May 7, 2021, from http://www.planalto.gov.br/ccivil_03/leis/l6766.htm

Brasil. Ministério do Desenvolvimento Regional – MCID (2004). *Capacitação em mapeamento e gerenciamento de risco* (in Portuguese). Retrieved in May 7, 2021, from http://www.defesacivil.mg.gov.br/images/documentos/Defesa%20Civil/manuais/mapeamento/mapeamento-grafica.pdf.

Brasil. (2012a). Lei nº 12.608, de 10 de Abril de 2012. Institui a Política Nacional de Proteção e Defesa Civil - PNPDEC; dispõe sobre o Sistema Nacional de Proteção e Defesa Civil - SINPDEC e o Conselho Nacional de Proteção e Defesa Civil - CONPDEC; autoriza a criação de sistema de informações e monitoramento de desastres; altera as Leis nºs 12.340, de 1º de dezembro de 2010, 10.257, de 10 de julho de 2001, 6.766, de 19 de dezembro de 1979, 8.239, de 4 de outubro de 1991, e 9.394, de 20 de dezembro de 1996; e dá outras providências. *Diário Oficial [da] República Federativa do Brasil.* Retrieved in May 7, 2021, from http://www.planalto.gov.br/ccivil_03/_Ato2011-2014/2012/Lei/L12608.htm

Brasil. (2012b). Lei nº 12.651, de 25 de Maio de 2012. Prevê a proteção da vegetação nativa; altera as Leis nº 6.938, de 31 de agosto de 1981, 9.393, de 19 de dezembro de 1996, e 11.428, de 22 de dezembro de 2006; revoga as Leis 4.771, de 15 de setembro de 1965, e 7.754, de 14 de abril de 1989, e a Medida Provisória nº 2.166-67, de 24 de agosto de 2001; e dá outras providências. *Diário Oficial [da] República Federativa do Brasil.* Retrieved in May 7, 2021, from http://www.planalto.gov.br/ccivil_03/_Ato2011-2014/2012/Lei/L12651.htm

Brasil. Ministério do Desenvolvimento Regional – MCID. (2018). *Technical manual for disaster risk reduction applied to urban planning – Project to Strengthen the National Strategy for Integrated Risk Management in Natural Disasters – GIDES Project.* (in Portuguese). Retrieved in May 7, 2021, from https://www.gov.br/mdr/pt-br/centrais-de-conteudo/publicacoes/protecao-e-defesa-civil-sedec

Bressani, L.A., Bica, A.V.D., Pinheiro, R.J.B., & Rigo, M.L. (2001). Residual shear strength of some tropical soils from Rio Grande do Sul. *Solos e Rochas*, 23(2), 103-113.

BSI BS 1377-7. (1990). *Methods of test for soils for civil engineering purposes. Shear strength tests (total stress)*. BSI - British Standards Institution, London.

Duncan, J.M., Wright, S.G., & Brandon, T.L. (2014). *Soil strength and slope stability*. John Wiley & Sons.

Gerscovich, D.M. (2016). *Estabilidade de Taludes*. Oficina de Textos.

Gibson, R.E., & Henkel, D.J. (1954). Influence of duration of test at constant rate of strain on measured "drained" strength. *Geotechnique*, 4(1), 6-15. http://dx.doi.org/10.1680/geot.1954.4.1.6.

Instituto Água e Terra – IAT. (2000). *Mapas e dados espaciais*. Retrieved in May 7, 2021, from http://www.iat.pr.gov.br/Pagina/Mapas-e-Dados-Espaciais

Instituto Água e Terra – IAT. (2005). *Mapas e dados espaciais*. Retrieved in May 7, 2021, from http://www.iat.pr.gov.br/Pagina/Mapas-e-Dados-Espaciais

Instituto de Geografia e Estatística – IBGE. (2017). *Perfil dos Municípios Brasileiros – Pesquisa de Informações Básicas Municipais*. Retrieved in May 7, 2021, from https://biblioteca.ibge.gov.br/index.php/biblioteca-catalogo?view=detalhes&id=2101595

Lambe, T.W., & Whitman, R.V. (1969). *Soil mechanics, SI version*. John Wiley & Sons.

Pontes, C.V. (2019). *Análise da susceptibilidade a movimentos gravitacionais de massa da comunidade de Vila Nova, Colombo/PR* [Undergraduate Final Work, Federal University of Paraná]. Federal University of Paraná's repository. http://www.dcc.ufpr.br/portal/index.php/2020/05/05/analise-da-susceptibilidade-a-movimentos-gravitacionais-de-massa-da-comunidade-de-vila-nova-colombo-pr/

Prandini, F.L., Nakazawa, V.A., Freitas, C.G.L., & Diniz, N.C. (1995). Cartografia Geotécnica nos Planos Diretores Regionais e Municipais. In: O.Y. Bitar (Coord.). *Course in Geology Applied to the Environment* (pp. 187-202). ABGE - Brazilian Association of Engineering Geology e IPT – Technological Research Institute.

Salamuni, E. (1998). *Tectônica da Bacia Sedimentar de Curitiba (PR)* [Doctoral thesis, São Paulo State University]. Neotectonics Research Group of UFPR's repository. http://www.neotectonica.ufpr.br/grupo-teses/tese-salamuni.pdf

Serviço Geológico do Brasil – CPRM. (2018). *Manual of Mapping of Danger and Risk to Gravitational Movements of Mass - Project to Strengthen the National Strategy for Integrated Management of Natural Disasters - GIDES Project* (in Portuguese). Retrieved in May 7, 2021, from http://www.cprm.gov.br/publique/Gestao-Territorial/Prevencao-de-Desastres-Naturais/Projeto-GIDES-JICA-5393.html

Soeters, R., & van Westen, C.J. (1996). Slope stability: recognition, analysis and zonation. In: K.T. Turner & R.L.

Schuster (Eds.). *Landslides: investigation and mitigation* (pp. 129-177). National Academy Press.

Tchalenko, J.S. (1970). Similarities between shear zones of different magnitudes. *Geological Society of America Bulletin*, 81(6), 1625-1640. http://dx.doi.org/10.1130/0016-7606(1970)81[1625:SBSZOD]2.0.CO;2.

Trevizolli, M.N.B. (2018). *Proposta de modelo para avaliação de risco de deslizamentos baseado em cenários de eventos pluviométricos: aplicação em um talude da serra do mar no trecho PR/SP* [Master's Dissertation, Federal University of Paraná]. Federal University of Paraná's repository. https://hdl.handle.net/1884/58845